Optically anisotropic planar microcavities

Von der Fakultät für Physik und Geowissenschaften
der Universität Leipzig
genehmigte

DISSERTATION

zur Erlangung des akademischen Grades

Doctor rerum naturalium
Dr. rer. nat.

vorgelegt
von Herrn M. Sc. Steffen Richter
geboren am 01.10.1987 in Leipzig

Gutachter: Prof. Dr. Marius Grundmann (Universität Leipzig)
Prof. Dr. Kurt Hingerl (Johannes Kepler Universität Linz)

Tag der Verleihung: 22.01.2018

This work is published under Creative Commons license BY-NC-ND 4.0.

Bibliographische Beschreibung:

Richter, Steffen
Optically anisotropic planar microcavities
Universität Leipzig, Dissertation
166(+4) S., 182 Lit., 40 Abb., 5 Tab., 4 Anh.

Referat:

Die Arbeit untersucht planare optische Mikrokavitäten, welche aus einer beidseitig von Multischichtspiegeln umgebenen Kavitätsschicht bestehen. Im Rahmen einer Transfermatrixbeschreibung für ebene Wellen wird ein genereller Ansatz zur Berechnung von optischen Kavitätsmoden von planaren Mikrokavitäten entwickelt, welche aus optisch beliebig anisotropen Medien bestehen. Die zugrunde liegende Modenbedingung kommt ohne vorherige Einschränkungen bezüglich der betrachteten Lichtpolarisation aus. Basierend auf diesem Ansatz werden numerische Modenberechnungen von Mikrokavitäten mit optisch uniaxialen Kavitätsschichten vorgenommen. Generell sind die Moden in einem solchen System elliptisch polarisiert, und zudem i.A. nicht orthogonal. Ein besonderes Phänomen stellen sogenannte *exzeptionelle Punkte* dar. Dies sind Richtungen, für welche Energie und Verbreiterung der zwei Kavitätsphotonmoden zugleich entarten. Die Moden werden an solchen Punkten zirkular ko-polarisiert, die Orientierung der linearen Modenpolarisation windet sich im Impulsraum um diese Punkte herum. Die Eigenschaften der anisotropen Mikrokavitäten und exzeptionellen Punkte sind charakteristisch für singuläre, biaxiale Optik. So entsprechen die exzeptionellen Punkte Richtungen sogenannter *singulärer optischer Achsen* der effektiv biaxialen Strukturen, und können als Entartung nicht-Hermitescher Operatoren beschrieben werden.

Die experimentelle Realisierung wird am Beispiel ZnO-basierter Mikrokavitäten gezeigt und bestätigt die theoretischen Vorhersagen im Wesentlichen, wenngleich im Experiment keine komplett zirkular polarisierten Zustände an den Entartungspunkten beobachtet wurden.

Bibliographic Record:

Richter, Steffen
Optically anisotropic planar microcavities
Universität Leipzig, Dissertation
166(+4) pp., 182 refs., 40 figs., 5 tabs., 4 apps.

Abstract:

In this thesis, planar optical cavities are investigated. They consist of a cavity layer which is surrounded by multi-layer mirrors. Using a transfer matrix technique for planar structures, a general mode condition is developed, which allows computation of cavity-photon modes for planar microcavities, which consist of optically arbitrarily anisotropic media. With this approach, no prior restriction of the considered light polarization is required. Based on this formalism, numerical computations of planar microcavities with optically uniaxial cavity layers are performed. Generally, the cavity-photon modes in such systems obtain elliptic polarization. Furthermore, they are in general not orthogonal to each other. A particular phenomenon is the occurrence of so called *exceptional points*. Here, the two cavity-photon modes degenerate in energy and broadening simultaneously, and the modes become circularly co-polarized. In addition, the exceptional points are vortex centers in momentum space for the orientation of the linear polarization of the modes. With this, anisotropic planar microcavities show typical characteristics of singular as well as biaxial optics. The exceptional points can be regarded as *singular optic axes* of the effectively biaxial structures. They can be described by the degeneracy of non-Hermitian operators.

Experimental implementation is demonstrated by ZnO-based microcavities. In general, experimental findings prove the theoretical predictions, albeit the degree of circular polarization does not approach 100% at the exceptional points.

Wir irren allesamt, nur jeder irret anders.

G.C. Lichtenberg (1742-1799) [Lic]

first professor for experimental physics in Germany

Contents

Chapter 0

Introduction

Planar optical microcavities are stratified structures, typically consisting of a cavity layer which is surrounded by multi-layer mirrors. They are great model systems to study light-matter interaction and in particular the coupling between spin-polarization and momentum of cavity photons and polaritons [Kav+04; She+05; She+10; Dev15]. During the last years, a number of polarization-related effects have been studied in such microcavities, as e.g. the optical spin Hall effect [Kav+06; Ley+07; Mar+11], polarization rotation [Kri+06; Sol+08; Gir+12], polarization pinning/switching [Mar+02; Kło+06; She+04; Amo+10; Bha+16], evolution of non-trivial polarization patterns upon propagation [Kam+12; Mor+13; Cil+15], and a variety of polarization vortices [Lag+09; Man+11; Sal+15; Duf+15; Cil+16]. Most of these effects are based on the intrinsic splitting of a cavity mode into a transverse-electric (TE) and a transverse-magnetic (TM) polarized one, as it occurs for microcavities consisting of isotropic materials. In some cases, spontaneous symmetry breaking and a quasi-magnetization occur. Nevertheless, the main interest in such microcavities was raised by the possibility to achieve Bose-Einstein-like condensates of exciton-polaritons [Kas+06; Den+10; Dev15]. Here again, polarization plays an important role for scattering of polaritons towards the ground state, and propagation of condensates. In both cases, the linear as well as the condensate regime, quasi-particle Hamiltonians have been developed to describe the phenomena. If they consider polarization at all, they do most often rely on orthogonal polarization states, e.g. TE and TM.

Attractive materials to study exciton-polaritons in microcavities are e.g. wide-gap semiconductors like ZnO or GaN because their excitons have high binding energies and, hence, are stable at room temperature. Both are optically uniaxial [Gru06]. If optically anisotropic media are incorporated into planar microcavities, the cylindrical symmetry of the structure can be lifted. Depending on the considered propagation directions, this can yield mode conversion between TE and TM polarizations. As a consequence, modes become generally elliptically polarized and, furthermore, non-orthogonal to each other. Of similar nature are absorptive, optically biaxial media. Here, the optical propagation-eigenmodes are also generally elliptically polarized and can degenerate, resulting in so called *singular optic axes* [Voi02; Stu+16]. Along such an axis, only one circular polarization is allowed to propagate without conversion. Beyond that, the directions of the singular axes establish vortex centers for the orientation of the linear polarization components in momentum space. Mathematically, such mode degeneracies can be described as so called *exceptional points*, which require non-Hermitian operators [Ber04; Hei04a]. Non-Hermitian transfer matrices and the occurrence of exceptional points in the dispersion of cavity-photon modes are a central subject of this thesis.
Polarization vortices, again, are a typical topic in the field of singular optics [Den+09; Sos+01] where such vortices are observed in distorted wavefronts [Flo+05; Bli+08; Car+13] or even in the polarization of the sky [Cha50; Gál+01; Ber+04]. The winding number of a polarization vortex is typically either an integer or half-integer and defines a topological charge [Ang+02; Den01]. Consequently, anisotropic microcavities touch also the field of topological photonics [Lu+14]. Moreover, microcavities can even be understood as layered meta-materials [Che13].

As anisotropic microcavities span a wide field of topics, this thesis aims to summarize their characteristics and related phenomena, and compare them to other optical systems. The focus is set on microcavities with optically uniaxial, transparent cavity layer. But also the case of exciton-polaritons is discussed. This thesis is restricted to a semi-classical description based on a plane-wave approach, i.e. photons are quantized through the structure but not treated in a quantum-mechanical sense. Only the regime of linear optics is considered. Furthermore, only radiative modes are investigated and bulky microcavities

are assumed, i.e. no quantum wells are embedded in a cavity layer.
An important initial question is how to obtain optical mode energies and polarization without restricting the possible polarization before-hand. Therefore, the thesis consists of a comprehensive theory part (chapters 1 and 2). These chapters provide the physical and mathematical basis for the description of optical modes in anisotropic, planar structures. Many important aspects of biaxial optics and the mathematical description of optical modes are neither examined in detail in textbooks nor sufficiently considered in published research articles. The theory chapters aim to fill this gap. Most important within the scope of this thesis is the generalization of the mode condition in the frame of a complex 4×4 transfer matrix which had not been shown before. Application of the presented theory by numerical computations of modes in anisotropic planar microcavity structures yields the observation of generally elliptically polarized modes and exceptional points where the modes coalesce and can become circularly polarized. These phenomena are presented, interpreted and classified in chapter 3.

Anisotropic microcavities are not a new subject in the Semiconductor Physics Group in Leipzig. In particular, this thesis builds on great experience with ZnO-based microcavities [Sch07; Stu11; Fra12]. ZnO has been of special interest because it reveals excitons which are stable at room temperature (60 meV binding energy). This and other reasons make it advantageous to achieve Bose-Einstein-like condensation of exciton-polaritons [Zam+02; Fau+08]. Indeed, condensation in ZnO-based microcavities has been observed at temperatures close too and even at room temperature [Fra+12; Gui+11; Li+13; Jam+17]. ZnO crystallizes in wurtzite structure and, hence, is optically uniaxial [Sch07; Kli+10; Has+14]. So far, the microcavities grown in Leipzig had a c-plane oriented ZnO cavity layer [Fra12]. However, already some years ago, the question arose, how cavity-photon modes evolve if the optic axis is tilted into the cavity plane [Stu11]. Though, the solutions which had been found so far are only valid for pseudo-isotropic configurations, i.e. if propagation directions exactly perpendicular or parallel to the optic axis of the ZnO cavity layer are considered. In other cases, TE and TM polarization must not be considered independently, as mentioned above. This thesis continues the existing considerations at that point.

Meanwhile, also experimental realization has become possible [Zúñ+16]. Epitaxially grown m- and r-plane oriented samples have been provided by Jesús Zúñiga-Pérez and Christiane Deparis from *Centre de Recherche sur l'Hétéro-Epitaxie et ses Applications* (CRHEA), *Centre national de la recherche scientifique* (CNRS), Valbonne, France. The experimental work is still in progress. First experimental results are presented in chapter 4.

Chapter 1

Theory I: Linear optics principles

In this chapter, principles of the description of light and its interaction with matter are introduced. They are the basis of the considerations regarding the microcavities. Accordingly, it is focused on those parts of the theory, which are substantial for optical modes in anisotropic microcavities; in particular:

- the complex-valued nature of the wave vector,
- effects of optically biaxial crystals and related tensors, including the role of optic axes,
- derivation of polariton energies and related Hamiltonians, and
- 4×4 transfer matrix formalism for planar structures.

A more comprehensive introduction can be found in e.g. [Bor+80; Lan+67; Jac83; Kli07; Mac61; Str41; Cle66; Yar+84]. Within this thesis, SI unit conventions are chosen. The respective expressions in Gaußian CGS units can be found in appendix A.3.

1.1 Maxwell theory

The laws of classical electrodynamics and hence light propagation are set by Maxwell's equations which read in macroscopic form

$$
\begin{aligned}
\vec{\nabla}\vec{\mathcal{D}} &= \rho\,, & (1.1)\\
\vec{\nabla}\vec{\mathcal{B}} &= 0\,, & (1.2)\\
\vec{\nabla}\times\vec{\mathcal{E}} &= -\frac{\partial\vec{\mathcal{B}}}{\partial t}\,, & (1.3)\\
\vec{\nabla}\times\vec{\mathcal{H}} &= \frac{\partial\vec{\mathcal{D}}}{\partial t}+\vec{j}\,. & (1.4)
\end{aligned}
$$

Gauß's law, Eq. 1.1, defines an electric charge density ρ as source of an electric displacement field $\vec{\mathcal{D}}$, while Gauß's law for magnetism, Eq. 1.2, states that no monopoles of the magnetic flux $\vec{\mathcal{B}}$ exist. Faraday's law, Eq. 1.3, describes how a magnetic flux density, which changes in time, induces electric fields $\vec{\mathcal{E}}$. And Ampère's law, Eq. 1.4, explains how a time-varying electric displacement as well as an electric current $\vec{j}$ can create a magnetic field $\vec{\mathcal{H}}$. ρ is the density of free charge carriers. The additional effect of bound carriers would be given by an additional component $\rho_b = -\vec{\nabla}\vec{\mathcal{P}}_{rem}$ on the r.h.s. of Eq. 1.1, related to a remanent electric polarization $\vec{\mathcal{P}}_{rem}$. Similarly, $\vec{j}$ is the current density due to free charge carriers only. An additional bound component to the r.h.s. of Eq. 1.4 due to remanent magnetization $\vec{\mathcal{M}}_{rem}$ and polarization $\vec{\mathcal{P}}_{rem}$ would be given as $\vec{j}_b = \vec{\nabla}\times\vec{\mathcal{M}}_{rem} + \frac{\partial\vec{\mathcal{P}}_{rem}}{\partial t}$. Remanent fields play usually no direct role for the rapidly varying ac-fields of visible light.

Maxwell's equations go along with the material equations (or constitutive relations) which read in SI units[1]

$$
\begin{aligned}
\vec{\mathcal{D}} &= \varepsilon_0\vec{\mathcal{E}}+\vec{\mathcal{P}} &&= \varepsilon_0\hat{\varepsilon}\vec{\mathcal{E}}\,, & (1.5)\\
\vec{\mathcal{B}} &= \mu_0(\vec{\mathcal{H}}+\vec{\mathcal{M}}) &&= \mu_0\hat{\mu}\vec{\mathcal{H}}\,, & (1.6)
\end{aligned}
$$

with the electric field ($\vec{\mathcal{E}}$) induced electric polarization $\vec{\mathcal{P}}$ and magnetic field ($\vec{\mathcal{H}}$) induced magnetization $\vec{\mathcal{M}}$, and with vacuum permittivity ε_0 and vacuum permeability μ_0. $\hat{\varepsilon}$ and $\hat{\mu}$ are the unitless tensors of the dielectric function (also called permittivity) and magnetic permeability, respectively. Both are directly connected to the respective susceptibility tensors by $\hat{\varepsilon} = (\hat{\mathbb{1}} + \hat{\chi}_{\mathcal{E}})$ and $\hat{\mu} = (\hat{\mathbb{1}} + \hat{\chi}_{\mathcal{H}})$. Within the frame of linear optics, both, $\hat{\epsilon}$ and $\hat{\mu}$ are represented by 3×3 matrices. For magnetic fields varying at high (i.e. optical) frequency $f \gg 0$, $\hat{\mu} = \hat{\mathbb{1}}$ can be assumed. If not indicated otherwise this will be applied

---

[1] Magneto-electric coupling shall be neglected.

throughout this thesis. The connection between the generally complex-valued tensors of the dielectric function $\hat{\epsilon} = \hat{\epsilon}_1 + i\hat{\epsilon}_2$ and the complex refractive index $\hat{\tilde{n}} = \hat{n} + i\hat{\kappa}$ is given by Maxwell's relation:

$$\hat{\varepsilon} \;=\; \hat{\varepsilon}\hat{\mu} \;=\; \hat{\tilde{n}}^2\,. \tag{1.7}$$

In isotropic media, it holds $\hat{\varepsilon} = \varepsilon\hat{\mathbb{1}}$. Hence, the optical constants can be described by a scalar $\varepsilon = \tilde{n}^2 = (n+i\kappa)^2$. It should be noted that the extinction coefficient (or absorption index) κ differs from the attenuation coefficient (or absorption coefficient) α which is used in the Lambert-Beer law. It holds $\alpha = 4\pi\frac{\kappa}{\lambda} = \frac{2}{\hbar c_0}\kappa E$, with reduced Planck constant $\hbar = h/(2\pi)$, vacuum speed of light c_0, photon energy E and wavelength λ. It is also common to express the material response to electric fields in terms of a complex-valued optical conductivity (in SI units) $\hat{\sigma} = -i\frac{\varepsilon_0 E}{\hbar}\hat{\varepsilon}$.

Resolving Eq. 1.7 for vacuum, the speed of light can be expressed as $c_0 = 1/\sqrt{\varepsilon_0\mu_0}$.

1.1.1 Plane-wave ansatz

First a homogeneous dielectric medium is assumed, i.e. $\rho = 0$, $\vec{j} = \vec{0}$ and thus $\hat{\varepsilon} \in \mathbb{R}^{3\times3}$. Furthermore, at least $\hat{\mu} = \mu\hat{\mathbb{1}}$ is required to ensure $\vec{\nabla} \times \vec{\mathcal{B}} = \mu_0\hat{\mu}(\vec{\nabla} \times \vec{\mathcal{H}})$. In general, the rotation operator does not commute with the transformation of the fields, e.g., $\vec{\nabla} \times \vec{\mathcal{D}} \not\equiv \varepsilon_0\hat{\varepsilon}(\vec{\nabla} \times \vec{\mathcal{E}})$. With those assumptions, the rotation operator $\vec{\nabla}\times$ can be applied to the l.h.s. and r.h.s of Faraday's law, Eq. 1.3, and the time derivative $\frac{\partial}{\partial t}$ to the l.h.s. and r.h.s of Ampère's law, Eq. 1.4. Deploying one to the other yields the homogeneous wave equation[2]

$$\vec{\nabla} \times (\vec{\nabla} \times \vec{\mathcal{E}}) + \frac{\partial^2}{\partial t^2}\mu_0\mu\varepsilon_0\hat{\varepsilon}\vec{\mathcal{E}} = \vec{\nabla}(\vec{\nabla}\vec{\mathcal{E}}) - \vec{\nabla}^2\vec{\mathcal{E}} + \frac{\mu}{c_0^2}\frac{\partial^2}{\partial t^2}(\hat{\varepsilon}\vec{\mathcal{E}}) = \vec{0}\,. \tag{1.8}$$

For isotropic media, the divergence of $\vec{\mathcal{E}}$ disappears and the wave equation takes the following form, which yields a Helmholtz equation:

$$\nabla^2\vec{\mathcal{E}} - \frac{\mu}{c_0^2}\frac{\partial^2}{\partial t^2}(\varepsilon\vec{\mathcal{E}}) = \vec{0}\,. \tag{1.9}$$

A particular solution to the wave equation which describes propagation of light in a homogeneous medium is given by a plane harmonic wave as

$$\vec{\mathcal{E}} = \vec{\mathcal{E}}_0\; e^{i(\vec{k}\vec{r}-\omega t)}\,, \tag{1.10}$$

---

[2] For derivation of a more rigorous matrix wave equation, see [Ber72].

with $\vec{\mathcal{E}}_0 \in \mathbb{C}^3$ describing the amplitude and initial phase of the electric field. The actual measurable fields are given then as the real part of the plane-wave function. Temporal evolution of the fields is determined by the angular frequency ω as $\frac{\partial}{\partial t}\vec{\mathcal{E}} = -i\omega\vec{\mathcal{E}}$; spatial evolution by the wave vector[3] $\vec{k}$ with $\vec{\nabla}\vec{\mathcal{E}} = i\vec{k}\vec{\mathcal{E}}$. Plane-wave functions for $\vec{\mathcal{H}}$, $\vec{\mathcal{D}}$ and $\vec{\mathcal{B}}$ can be deduced from Eq. 1.10 accordingly by applying Eqs. 1.1-1.6. Due to the rotation operator not commuting with $\hat{\varepsilon}$, Eq.1.8 becomes more complicated then (cf. appendix A.1). For the relation between the light's angular frequency ω, its frequency f, related photon energy E, and (isotropic) wavelength in the medium λ and in vacuum λ_0, it holds

$$\hbar\omega = hf = E = \frac{hc_0}{\lambda_0} = \frac{hc_0}{n\lambda}\,. \tag{1.11}$$

It should be noted that the wavelength is shortened in a medium where the light propagates slower than in vacuum ($n > 1$)[4].

Applying the plane-wave solution, $\frac{\partial}{\partial t} = -i\omega$ and $\vec{\nabla} = i\vec{k}$ to Faraday's law, Eq. 1.3, and Ampère's law, Eq. 1.4, yields $\omega\mu_0\hat{\mu}\vec{\mathcal{H}} = \vec{k} \times \vec{\mathcal{E}}$ and $\omega\vec{\mathcal{D}} = \vec{\mathcal{H}} \times \vec{k}$, respectively. That means, $\vec{k} \perp \vec{\mathcal{D}}$ and $\vec{k} \perp \vec{\mathcal{B}}$, as well as $\vec{\mathcal{H}} \perp \vec{\mathcal{D}}$ and $\vec{\mathcal{E}} \perp \vec{\mathcal{B}}$. With $\hat{\mu} = \mu\hat{\mathbb{1}}$, it holds also $\vec{k} \perp \vec{\mathcal{H}}$ and $\vec{\mathcal{E}} \perp \vec{\mathcal{H}}$. Then, there are two orthogonal tripods: $\vec{k}$, $\vec{\mathcal{D}}$ and $\vec{\mathcal{H}}$ with $\vec{e}_k = \vec{e}_{\mathcal{D}} \times \vec{e}_{\mathcal{H}}$, and $\vec{k}$, $\vec{\mathcal{D}}$ and $\vec{\mathcal{B}}$ with $\vec{e}_k = \vec{e}_{\mathcal{D}} \times \vec{e}_{\mathcal{B}}$. In general, $\vec{\mathcal{E}}$ is in optically anisotropic media ($\hat{\varepsilon} = \varepsilon\hat{\mathbb{1}}$) not orthogonal to $\vec{k}$. Hence, as a normal vector, $\vec{k}$ describes only the orientation of the wave fronts. The direction of the energy flux and hence orientation of a light ray is given by the Poynting vector[5] $\vec{\mathcal{S}}$ [Jac83]:

$$\vec{\mathcal{S}} = \vec{\mathcal{E}} \times \vec{\mathcal{H}}^*\,, \tag{1.12}$$

Now, $\vec{\mathcal{S}}$, $\vec{\mathcal{E}}$ and $\vec{\mathcal{H}}$ are found as an orthogonal tripod and $\vec{\mathcal{S}} \in \mathbb{R}^3$ in transparent media. Still, $|\vec{\mathcal{S}}|$ oscillates in time. Usually, the time-averaged effective value

---

[3] Within this thesis, wave vector, momentum, and propagation direction are partly used as synonyms. Also, the magnitude of the wave vector, k ($\vec{k} = k\vec{e}_k$), is still called wave *vector* instead of wave *number*.

[4] In absorbing media ($\tilde{n} = n + i\kappa$), the relation $\lambda = \lambda_0/n$ does only hold for complex wave-vectors and real-valued photon-energies. If a real-valued wave-vector and a complex frequency is considered, it is replaced by $\lambda = \frac{\lambda_0}{n+\kappa^2/n}$ [Mic17]. See section 1.1.4.

[5] Note the complex conjugation. Otherwise, the direction of the light ray would oscillate in time. However, there are cases where indeed the direction oscillates in time, yielding an angular spread. In particular, this occurs if an inhomogeneous plane wave with $\mathrm{Im}(\vec{k}) \nparallel \mathrm{Re}(\vec{k})$ hits an interface [Cha+05; Che+11].

$\langle|\vec{\mathcal{S}}|\rangle = \frac{1}{2}\mathcal{S}_0$ (with amplitude $\mathcal{S}_0$) is treated as light intensity I or field energy [Yar+84]. Only in isotropic media, it holds generally $\vec{\mathcal{S}}||\vec{k}$.

If a medium is absorptive it holds $\hat{\varepsilon} \in \mathbb{C}^{3\times 3}$. Then, Ampère's law, Eq. 1.4, can be reduced to $\vec{\nabla} \times \vec{\mathcal{H}} = \frac{\partial \vec{\mathcal{D}}}{\partial t}$ if the only currents are those induced by the electric fields of the light $\vec{j} = \vec{j}_{opt}$, which are intrinsically expressed through the optical conductivity tensor $\hat{\sigma}$ (see above) as $\mathrm{Im}(\hat{\varepsilon})$ as follows:

$$\vec{j}_{opt} \equiv \mathrm{Re}(\hat{\sigma})\vec{\mathcal{E}} = \omega\varepsilon_0\mathrm{Im}(\hat{\varepsilon})\vec{\mathcal{E}} = i\varepsilon_0\mathrm{Im}(\hat{\varepsilon})\frac{\partial}{\partial t}\vec{\mathcal{E}} = i\mathrm{Im}(\frac{\partial}{\partial t}\vec{\mathcal{D}})\,, \tag{1.13}$$

$$\text{while} \qquad \varepsilon_0\mathrm{Re}(\hat{\varepsilon})\frac{\partial}{\partial t}\vec{\mathcal{E}} = \mathrm{Re}(\frac{\partial}{\partial t}\vec{\mathcal{D}})\,. \tag{1.14}$$

Furthermore, it still can be assumed that the medium is homogeneous on a local range corresponding to the wavelength of the light and on a temporal scale corresponding to the light frequency (due to relaxation times in the order of 10^{-18}s [Bor+80]). Thus, $\vec{\nabla}\rho = \vec{0}$ and one gets the same homogeneous wave equation as Eq. 1.8 with complex-valued $\hat{\varepsilon} \in \mathbb{C}^{3\times 3}$ and $\vec{\tilde{k}} = \vec{k} + i\vec{\eta}$:

$$-\vec{\tilde{k}}(\vec{\tilde{k}}\vec{\mathcal{E}}) + \vec{\tilde{k}}^2\vec{\mathcal{E}} - \frac{\omega^2\mu}{c_0^2}(\hat{\varepsilon}\vec{\mathcal{E}}) = \vec{0}\,. \tag{1.15}$$

Hence, Eq. 1.10 remains valid but with complex optical constants and a complex wave-vector $\vec{k} \in \mathbb{C}^3$:

$$\vec{\tilde{k}}^2 = \frac{\tilde{n}^2\omega^2}{c_0^2} = \varepsilon\frac{E^2}{\hbar^2 c_0^2}\,. \tag{1.16}$$

This equation is referred to as polariton equation or dispersion relation. Its importance lies in the fact that generally $\varepsilon = \varepsilon(E)$ (cf. section 1.1.4). In Eq. 1.16, $\tilde{n}$ or ε are the scalar optical constants which belong to the considered wave with a given polarization (cf. sections 1.1.2 and 1.2). The simplest solution to Eq. 1.16 is $\tilde{k} = \tilde{n}\frac{E}{\hbar c_0}$ with $\vec{\tilde{k}} = (k + i\eta)\vec{e}_k$. If $\tilde{k} = k \in \mathbb{R}$, it holds $k = 2\pi/\lambda$. Otherwise it should also be noted that $\vec{\tilde{k}}^2 \neq \vec{\tilde{k}}\vec{\tilde{k}}^*$.

With complex $\vec{\tilde{k}}$, the plane wave is generally called *inhomogeneous*[6] [Str41; Cle66]. The positive imaginary part of the wave vector $\vec{\eta} = \mathrm{Im}(\vec{\tilde{k}})$ describes the direction of damping of the wave amplitude while its real part $\vec{k} = \mathrm{Re}(\vec{\tilde{k}})$ describes the propagation direction of the wave front. The above discussed orthogonality relations remain valid only in a sense that the cross-products

---

[6] Depending on the source in the literature, a plane wave in absorbing medium is still called *homogeneous* if $\mathrm{Re}(\vec{\tilde{k}}) \parallel \mathrm{Im}(\vec{\tilde{k}})$.

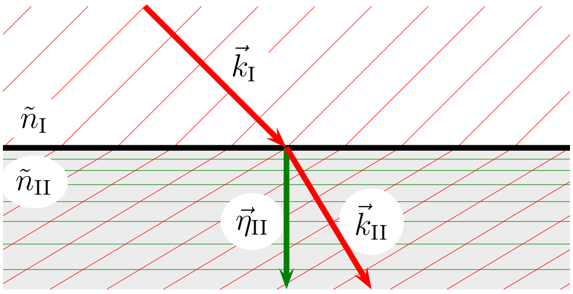

Figure 1.1: Inhomogeneous plane wave in an absorbing medium II ($\tilde{n}_{\mathrm{II}} \in \mathbb{C}$), induced by an incident homogeneous plane wave in medium I ($\tilde{n}_{\mathrm{I}}$). The real part of the wave vector $\vec{k}_{\mathrm{II}} = \mathrm{Re}(\tilde{\vec{k}}_{\mathrm{II}})$ is the normal to the wave front (red) and is determined by the incoming wave front $\tilde{\vec{k}}_{\mathrm{I}} = \vec{k}_{\mathrm{I}} \in \mathbb{R}^3$; the imaginary part $\vec{\eta} = \mathrm{Im}(\tilde{\vec{k}}_{\mathrm{II}})$ is the normal to planes of constant amplitude (green) and determined by the interface.

in Faraday's and Ampère's law, Eqs. 1.3 and 1.4, remain valid. Consequently, the direction of $\vec{k}$ is slightly changed by the absorption and the Snell-Descartes law needs to be modified [Str41; Dup+94]. Further, $\vec{k}$ and $\vec{\eta}$ do not need to be collinear; instead, their directions are defined by boundary conditions. If, e.g., a homogeneous plane wave passes an interface to an absorbing medium under oblique angle, the angle of the wave front ($\vec{k}$, normal to the planes of constant phase) in the medium is determined by a modified Snell-Descartes law. However, the direction of the damping ($\vec{\eta}$, normal to planes of constant amplitude) is perpendicular to the interface. This situation is illustrated in Fig. 1.1. This is also the common approach applied by transfer matrix techniques for planar stratified systems in a transparent ambient medium (e.g. vacuum), where it is assumed that $\mathrm{Im}(\tilde{k}_x) = \mathrm{Im}(\tilde{k}_y) = 0$ and only $\mathrm{Im}(\tilde{k}_z) \neq 0$ (cf. section 1.2).
If one assumes $\vec{k}$ and $\vec{\eta}$ to be collinear, $\tilde{\vec{k}} = (k + i\eta)\vec{e}_k$, Eq. 1.10 can also be written with a real-valued wave-vector such that $\eta = 0$, introducing a complex angular frequency $\tilde{\omega} = \omega - i\gamma$ (or photon energy $\tilde{E} = E - i\Gamma$) with negative imaginary part:

$$e^{i(\tilde{\vec{k}}\vec{r}-\omega t)} = e^{i(\vec{k}\vec{r}-\omega t)-\vec{\eta}\vec{r}} = e^{i(\vec{k}\vec{r}-\omega t)-\gamma t} = e^{i(\vec{k}\vec{r}-\tilde{\omega} t)}\,. \tag{1.17}$$

Accordingly, $\gamma = \frac{1}{t}\vec{r}\vec{\eta} = \frac{c_0}{n}\eta$ would express the damping of an electromagnetic field in time at a certain point in space in an absorbing medium. Whether this formulation is reasonable, depends on the experimental setup to be described [Kli07; Mic17]. Special cases are the computation of optical modes of a structure embedded in a transparent ambient medium like vacuum. Here a diverging-wave ansatz can be chosen where $\vec{k}$ and $\vec{\eta}$ point into opposite directions, similarly to a negative value for η, and at the same time it holds $\Gamma = \hbar\gamma = -\mathrm{Im}(\tilde{E}) > 0$ in order to fulfill Gauß's law, Eq. 1.1, in a transparent ambient medium like the vacuum (see section 2.2).

1.1.2 Light polarization

Assuming a light ray propagates along the z direction in a Cartesian coordinate system, $\vec{\mathcal{S}} \parallel \vec{e}_z$. Then, the electric-field vector can be oriented arbitrarily in the xy plane, $\vec{\mathcal{E}} = (\mathcal{E}_x, \mathcal{E}_y)^{\mathrm{T}}$. According to Ampère's or Faraday's laws Eqs. 1.3/1.4, the magnetic field flux in SI units is directly given with the electric field as[7] $\vec{\mathcal{B}} = (\mathcal{B}_x, \mathcal{B}_y)^{\mathrm{T}} = \frac{\tilde{n}}{c_0}(-\mathcal{E}_y, \mathcal{E}_x)^{\mathrm{T}}$. Similarly, $\vec{\mathcal{D}}$ and $\vec{\mathcal{B}}$ are directly determined by $\vec{\mathcal{E}}$, although $\vec{k}$ is generally not parallel to the z axis. Hence, it is sufficient to describe the light ray by only considering its electric field. The orientation of the electric field in the xy plane and the relative phase of the two linearly independent basis field-vectors, e.g. $\vec{\mathcal{E}_x} = (\mathcal{E}_x, 0)^{\mathrm{T}}$ and $\vec{\mathcal{E}_y} = (0, \mathcal{E}_y)^{\mathrm{T}}$, defines the light polarization. The notation of polarization as two-dimensional, complex-valued vector is called Jones vector $\vec{J}$. If only the light polarization is of interest but not its intensity $I \propto \vec{\mathcal{E}}\vec{\mathcal{E}}^*$ and absolute light phase, a normalized Jones vector $\vec{J}\vec{J}^* = 1$ can be used, e.g. [Fuj07]

$$\vec{J} = \begin{pmatrix} \mathcal{E}_x \\ \mathcal{E}_y \end{pmatrix} = \begin{pmatrix} \sin(\Psi) e^{i\Delta} \\ \cos(\Psi) \end{pmatrix} , \tag{1.18}$$

with the ratio between the field amplitudes of the linear basis polarization $\vec{\mathcal{E}} || \vec{x}$ and $\vec{\mathcal{E}} || \vec{y}$ given by $\tan\Psi = |\mathcal{E}_x / \mathcal{E}_x|$ (with $0 \leq \Psi \leq \frac{\pi}{2}$) and their relative phase by Δ. With the basis polarizations $\vec{\mathcal{E}_x}$, $\vec{\mathcal{E}_y}$, a value of Δ corresponding to a multiple of π expresses linearly polarized light; a multiple of π plus $\frac{\pi}{2}$ expresses circularly polarized light. Other values yield elliptic polarizations. Depending on the problem, parametrizations different from (Ψ, Δ) may be more useful [Azz+77]. In the Jones calculus, Jones matrices $\hat{J}$ describe the evolution of a Jones vector upon propagation, reflection, transmission or similar: $\vec{J}_{out} = \hat{J}\vec{J}_{in}$ (cf. section 1.2.2). Usually, Jones matrices are defined as being norm-conserving. However, an unnormalized Jones matrix can not only describe the change of light polarization but also the change of intensity (cf. section 1.2).

---

[7] in Gaußian CGS system it would hold $\vec{\mathcal{B}} = \tilde{n}(-\mathcal{E}_y, \mathcal{E}_x)^{\mathrm{T}}$

A Jones vector is not capable of describing unpolarized light, i.e. a statistical mixture of light waves with different polarizations. The real-valued 4-component Stokes vector $\vec{S}$ serves for that purpose. It is defined by the absolute light intensity (S_0, if normalized $S_0 = 1$), as well as the intensity ratios between the basis polarizations (S_1), and the intensity ratios of their superpositions (S_2, S_3): For the linear basis polarizations $\vec{\mathcal{E}}_x$ and $\vec{\mathcal{E}}_y$, the S_2 value corresponds to the intensity difference of light which is linearly polarized with orientation $+45°$ and $-45°$ tilted against the x axis. S_3 corresponds to the difference between right or left circularly polarized intensities:

$$\vec{S} = \begin{pmatrix} S_0 \\ S_1 \\ S_2 \\ S_3 \end{pmatrix} = \begin{pmatrix} I \\ I_x - I_y \\ I_{+45} - I_{-45} \\ I_R - I_L \end{pmatrix} = \begin{pmatrix} \mathcal{E}_x\mathcal{E}_x^* + \mathcal{E}_y\mathcal{E}_y^* \\ \mathcal{E}_x\mathcal{E}_x^* - \mathcal{E}_y\mathcal{E}_y^* \\ \mathcal{E}_x\mathcal{E}_y^* + \mathcal{E}_x^*\mathcal{E}_y \\ i(\mathcal{E}_x^*\mathcal{E}_y - \mathcal{E}_x\mathcal{E}_y^*) \end{pmatrix} = \begin{pmatrix} 1 \\ -\cos(2\Psi) \\ \sin(2\Psi)\cos(\Delta) \\ -\sin(2\Psi)\sin(\Delta) \end{pmatrix} . \tag{1.19}$$

It is a matter of definition if i) $S_3 = 1$ represents right or left circularly polarized light and ii) if $\Delta = +\frac{\pi}{2}$ is associated with right or left circular polarization. With Δ defined as in Eq. 1.18, $\Delta = +\frac{\pi}{2}$, i.e. $\mathcal{E}_x$ is a quarter wave ahead $\mathcal{E}_y$ during the forward propagation in space, is commonly referred to as left circular polarization. This expresses the handedness of the rotation of the electric-field vector in space. However, at the same time $\mathcal{E}_y$ is a quarter period ahead $\mathcal{E}_x$ in time. Hence, in time domain, $\Delta = +\frac{\pi}{2}$ corresponds to right-handedness. Likewise this is true for a receiver of light, looking towards the source. Equation 1.19 implies $\Delta = +\frac{\pi}{2} \Leftrightarrow S_3 < 0 \Leftrightarrow$ left circular polarization.

The degree of light polarization is given by $\sqrt{S_1^2 + S_2^2 + S_3^2}/S_0$. The corresponding matrices, describing the evolution of the polarization given by a Stokes vector, are Müller matrices: $\vec{S}_{out} = \hat{M}\vec{S}_{in}$. Again, it is common to normalize a Müller matrix by dividing all elements by M_{11} which expresses unpolarized absolute reflectance or transmittance.

Any two-state system can be described as a pseudo-$\frac{1}{2}$-spin system, where an arbitrary (polarization) state is given by a pseudospin Bloch-vector $\vec{P}$ as superposition of the pseudospin-up and pseudospin-down state. The complex coefficients are formally equivalent to the Jones vector components. The Jones vector itself is formally equivalent to a pseudospin Bloch-vector with respec-

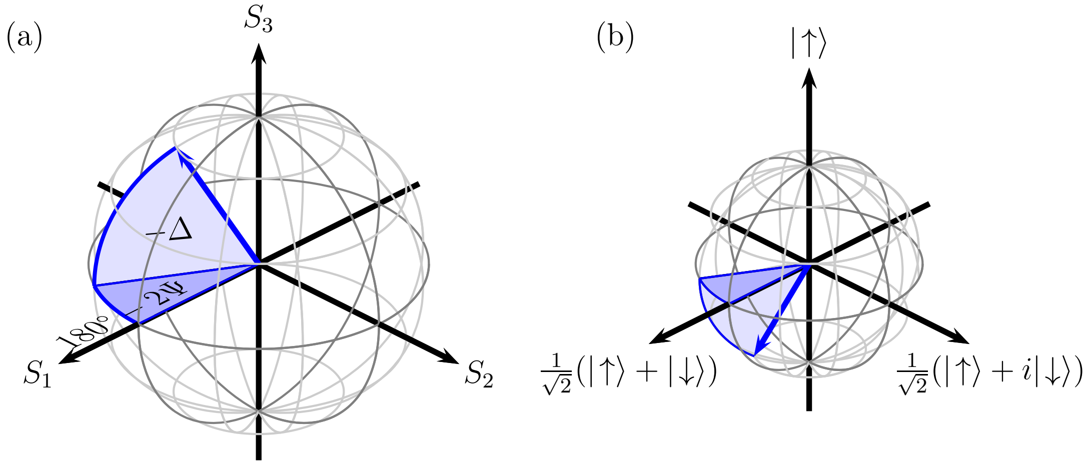

Figure 1.2: (a) Poincaré sphere (radius 1) representing the polarization states as (normalized) Stokes vector $\vec{S} = \frac{1}{S_0}(S_1, S_2, S_3)^{\mathrm{T}}$ in the basis of right (north pole) and left (south pole) circularly polarized light. Linear polarization states are represented by points on the equator line. (b) Bloch sphere (radius $\frac{1}{2}$) representing a pseudospin state $\vec{P}$ in the basis spin-up $|\uparrow\rangle$ and spin-down $|\downarrow\rangle$.

tive basis states. However, while a Bloch vector or pseudospin has a length of $\frac{1}{2}$, a Jones vector (and Stokes vector) is normalized with $\vec{J}\vec{J}^* = S_0 = 1$. Thus, the pseudospin Bloch-sphere (radius $\frac{1}{2}$) becomes a unit sphere for the Jones or Stokes vector. Commonly, left and right circularly polarized light (corresponding to spin up and down, respectively) are chosen as basis states and the respective unit sphere is called Poincaré sphere. Usually, right circular polarization is chosen as north pole of the Poincaré sphere while spin-up is often chosen as north pole for the pseudospin Bloch sphere. As left-handedness means mathematical positive orientation of a corresponding rotation vector (i.e., aligned with the propagation direction), left-handedness is usually associated with spin-up. Figure 1.2 illustrates the correspondence of polarization and pseudospin vectors. Any Jones vector or pseudospin specifies a point on the Poincaré sphere's surface. The related three-dimensional coordinates correspond to the (fully polarized) Stokes vector according to Eq. 1.19. Hence, the intersections with the principal coordinate system axes correspond to linearly polarized light parallel x, parallel y, tilted +45° and −45° against the x axis (principal states on the equator), as well as right and left circularly polarized (poles). For the pseudo-$\frac{1}{2}$-spin, the x, y and z coordinates correspond to the eigenvalues of the respective Pauli spin-matrices, applied to the given state ($s_{x,y,z} \leq \frac{1}{2}$). Additionally, a Stokes vector representing depolarized light does

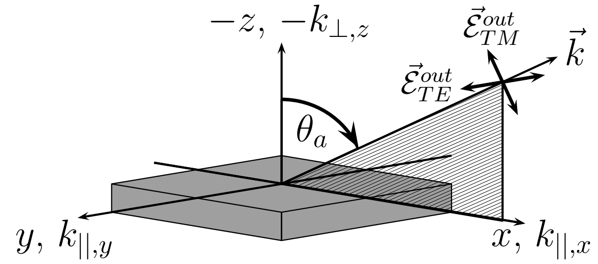

Figure 1.3: Definition of the laboratory coordinate system $\vec{r} = (x, y, z)^{\mathrm{T}}$ and photon wave-vector $\vec{k}$. The POI (marked plane) defines TE and TM basis polarization states. In the ambient medium (n_a), it holds $\vec{k}_{||} = \frac{E}{\hbar c_0} n_a \sin(\theta_a)$.

not point to the surface of the Poincaré sphere but is shorter. Fully depolarized light ($\vec{S} = (1, 0, 0, 0)^{\mathrm{T}}$) would be represented as zero vector. In terms of pseudospin, depolarized light is no pure state but an incoherent superposition. This is the reason why a Jones vector cannot express depolarized light. From considering the different representations, it is clear that, for a fully polarized Stokes vector, $(S_1, S_2, S_3)^{\mathrm{T}}$ is the $SO(3)$ representation of a $SU(2)$ group Jones or pseudospin vector, i.e. they are homomorph [Kos+08].

The choice of basis polarization states is generally arbitrary as long as they are linearly independent, i.e. their linear hull spans the whole Poincaré sphere. With respect to planar structures, it is convenient to define the basis polarizations according to the direction of light propagation and the orientation of the planar interface (surface): The surface normal and an incident light ray span the so called plane of incidence (POI) and define two linear basis polarizations: transverse-electric (TE) light is that one with electric-field vector always perpendicular to the POI, transverse-magnetic (TM) the one with electric-field vector parallel to the POI. $\vec{\mathcal{E}}_{TE}$ and $\vec{\mathcal{E}}_{TM}$ are depicted in Fig. 1.3. Commonly, TE is also referred to as s polarization (*senkrecht*) and TM as p polarization (*parallel*). The advantage of those orthogonal basis polarization states is that no polarization conversion occurs upon propagation through isotropic media, including reflection at and transmission through interfaces, even at oblique angle. TE and TM polarization are the eigenstates of the respective propagators (cf. section 1.2.1).

1.1.3 Crystal optics

In the frame of linear optics, according to Eq. 1.5, the dielectric function is a complex tensor of rank 2, i.e. $\hat{\varepsilon} \in \mathbb{C}^{3\times 3}$. As long as no magnetic fields are considered, $\hat{\varepsilon}$ is symmetric (generally not Hermitian) for all wavelengths. Magnetic fields would yield anti-symmetric contributions[8].

For application, a dielectric function tensor generally needs to be oriented according to the laboratory coordinate system. For $\hat{\varepsilon}$ defined in a Cartesian coordinate system (x_0, y_0, z_0) aligned with some principal axes of the crystal, a coordinate transformation from the laboratory system (x, y, z) to the (x_0, y_0, z_0) system is carried out by Euler rotation matrices $\hat{\mathcal{R}}$ as

$$\hat{\varepsilon} = \begin{pmatrix} \varepsilon_{xx} & \varepsilon_{xy} & \varepsilon_{xz} \\ \varepsilon_{xy} & \varepsilon_{yy} & \varepsilon_{yz} \\ \varepsilon_{xz} & \varepsilon_{yz} & \varepsilon_{zz} \end{pmatrix} = \hat{\mathcal{R}} \hat{\varepsilon}_{x0,y0,z0} \hat{\mathcal{R}}^{-1} , \tag{1.20}$$

where $\hat{\mathcal{R}} = \hat{\mathcal{R}}(\phi, \vartheta, \xi)$ is given by [Gol59; Woo10]

$$\hat{\mathcal{R}}(\phi, \vartheta, \xi) =$$
$$\begin{pmatrix} \cos(\phi) & -\sin(\phi) & 0 \\ \sin(\phi) & \cos(\phi) & 0 \\ 0 & 0 & 1 \end{pmatrix} \begin{pmatrix} 1 & 0 & 0 \\ 0 & \cos(\vartheta) & -\sin(\vartheta) \\ 0 & \sin(\vartheta) & \cos(\vartheta) \end{pmatrix} \begin{pmatrix} \cos(\xi) & -\sin(\xi) & 0 \\ \sin(\xi) & \cos(\xi) & 0 \\ 0 & 0 & 1 \end{pmatrix} ,$$

with the Euler angles (ϕ, ϑ, ξ). Physically, this transformation describes 1) ϕ rotation about $\vec{z}$ (mathematically positive in the xy plane, $\vec{z}' = \vec{z}$); 2) ϑ rotation about $\vec{x}'$ (mathematically positive in the $y'z$ plane); 3) ξ rotation about $\vec{z}''$. The resulting coordinates correspond to x_0, y_0 and z_0.

For optically isotropic, cubic crystals, rotation of the dielectric tensor is not necessary because $\hat{\varepsilon} = \varepsilon \hat{\mathbb{1}}$. However, the shape of $\hat{\varepsilon}$ does generally reflect the crystal family of the medium: If the crystal is properly oriented in space such that the crystallographic main axes coincide with the laboratory coordinate system, crystals of trigonal, tetragonal and hexagonal point groups have also

---

[8] However, circular dichroism due to chiral materials cannot be expressed by a homogeneous dielectric function tensor. Instead, Eqs. 1.6 and 1.5 need to be generalized with the so called optical matrix to $\begin{pmatrix} \vec{\mathcal{D}} \\ \vec{\mathcal{B}} \end{pmatrix} = \begin{pmatrix} \varepsilon_0 \hat{\varepsilon} & i \frac{1}{c_0} \hat{\zeta} \\ -i \frac{1}{c_0} \hat{\zeta} & \mu_0 \hat{\mu} \end{pmatrix} \begin{pmatrix} \vec{\mathcal{E}} \\ \vec{\mathcal{H}} \end{pmatrix}$ with $\hat{\zeta}$ related to the tensor of gyrotropy [Art10]. A feasible approach to describe such materials is considering a twisted stack of anisotropic layers [Ber72; Sch96; Yar+84].

diagonal $\hat{\varepsilon}$ but with two different entries, e.g. $\varepsilon_{xx} = \varepsilon_{yy} = \varepsilon_{\perp}$ and $\varepsilon_{zz} = \varepsilon_{\parallel}$. The dielectric function tensor of orthorhombic crystals is a diagonal matrix with three different entries. If the symmetry is further lowered, real and imaginary part of $\hat{\varepsilon}$ can generally not be diagonalized simultaneously, i.e. different Euler angles would be necessary in order to get either $\mathrm{Re}(\hat{\varepsilon})$ or $\mathrm{Im}(\hat{\varepsilon})$ to diagonal form. Furthermore, in contrast to orthorhombic or higher symmetries, those diagonalization angles differ for different photon energies. Hence, a fourth non-zero entry remains even in the reduced form of $\hat{\varepsilon}$ for monoclinic crystals (e.g. $\varepsilon_{xy} = \varepsilon_{yx} \neq 0$). In triclinic systems, there is no element of $\hat{\varepsilon}$ generally left zero. For all those considerations, it should be noted that, coincidentally, the dielectric tensor can obtain the shape associated with a crystal of higher symmetry: The optical properties of a monoclinic crystal can e.g. become isotropic for a certain photon energy. However, this does never hold generally for all photon energies.

The symmetry properties of $\hat{\varepsilon}$ have crucial consequences for the propagation of light with certain propagation direction and polarization. In the following, monochromatic[9] light is considered. The dependence of $\hat{\varepsilon}(E, \vec{k})$ on photon energy E and wave vector $\vec{k}$ will be discussed in section 1.1.4. As mentioned above, in anisotropic media, $\vec{\mathcal{E}}$ and $\vec{\mathcal{D}}$ are generally not parallel. Thus, $\vec{k}$ and $\vec{\mathcal{S}}$ are generally not parallel either, i.e. the wave front normal is tilted against the light ray (i.e., the direction of energy flow).

Transparent anisotropic media

First, generally anisotropic, transparent media, shall be discussed here, i.e. $\hat{\varepsilon}$ can be expressed as real-valued diagonal matrix[10]: Light waves with different propagation directions and polarization but constant intensity shall be considered. As the dielectric tensor is anisotropic, it is more reasonable to exploit the magnetic permeability being isotropic: A constant intensity (conserved field energy) can be expressed via a constant magnetic field strength $\mathcal{H}_0$. In vacuum, this would correspond to an intensity $I_0 = \vec{\mathcal{E}}_0 \vec{\mathcal{H}}_0^* = \frac{1}{c_0} \vec{\mathcal{H}}_0 \vec{\mathcal{H}}_0^*$. With this one can

---

[9] It should be noted that monochromatic light is defined by a single photon-energy E, not by a single wavelength, because the light wavelength differs generally, depending on the polarization and propagation direction.

[10] Even for monoclinic and triclinic materials, $\vec{\varepsilon}$ can be diagonalized for a single photon-energy in the transparent case.

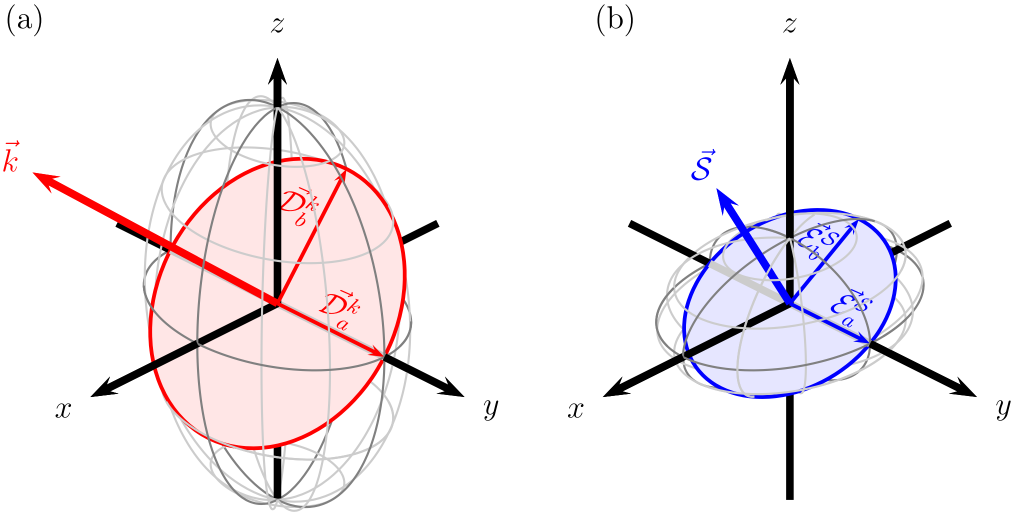

Figure 1.4: Ellipsoid representations of an optically biaxial, transparent crystal (single photon-energy) with coordinate system chosen such that $\hat{\varepsilon} = \mathrm{diag}(\epsilon_{xx}, \epsilon_{yy}, \epsilon_{zz})$: (a) Wave-front-normal ellipsoid (indicatrix) with a wave vector $\vec{k}$ for propagation along an optic normal axis. The ellipse of the related $\mathcal{D}$-field eigenmodes for a wave front is degenerate to a circle $\mathcal{D}_a = \mathcal{D}_b$. (b) Ray ellipsoid with a Poynting vector $\vec{\mathcal{S}}$ for propagation along an optic ray axis; and the plane spanned by the (degenerate) $\mathcal{E}$-field eigenmodes for a light ray. (a) and (b) correspond to the same $\hat{\varepsilon}$. While the intersections with the coordinate axes correspond to $n_{xx/yy/zz}\mathcal{D}_0$ with unit field $\mathcal{D}_0 = \sqrt{\frac{1}{c_0} I_0}$ in (a), they are related to the inverse values $\frac{1}{n_{xx/yy/zz}}\mathcal{E}_0$ with unit field $\mathcal{E}_0 = \sqrt{\frac{1}{c_0} I_0}$ in (b) (with I_0 being unit light intensity).

write $\frac{1}{c_0} I_0 = \frac{1}{c_0^2}\vec{\mathcal{H}}_0\vec{\mathcal{H}}_0^* = \hat{\varepsilon}^{-1}\vec{\mathcal{D}}\vec{\mathcal{D}}^* = \frac{|\mathcal{D}_{x0}|^2}{\varepsilon_{xx}} + \frac{|\mathcal{D}_{y0}|^2}{\varepsilon_{yy}} + \frac{|\mathcal{D}_{z0}|^2}{\varepsilon_{zz}} = const$, where $\mathcal{D}_{x0,y0,z0}$ are the complex amplitude coefficients in the principal spatial directions. This equation defines an ellipsoid which is commonly known as *index ellipsoid*, also called *indicatrix* or *wave-front-normal ellipsoid* [Bor+80]. It provides a geometrical representation of the $\vec{\mathcal{D}}$-field components in the (x, y, z) coordinate space, as depicted in Fig. 1.4 (a). For an arbitrary propagation direction of a wave front given by $\vec{k}$ or $\vec{e}_k$, the ellipse in the related normal surface (through the origin) represents the plane of vibrations (*Schwingungsebene*): The length of the ellipse's main axes is proportional to the principal refractive indices $n_{a/b}$ of the linearly polarized eigenmodes $\vec{\mathcal{D}}_{a/b}^k$. They are directly related to linearly polarized electric-field vectors $\vec{\mathcal{E}}_{a/b}^k = \frac{1}{\varepsilon_0}\hat{\varepsilon}^{-1}\vec{\mathcal{D}}_{a/b}^k$, which generally contain also components along the direction of $\vec{k}$. In the eigenmode basis, the spatially dependent part of the propagator in Eq. 1.10 becomes a matrix exponential and propagation in the direction of $\vec{k}$ takes the following form:

$$\begin{pmatrix} \mathcal{E}_a^k(r+d) \\ \mathcal{E}_b^k(r+d) \end{pmatrix} = e^{i\frac{Ed}{\hbar c_0}\begin{pmatrix} n_a & 0 \\ 0 & n_b \end{pmatrix}} \begin{pmatrix} \mathcal{E}_a^k(r) \\ \mathcal{E}_b^k(r) \end{pmatrix}, \tag{1.21}$$

where d is a propagation distance in the direction $\vec{e}_k$ and $\mathcal{E}_{a/b}^k$ are the complex coefficients for the electric fields of the eigenmodes.

In a similar approach (although less common) one can define the *ellipsoid of rays* using $\frac{1}{c_0}I_0 = \hat{\varepsilon}\vec{\mathcal{E}}_0\vec{\mathcal{E}}_0^* = \varepsilon_{xx}|\mathcal{E}_{x0}|^2 + \varepsilon_{yy}|\mathcal{E}_{y0}|^2 + \varepsilon_{zz}|\mathcal{E}_{z0}|^2 = const$ as illustrated in Fig. 1.4 (b). Now, the normal to a cross-section through the origin points in the direction of a related Poynting vector, i.e. light ray [Bor+80; Lan+67]. The lengths of the ellipse's main axes are proportional to the inverse of the principal refractive indices, $1/n_{a/b}$ for the propagation of a light ray in direction $\vec{e}_{\mathcal{S}}$ with eigenmodes $\vec{\mathcal{E}}_{a/b}^{\mathcal{S}}$. It should be noted that, in general, to a given wave front direction $\vec{e}_{\|}$, there are (at least) two differently polarized light rays $\vec{\mathcal{S}}$ propagating at different angles. The other way around, different waves with different polarization and wave front orientation are connected to the same ray direction $\vec{e}_{\mathcal{S}}$ in anisotropic media. The conditions on how to obtain the principal refractive indices are elaborated in appendix A.1.

As Eq. 1.21 manifests, light which is polarized parallel to one of the main axes of a cross-section ellipse of the indicatrix, propagates with a certain refractive index, light which is polarized perpendicular (parallel to the other main axis) propagates with a different refractive index, n_a and n_b respectively. If light is arbitrarily polarized and expressed as superposition of the eigenmodes in Eq. 1.21, then propagation through the crystal yields a phase shift between the two components. Thus, the light polarization is changed. A direction of $\vec{e}_k$ or $\vec{e}_{\mathcal{S}}$, where the cross-section ellipse becomes a circle, means that the light propagates as through an isotropic medium. Hence, the light polarization does not matter and any polarization state remains unchanged. Any polarization is eigenstate of the propagator. Such special directions mark *(classic) optic axes.* If the above is true for a certain orientation of the wave vector, $\vec{k}$, this direction is referred to as *optic normal axes* [Bor+80; Lan+67; Stu+16]; if it is true for an orientation of the light ray $\vec{e}_{\mathcal{S}}$, this is called *optic ray axis* [Bor+80; Lan+67]. Crystals with trigonal, tetragonal and hexagonal point

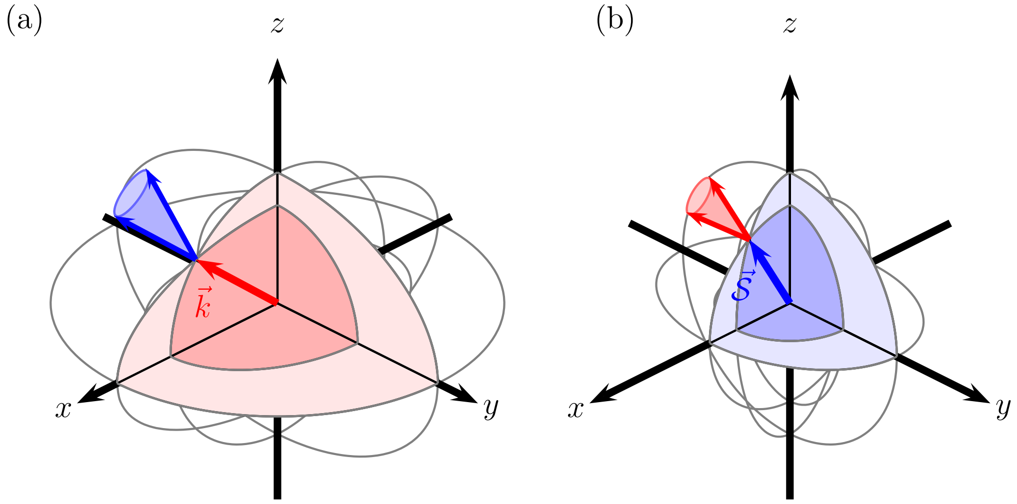

Figure 1.5: Double-shelled Fresnel surfaces for a biaxial crystal in accordance with the ellipsoids shown in Fig. 1.4. (a) Wave-front-normal surface representing the possible lengths of wave vector $\vec{k}$ in any direction. The red arrow shows a wave vector pointing along an optic normal axis. The slanted blue cone illustrates the related Poynting vectors (internal conical refraction). (b) Ray surface representing the possible lengths of a normalized Poynting vector $\vec{\mathcal{S}}$ depending on its direction. The blue arrow points along an optic ray axis, with related wave vectors on a cone (red, external conical refraction). The surface from (a) is depicted in a different manner in Fig.1.6 (a).

group symmetry are uniaxial, i.e. there is only one such optic axis. Normal axis and ray axis coincide here. For optically uniaxial materials, the principal polarizations $\vec{\mathcal{E}}_{a/b}$ are referred to as ordinary (o) and extra-ordinary (eo) polarization component, where the ordinary one is only composed of electric-field vectors perpendicular to the optic axis. Orthorhombic, monoclinic and triclinic crystals are optically biaxial, i.e. they possess two optic axes. They do not coincide with the principle axes of the dielectric function tensor ($\vec{x}$, $\vec{y}$, $\vec{z}$) and also optic normal axes mark directions different from those of optic ray axes. This is exemplarily shown in Figs. 1.4 and 1.5.

Another geometrical representation for transparent crystals of arbitrary symmetry is the *Fresnel wave surface* [Knö86; Bor+80] which is shown in Fig. 1.5. For the respective wave-front-normal surface, the approach is to illustrate for each direction of the wave front given by $\vec{e}_k$ the two eigen-solutions for $|\vec{k}| = \frac{E}{\hbar c_0} n_{a/b}$ from above (still, $\vec{k} \in \mathbb{R}^3$). The resulting surface does not reveal information on the polarization of the corresponding light wave; but the optic normal axes can directly be identified as degeneracies of the two solutions, i.e. intersections of the two surfaces. Again, it is also possible to depict the two solutions $|\vec{\mathcal{S}}|$ to each possible direction of a light ray $\vec{e}_{\mathcal{S}}$, related to the lengths of the main axes for the cross-section ellipses in the ray ellipsoid. This so called *ray surface* reveals, of course, the directions of optic ray axes. The principal shapes of the related dielectric tensors and their inverse tensors are shown in Tab. 1.1.

Remarkable is the relation between ray surface and wave-front-normal surface: The normal vector on the ray surface gives the direction of the wave-front normal $\vec{e}_k$ for the respective ray direction $\vec{e}_{\mathcal{S}}$; and vice versa, the normal vector on the wave-front-normal surface gives the direction of the ray $\vec{e}_{\mathcal{S}}$ for the respective wave front direction $\vec{e}_k$ [Bor+80; Lan+67]. For optically biaxial media, the Fresnel surfaces of the two solutions have diabolically shaped intersections at the directions of the optic axes, i.e. there is not one surface normal but a span of normal vectors, being all located on a cone in (x, y, z)-directional space. Those diabolical points yield so called *conical refraction*[11], i.e. a wave front parallel to an optic normal axes results in a cone of light rays (internal conical refraction), while a light ray propagating along an optic ray axis results in a cone of wave vectors [Lan+67; Ber+08]. With the dielectric function tensor for propagation along an optic normal axis according to Tab. 1.1 one finds the electric-field vectors for $\vec{k} = (0, 0, k_z)^{\mathrm{T}}$ being equivalent to

$$\vec{\mathcal{E}} = \begin{pmatrix} \text{ɜ}_a & 0 & 0 \\ 0 & \text{ɜ}_a & \text{ɜ}_{yz} \\ 0 & \text{ɜ}_{yz} & \text{ɜ}_{zz} \end{pmatrix} \begin{pmatrix} \mathcal{D}_x \\ \mathcal{D}_y \\ 0 \end{pmatrix} = \begin{pmatrix} \text{ɜ}_a \mathcal{D}_x \\ \text{ɜ}_a \mathcal{D}_y \\ \text{ɜ}_{yz} \mathcal{D}_y \end{pmatrix} , \tag{1.22}$$

where ɜ_{ij} are the entries of the inverse dielectric tensor $\hat{\varepsilon}^{-1}$. Despite the wave front is perpendicular to the optic normal axis, each corresponding light ray is tilted against it and the tilt direction depends on the polarization of the $\vec{\mathcal{D}}$ fields. Even the tilt degree depends on the polarization (in the formulation above, it depends on $\mathcal{D}_y$). The sum of all possible polarizations establishes indeed a cone of light rays (internal conical refraction). Hence, the cone is not symmetrically aligned with respect to the particular optic axis and there is

---

[11] Also the term *conical diffraction* is common.

Table 1.1: Reduced dielectric function tensors $\hat{\varepsilon}$ and inverse tensors $\hat{\varepsilon}^{-1} =: \hat{з}$ for optic axes aligned with the z axis. The refractive indices corresponding to the optic axes are $\tilde{n}_a^2 = \frac{1}{з_a}$ or $\tilde{n}_a^2 = \varepsilon_a$ for optic normal and optic ray axes, respectively. Generally, the direction of an optic normal axis is just any ordinary direction for a light ray $\vec{\mathcal{S}}$; an optic ray axis is just any ordinary direction for a wave front defined by $\vec{k}$. Note that all entries $\varepsilon_{ij}, з_{ij} \in \mathbb{C}$ in the absorptive case.

optic normal axis $\vec{k} \parallel \vec{e}_z$	optic ray axis $\vec{\mathcal{S}} \parallel \vec{e}_z$
uniaxial[a]	
$\begin{pmatrix}\mathcal{D}_x\\ \mathcal{D}_y\\ 0\end{pmatrix} = \begin{pmatrix}\varepsilon_\perp & 0 & 0\\ 0 & \varepsilon_\perp & 0\\ 0 & 0 & \varepsilon_\parallel\end{pmatrix}\begin{pmatrix}\mathcal{E}_x\\ \mathcal{E}_y\\ 0\end{pmatrix}$	
$\begin{pmatrix}\mathcal{E}_x\\ \mathcal{E}_y\\ 0\end{pmatrix} = \begin{pmatrix}\frac{1}{\varepsilon_\perp} & 0 & 0\\ 0 & \frac{1}{\varepsilon_\perp} & 0\\ 0 & 0 & \frac{1}{\varepsilon_\parallel}\end{pmatrix}\begin{pmatrix}\mathcal{D}_x\\ \mathcal{D}_y\\ 0\end{pmatrix}$	
biaxial transparent[b]	
$\begin{pmatrix}\mathcal{E}_x\\ \mathcal{E}_y\\ \mathcal{E}_z\end{pmatrix} = \begin{pmatrix}з_a & 0 & 0\\ 0 & з_a & з_{yz}\\ 0 & з_{yz} & з_{zz}\end{pmatrix}\begin{pmatrix}\mathcal{D}_x\\ \mathcal{D}_y\\ 0\end{pmatrix}$	$\begin{pmatrix}\mathcal{D}_x\\ \mathcal{D}_y\\ \mathcal{D}_z\end{pmatrix} = \begin{pmatrix}\varepsilon_a & 0 & 0\\ 0 & \varepsilon_a & \varepsilon_{yz}\\ 0 & \varepsilon_{yz} & \varepsilon_{zz}\end{pmatrix}\begin{pmatrix}\mathcal{E}_x\\ \mathcal{E}_y\\ 0\end{pmatrix}$
$\begin{pmatrix}\mathcal{D}_x\\ \mathcal{D}_y\\ 0\end{pmatrix} = \begin{pmatrix}\varepsilon_{xx} & 0 & 0\\ 0 & \varepsilon_{yy} & \varepsilon_{yz}\\ 0 & \varepsilon_{yz} & \varepsilon_{zz}\end{pmatrix}\begin{pmatrix}\mathcal{E}_x\\ \mathcal{E}_y\\ \mathcal{E}_z\end{pmatrix}$	$\begin{pmatrix}\mathcal{E}_x\\ \mathcal{E}_y\\ 0\end{pmatrix} = \begin{pmatrix}з_{xx} & 0 & 0\\ 0 & з_{yy} & з_{yz}\\ 0 & з_{yz} & з_{zz}\end{pmatrix}\begin{pmatrix}\mathcal{D}_x\\ \mathcal{D}_y\\ \mathcal{D}_z\end{pmatrix}$
biaxial absorptive[c] (singular axes)	
$\begin{pmatrix}\mathcal{E}_x\\ \mathcal{E}_y\\ \mathcal{E}_z\end{pmatrix} = \begin{pmatrix}з_a+з_\eta & \pm iз_\eta & з_{xz}\\ \pm iз_\eta & з_a-з_\eta & з_\eta\\ з_{xz} & з_{yz} & з_{zz}\end{pmatrix}\begin{pmatrix}\mathcal{D}_x\\ \mathcal{D}_y\\ 0\end{pmatrix}$	$\begin{pmatrix}\mathcal{D}_x\\ \mathcal{D}_y\\ \mathcal{D}_z\end{pmatrix} = \begin{pmatrix}\varepsilon_a+\varepsilon_\eta & \pm i\varepsilon_\eta & \varepsilon_{xz}\\ \pm i\varepsilon_\eta & \varepsilon_a-\varepsilon_\eta & \varepsilon_{yz}\\ \varepsilon_{xz} & \varepsilon_{yz} & \varepsilon_{zz}\end{pmatrix}\begin{pmatrix}\mathcal{E}_x\\ \mathcal{E}_y\\ 0\end{pmatrix}$
$\begin{pmatrix}\mathcal{D}_x\\ \mathcal{D}_y\\ 0\end{pmatrix} = \begin{pmatrix}\varepsilon_{xx} & \varepsilon_{xy} & \varepsilon_{xz}\\ \varepsilon_{xy} & \varepsilon_{yy} & \varepsilon_{yz}\\ \varepsilon_{xz} & \varepsilon_{yz} & \varepsilon_{zz}\end{pmatrix}\begin{pmatrix}\mathcal{E}_x\\ \mathcal{E}_y\\ \mathcal{E}_z\end{pmatrix}$	$\begin{pmatrix}\mathcal{E}_x\\ \mathcal{E}_y\\ 0\end{pmatrix} = \begin{pmatrix}з_{xx} & з_{xy} & з_{xz}\\ з_{xy} & з_{yy} & з_{yz}\\ з_{xz} & з_{yz} & з_{zz}\end{pmatrix}\begin{pmatrix}\mathcal{D}_x\\ \mathcal{D}_y\\ \mathcal{D}_z\end{pmatrix}$

a: $\varepsilon_a = \varepsilon_\perp = \frac{1}{з_a}$ here.

b: The xz and yz entries are exchangeable here. In rare cases, the tensor of an orthorhombic, absorbing crystal can also take this form, yielding a classic but absorbing optic axis.

c: Now with complex wave-vector $\vec{\tilde{k}} = (k + i\eta)\vec{e}_z$ and complex Poynting vector $\vec{\tilde{\mathcal{S}}} = \tilde{\mathcal{S}}_0\vec{e}_z$. ε_η and $з_\eta$ are generally arbitrary complex numbers, although non-zero. It holds $\varepsilon_a = \frac{1}{2}(\varepsilon_{xx} + \varepsilon_{yy})$, $\varepsilon_\eta = \frac{1}{2}(\varepsilon_{xx} - \varepsilon_{yy})$, and likewise for $з_a$ and $з_\eta$.

one polarization for which $\vec{\mathcal{S}} \parallel \vec{k}$ (cf. Fig. 1.5).
Finally, as indicated above, the direction of optic axes is the same for all wavelengths in uniaxial and orthorhombic crystals. This is not true for monoclinic and triclinic crystals, yielding so called *color dispersion* or *dispersion of the axes* [Bor+80].

Absorptive anisotropic media

If an anisotropic crystal is absorptive, optic axes need to be found more rigorously. For uniaxial symmetries, even a complex-valued $\hat{\varepsilon}$ can be diagonalized as shown in Tab. 1.1. Biaxial absorptive media yield elliptically polarized eigenstates which are generally not orthogonal to each other. The ellipsoid representations break down. Under the assumption $\vec{k} = \mathrm{Re}(\vec{\tilde{k}}) \parallel \vec{\eta} = \mathrm{Im}(\vec{\tilde{k}})$, representations can still be found for the real and imaginary parts of the wave surface which are not independent of each other [Pet+13]. An example is shown in Fig. 1.6. The wave surfaces for $\vec{k}$ reveal that a classic optic axis from the transparent biaxial material spreads into a line of directions along which $\vec{k}$ degenerates. At the same time, a wave surface representing $\vec{\eta}$ reveals complementary lines of degenerate $\vec{\eta}$. The end points of the respective lines overlap, giving rise to four so called *singular optic axes* [Stu+16; Gru+17b; Voi02; Ber+03]. Hence, a crystal with orthorhombic, monoclinic or triclinic symmetry is biaxial if it is transparent but turns generally tetraxial if it is absorptive. Again, it can be distinguished between singular normal axes and singular ray axes. Conical refraction turns into a similar phenomenon but with largely deformed and opened cones (and generally no part of the cone coincides with the direction of the singular axis). Furthermore, light propagating as an eigenmode along a singular axis is absorbed (albeit its polarization is not changed).

A more exhaustive derivation of how to obtain optic axes can be found in appendix A.1. The consequences on the dielectric tensors $\hat{\varepsilon}$ or its inverse $\hat{\varepsilon}^{-1} =: \hat{\text{ɜ}}$ can be found in Tab. 1.1. While a classic (not singular) optic axis is characterized by a 2×2 submatrix of the dielectric function tensor $\begin{pmatrix} \varepsilon_{xx} & \varepsilon_{xy} \\ \varepsilon_{xy} & \varepsilon_{yy} \end{pmatrix}$ or of its inverse tensor $\begin{pmatrix} \text{ɜ}_{xx} & \text{ɜ}_{xy} \\ \text{ɜ}_{xy} & \text{ɜ}_{yy} \end{pmatrix}$ turning diagonal, the degeneracy is differ-

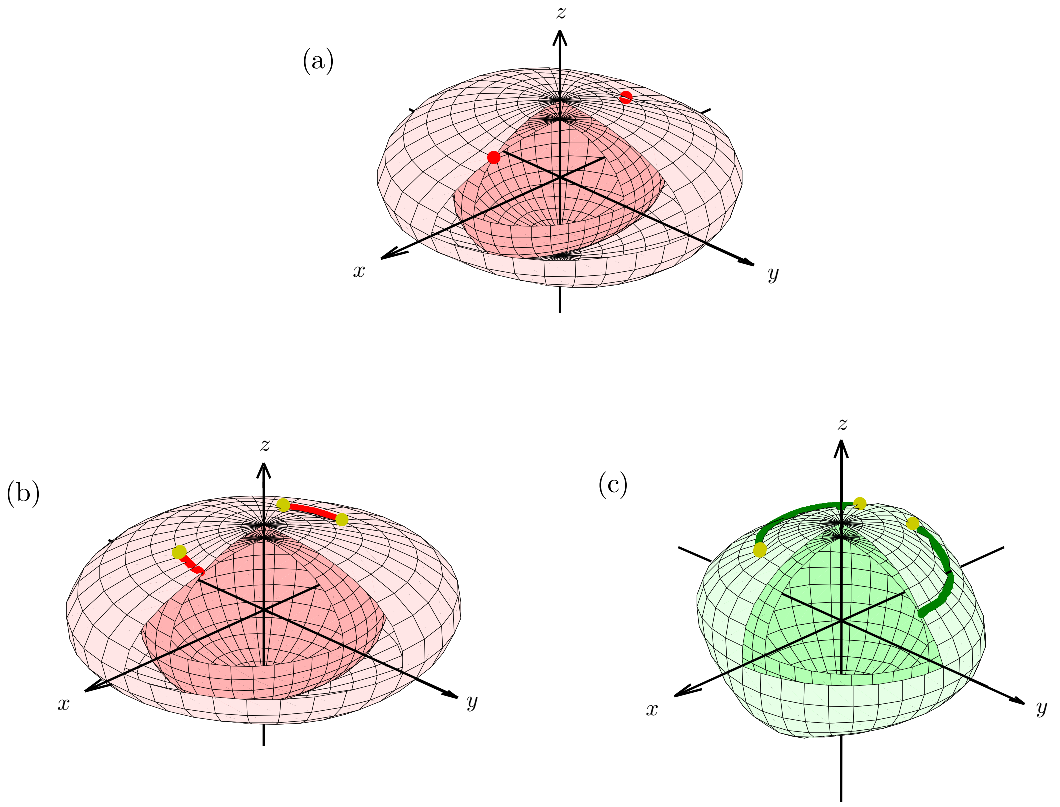

Figure 1.6: Fresnel wave-front-normal surfaces. (a): $\vec{k}$ surface for a biaxial transparent crystal (same as Fig. 1.5 (a)). The red dots mark the orientation of the optic normal axes. (b,c): Same exemplarily for a monoclinic biaxial crystal which is absorbing. (b): $\vec{k}$ surface, (c): $\vec{\eta}$ surface. The red (green) lines mark the directions of degenerate k (η). Note that their endpoints overlap at singular axes (yellow dots). The xy plane is a mirror plane for the surfaces and the same degeneracies occur at the bottom side.

ent for singular axes (see Tab. 1.1). Here, a degenerate eigenvalue of such a submatrix is related to an eigenspace consisting of only one eigenvector (without leading to a singular matrix though). It turns out that, while polarization does not matter for classic optic axes, only either left or right circularly polarized waves are allowed at all to propagate along a singular optic axis (*Voigt waves*). This is a direct consequence of $\hat{\varepsilon}$ being a symmetric matrix and hence non-Hermitian [Ber04]. However, solutions to the wave equation for other polarizations can be found beyond the plane-wave ansatz [Kha62].

The mathematical requirements for a singular axis (a complex-valued, non-Hermitian dielectric tensor) are similar to the mathematical formulation of so called *exceptional points* (cf. appendix A.2). This explains also the origin of the topology of the complex wave-surfaces shown in Fig. 1.6 (a) and (b) which is referred to as complex square-root topology (cf. Fig. A.1). One might call singular axes *exceptional points* in momentum space, while classic optic axes in biaxial media are *diabolical points* in momentum space.

1.1.4 The polariton concept

For simplicity, the dependence of the dielectric function ε on the photon energy E is considered isotropically in the following. The shape of $\varepsilon(E)$ is governed by the interplay between the electromagnetic wave and electric dipoles in the medium. Those dipoles can be established by (quasi-)free electrons, holes (defect-electrons), excitons (electron-hole pairs), or other excitations of a crystal like phonons, magnons and so on, which couple via electric dipole interaction. Without loss of generality, excitonic excitations with a transverse groundstate-energy E_{X0} are chosen here. Excitons can be regarded as being embedded in a harmonic potential in a crystal. Hence they obtain an effective mass m_X which yields a wave-vector dependence of the resonant energy via its kinetic term: $E_X(k) = E_{X0} + \frac{\hbar^2 k^2}{2m_X}$. If light drives the excitonic dipole oscillation as an external electric field with frequency $f = E/h$, the stationary solution for the electric displacement field $\mathcal{D} = \varepsilon_0 \varepsilon \mathcal{E}$ is given by a Lorentz oscillator [Yu+03; Kli07; Agr72; And95] which depends on the wave vector $\tilde{k}$ and photon energy $\tilde{E}$. Both are allowed to be complex, $\tilde{E} = E - i\Gamma$ and

$\tilde{k} = k + i\eta$, respectively (see Fig. 1.8):

$$\varepsilon(\tilde{E}, \tilde{k}) = \varepsilon_\infty + \frac{\varepsilon_\infty(E_{XL}^2 - E_{X0}^2)}{(E_{X0} + \frac{\hbar^2\tilde{k}^2}{2m_X})^2 - \tilde{E}^2 - 2i\tilde{E}\Gamma_X}\,, \tag{1.23}$$

with the real-valued high-frequency background-dielectric constant ε_∞ and the longitudinal exciton energy E_{XL}. The longitudinal-transverse splitting $\Delta_{\mathrm{LT}} = E_L - E_T = E_{XL} - E_{XO}$ is directly related to the optical transition probability. There are different ways to define a related oscillator strength, e.g. $\mathcal{F} = \varepsilon_\infty(\frac{E_{XL}^2}{E_{X0}^2} - 1)$ [Kli07; Che+95; Agr72][12]. In general, the longitudinal exciton energy E_{XL} and the spectral exciton-broadening $\Gamma_X \approx HWHM$ depend also on k but can be assumed in a good approximation to be constant [Kli07].

Equation 1.23 can be put into the polariton equation 1.16 [And95]. Then, under the assumption $\vec{k} \parallel \vec{\eta}$ [13], it can be reduced to

$$\sqrt{\varepsilon(E, \tilde{k})} = \hbar c_0 \frac{\tilde{k}}{E} \quad \text{or} \quad \sqrt{\varepsilon(\tilde{E}, k)} = \hbar c_0 \frac{k}{\tilde{E}}\,. \tag{1.24}$$

The solutions $(\tilde{k}, E)$ or $(k, \tilde{E})$ define the dispersion of the polariton branches either with $\tilde{k} = (k + i\eta) \in \mathbb{C}$ and $E \in \mathbb{R}$ (damping of a monochromatic wave in space), or for real-valued k and complex $\tilde{E} = E - i\Gamma$ (spatially independent damping in time). They differ from each other. The solutions $(\tilde{k}, E)$ are shown in Fig. 1.7. The polariton branches describe a mixed characteristic of the electronic (*matter-like*, here excitonic) properties $\tilde{k} = \tilde{k}_X = \pm\sqrt{\frac{2m_X}{\hbar^2}(E - E_{X0})}$ as well as the photonic properties $\tilde{k} = k_\Lambda = \frac{E}{\hbar c_0}\sqrt{\varepsilon_\infty}$. In that respect, polaritons can be understood as quasi-particles of light-matter interaction, combining properties of a photon as well as those of an exciton. As figure 1.7 shows schematically, an upper (UPB) and a lower (LPB) polariton branch exist: Instead of the original dispersion relation $(\tilde{k}_X, E_X)$ and (k_Λ, E_Λ) which cross each other, an anti-crossing between the polariton branches $(\tilde{k}_{LPB}, E_{LPB})$ and $(\tilde{k}_{UPB}, E_{UPB})$ is observed.

Utilizing once again the polariton equation 1.16, the resulting complex refractive indices can be obtained from the polariton branches as $\tilde{n}(E) = \hbar c_0 \frac{\tilde{k}}{E}$.

---

[12] In that definiton of a unitless oscillator strength, the Lyddane-Sachs-Teller relation becomes obvious which states $\frac{\varepsilon_{st}}{\varepsilon_\infty} = \frac{E_L^2}{E_T^2} = \frac{E_{X0}^2}{E_{XL}^2}$ where ε_{st} is the static (low-frequency) background dielectric constant [Yu+03].

[13] Considerations for a semi-infinite crystal with a planar surface and hence $\vec{\eta}$ parallel to the surface normal (see section 1.1.1), can be found e.g. in [Mar+73]

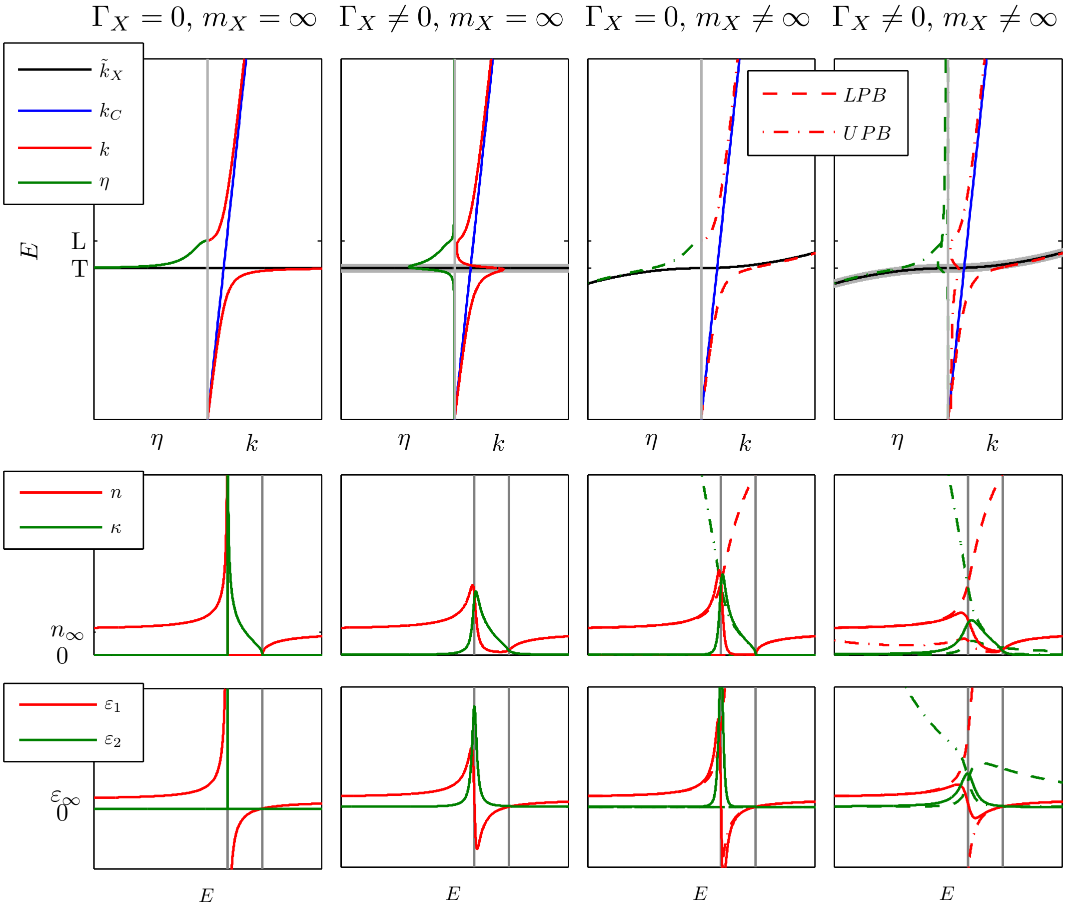

Figure 1.7: Exciton-polariton dispersion $(\tilde{k}, E)$, top row, and its effect on the optical constants according to Eq. 1.23: The complex refractive index, middle row, is obtained from the dispersion as $\tilde{n} = (\hbar c_0 \tilde{k})/E$. The dielectric function, bottom row, $\varepsilon = \tilde{n}^2$, reveals the shape of the Lorentz oscillator. Different columns consider different situations with respect to exciton broadening Γ_X and effective mass m_x. A finite Γ_X is also illustrated as thick, gray line along $\tilde{k}_X$. With $m_X = \infty$, LPB and UPB do not occur simultaneously at any E, with $m_X \neq \infty$, they do. In the third and fourth column, they are hence plotted with different line types. Also, an effective refractive index (solid line) is shown additionally to the LPB and UPB values, then. Ticks on the energy scales in the top row and vertical, gray lines in the middle and bottom row mark the transverse (T) and longitudinal (L) exciton energies. It holds $E_{UPB}(\tilde{k}=0) = E_{XL}$.

Interestingly, if spatial dispersion, i.e. $m_X \neq \infty$ is considered, the LPB and UPB solutions can coexist at a given photon energy E. That means, two different refractive indices are simultaneously valid. Commonly, additional boundary conditions are used to determine which polariton branch is populated under certain conditions, e.g. upon transfer of light from vacuum into a medium with a dielectric function according to Eq. 1.23, one can assume $\vec{\mathcal{P}} = \vec{0}$ at the surface [Pek58]. However, for bulk polaritons with $\vec{k} \parallel \vec{\eta}$ it is also possible to simply compute the photon-likeliness of the polariton branches, $\Lambda_{LPB/UPB} = \pm \frac{\tilde{k}_X^2 - \tilde{k}_{LPB/UPB}^2}{\tilde{k}_{LPB}^2 - \tilde{k}_{UPB}^2}$. These complex-valued quantities are also referred to as *Hopfield coefficients*. Here, $+$ holds for the UPB, $-$ for the LPB, and further $\Lambda_{LPB} + \Lambda_{UPB} = 1$. With this, one can construct an effective refractive index as $\frac{1}{\tilde{n}_{eff}} = \frac{\Lambda_{LPB}}{\tilde{n}_{LPB}} + \frac{\Lambda_{UPB}}{\tilde{n}_{UPB}}$ [Hen98]. Now, $\tilde{n}_{eff}$ fulfills Kramers-Kronig relations and does not depend on $\tilde{k}$ any more, i.e. spatial exciton dispersion is effectively incorporated. Exemplarily, the effect of spatial dispersion is shown in Fig. 1.7. Comparing the resulting optical constants proves that neglecting spatial exciton-dispersion is a sufficient approximation if its effect is accounted for in terms of an artificial, finite spectral broadening Γ_X of the excitonic resonance[14]. Nevertheless, if spatial dispersion is neglected, an additional solution with $\frac{\partial E}{\partial k} < 0$ arises theoretically within the reststrahlen band, i.e., between E_{X0} and E_{XL} (second column in Fig. 1.7). This is also a transverse-wave solution and should not be mixed with the longitudinal polariton mode which is related to evanescent waves at interfaces [Kli07]. This extension of the UPB is strongly damped and hence *de facto* negligible here. Furthermore, ε is still a function of a complex energy $\tilde{E}$, see Fig. 1.8.

An alternative approach to the Lorentz oscillator is an undriven harmonic oscillator. For that, the dielectric function is written e.g. as [Kav+07; Kav06; And95]

$$\varepsilon(\tilde{E}, \tilde{k}) = \varepsilon_\infty + \frac{\varepsilon_\infty \Delta_{\mathrm{LT}}}{E_{X0} + \frac{\hbar^2 \tilde{k}^2}{2m_X} - \tilde{E} - i\Gamma_X}\,. \tag{1.25}$$

The shape of $\varepsilon(E)$ is quite similar for Lorentz and harmonic oscillators near

---

[14] In a more generalized sense, $\varepsilon(\tilde{E}, \tilde{k}) \approx \varepsilon(\tilde{E}, 0)$ is true if the considered wavelength in the background medium, $\lambda = \frac{hc_0}{\varepsilon_\infty E}$ is large against the inverse of the relevant exciton/electron wave-vector k. For electrons in a crystal and Wannier-Mott excitons, that is the case if λ is much larger than the unit cell of the crystal. This is usually true for optical frequencies [Kav+07].

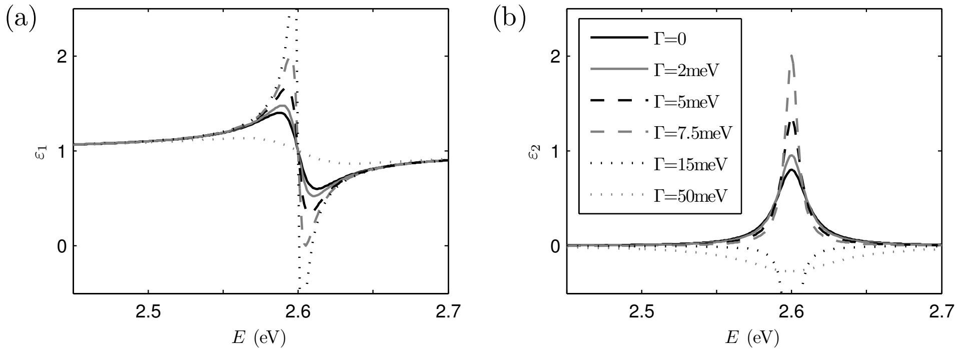

Figure 1.8: Dielectric function ε with a Lorentz oscillator according to Eq. 1.23 for $\tilde{k} = 0$ and complex photon energy $\tilde{E} = E - i\Gamma$. Chosen values are $E_{X0} = 2.60\text{eV}$, $E_{XL} = 2.61\text{eV}$, $2\Gamma_X = 25\text{meV}$ and $\varepsilon_\infty = 1$. Different lines show the effect of the imaginary part Γ of the photon energy. (a): real part, (b): imaginary part of ε.

resonance but differs for energies E far from E_{X0}. Note that there is no factor 2 with Γ_X in the denominator in contrast to the Lorentz oscillator.

The above described semi-classical treatment is in principal equivalent to the quantum-mechanical description as coupled oscillator system [Hop58]. For convenience, here, the energy shall be complex $\tilde{E}_{LPB/UPB} = E_{LPB/UPB} - i\Gamma_{LPB/UPB}$ and the wave vector $k_{LPB/UPB}$ real-valued, i.e. $\sqrt{\varepsilon(\tilde{E}, k)} = \hbar c_0 \frac{k}{E}$. It holds $\Gamma \approx \frac{\hbar c_0}{n}\eta$ where $n = \mathrm{Re}(\sqrt{\varepsilon})$ is the real part of the complex refractive index $\tilde{n}$. With the complex polariton energies, a polaritonic wave function $\Xi_{LPB/UPB}$ is expressed as superposition of the excitonic and photonic wave-functions, Ξ_X and Ξ_Λ, respectively. In a simplified manner, the Schrödinger equation related to the coupled-oscillator model with the quasi-particle Hamiltonian in matrix form and complex polariton energies reads with $\tilde{E}_X = E_X - i\Gamma_X$, $E_X \equiv E_{X0}$

$$\tilde{E}_{LPB/UPB}\,\vec{\Xi}_{LPB/UPB} = \begin{pmatrix} \tilde{E}_X & V(k) \\ V(k)^* & E_\Lambda \end{pmatrix} \begin{pmatrix} \Xi_X \\ \Xi_\Lambda \end{pmatrix} . \tag{1.26}$$

The coupling strength $V(k)$ has units of energy and its relation with the oscillator strength or LT-splitting for bulk polaritons is directly determined by Eq. 1.23 or 1.25. Since the Hamiltonian is Hermitian, only $|V|^2$ appears in the respective eigenvalue equation and practically $V \in \mathbb{R}$ is sufficient, here[15]. How-

---

[15] According to [Hop58; Ger+07], the off-diagonal elements of the respective Hamiltonian are actually purely imaginary. Still, here, only their absolute values count.

ever, Eq. 1.26 defines a quadratic equation in $\tilde{E}$ while the polariton equation results in a complex bi-quadratic equation in $\tilde{E}$ with Lorentz oscillator and in a third-order equation in $\tilde{E}$ with a harmonic oscillator. Consequently, there is no simple mapping between $V(k)$ and $\mathcal{F}$ or Δ_{LT}. According to [Hop58], $V \propto \sqrt{\mathcal{F}/k}$. In particular, if $\Gamma_X = 0$ and $m_X = \infty$, the solutions become real-valued $\tilde{E}_{LPB/UPB} = E_{LPB/UPB}$ and yield a quadratic equation in E^2 from Eq.1.23, with $E_\Lambda = \frac{\hbar c_0}{\sqrt{\varepsilon_\infty}} k$:

$$E^2_{LPB/UPB} = \frac{E^2_{XL} + E^2_\Lambda}{2} \pm \sqrt{\left(\frac{E^2_{XL} + E^2_\Lambda}{2}\right)^2 - E^2_\Lambda E^2_{X0}}\,, \tag{1.27}$$

while one gets from Eq. 1.26

$$E_{LPB/UPB} = \frac{E_{X0} + E_\Lambda}{2} \pm \sqrt{\left(\frac{E_{X0} - E_\Lambda}{2}\right)^2 + |V(k)|^2}\,. \tag{1.28}$$

Note that there is still an intrinsic k dependence through E_Λ, even if spatial exciton dispersion is neglected. Assuming V being independent of k or another kind of detuning between E_Λ and E_X is only a sufficient approximation for narrow parameter ranges and becomes more relevant in the case of cavity polaritons, i.e. coupling between cavity photons and exciton which can be described similarly to Eq. 1.26 (section 2.3).

In quantum-mechanical quasi-particle formalisms, polaritons are connected to Rabi oscillations between the matter-like exciton state and the photon [Dev07]. The Rabi frequency Ω_R is directly given by the energetic *UPB-LPB* splitting at the original crossing point of the uncoupled exciton and photon dispersions[16] of k_X and k_Λ, i.e. $E_\Lambda = \frac{\hbar c_0}{\sqrt{\varepsilon_\infty}} k_\Lambda = E_X$. If still $\Gamma_X = 0$ and

---

[16] In the literature, also the definition for the Rabi frequency being half of this value is found, e.g. [Dev15]. However, Rabi oscillations can also be understood in terms of a beating between photon and exciton if the group velocity of the polariton branches equal each other, i.e., $\left(\frac{\partial E}{\partial k}\right)_{LPB} = \left(\frac{\partial E}{\partial k}\right)_{UPB}$. As the beating frequency is directly given by the frequency difference, keeping Ω_R twice the energy shift is favorable.

$m_X = \infty$, it holds[17]

$$\hbar\Omega_R = 2|V|\,, \qquad \text{quasiparticle Hamiltonian Eq. 1.28,} \tag{1.29}$$

$$\hbar\Omega_R = \sqrt{E_{XL}^2 - E_{X0}^2} = \sqrt{\mathcal{F}\frac{E_{X0}^2}{\varepsilon_\infty}}\,, \qquad \text{Lorentz osc. polariton Eq. 1.23,} \tag{1.30}$$

$$\hbar\Omega_R \approx \sqrt{2E_{X0}\Delta_{\mathrm{LT}}}\,, \qquad \text{harm. osc. polariton Eq. 1.25,} \tag{1.31}$$

where the latter is an approximation according to [And95; Vla+96; Gon+15][18]. It results also from expanding Eq. 1.30 for $\Delta_{\mathrm{LT}} \ll E_{X0}$.

Accordingly, the above equations provide an expression to relate $V(k = \sqrt{\varepsilon_\infty}\frac{E_{X0}}{\hbar c_0})$ with the oscillator strength $\mathcal{F}$ or LT-splitting Δ_{LT} if exciton and photon are exactly in resonance and the excitonic broadening is negligible. The Rabi splitting is reduced by a finite exciton-broadening Γ_X. In the frame of Eq. 1.26, it holds $\hbar\Omega_R = \sqrt{4|V|^2 - \Gamma_X^2}$ [Mic17].

---

[17] With a different definiton of the oscillator strength as $\mathcal{F}' = E_{XO}^2\mathcal{F}$, Eq. 1.30 reads $\Omega_R = \sqrt{\mathcal{F}'/\varepsilon_\infty}$. This version is also widely used in the literature, e.g. [Hou+94; Dev07].

[18] In the literature it is also found $V = \sqrt{2E_{X0}\Delta_{\mathrm{LT}}}$ [Kav+07; Kav06] which, however, seems to be rather a term for the energetic splitting (Eq. 1.31).

1.2 Matrix formalisms for planar structures

Reflection and transmission through single interfaces can be described using Fresnel equations. However, for anisotropic and/or absorptive materials under oblique angle, or if more than one or two interface are considered, this approach quickly becomes way too complex to be suitable. Instead, transfer matrix formalisms are utilized.

From Gauß' laws Eqs. 1.1 and 1.2, it follows that tangential components of electric and magnetic fields are continuous through an interface. This boundary condition can be used to simplify the description of light through planar, stratified structures, using transfer matrix techniques. The here presented matrix calculus for transfer of electromagnetic fields through planar structures is based on plane-wave descriptions (see section 1.1.1). Furthermore the approach is non-local in the interface plane (xy plane), i.e. full translational invariance within this plane is assumed. Accordingly, wedge-shaped layers or edges and related states, breaking this translational symmetry, can not directly be described. However, the translational invariance ensures that the tangential wave-vector is conserved. Utilizing this allows to avoid modifying the Snell-Descartes law.

1.2.1 Transfer-matrix approach

Transfer matrices can be used to describe the evolution of electromagnetic fields through a piece or stack of material as shown in Eq. 1.21 above. For many computations, separation of TE and TM polarization is useful to reduce the computational amount [Vla+96; Che+95; Kav+07]. A 2×2 matrix approach is sufficient then. However, this is only valid for isotropic or pseudo-isotropic structures. The latter refers to structures with at least orthorhombic symmetry and their principle axes aligned with the laboratory coordinates system. However, for arbitrarily oriented anisotropic structures, polarization mixing and conversion occurs. Hence, full polarization treatment is necessary to account for coherent superposition of TE- and TM-polarized waves. This requires a complex 4×4 calculus. The formalism presented here is based on the description by Berreman [Ber72]. The particular formulation follows Schubert [Sch96; Sch05]; the relations with complex reflection and transmission coefficients have been shown by Yeh [Yeh80]. There are further similar formulations of electromagnetic 4 × 4 matrix approaches which differ in (partly very important) details, e.g. [Wöh+88; Jel98; Lin+84; Old89; Art10].

The coordinate system is chosen according to Fig. 1.3 with the surface normal of the plane layer stack oriented parallel to z. Without loss of generality, the considered propagation shall rely upon a wave vector in the xz plane; $k_y = 0$, $\vec{k}_{||} = (k_x, 0)^{\mathrm{T}}$. The in-plane wave-vector is directly related to the angle from the surface normal θ_j in an isotropic transparent medium n_j by $k_x = \frac{E}{\hbar c_0} n_j \sin(\theta_j)$. For ambient ($n_a$) being vacuum, $n_j = n_a = 1$ and $\theta_j = \theta_a$. In the following, the photon energy E and in-plane wave-vector k_x will be real-valued.

The electromagnetic wave shall be described by the tangential fields in the basis $(\mathcal{E}_x, \mathcal{E}_y, \mathcal{H}_x, \mathcal{H}_y)^{\mathrm{T}}$. The angle θ_j and propagation direction (towards $+z$ or $-z$) as well as light polarization are inscribed in the relative phases between the tangential field components. As these tangential fields are continuous through any interface, no special care must be taken to describe interfaces. This is the kind of additional boundary conditions (cf. inhomogeneous plane waves, section 1.1.1) which is intrinsically inscribed into the transfer matrix approach. The remaining task is then to find the propagator which describes the evolution of light upon propagation through a certain medium: Assuming propagation through medium j over a distance (respectively, layer thickness) d_j along z. One can write [Ber72]

$$\begin{pmatrix} \mathcal{E}_x(z_0+d) \\ \mathcal{E}_y(z_0+d) \\ \mathcal{H}_x(z_0+d) \\ \mathcal{H}_y(z_0+d) \end{pmatrix} = e^{i\frac{E}{\hbar c_0} d_j \hat{\Delta}_j} \begin{pmatrix} \mathcal{E}_x(z_0) \\ \mathcal{E}_y(z_0) \\ \mathcal{H}_x(z_0) \\ \mathcal{H}_y(z_0) \end{pmatrix} , \tag{1.32}$$

where the propagator is referred to as partial transfer matrix and the differential transfer matrix $\hat{\Delta}_j$ is given in SI units as [Sch05]

$$\hat{\Delta}_j = -i \frac{\hbar c_0}{E} \frac{\partial}{\partial z} = \tag{1.33}$$

$$\begin{pmatrix} -\sigma_x \frac{\varepsilon_{31}^j}{\varepsilon_{33}^j} & -\sigma_x \frac{\varepsilon_{32}^j}{\varepsilon_{33}^j} & 0 & c_0\mu_0(1-\frac{\sigma_x^2}{\varepsilon_{33}^j}) \\ 0 & 0 & -c_0\mu_0 & 0 \\ c_0\varepsilon_0(\frac{\varepsilon_{23}^j\varepsilon_{31}^j}{\varepsilon_{33}^j}-\varepsilon_{21}^j) & c_0\varepsilon_0(\sigma_x^2-\varepsilon_{22}^j+\frac{\varepsilon_{23}^j\varepsilon_{32}^j}{\varepsilon_{33}^j}) & 0 & \sigma_x\frac{\varepsilon_{23}^j}{\varepsilon_{33}^j} \\ c_0\varepsilon_0(\varepsilon_{11}^j-\frac{\varepsilon_{13}^j\varepsilon_{31}^j}{\varepsilon_{33}^j}) & c_0\varepsilon_0(\varepsilon_{12}^j-\frac{\varepsilon_{13}^j\varepsilon_{32}^j}{\varepsilon_{33}^j}) & 0 & -\sigma_x\frac{\varepsilon_{13}^j}{\varepsilon_{33}^j} \end{pmatrix},$$

where σ_x is the projection of the wave vector along x, $k_x = \frac{E}{\hbar c_0}\sigma_x$. If $k_x \in \mathbb{R}$ is required even if $k_z \in \mathbb{C}$ in an absorbing layer/medium, then $\sigma_x \in \mathbb{R}$ as well[19]. $\vec{k}_{||}$ and σ_x are conserved quantities, independent of the layer/medium j. With transparent ambient medium it holds $\sigma_x = n_a \sin(\theta_a)$. Equation 1.33 results directly from Maxwell's equations 1.1-1.4 [Ber72]. The dielectric function tensor $\hat{\varepsilon}^j$ of layer/medium j is assumed to result from Eq. 1.20 to describe the respective orientation of an anisotropic crystal which shall be considered. For generality, the entries of $\hat{\varepsilon}^j$ are numbered with $x \equiv 1$, $y \equiv 2$ and $z \equiv 3$. As long as no magneto-optic effects arise, $\hat{\varepsilon}^j$ is still symmetric, i.e. $\varepsilon_{ij} = \varepsilon_{ji}$. For (pseudo-)isotropic media, $\hat{\Delta}^j$ simplifies to being anti-diagonal.

In order to describe not only the tangential fields $(\mathcal{E}_x, \mathcal{E}_y, \mathcal{H}_x, \mathcal{H}_y)^{\mathrm{T}}$ but the electric fields $(\mathcal{E}_x, \mathcal{E}_y, \mathcal{E}_z)^{\mathrm{T}}$ in the ambient (superstrate) or substrate medium, $\tilde{n}_a$ or $\tilde{n}_s$, respectively, a basis transformation is necessary. A suitable basis is formed by the polarization eigenmodes in those media. They are found as eigenvectors of the respective propagators of Eq. 1.32 and hence eigenvectors of $\hat{\Delta}_a$ or $\hat{\Delta}_s$, respectively. The related eigenvalues are again the principle refractive indices (see section 1.1.3 and appendix A.1). If isotropic media are considered, the eigenmodes are given as forward- and backward-traveling TE- and TM-polarized states (section 1.1.2). Thus, the basis is chosen as $(\mathcal{E}_{TE}^{\rightarrow}, \mathcal{E}_{TE}^{\leftarrow}, \mathcal{E}_{TM}^{\rightarrow}, \mathcal{E}_{TM}^{\leftarrow})^{\mathrm{T}}$. Here, $\rightarrow$ means propagation towards $+z$ and $\leftarrow$ towards $-z$. The basis transformation is provided by the matrix $\hat{T}_{I/O}^{a/s}$, in SI

---

[19] For the mode computation with complex energy $\tilde{E}$ later, $\tilde{k}_x$ becomes complex as well and σ_x is still real-valued. However, if guided modes in transparent media are considered which cannot couple to the ambient due to total internal reflection, σ_x becomes purely imaginary. Similarly, for leaky modes in absorptive media (total internal reflection is disturbed by the absorption), σ_x and θ_j become complex [Bor+80].

units again [Sch05]:

$$\begin{pmatrix}\mathcal{E}_x\\ \mathcal{E}_y\\ \mathcal{H}_x\\ \mathcal{H}_y\end{pmatrix} = \hat{T}^{a/s}_{I/O} \begin{pmatrix}\mathcal{E}^{\rightarrow}_{TE}\\ \mathcal{E}^{\leftarrow}_{TE}\\ \mathcal{E}^{\rightarrow}_{TM}\\ \mathcal{E}^{\leftarrow}_{TM}\end{pmatrix} \tag{1.34}$$

$$= \begin{pmatrix} 0 & 0 & \frac{\sqrt{n^2_{a/s}-\sigma^2_x}}{n_{a/s}} & -\frac{\sqrt{n^2_{a/s}-\sigma^2_x}}{n_{a/s}} \\ 1 & 1 & 0 & 0 \\ -\frac{\sqrt{n^2_{a/s}-\sigma^2_x}}{\mu_0 c_0} & \frac{\sqrt{n^2_{a/s}-\sigma^2_x}}{\mu_0 c_0} & 0 & 0 \\ 0 & 0 & \frac{n_{a/s}}{\mu_0 c_0} & \frac{n_{a/s}}{\mu_0 c_0} \end{pmatrix} \begin{pmatrix}\mathcal{E}^{\rightarrow}_{TE}\\ \mathcal{E}^{\leftarrow}_{TE}\\ \mathcal{E}^{\rightarrow}_{TM}\\ \mathcal{E}^{\leftarrow}_{TM}\end{pmatrix}.$$

Accordingly, the back transformation is provided by the inverse matrix:

$$\begin{pmatrix}\mathcal{E}^{\rightarrow}_{TE}\\ \mathcal{E}^{\leftarrow}_{TE}\\ \mathcal{E}^{\rightarrow}_{TM}\\ \mathcal{E}^{\leftarrow}_{TM}\end{pmatrix} = (\hat{T}^{a/s}_{I/O})^{-1} \begin{pmatrix}\mathcal{E}_x\\ \mathcal{E}_y\\ \mathcal{H}_x\\ \mathcal{H}_y\end{pmatrix} \tag{1.35}$$

$$= \frac{1}{2} \begin{pmatrix} 0 & 1 & \frac{-1}{\varepsilon_0 c_0 \sqrt{n^2_{a/s}-\sigma^2_x}} & 0 \\ 0 & 1 & \frac{1}{\varepsilon_0 c_0 \sqrt{n^2_{a/s}-\sigma^2_x}} & 0 \\ \frac{n_{a/s}}{\sqrt{n^2_{a/s}-\sigma^2_x}} & 0 & 0 & \frac{1}{\varepsilon_0 c_0 n_{a/s}} \\ \frac{-n_{a/s}}{\sqrt{n^2_{a/s}-\sigma^2_x}} & 0 & 0 & \frac{1}{\varepsilon_0 c_0 n_{a/s}} \end{pmatrix} \begin{pmatrix}\mathcal{E}_x\\ \mathcal{E}_y\\ \mathcal{H}_x\\ \mathcal{H}_y\end{pmatrix}.$$

These definitions of $\hat{T}^{a/s}_{I/O}$ imply a right-handed polarization coordinate systems where the x axis is inverted for backward compared to forward traveling waves: $x^{\leftarrow}_{pol} = -x^{\rightarrow}_{pol}$ and $y^{\leftarrow}_{pol} = y^{\rightarrow}_{pol}$. If $\tilde{n}_a$ or $\tilde{n}_s$ are complex, it should be noted that only the electric fields at the interface can be expressed. Propagation through absorbing ambient or substrate media decreases the light intensity.

For arbitrary anisotropic substrate or superstrate media, $\hat{T}_{I/O}$ consists of the eigenvectors of $\hat{\Delta}_{a/s}$ [Sch96]. For uniaxial media, they correspond to ordinary and extra-ordinary waves, propagating forward and backward, respectively. As $\hat{\Delta}$ has generally full rank, four orthogonal eigenmodes can generally be found and $\hat{T}_{I/O}$ will be invertible[20]. In order to maintain the introduced notation, it is important to make sure that the first and third eigenmode correspond to

---

[20] This does not hold for propagation along a singular ray axis in absorbing biaxial medium.

forward-traveling waves (→), the second and fourth one to backward-traveling ones (←). This can easily be verified by examining the Poynting vector $\vec{\mathcal{S}} = (0, 0, \mathcal{S}_z)^{\mathrm{T}}$, $\mathcal{S}_z = \mathcal{E}_x\mathcal{H}_y^* - \mathcal{E}_y\mathcal{H}_x^*$. The sign of $\mathrm{Re}(\mathcal{S}_z)$ gives the propagation direction. Scaling of the eigenvectors is in principle arbitrary. However, if the obtained field strengths shall be utilized to calculate e.g. the transmittance of a sample structure (see section 1.2.2 below), it is reasonable to require unity: in SI units, $\mathcal{E}_y\mathcal{E}_y^* + (\mu_0 c_0)^2 \frac{\mathcal{H}_y}{\tilde{n}_j}\left(\frac{\mathcal{H}_y}{\tilde{n}_j}\right)^* = 1$ for an eigenmode j with refractive index $\tilde{n}_j$. Finally, it should be noted that the eigenmodes in a general anisotropic medium correspond to wave fronts propagating under different angles, because their propagation relies on different refractive indices $\tilde{n}_j$.

Now, one can write the transfer matrix $\hat{T}$ for a slab of N plane-parallel layers, depending on the in-plane wave-vector k_x and photon energy E, as [Sch05]

$$\hat{T} = (\hat{T}^a_{I/O})^{-1} \prod_{j=1}^{N} e^{-i\frac{Ed_j}{\hbar c_0}\hat{\Delta}_j} \hat{T}^s_{I/O} \ , \tag{1.36}$$

with layer thicknesses d_j. This transfer matrix connects the complex amplitude coefficients of the electric field waves on top of the sample with those on the back side, e.g. in the TE/TM basis:

$$\begin{pmatrix} \mathcal{E}^{\rightarrow}_{TE} \\ \mathcal{E}^{\leftarrow}_{TE} \\ \mathcal{E}^{\rightarrow}_{TM} \\ \mathcal{E}^{\leftarrow}_{TM} \end{pmatrix}_{front} = \hat{T} \begin{pmatrix} \mathcal{E}^{\rightarrow}_{TE} \\ \mathcal{E}^{\leftarrow}_{TE} \\ \mathcal{E}^{\rightarrow}_{TM} \\ \mathcal{E}^{\leftarrow}_{TM} \end{pmatrix}_{back} . \tag{1.37}$$

1.2.2 Scattering, Jones and Müller matrices

The usual purpose for carrying out transfer matrix computation is obtaining complex reflection or transmission coefficients, r, t, or reflectance or transmittance intensities, R, T, for a given planar sample structure. All those quantities depend on the photon energy E, the angle of incidence (AOI, θ_a) and the considered polarization.

For the respective transmittance and reflectance, it holds[21] [Byr16; Kli07]

$$R = rr^* \,, \qquad T = \frac{\mathrm{Re}(\tilde{n}_\mathrm{I}\cos(\theta_\mathrm{I}))}{\mathrm{Re}(\tilde{n}_\mathrm{II}\cos(\theta_\mathrm{II}))}\, tt^* \,, \tag{1.38}$$

where transmission from medium I (e.g. ambient n_a) into medium II (e.g. substrate n_s) is considered and $\tilde{n}_j$ and θ_j are the refractive index and wave-front propagation-angle of the considered eigenmode (polarization) in medium j. As described above, in anisotropic media, $\tilde{n}_j$ and θ_j differ for the different eigenmodes. Thus, it must be declared which kind of reflection and transmission is considered, i.e. from which eigenmode into which eigenmode. It is convenient to choose TE/TM-polarized basis states as described above, because usually the ambient medium n_a is vacuum. Then, the polarization is given by a Jones vector $\vec{J} = (\mathcal{E}_{TM}, \mathcal{E}_{TE})^\mathrm{T}$; the unnormalized reflection or transmission Jones matrix $\hat{J}$ contains direct and polarization-mixing coefficients:

$$\hat{J}_r = \begin{pmatrix} r_{pp} & r_{sp} \\ r_{ps} & r_{ss} \end{pmatrix} \,, \qquad \hat{J}_t = \begin{pmatrix} t_{pp} & t_{sp} \\ t_{ps} & t_{ss} \end{pmatrix} \,. \tag{1.39}$$

Here, traditionally, TE is associated with p, TM with s. The complex coefficients can directly be obtained from the transfer matrix $\hat{T}$ of a structure, which can be rewritten into the principle shape of a scattering matrix $\hat{S}$ [Wei11] such that[22]

$$\begin{pmatrix} \mathcal{E}_{TM}^{front} \\ \mathcal{E}_{TE}^{front} \\ \mathcal{E}_{TM}^{back} \\ \mathcal{E}_{TE}^{back} \end{pmatrix}_{out} = \hat{S} \begin{pmatrix} \mathcal{E}_{TM}^{front} \\ \mathcal{E}_{TE}^{front} \\ \mathcal{E}_{TM}^{back} \\ \mathcal{E}_{TE}^{back} \end{pmatrix}_{in} \,. \tag{1.40}$$

Here, forward ($\rightarrow$) and backward ($\leftarrow$) notations from Eq. 1.37 have been replaced considering light propagating in the ambient or superstrate towards (in) or away from (out) the planar structure. Thus, instead of linking the electric

---

[21] According to [Byr16], the complex conjugate angle θ_j^* should be used for TM polarization. This is only relevant in absorbing media or for total internal reflection; see notes about σ_x in section 1.2.1.

[22] For simplicity but without loss of generality, the notation is still kept in TE/TM polarization basis here. However, for anisotropic ambient or substrate media, if the eigenmode basis is changed, the reflection and transmission coefficients will express the transfer from one eigenmode to another, e.g. r_{uv} for reflection with conversion from eigenmode u to eigenmode v.

fields on one or the other side of the structure as $\hat{T}$ does, $\hat{S}$ converts incident into outgoing light waves. $\hat{S}$ is then given through $\hat{T}$ as [Yeh80]

$$\begin{aligned}
\hat{S} =& \frac{1}{T_{13}T_{31}-T_{11}T_{33}} \cdots \\
& \left(\begin{matrix}
T_{13}T_{41}-T_{11}T_{43} & -T_{33}T_{41}+T_{31}T_{43} \\
T_{13}T_{21}-T_{11}T_{23} & T_{23}T_{31}-T_{21}T_{33} \\
-T_{11} & T_{31} \\
T_{13} & -T_{33}
\end{matrix} \right. \cdots \\
& \begin{matrix}
T_{14}(T_{33}T_{41}-T_{31}T_{43})+T_{13}(-T_{34}T_{41}+T_{31}T_{44})+T_{11}(T_{34}T_{43}-T_{33}T_{44}) \\
T_{14}(-T_{23}T_{31}+T_{21}T_{33})+T_{13}(T_{24}T_{31}-T_{21}T_{34})+T_{11}(-T_{24}T_{33}+T_{23}T_{34}) \\
-T_{14}T_{31}+T_{11}T_{34} \\
T_{14}T_{33}-T_{13}T_{34}
\end{matrix} \cdots \\
& \left. \begin{matrix}
T_{13}(-T_{32}T_{41}+T_{31}T_{42})+T_{12}(T_{33}T_{41}-T_{31}T_{43})+T_{11}(-T_{33}T_{42}+T_{32}T_{43}) \\
T_{13}(T_{22}T_{31}-T_{21}T_{32})+T_{12}(-T_{23}T_{31}+T_{21}T_{33})+T_{11}(T_{23}T_{32}-T_{22}T_{33}) \\
-T_{12}T_{31}+T_{11}T_{32} \\
-T_{13}T_{32}+T_{12}T_{33}
\end{matrix} \right) .
\end{aligned} \tag{1.41}$$

Accordingly, $\hat{S}$ can be expressed by the respective Jones matrices as

$$\hat{S} = \left(\begin{array}{cc|cc}
r_{pp} & r_{sp} & \tilde{t}_{pp} & \tilde{t}_{sp} \\
r_{ps} & r_{ss} & \tilde{t}_{ps} & \tilde{t}_{ss} \\
\hline
t_{pp} & t_{sp} & \tilde{r}_{pp} & \tilde{r}_{sp} \\
t_{ps} & t_{ss} & \tilde{r}_{ps} & \tilde{r}_{ss}
\end{array} \right) = \left(\begin{array}{c|c}
\hat{J}_r & \hat{\hat{J}}_t \\
\hline
\hat{J}_t & \hat{\hat{J}}_r
\end{array} \right) , \tag{1.42}$$

where $\hat{J}_r$ describe front-side reflection, $\hat{\hat{J}}_r$ backside reflection, $\hat{J}_t$ forward transmission, and $\hat{\hat{J}}_t$ backward transmission. Consequently, Eq. 1.40 provides expressions for complex reflection and transmission coefficients if the transfer matrix has been calculated.

With knowledge of the Jones matrices, one can construct respective Müller matrices similar to constructing a Stokes vector. According to Eq. 1.19, a Jones vector can be converted into a Stokes vector as

$$\vec{S} = \hat{A}(\vec{J} \otimes \vec{J}^*)\,, \tag{1.43}$$

$$\text{with} \quad \hat{A} = \begin{pmatrix} 1 & 0 & 0 & 1 \\ 1 & 0 & 0 & -1 \\ 0 & 1 & 1 & 0 \\ 0 & -i & i & 0 \end{pmatrix}\,,$$

where $\vec{J} \otimes \vec{J}^* = (\mathcal{E}_x\mathcal{E}_x^*, \mathcal{E}_x\mathcal{E}_y^*, \mathcal{E}_x^*\mathcal{E}_y, \mathcal{E}_y\mathcal{E}_y^*)^{\mathrm{T}}$ is the direct tensor product of the Jones vector with its complex conjugate. Then, a Müller matrix $\hat{M}$ can be obtained from a Jones matrix $\hat{J}$ as [Azz+77; Jel98; Fuj07; Hun08]

$$\hat{M} = \hat{A}\hat{J} \otimes \hat{J}^*\hat{A}^{-1}\,. \tag{1.44}$$

Again, $\hat{J} \otimes \hat{J}^*$ is the direct tensor product, of the Jones matrix and its complex conjugate (not adjunct) matrix, here. The auxiliary matrix $\hat{A}$ is in principal independent of the choice of polarization, albeit the meaning of a Stokes vector differs with the chosen polarization basis states.

While any Jones matrix can be converted into a Müller matrix, the inversion of Eq. 1.44 is only possible for non-depolarizing Müller matrices. Inversion is made by solving the equation system 1.44 for J_{pp}, J_{ss}, J_{sp} and J_{ps}.

Symmetry aspects of Jones and Müller matrices

Müller and Jones matrices for reflection or transmission reveal symmetries related to the sample structure's symmetry.

If the system consisting of substrate-structure-ambient has at least monoclinic symmetry with the base plane[23] aligned with the POI, the matrices for transmission as well as reflection reduce to [Art14]

$$\hat{M} = M_{11} \begin{pmatrix} 1 & -N & 0 & 0 \\ -N & 1 & 0 & 0 \\ 0 & 0 & C & S \\ 0 & 0 & -S & C \end{pmatrix}\,, \qquad \hat{J} = \begin{pmatrix} J_{pp} & 0 \\ 0 & J_{ss} \end{pmatrix}\,. \tag{1.45}$$

In particular, this is realized e.g. by:

---

[23] This is either a mirror plane or the plane perpendicular to an axis of two-fold rotation symmetry.

- A single layer of an isotropic medium embedded in vacuum or an top of a semi-infinite substrate. The first case yields uniaxial symmetry corresponding to point group $D_{\infty h}$, the second one a $C_{\infty v}$ symmetry. Similarly, this holds for an optically uniaxial medium if its optic axis is aligned with the surface normal (e.g. c-plane oriented ZnO).

- A single layer of an optically uniaxial medium and the optic axis aligned in the surface plane either parallel or perpendicular to the POI (e.g. aligned m-plane oriented ZnO). This configuration has D_{2h} symmetry if embedded in vacuum and C_{2v} with substrate.

- A single layer of an optically uniaxial medium and the optic axis aligned in the POI, resulting in C_{2h} or C_{1h} pointgroup symmetry, without and with substrate, respectively (e.g. aligned r-plane oriented ZnO).

The principal shape of Eqs. 1.45 holds also if respective layer stacks are considered. If the structure has cylindrical $D_{\infty h}$ symmetry, the matrix entries are those of standard ellipsometry [Azz+77; Fuj07]: $N = \cos(2\Psi_{SE})$, $C = \sin(2\Psi_{SE})\cos(\Delta_{SE})$ and $S = \sin(2\Psi_{SE})\sin(\Delta_{SE})$, where $\tan(\Psi_{SE})e^{i\Delta_{SE}} = J_{pp}/J_{ss}$.

If the symmetry of the system is reduced, Jones matrices are not diagonal, Müller matrices not block-diagonal any more. This induces polarization conversion. In such cases, it is of relevance whether the Jones matrix becomes symmetric, Hermitian or without particular symmetry.

For reflection geometries it holds for systems with at least monoclinic symmetry and the base plane (see above) aligned with the surface [Art14]:

$$\hat{M} = M_{11}\begin{pmatrix} 1 & M_{12} & M_{13} & M_{14} \\ M_{12} & M_{22} & M_{23} & M_{24} \\ -M_{13} & -M_{23} & M_{33} & M_{34} \\ M_{14} & M_{24} & -M_{34} & M_{44} \end{pmatrix}, \qquad \hat{J} = \begin{pmatrix} J_{pp} & J_{sp} \\ -J_{sp} & J_{ss} \end{pmatrix}. \tag{1.46}$$

For example, such a symmetry is realized by a single layer of an optically uniaxial medium and the optic axis aligned arbitrarily in the surface plane (e.g. arbitrarily oriented m-plane oriented ZnO).

For reflection on systems with at least monoclinic symmetry and the base plane aligned perpendicular to both, the surface and POI, it holds [Art14]:

$$\hat{M} = M_{11} \begin{pmatrix} 1 & M_{12} & M_{13} & M_{14} \\ M_{12} & M_{22} & M_{23} & M_{24} \\ M_{13} & M_{23} & M_{33} & M_{34} \\ -M_{14} & -M_{24} & -M_{34} & M_{44} \end{pmatrix}, \qquad \hat{J} = \begin{pmatrix} J_{pp} & J_{sp} \\ J_{sp} & J_{ss} \end{pmatrix}. \tag{1.47}$$

Such a symmetry can be established by a single layer of an optically uniaxial medium and the optic axis aligned in the plane perpendicular to the POI and the surface, without and with substrate, respectively (e.g. aligned r-plane oriented ZnO).

In other cases (e.g. arbitrarily oriented r-plane ZnO), no general simple symmetry relations can be obtained for reflection Jones and Mueller matrices, as long as oblique angles and no magnetic fields, i.e. symmetric $\hat{\varepsilon}^j$ are assumed.

For transmission into arbitrary anisotropic substrates (cf. section 1.2.1), a forward Jones matrix transfers electric fields from the p- and s-polarized states into the polarization eigenstates u and v, i.e. $\hat{J} = \begin{pmatrix} J_{pu} & J_{su} \\ J_{pv} & J_{sv} \end{pmatrix}$, where the Jones vector in the substrate is expressed as $\vec{J} = (\mathcal{E}_u, \mathcal{E}_v)^{\mathrm{T}}$. Even then, it is worth investigating if and when the Jones matrices become symmetric or Hermitian. As can be seen from Eq. 1.37, the submatrix $\begin{pmatrix} T_{33} & T_{31} \\ T_{13} & T_{11} \end{pmatrix}$ of the transfer matrix is an inverse transmission Jones matrix. If a matrix is symmetric and invertible, its inverse is as well. Consequently, the symmetry of the structure matters, because it determines the symmetry of $\hat{T}$. If $\hat{J}$ is symmetric, that means not only that the forward-conversion form TE to u equals the forward-conversion from TM to v, but also that the backward-conversion from u to TE equals the backward-conversion from v to TM. According to [Pot04], this is especially the case if the xy plane is a mirror plane of the system (*mid-plane symmetry*). Then, Eq. 1.47 is valid for the transmission Jones matrices. This is provided e.g. for an arbitrarily aligned film of m-plane oriented ZnO. This film can even be symmetrically surrounded by other layers (like DBRs) while still having a symmetric transmission Jones matrix. If there is no mid-plane symmetry, e.g. due to a substrate, the Jones matrix is not generally symmetric. However, such a symmetry can occasionally occur for certain photon energies.

Chapter 2

Theory II: Planar optical microcavities

The theory of optical modes in a Fabry-Pérot-type resonator is presented in this chapter. Sections 2.1 and 2.2 comprise the electromagnetic-wave approach to cavity-photon modes and explain how they are computed for planar microcavities within the framework of this thesis. Section 2.3 compares the results of the wave treatment to those of quasiparticle Hamiltonians, including a compilation of the findings published in [Ric+15].

2.1 Fabry-Pérot resonators and photonic modes

In the simplest case, a one-dimensional optical resonator consists of a single layer of width d_c which is called cavity. An optical eigenmode corresponds to a standing wave in this cavity layer. With the coordinate system introduced by Fig. 1.3, the respective condition for a forward-propagating electric field $\mathcal{E}^{\rightarrow}$ and a wave front propagating at angle θ_c with respect to the surface normal is determined as (cf. Eq. 1.10)

$$\begin{aligned} \mathcal{E}^{\rightarrow}(z_0) &= r_t\, e^{i\tilde{n}_c d_c \cos(\theta_c)\frac{\tilde{E}}{\hbar c_0}}\, \mathcal{E}^{\leftarrow}(z_0 + d_c) \\ &= r_t\, e^{i\tilde{n}_c d_c \cos(\theta_c)\frac{\tilde{E}}{\hbar c_0}}\, r_b\, e^{i\tilde{n}_c d_c \cos(\theta_c)\frac{\tilde{E}}{\hbar c_0}}\, \mathcal{E}^{\rightarrow}(z_0)\,, \end{aligned} \tag{2.1}$$

where $r_{t/b} = |r_{t/b}| e^{i\varphi_r^{t/b}}$ are the complex reflection coefficient for reflection of light at the top (t) and bottom (b) boundaries, $z = z_0$ and $z = z_0 + d_c$, respectively. Further with $\tilde{n}_c$ being the complex refractive index of the cavity

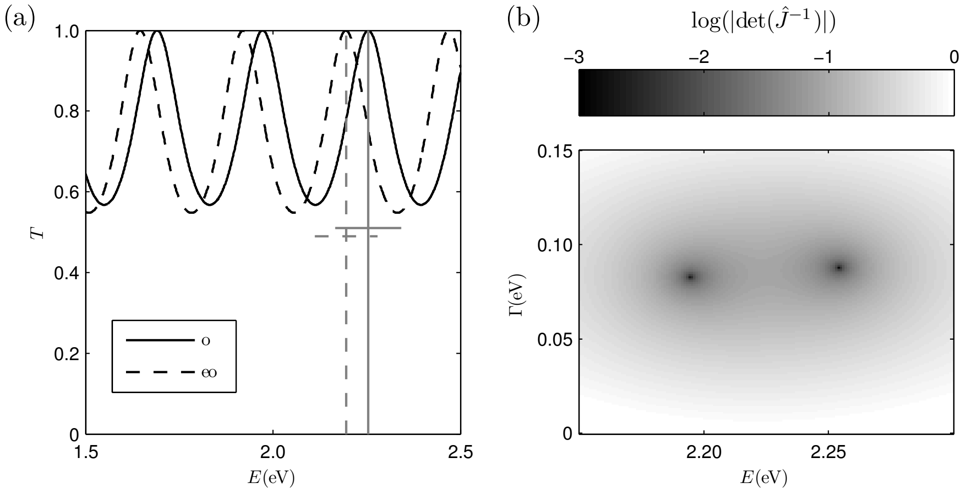

Figure 2.1: Single, 1μm thick, optically uniaxial ($n_o = 2.20$, $n_{eo} = 2.26$) cavity layer in vacuum under normal incidence. (a): Transmittance spectrum. The optic axis is aligned in the cavity plane, resulting in different spectra for ordinary (o) and extra-ordinary (eo) polarizations. (b) Logarithmic gray-scale plot of absolute value of the determinant of the inverse transmission Jones matrix, depending on the complex photon energy $\tilde{E} = E - i\Gamma$. The chosen spectral range contains two (differently polarized) modes. The values obtained for E_c and Γ_c ($HWHM$) are depicted in (a) by the gray lines oriented vertically, and horizontally, respectively.

medium. Complex photon energies $\tilde{E}$ which fulfill Eq. 2.1 define cavity-photon modes, $\tilde{E}_c$. It should be noted that $r_{t/b}$ generally differ for TE and TM polarization. Eq. 2.1 can be reduced for the isotropic, one-dimensional case to [Stu11; Kav+07; Kav06; Pan+99b]

$$e^{2i\tilde{n}_c d_c \cos(\theta_c)\frac{\tilde{E}}{\hbar c_0}} r_t r_b = 1\,. \tag{2.2}$$

Now, $E_c = \mathrm{Re}(\tilde{E}_c)$ results mostly from the phase matching condition, while $\Gamma_c = -\mathrm{Im}(\tilde{E}_c)$ compensates for reflection losses at the boundaries, $|r_{t/b}| < 1$ (which, though, also affect E_c). However, phase and amplitude matching is required at the same time. In the following, $r_t = r_b = r$ is assumed: From Eq. 2.2, it follows

$$E_c = \frac{\hbar c_0}{d_c \cos\theta_c} \frac{\kappa_c \ln|r| + n_c(m\pi - \varphi_r)}{n_c^2 + \kappa_c^2}\,, \tag{2.3}$$

$$\Gamma_c = \frac{\hbar c_0}{d_c \cos\theta_c} \frac{-n_c \ln|r| + \kappa_c(m\pi - \varphi_r)}{n_c^2 + \kappa_c^2}\,, \tag{2.4}$$

with mode number $m \in \mathbb{N}$ being a non-negative integer[1]. In the literature, sometimes $-\ln(|r|)$ is replaced by the approximation $\frac{1-|r|}{2|r|}$ here [Sav+99; Kav+07]. In the case of a transparent cavity medium ($\kappa_c = 0$) these equations reduce to

$$E_c = \frac{\hbar c_0}{n_c d_c \cos\theta_c}(m\pi - \varphi_r)\,, \tag{2.5}$$

$$\Gamma_c = -\frac{\hbar c_0}{n_c d_c \cos\theta_c}\ln|r|\,. \tag{2.6}$$

Still, for a general $\tilde{n}(\tilde{E})$, those equations are implicit and it mostly remains a numerical task to find $\tilde{E}_c$ which fulfill this mode condition. Also, it should be noted that r differs for TE and TM polarization if $\theta_c \neq 0$ [Stu11]. Furthermore, r depends on the relation between $\vec{k}$ and $\vec{\eta}$. This could in principle modify results of photoluminescence compared to transmission experiments.

Depending on the cavity layer thickness, several mode orders with different mode numbers m can occur: Usually, the energetically lowest cavity mode[2], $m = 1$, is the so called *$\lambda/2$-mode*, i.e., the cavity's optical thickness, $n_c d_c$, modified by the phase shifts φ_r upon reflection at the cavity's boundary, fits to exactly half a vacuum wavelength, $\lambda_0/2 = \frac{n_c d_c}{1-\varphi_r/\pi}$. With $\theta_c = 0$ (normal incidence), it follows $k_\perp = k_z = 2\pi/\lambda_c = (m\pi - \varphi_r)/d_c$. This is the quantization of a free photon in the cavity, which creates a quantum pot or well. The modes, exemplarily depicted in Fig. 2.1, have mode number $m = 8$.

For perfect reflection (e.g. by total internal reflection), $\Gamma_c = 0$ and the cavity-photon energy would become real-valued. Otherwise, a cavity photon, in contrast to a free photon, is always described by a complex energy with negative imaginary part. Comparison with a transmittance spectrum for such a cavity shows that Γ_c corresponds approximately to half the width at half maximum if a transmission peak is considered as Lorentzian peak [Sav+99] (cf.

---

[1] It is also possible to require only phase matching and omit compensation of the losses caused by $|r| < 1$, i.e. $e^{2i(\tilde{n}_c d_c \cos(\theta_c)\frac{\tilde{E}}{\hbar c_0} + \varphi_r)} = 1$ [Mic17]. Or, in a similar manner, one can consider the effect of the damped wave on the effectively shortened wavelength, i.e. $e^{i(2\tilde{n}_c d_c \cos(\theta_c)\frac{\tilde{E}}{\hbar c_0} - \frac{\Gamma}{E}\ln|r|)} r^2 = 1$. Both would result in relations with slightly changed energies E_c. With the first ansatz, E_c would become independent of $|r|$ even in the case of an absorbing medium, $\kappa_c \neq 0$ (cf. Eq. 2.3). The distinction regarding the mode condition is generally only relevant for either large losses or large absorption, and is not considered here.

[2] There is also a zero-λ mode which only obtains non-zero energies at oblique angles $\theta_c \neq 0$.

section 2.3 below). Depending on the reflection losses, there is a continuous transition from so called layer thickness oscillations to distinguishable cavity-photon modes [Sav+99; Sav]. In fact, $E_c = \mathrm{Re}(\tilde{E}_c)$ does not exactly match the energy of a peaks in a transmittance spectrum, dips in a reflectance spectrum, or peaks in an absorbance spectrum [Sav+95]. They all differ slightly but are very close together for sufficiently well defined modes, i.e. Γ_c being small. If Γ_c would be considerably large, the central peak energy of the Lorentz oscillator would also significantly differ from the resonance energy (cf. also Eq. 2.25).

Rigorous mode condition

If polarization and oblique angles are rigorously considered, Eq. 2.2 becomes a matrix equation with non-commuting matrices. With the coordinate system and notation introduced in section 1.2.1, and in the basis of for- and backward-propagating fields $(\mathcal{E}_{TE}^{\rightarrow}, \mathcal{E}_{TE}^{\leftarrow}, \mathcal{E}_{TM}^{\rightarrow}, \mathcal{E}_{TM}^{\leftarrow})^{\mathrm{T}}$ at the boundaries but still inside the cavity layer, $z = z_0$ and $z = z_0 + d_c$, it reads

$$\begin{pmatrix} 0 & r_{ss}^c & 0 & r_{ps}^c \\ 0 & 1 & 0 & 0 \\ 0 & r_{sp}^c & 0 & r_{pp}^c \\ 0 & 0 & 0 & 1 \end{pmatrix} \begin{pmatrix} \mathcal{E}_{TE}^{\rightarrow}(z_0) \\ \mathcal{E}_{TE}^{\leftarrow}(z_0) \\ \mathcal{E}_{TM}^{\rightarrow}(z_0) \\ \mathcal{E}_{TM}^{\leftarrow}(z_0) \end{pmatrix} \tag{2.7}$$

$$= \hat{T}_{I/O}^{-1} e^{-i\frac{\tilde{E}}{\hbar c_0} d_c \hat{\Delta}_c} \hat{T}_{I/O} \begin{pmatrix} 1 & 0 & 0 & 0 \\ r_{ss}^c & 0 & r_{ps}^c & 0 \\ 0 & 0 & 1 & 0 \\ r_{sp}^c & 0 & r_{pp}^c & 0 \end{pmatrix} \begin{pmatrix} \mathcal{E}_{TE}^{\rightarrow}(z_0 + d_c) \\ \mathcal{E}_{TE}^{\leftarrow}(z_0 + d_c) \\ \mathcal{E}_{TM}^{\rightarrow}(z_0 + d_c) \\ \mathcal{E}_{TM}^{\leftarrow}(z_0 + d_c) \end{pmatrix},$$

where again $\hat{T}_{I/O}$ transforms the basis $(\mathcal{E}_x, \mathcal{E}_y, \mathcal{H}_x, \mathcal{H}_y)^{\mathrm{T}}$ in the cavity medium into the basis $(\mathcal{E}_{TE}^{\rightarrow}, \mathcal{E}_{TE}^{\leftarrow}, \mathcal{E}_{TM}^{\rightarrow}, \mathcal{E}_{TM}^{\leftarrow})^{\mathrm{T}}$. Here, r_{ij}^c are the polarization-dependent complex reflection coefficients (Jones matrix entries) for light inside the cavity layer which is reflected off the boundaries. For simplicity, mid-plane symmetry with equal r_{ij}^c at the top and bottom side of the cavity plane is considered here. In the case of asymmetric surroundings, r_{ij}^c on the l.h.s and r.h.s of Eq. 2.7 would be different. This mode equation can also be written for the fields outside the entire structure at $z = z_0 - \delta$ and $z = z_0 + d_c + \delta$. Utilizing the transmission through the boundaries of the cavity layer and the distance

δ, described with the complex transmission coefficients t^c_{ij}, it holds

$$\begin{pmatrix} \mathcal{E}^{\rightarrow}_{TE}(z_0-\delta) \\ \mathcal{E}^{\leftarrow}_{TE}(z_0-\delta) \\ \mathcal{E}^{\rightarrow}_{TM}(z_0-\delta) \\ \mathcal{E}^{\leftarrow}_{TM}(z_0-\delta) \end{pmatrix} = \begin{pmatrix} 0 & 0 & 0 & 0 \\ 0 & t^c_{ss} & 0 & t^c_{ps} \\ 0 & 0 & 0 & 0 \\ 0 & t^c_{sp} & 0 & t^c_{pp} \end{pmatrix} \begin{pmatrix} \mathcal{E}^{\rightarrow}_{TE}(z_0) \\ \mathcal{E}^{\leftarrow}_{TE}(z_0) \\ \mathcal{E}^{\rightarrow}_{TM}(z_0) \\ \mathcal{E}^{\leftarrow}_{TM}(z_0) \end{pmatrix} \tag{2.8}$$

$$\begin{pmatrix} \mathcal{E}^{\rightarrow}_{TE}(z_0+d_c+\delta) \\ \mathcal{E}^{\leftarrow}_{TE}(z_0+d_c+\delta) \\ \mathcal{E}^{\rightarrow}_{TM}(z_0+d_c+\delta) \\ \mathcal{E}^{\leftarrow}_{TM}(z_0+d_c+\delta) \end{pmatrix} = \begin{pmatrix} t^c_{ss} & 0 & t^c_{ps} & 0 \\ 0 & 0 & 0 & 0 \\ t^c_{sp} & 0 & t^c_{pp} & 0 \\ 0 & 0 & 0 & 0 \end{pmatrix} \begin{pmatrix} \mathcal{E}^{\rightarrow}_{TE}(z_0+d_c) \\ \mathcal{E}^{\leftarrow}_{TE}(z_0+d_c) \\ \mathcal{E}^{\rightarrow}_{TM}(z_0+d_c) \\ \mathcal{E}^{\leftarrow}_{TM}(z_0+d_c) \end{pmatrix} . \tag{2.9}$$

Now, according to Eq. 1.37, it follows with the transfer matrix $\hat{T}_c$ for the entire microcavity:

$$\begin{pmatrix} 0 \\ \mathcal{E}^{\leftarrow}_{TE} \\ 0 \\ \mathcal{E}^{\leftarrow}_{TM} \end{pmatrix}_{front} = \hat{T}_c \begin{pmatrix} \mathcal{E}^{\rightarrow}_{TE} \\ 0 \\ \mathcal{E}^{\rightarrow}_{TM} \\ 0 \end{pmatrix}_{back} . \tag{2.10}$$

This is the generalized mode condition. It is fulfilled if the determinant of the following sub-matrix vanishes:

$$\begin{vmatrix} T_{33} & T_{31} \\ T_{13} & T_{11} \end{vmatrix} = \det(\hat{J}_t^{-1}) = 0 \,. \tag{2.11}$$

This sub-matrix is the inverse Jones matrix for forward-transmission through the cavity. Figure 2.1 (b) shows exemplarily when $\hat{J}_t^{-1}$ depending on E and Γ becomes singular for $\tilde{E} = \tilde{E}_c$. Equation 2.10 is nothing else than claiming that photonic eigenmodes of the system are a mathematical singularity which consists in escaping electromagnetic fields despite no fields are incident, i.e. infinite transmission [Mak94; Sav+95; Kav+07]. This is well known from scattering theory, where modes are found as poles of the scatter matrix [Yeh80; Fel01; Byk+13; Wei11]:

$$\begin{pmatrix} \mathcal{E}^{front}_{TM} \\ \mathcal{E}^{front}_{TE} \\ \mathcal{E}^{back}_{TM} \\ \mathcal{E}^{back}_{TE} \end{pmatrix}_{out} = \hat{S} \begin{pmatrix} 0 \\ 0 \\ 0 \\ 0 \end{pmatrix}_{in} . \tag{2.12}$$

Accordingly, the determinant of $\hat{S}$ diverges, $\det(\hat{S}) \to \infty$ if the conditions of a mode are fulfilled. The same is true for its submatrices $\hat{J}_t$ and $\hat{\hat{J}}_t$ which describe forward- and backward-transmission (cf. Eq. 1.42), respectively. Eqs. 2.10 and 2.12 are the most general notation for the Fabry-Pérot-mode condition of a planar bulk microcavity[3]. No pre-selection of certain polarization states is done here, in contrast to the often found separation into transfer matrix problems for TE and TM polarization [Kav06; Stu+11; Kav+03]. The approach is exact for microcavities consisting of arbitrarily anisotropic transparent layers. If a layer's dielectric function can properly be described by means of (Lorentz-) oscillators, the dependence of ε on the real and imaginary part of $\tilde{E}$ can properly be described, and the explained formalism is still exact with absorbing layers. This allows computation of cavity polariton modes.

Typical microcavities with DBRs

In order to improve the confinement of the light in the cavity layer, a cavity layer is usually surrounded by distributed Bragg reflectors (DBR). Such multilayer mirrors allow reflectance close to 100% within a narrow spectral range referred to as Bragg stop-band. An ideal DBR is constructed for a design vacuum-wavelength λ_{DBR} at normal incidence by layers of two alternating transparent media, n_1, n_2. The layer thicknesses $d_{1/2}$ should fulfill the condition $n_j d_j = \lambda_{\mathrm{DBR}}/4$. Figure 2.2 shows an example structure and its transmittance spectrum. Compared to Fig. 2.1 (a), the cavity-photon modes within the spectral range of the Bragg stop-band are much narrower and well separated now. In the following, it is focused on such cavity-photon modes. However, it should be mentioned that also Bragg-band edge modes which can be seen in Fig. 2.2 (b) as transmittance peaks much broader than the cavity modes, are in principle photonic modes of the structure as well [Fau+09].

In equation 2.10, the transmission through the boundaries turns into transmission through the top and bottom DBR, now. The transfer matrix in Eq. 2.10 and scattering matrix in Eq. 2.12 have to include the entire structure with cavity layer and DBRs. Otherwise, the mode conditions remain as discussed

---

[3] If electronic quantum wells in the cavity are considered, the electronic density of states is changed and $\hat{\varepsilon}_c$ has to be modified with knowledge beyond the formalism introduced here. See e.g. [Sav]

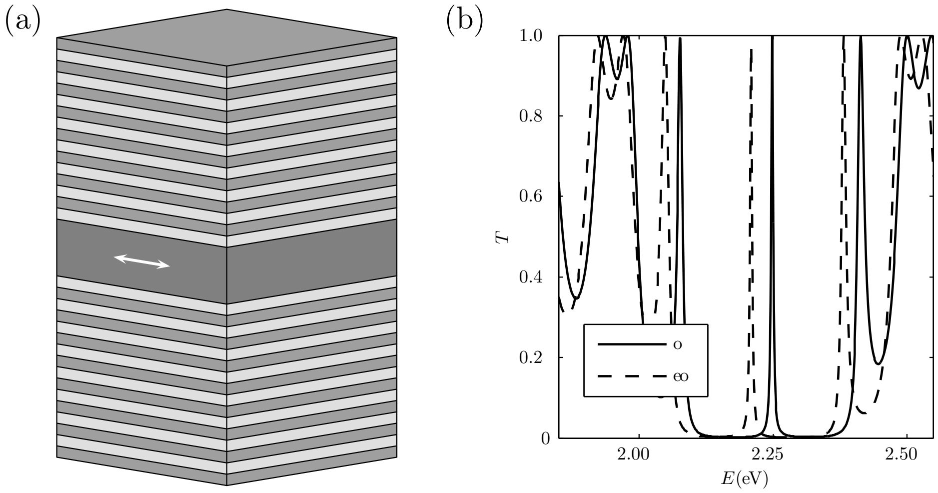

Figure 2.2: (a): Schematic example microcavity structure consisting of a cavity layer, symmetrically surrounded by DBRs. (b): Transmittance spectra at normal incidence if the microcavity structure is embedded in vacuum. Same 1µm-thick, optically uniaxial cavity layer as in Fig. 2.1, surrounded by 8 DBR layer pairs at top and bottom side with $n_1 = 1.8$, $n_2 = 2.2$, $d_1 = 77$nm, $d_2 = 63$nm. The Bragg stop-band ranges roughly from 2.1 to 2.4eV ($w_{\mathrm{DBR}} \approx 70$nm). Spectra for both polarizations, $\mathcal{E} \parallel$ optic axis of the cavity medium (*eo*) and $\mathcal{E} \perp$ optic axis (*o*). The double arrow in (a) marks the orientation of the optic axis.

above. The width w_{DBR} of the Bragg stop-band is determined by the contrast in refractive indices, $|n_1 - n_2|$, and can be estimated for normal incidence in units of wavelength as [Yeh88]

$$w^{\lambda}_{\mathrm{DBR}} \approx \frac{4\lambda_{\mathrm{DBR}}}{\pi} \sin^{-1}\Big(\frac{|n_1 - n_2|}{n_1 + n_2}\Big) \approx \frac{4\lambda_{\mathrm{DBR}}}{\pi} \frac{|n_1 - n_2|}{n_1 + n_2}\,, \tag{2.13}$$

or in units of photon energy as [Kav06; Kav+07]

$$w^{E}_{\mathrm{DBR}} \approx \frac{4hc_0}{\pi\lambda_{\mathrm{DBR}}} \left(\frac{\pi}{2} - \cos^{-1}\Big(\frac{|n_1 - n_2|}{n_1 + n_2}\Big)\right) \approx \frac{4hc_0}{\pi\lambda_{\mathrm{DBR}}} \frac{|n_1 - n_2|}{n_1 + n_2}\,. \tag{2.14}$$

The Bragg stop-band shifts toward higher photon energies at oblique angles. Its width at oblique angles depends on the polarization. The absolute reflectance of a DBR is mostly governed by the number of layer pairs. For normal incidence, the reflectivity at the center of the stop band can be estimated to $R = rr^* \approx 1 - 4\frac{n_a}{n_c}(\frac{n_1}{n_2})^{2N_{\mathrm{DBR}}}$ with layer pair number N_{DBR} and $n_1 < n_2$ [Sav+94; Bor+80]. In the spectral range around $E_{\mathrm{DBR}} = hc_0/\lambda_{\mathrm{DBR}}$, the phase upon reflection of a DBR depends approximately linearly on the photon energy, $\varphi_r^{DBR} \approx n_c L_{\mathrm{DBR}} \frac{E - E_{\mathrm{DBR}}}{\hbar c_0}$ [Sav+99; Pan+99b]. Here, L_{DBR} is the

DBR penetration depth at normal incidence. For $E \approx E_{\mathrm{DBR}}$ it holds [Sav+99; Kav+07]

$$L_{\mathrm{DBR}} \approx \frac{\lambda_{\mathrm{DBR}}}{2} \frac{n_1 n_2}{n_c |n_2 - n_1|} \,. \tag{2.15}$$

Now, as a mode is not only confined within the cavity layer itself, it is possible to assign an effective cavity thickness $d_c^{eff} = d_c + L_{\mathrm{DBR}}$ to account for the penetration of the DBRs. For normal incidence, Eq. 2.5 becomes [Sav+99; Sav]

$$E_c = \frac{\hbar c_0 \, m^{eff} \pi}{n_c^{eff} (d_c + L_{\mathrm{DBR}})} \,. \tag{2.16}$$

Still, this approximation holds only for $E \approx E_{\mathrm{DBR}}$ at normal incidence (and hence $\varphi_r = 0$) and a large number of DBR-layer pairs N_{DBR}. A different mode number m^{eff} is introduced instead of m because a larger number of wavelengths fits into d_c^{eff} compared to d_c. However, the assignment of mode numbers m in this thesis relates to the cavity layer thickness d_c. For angular- and hence polarization-dependent analytical approximations for φ_r^{DBR}, L_{DBR}, E_c and Γ_c for (pseudo-)isotropic planar microcavities, see e.g. [Stu11; Stu+11; Kav+07; Pan+99b].

2.2 Practical mode computation

As mentioned above, microcavity modes are found as mathematical singularities where transmission or reflection coefficients tend toward infinity [Vla+96; Sav+95; Kav+07; Sav]. In the general transfer matrix formulation here, the inverse transmission Jones matrix $\hat{J}_t^{-1}$ becomes singular if a complex energy fits a mode $\tilde{E} = \tilde{E}_c = E_c - i\Gamma_c$. Or, equivalently, the transmission Jones matrix $\hat{J}_t$ itself reveals a pole in the complex-energy space [Fel01; Byk+13]. Both expressions are identical here. Accordingly, for a given microcavity and given in-plane wave-vector $k_{||,x}$ under consideration, the transfer matrix $\hat{T}$ has to be computed for complex photon energies. Introducing a complex photon energy to the 4×4 transfer matrix described in section 1.2.1 has the following consequences:

- The partial transfer matrix propagator (Eq. 1.32) gets an exponentially increasing component $e^{\frac{d_j}{\hbar c_0}\Gamma \hat{\Delta}_j}$ in transparent media j, compensating for resonator losses. Hence $\Gamma_c \geq 0$.

- In general, $\hat{\varepsilon}^j$ and hence $\hat{\Delta}_j$ are also affected by $\mathrm{Im}(\tilde{E})$ if layer j is not dielectric.
- In order to fulfill Gauß's laws Eqs. 1.1 and 1.2 in vacuum (isotropic transparent ambient medium n_a), the wave vector is required to be complex as well, $\vec{\tilde{k}} = \vec{k} + i\vec{\eta}$.
    - For radiative modes considered here, it holds $\sigma_x = n_a\theta_a = \hbar c_0 k_x/E = \hbar c_0 \tilde{k}_x/\tilde{E} \in \mathbb{R}$ (without loss of generality, still $\tilde{k}_y = 0$) and hence $\eta_x = -\frac{1}{\hbar c_0}\sigma_x\Gamma$. In contrast to what has been discussed in section 1.1.1, now $\mathrm{Im}(\tilde{k}_x) < 0$ along with $\mathrm{Im}(\tilde{E}) < 0$. Still, $\tilde{k}_x$ is conserved along all layers.
    - As discussed in section 1.2.1, $\tilde{k}_z$ is not a conserved quantity along the structure. In vacuum (isotropic transparent ambient medium n_a) it holds $\eta_z = -\frac{1}{\hbar c_0} n_a \cos(\theta_a)\Gamma < 0$, similarly to η_x. This is also true for any transparent layer.
    - Neglecting spatial exciton dispersion ensures that $\hat{\varepsilon}^j$ and $\hat{\Delta}_j$ are not affected by $\mathrm{Im}(\tilde{k})$.

Accordingly, for the inhomogeneous plane wave in the microcavity structure, it holds generally $\vec{\eta} \nparallel \vec{k}$ and $\vec{\eta} \nparallel \vec{e}_z$ neither. While a free photon has no broadening and can be described by a real photon energy E_Λ and wave vector k_Λ, a cavity photon which is prone to loss processes can hence only be described by photon energy and wave vector, $\tilde{E}_c$, $\tilde{k}_c$, both being simultaneously complex. In particular, both having a negative imaginary part. This again is in contrast to a photon (polariton) in absorbing bulk medium, which can be described by either a complex energy with negative imaginary part and real wave-vector, or by a real energy and complex wave-vector with positive imaginary part (see section 1.1.1).

Within this thesis, cavity modes are described by complex mode energies $\tilde{E}_c = E_c - i\Gamma_c$ depending on real-valued $\vec{k}_{||}$. The related imaginary parts of the wave vector are uniquely determined by Γ_c and will not be depicted in plots further on.

Here, only radiative modes are considered, i.e., $\theta_a \leq 90°$ and $\sigma_x = n_a \sin(\theta_a)$ being real. However, in general, the formalism is also able to describe guided modes which cannot couple to vacuum due to total internal reflection [Yeh88]. Then, $\sin(\theta_j)$ and $\cos(\theta_j)$ become complex (for transparent ambient media, purely imaginary) and need to be replaced by the complex Pythagoras formula as e.g. $\sin^2(\theta_j) = 1 - \cos^2(\theta_j)$.

Singularities

As explained above, the cavity modes are described through their radiation fields in the embedding medium, usually vacuum, with $\vec{\mathcal{S}} \parallel \vec{k}$ there. This is not true inside the structure; a cavity-photon mode can consist of different wave fronts or light rays in the microcavity, depending on its polarization.

In order to find the complex mode energies $\tilde{E}_c$, it is sufficient to investigate $\det(\hat{J}_t^{-1})$ depending on E and Γ, as introduced by Eq. 2.11. The modes itself, i.e. the electric-field vectors are then found as matrix kernel if $\hat{T} = \hat{T}(k_{||,x}, \tilde{E}_c)$. It holds

$$\begin{pmatrix} \mathcal{E}_{TM}^{\rightarrow} \\ \mathcal{E}_{TE}^{\rightarrow} \end{pmatrix}_{back} \in \ker\left(\begin{pmatrix} T_{33} & T_{31} \\ T_{13} & T_{11} \end{pmatrix}\right), \tag{2.17}$$

$$\begin{pmatrix} \mathcal{E}_{TM}^{\leftarrow} \\ \mathcal{E}_{TE}^{\leftarrow} \end{pmatrix}_{front} = \begin{pmatrix} T_{43} & T_{41} \\ T_{23} & T_{21} \end{pmatrix} \begin{pmatrix} \mathcal{E}_{TM}^{\rightarrow} \\ \mathcal{E}_{TE}^{\rightarrow} \end{pmatrix}_{back}, \tag{2.18}$$

where $\mathcal{E}^{\rightarrow}$ describes forward-propagating modes, transmitted into the substrate, and $\mathcal{E}^{\leftarrow}$ backward-propagating modes spreading into the superstrate. This allows to obtain the polarization of an cavity-photon mode, described by the fields emitted into the ambient. The nullity, i.e. dimension of the kernel, is generally only one. Only for (isotropic) microcavities with cylindrical symmetry, $\hat{J}_t^{-1}$ becomes a zero-matrix for $k_{\|} = 0$ (normal incidence) and any field vector fulfills the mode condition. This situation is comparable to classic optic axes.

In principle, it is also possible to obtain the modes as residuals of the scattering matrix $\hat{S}$ by computing the matrix-valued Cauchy integral [Fel01; Byk+13]:

$$\mathrm{Res}(\hat{S}) = \frac{1}{2\pi i} \oint_{\mathcal{C}} \hat{S}\, d\tilde{E}\,, \tag{2.19}$$

where $\mathcal{C}$ is a closed curved in the complex-energy space around a mode energy. Then, the image of $\mathrm{Res}(\hat{S})$ is equivalent to the kernel of its inverse:

$$\begin{pmatrix} \mathcal{E}_{TM}^{front} \\ \mathcal{E}_{TE}^{front} \\ \mathcal{E}_{TM}^{back} \\ \mathcal{E}_{TE}^{back} \end{pmatrix}_{out} \in \ker(\hat{S}^{-1}) \equiv \mathrm{im}(\mathrm{Res}(\hat{S}))\,. \tag{2.20}$$

This is possible because $\hat{S}$ is a holomorphic function of $\tilde{E}$ around $\tilde{E}_c$.

Having obtained a mode in the form of a Jones vector, $(\mathcal{E}_{TM}, \mathcal{E}_{TM})^{\mathrm{T}}$, it can be expressed in terms of a Stokes or pseudospin vector by means of Eq. 1.19. It is reasonable to normalize such a Stokes vector.

$\vec{k}_{||}$ dependence

Knowing that k_z is quantized, the cavity-photon modes can be described depending on their in-plane wave-vector $\vec{k}_{||} = (k_x, k_y)^{\mathrm{T}}$. In the formalism described in section 1.2.1, $\vec{k}_{||} \equiv (k_x, 0)^{\mathrm{T}}$, and k_x is related to angle of incidence θ_a in the ambient medium n_a as

$$k_{||,x} = \frac{E}{\hbar c_0} n_a \sin(\theta_a)\,. \tag{2.21}$$

For coverage of the entire $\vec{k}_{||}$ space, Euler rotation angles $\tilde{\phi}$, $\tilde{\vartheta}$ and $\tilde{\xi}$ (cf. Eq. 1.20) are used to construct the transfer matrix $\hat{T}$. In the following, the formalism is explained for an optically uniaxial cavity medium like ZnO: For a given orientation of the optic axis described by the Euler angles ϕ and ϑ (ξ rotation is not needed for a uniaxial medium) and an arbitrary in-plane wave-vector described by $\vec{k}_{||} = (k_x, k_y)^{\mathrm{T}} = |\vec{k}_{||}|(\cos(\varphi), \sin(\varphi))^{\mathrm{T}}$, the Euler angles necessary construct the transfer matrix $\hat{T}$ are then given by

$$\tilde{\phi} = \phi - \varphi\,, \qquad \tilde{\vartheta} = \vartheta\,, \tag{2.22}$$

which replace ϕ and ϑ in order to transfer the laboratory xy coordinates of $\vec{k}_{||} = (k_x, k_y)^{\mathrm{T}}$ to $\tilde{x}\tilde{y}$ with $\vec{k}_{||} = (k_{\tilde{x}}, 0)^{\mathrm{T}}$. It holds $\tilde{\phi} = -\varphi$ for the optic axis in the cavity plane oriented along the y direction ($\phi = 0$, $\vartheta = 90°$). This would correspond to respectively aligned m-plane oriented ZnO.

In order to describe the linear polarization components with respect to its projections in the laboratory coordinate system in terms of $\mathcal{E}_x$ and $\mathcal{E}_y$ instead of using $\mathcal{E}_{TE}$ and $\mathcal{E}_{TM}$ from the $\tilde{x}\tilde{y}$ system, gnomonic projection is utilized:

$$\begin{pmatrix} \mathcal{E}_x \\ \mathcal{E}_y \end{pmatrix}_{xy} = \begin{pmatrix} 1 & 0 \\ 0 & e^{\pm 2i\varphi} \end{pmatrix} \begin{pmatrix} \mathcal{E}_{TM} \\ \mathcal{E}_{TE} \end{pmatrix}_{\tilde{x}\tilde{y}} . \tag{2.23}$$

Now, the z component of the TM field is tilted, i.e. gnomonically projected, into the xy plane as it would be observed experimentally in Fourier space imaging [Mic+14; Mic17]. Consequently, the first and second entries (the circular polarization is not affected) of the Stokes or pseudospin vector need to be modified. The new normalized Stokes vector $\tilde{\vec{S}}$ is given as

$$\begin{pmatrix} \tilde{S}_1 \\ \tilde{S}_2 \\ \tilde{S}_3 \end{pmatrix} = \begin{pmatrix} \cos(2\varphi) & \mp\sin(2\varphi) & 0 \\ \pm\sin(2\varphi) & \cos(2\varphi) & 0 \\ 0 & 0 & 1 \end{pmatrix} \begin{pmatrix} S_1 \\ S_2 \\ S_3 \end{pmatrix} , \tag{2.24}$$

where the upper signs of ± and ∓ are valid for forward traveling waves (towards $+z$, →) and the lower ones for backwards (towards $-z$, ←) traveling modes. Now, $\tilde{S}_1 = +1$ refers to linear polarization along the x axis of the laboratory coordinate system, $\tilde{S}_1 = -1$ to linear polarization along the y axis. The same basis transformation holds for the pseudospin $\vec{P}$ which becomes $\tilde{\vec{P}}$.

Polaritons

A cavity polariton, i.e. cavity photon in an absorbing cavity, is described similarly to a cavity photon in a transparent cavity. However, due to the strongly varying refractive index near e.g. an excitonic resonance (cf. Fig. 1.7), the density of cavity modes is strongly increased and proper separation between different modes with different mode numbers can become an issue. Figure 2.3 depicts the polariton modes in complex-energy space for a thick microcavity with a cavity medium revealing one excitonic resonance. Modes at energies higher than $E_{XL} = E_{X0} + \Delta_{\mathrm{LT}}$ are UPBs related to cavity-photon modes with mode number $m \leq 24$ here (decreasing energies with decreasing m). Modes at energies lower than $E_{X0} = 3.35\mathrm{eV}$ are LPBs with $m \geq 25$ (increasing energies with increasing mode number m) [Ric+15]. No radiative, transverse polariton modes occur in the reststrahlen-band range between E_{XL} and E_{X0}. Even for a thinner microcavity with the $m = 1$ cavity-photon mode in resonance with the

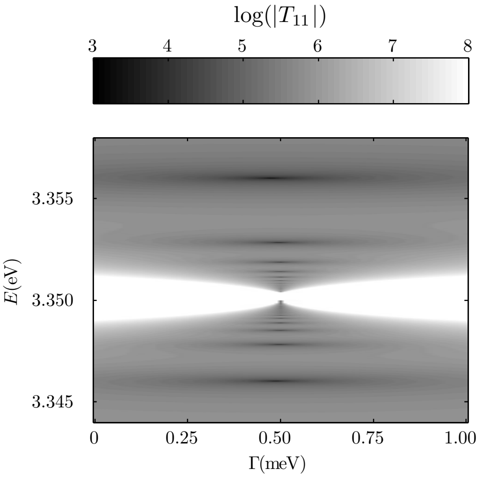

Figure 2.3: TE-polarized exciton-polariton modes, unveiled as minima of $|T_{11}|$ (transfer matrix element), of a microcavity with isotropic cavity medium at slightly oblique angle, $k_{||} = 4\text{µm}^{-1}$. The ≈ 2µm-thick cavity layer is symmetrically surrounded by DBRs consisting of 29.5 layer pairs and $E_{\mathrm{DBR}} = 3.1\,\mathrm{eV}$. The cavity layer's dielectric function is described by a Lorentz oscillator with $E_{X0} = 3.35\,\mathrm{eV}$, $2\Gamma_X = 1\,\mathrm{meV}$ and $\Delta_{\mathrm{LT}} = 0.4\,\mathrm{meV}$ [Ric+15]. Every minimum represents a polariton mode. Cf. also Fig. 2.4

exciton ($\lambda/2$ cavity), numerous LPBs appear close to E_{X0} (nearly exciton-like) while the UPBs for $m > 1$ are energetically far off. Practically, those LPB modes with mode number $m > 1$ are hardly distinguishable and establish a nearly dispersionless mode around E_{X0}, because their spectral separation becomes smaller than their broadenings (see Fig. 2.3). The dimension of the underlying Hilbert space of states is discussed in detail in section 2.3.

In practice, parametrization of the dielectric function is also an issue: If an absorbing layer cannot be sufficiently well described by (Lorentzian) oscillators, proper implementation of the effect of $\Gamma = -\mathrm{Im}(\tilde{E})$ on $\varepsilon(\tilde{E})$ is not possible. If, e.g., tabulated values of $\varepsilon_1(E)$ and $\varepsilon_2(E)$ are used, polaritonic microcavity modes can only be calculated in the approximation that the effect of Γ on the dielectric function (cf. Fig. 1.8) is negligible and $\varepsilon(\tilde{E}) \approx \varepsilon(E)$. This is true if modes are spectrally narrow (Γ small) or far from the resonance (cf. Fig. 1.8).

2.3 Quasi-particle approach

Finding solutions to the mode condition Eq. 2.10 in the transfer matrix notation gives exact complex mode energies of electromagnetic-wave poles based on Maxwell's equations. Alternatively, according to wave-particle dualism, cavity photons and polaritons can be described as quasi-particles as already introduced in section 1.1.4. In contrast to a free photon which only possess a relativistic mass, these quasi-particles gain effective rest mass due to the confinement potential of the cavity. With a quantized wave-vector component in z direction, they are quasi-free two-dimensional particles, having $\vec{k}_{||}$ as degree of freedom. In the following, the particle concept is explained for planar microcavities consisting of isotropic media or at least revealing cylindrical symmetry (e.g. c-plane oriented ZnO). Consequently, the considerations apply independently for both, TE- and TM-polarized modes.

Cavity photons

A cavity-photon mode obtained from the electromagnetic transfer matrix approach can be spectrally described as Lorentzian peak as it occurs from a Cauchy distribution as [Sav+99; And95; Kav+07]

$$\mathcal{E}\mathcal{E}^*(E) \propto \frac{1}{(E-E_c)^2+\Gamma_c^2}\,, \tag{2.25}$$

where Γ_c is the spectral $HWHM$. This expression is approximately proportional to $\frac{E}{(E^2-E_c^2)^2+4\Gamma_c^2E^2}$ which corresponds to the imaginary part of Eq. 1.23 (Lorentz oscillator), where exciton energy E_{X0} and spectral broadening Γ_X are replaced by the respective quantities for cavity photons, E_c and Γ_c. Thus, a cavity photon can be understood as quasi-particle.

The dispersion, i.e. $k_{||}$ dependence of E_c, can approximately be described in terms of a massive quasi-particle as [Pau+95; Kav+07; Sav+99]

$$E_c = \frac{\hbar c_0}{n_c^{eff}}|k| = \frac{\hbar c_0}{n_c^{eff}}\sqrt{k_\perp^2+k_{||}^2} \approx E_{c0} + \frac{\hbar^2}{2m_c}k_{||}^2\,, \tag{2.26}$$

where $k_{||} = \frac{E_c}{\hbar c_0} n_a \sin(\theta_a)$ with angle of incidence θ_a in the ambient medium n_a. Further, m_c is the cavity photon's mass, and the effective refractive index n_c^{eff}. Figure 2.4 (d) shows such a parabolic dispersion of cavity photons with

different mode quantum numbers m. This approximation is usually satisfactory for small values of $k_{||}$ but differs often from the true dispersion for large $k_{||}$; and m_c differs for TE and TM polarization [Kli+10]. It should be noted that usually $m_c \ll m_X$. As will be shown in section 3.3, Eq. 2.26 fails for generally arbitrary $\vec{k}_{||}$ direction if a microcavity is anisotropic and lacks cylindrical symmetry.
The dependence of (half the) mode broadening Γ_c on $k_{||}$ is principally more sophisticated. Analytic approximations for special cases can be found in [Stu+11; Stu11].

As mentioned above, if parts of the electromagnetic wave penetrate the DBRs, there are two different ways to define the ground state energy E_{c0}; either describing the quantization of the field in the cavity layer by $k_\perp$, or in the complete microcavity structure by $k_\perp^{eff}$ (see section 2.1 and Eq. 2.16). In the latter case, the fields within the DBRs determine an effective refractive index n_c^{eff} which deviates from n_c and depends on the polarization. For the ground state energy and hence the quantized $k_\perp$ or $k_\perp^{eff}$, it holds

$$\begin{aligned} E_{c0} &= \frac{\hbar c_0}{n_c} k_\perp &&= \frac{\hbar c_0}{n_c} \frac{m\pi - \varphi_r^{DBR}}{d_c} && (2.27) \\ &= \frac{\hbar c_0}{n_c^{eff}} k_\perp^{eff} &&\approx \frac{\hbar c_0}{n_c^{eff}} \frac{m^{eff}\pi}{d_c + L_{\mathrm{DBR}}}\,, && (2.28) \end{aligned}$$

with mode numbers $m < m^{eff}$. The approximation holds only for perfect tuning between DBR and cavity thickness, i.e. $E_c = E_{\mathrm{DBR}}$ (cf. Eq. 2.16 above), while Eq. 2.27 can also treat detunings between E_c and E_{DBR}.

Cavity polaritons

I order to describe cavity polaritons in the frame of quasi-particles, a coupled-oscillator Hamiltonian similar to Eq. 1.26 can be utilized. It reads

$$\tilde{E}_{LPB/UPB}\,\vec{\Xi}_{LPB/UPB} = \begin{pmatrix} \tilde{E}_X & V \\ V^* & \tilde{E}_c \end{pmatrix} \begin{pmatrix} \Xi_X \\ \Xi_c \end{pmatrix}\,. \qquad (2.29)$$

The condition for applicability of this Hamiltonian is $\Delta_{\mathrm{LT}} \ll E$, $\Gamma_X \ll E$ and most of all, the reflectivity in the cavity is large, $1 - R \ll 1$, which results in small mode broadening $\Gamma_c \ll E$ [Kav+07]. Figure 2.4 (e) illustrates such exciton-polariton dispersions for different mode numbers m. In the vicinity of

$k_{||} = 0$, the polariton branches can still be approximated parabolically following Eq. 2.26. Depending on the detuning between E_{c0} and E_{X0}, the related effective mass can be closer to m_X or m_c. Usually, the polariton effective mass is reduced compared to the one of the exciton. This is of utter importance for phenomena as Bose-Einstein-like condensation of exciton-polaritons [Den+10; Kav+03; Kav+07]. In contrast to Eq. 1.26 describing bulk polaritons, i.e. the coupling of excitonic resonances to free photons, both energies, $\tilde{E}_X$ and $\tilde{E}_c$, are complex now. Approximately, the coupling strength V can be taken independent of k or $k_{||}$ if E_c does not vary strongly in the considered spectral range. Though, exactly it is not independent. Empirically, especially if Γ_c becomes large, cavity polariton energies can only properly be described if $V = V(k_{||})$. Nevertheless, V is effectively decreased because parts of the wave penetrate the dielectric DBR layers. It holds[4] [Kav+07; Gon+15]

$$V \approx V_{bulk}\sqrt{\frac{d_c}{d_c + L_{\mathrm{DBR}}}}\,. \tag{2.30}$$

Similarly to the bulk exciton-polariton, the Rabi splitting is reduced by the spectral broadenings of exciton and cavity photon [Kav+07; Sav+99; Sav+95]:

$$\hbar\Omega_R = \sqrt{4|V|^2 - (\Gamma_X - \Gamma_c)^2}\,. \tag{2.31}$$

However, slightly different splittings can be observed in reflectance, transmittance, absorbance and luminescence spectra because of slightly varying broadenings and peak overlaps [Sav+95; Kav+07]. The differently obtained splittings do only exactly coincide if $\Gamma_X = \Gamma_c = 0$.

Multi-level systems

As already introduced in the discussion of Fig. 2.3, unlike bulk polaritons, there is never only one photon mode to be considered in microcavities but a whole bunch with different mode numbers m [And95]. In particular, as the exciton center-of-mass is quantized, the mode number m is a principle quantum number. Thus, each mode number represents an independent sub-space of polariton states. If a single excitonic resonance couples to cavity photons with

---

[4] If quantum wells are incorporated in the cavity, it holds for the coupling strength $V \propto 1/\sqrt{d_c + L_{\mathrm{DBR}}}$ instead of $V \propto \sqrt{d_c/(d_c + L_{\mathrm{DBR}})}$ [Dev07; Hou+94; Sav+95; Kav+07].

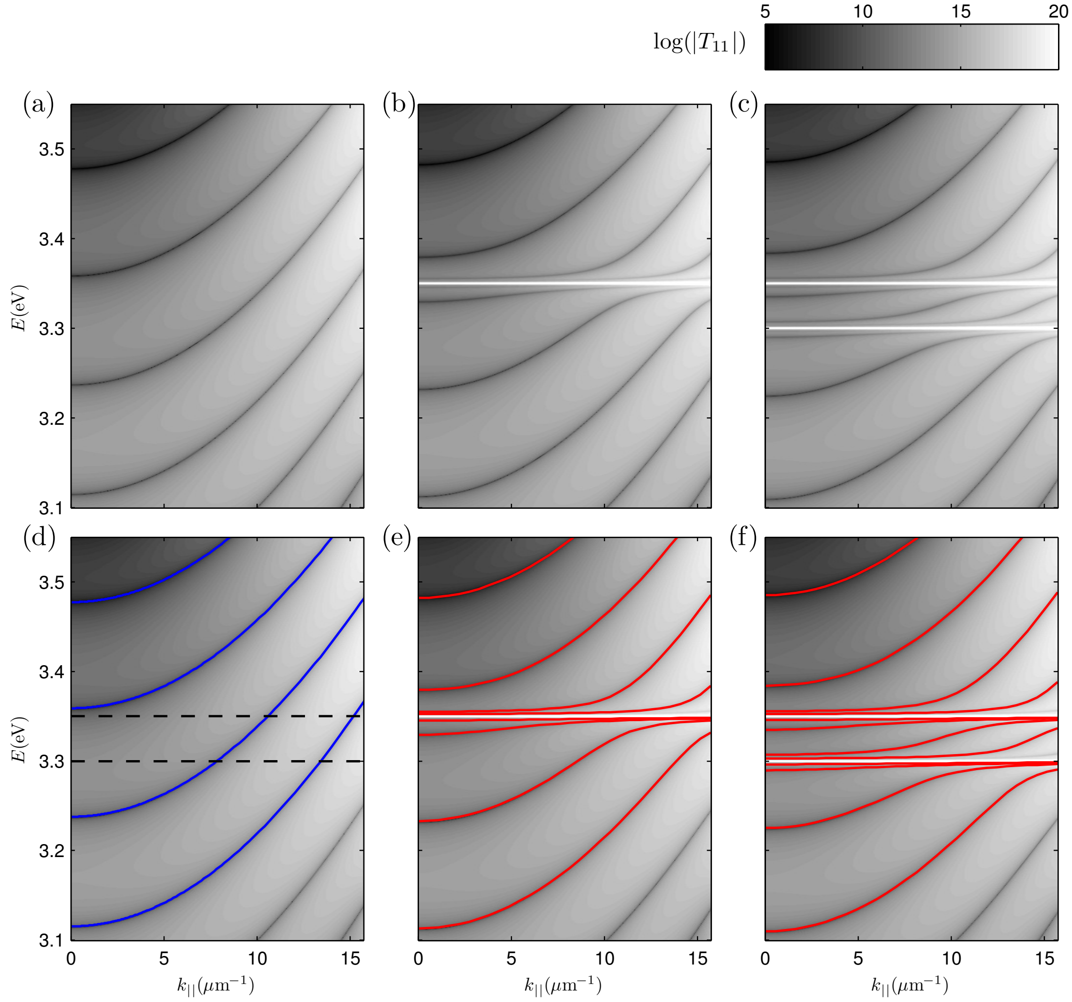

Figure 2.4: TE-polarized exciton-polariton modes of an $\approx 2\,\mu$m-thick isotropic cavity layer symmetrically surrounded by DBRs consisting of 29.5 layer pairs and $E_{\mathrm{DBR}} = 3.1$eV. The transfer matrix element T_{11} is shown depending on real-valued energy E and in-plane wave-vector $k_{||}$ such that the gray images correspond to the modulus of inverse transmission coefficients. For clarity, all images are shown twice. (a,d): Dielectric cavity layer with $\varepsilon_{\infty} = 6.25$. Blue lines in (d) show modeling using Eq. 2.26 for mode numbers $m = 23 - 26$. (b,e): The cavity layer's dielectric function contains an excitonic resonance with $E_{X0} = 3.35$eV, $2\Gamma_X = 1$meV and $\Delta_{\mathrm{LT}} = 0.4$meV. Red lines in (e) illustrate the modeled polariton dispersion according to Eq. 2.32 for the same mode numbers. (c,f): Same with a second excitonic resonance at $E_{X0} = 3.30$eV and model using Eq. 2.33 in (f). The exciton energies are also depicted as dashed lines in (d).

mode number $m = 1 \ldots N_c$, the dimension of the related polariton Hilbert-space is given as $2N_c$. Consequently, this Hilbert space consists of the direct sum of the two-dimensional sub-spaces for each m, as can be shown with the introduced transfer-matrix approach [Ric+15]. Accordingly, also the Hamiltonian of Eq. 2.29 changes to

$$\hat{H} = \bigoplus_{m=1}^{N_c} \begin{pmatrix} \tilde{E}_X & V_m \\ V_m & \tilde{E}_{cm} \end{pmatrix} \tag{2.32}$$

$$\equiv \begin{pmatrix} \tilde{E}_X & V_1 & 0 & 0 & \ldots & 0 & 0 \\ V_1 & \tilde{E}_{c1} & 0 & 0 & \ldots & 0 & 0 \\ 0 & 0 & \tilde{E}_X & V_2 & & \vdots & \vdots \\ 0 & 0 & V_2 & \tilde{E}_{c2} & & & \\ \vdots & & & & \ddots & & \\ 0 & 0 & \ldots & & & \tilde{E}_X & V_{N_c} \\ 0 & 0 & \ldots & & & V_{N_c} & \tilde{E}_{cN_c} \end{pmatrix} .$$

This becomes especially important for thick microcavities as shown examplewise in Fig. 2.4 (b) and (e). Here, a high-quality microcavity is chosen such that the cavity-photon broadening becomes negligible, $\Gamma_c \approx 0$. It is important to mention that no polariton dispersion line crosses the line of the exciton energy (dashed in Fig. 2.4 (c)). One might say, that coupling of the exciton with the cavity photons lifts the degeneracy of excitons with different mode number m. In the literature, also approaches utilizing a (N_c+1)-dimensional Hilbert space are found, e.g. [Sch+10; Rév+12; Fau+09; Oro+11; Ric+05; Sav; Sav+94]. Those seem to fail because the formalism introduces an effective coupling between cavity photons of different mode number and results in meaningless coupling strengths deduced from modeling. In fact, the coupling strengths V_m depend on the overlap of the cavity photon with mode number m with the *active* cavity medium according to Eq. 2.30, where L_{DBR} differs in principal for different m. For a thick microcavity, $V_m \approx V_{bulk}$ and hence independent of m if the modes are located in the center of the Bragg stop-band.
As discussed above, for a $\lambda/2$ cavity with the focus on $m = 1$, only LPBs with $m \leq 1$ can play a role. However, if the related photonic modes are very broad and the confinement weak, peaks in transmittance or luminescence as well as dips in reflectance spectra are washed out and disappear. Hence, it is sufficient

to consider only $m = 1$ then with a two-dimensional Hilbert space according to E. 2.29.

If N_X excitons are involved [Oue+15; Vla+96; Lag77; Rév+10; Blo+97; Nak+08], the dimension of the polariton Hilbert-space increases to $N_c(N_X+1)$ and the coupled-oscillator quasi-particle Hamiltonian becomes

$$\hat{H} = \bigoplus_{m=1}^{N_c} \begin{pmatrix} \tilde{E}_{X1} & 0 & \dots & 0 & V_{1m} \\ 0 & \tilde{E}_{X2} & & & V_{2m} \\ \vdots & & \ddots & & \vdots \\ 0 & & & \tilde{E}_{XN_X} & V_{N_Xm} \\ V_{1m} & V_{2m} & \dots & V_{N_Xm} & \tilde{E}_{cm} \end{pmatrix} . \tag{2.33}$$

The necessity for such a Hamiltonian is also clear from comparison with the polariton equation 1.16 if more than one Lorentz oscillator (Eq. 1.23) is added to the dielectric function of the cavity medium. A respective situation with 2 excitons is shown in Fig. 2.4 (c) and (f). Although in Fig. 2.4 only TE-polarized modes of a cylindrically symmetric microcavity are shown, the same principals hold for TM polarization. If anisotropic media are considered, the coupling strengths are generally no longer independent of $\vec{k}_{||}$ because excitons are not dipole-active for all polarization directions. However, for given $\vec{k}_{||}$, $\tilde{E}_{cm}$ and $\tilde{E}_{Xj}$, a V_{jm} can always be found in order to describe the cavity polariton energies according to Eq. 2.33. Besides that, the consideration leading to Eqs. 2.32 and 2.33 are also valid for microcavities with confinement dimensions differing from the planar case, e.g. wire resonators with whispering-gallery modes [Nob+04; Sch+10; Sun+08; Pan+99a; Mic17].

In practice, if the mode broadenings are large, it can occur that no proper distinction is possible. Furthermore, the assumption V being independent of $\vec{k}_{||}$ becomes critical then. Nevertheless, the underlying number of states, i.e. dimension of the Hilbert space, is as large as required by Eq. 2.33, and no polariton-dispersion line must cross an exciton energy unless the respective coupling strength vanishes.

Eventually, it should be noted again, that the considerations apply separately for TE- and TM-polarized cavity modes. Thus, the total number of modes is twice the here mentioned one.

Chapter 3

Computation:
Exceptional points in anisotropic microcavities

It is hardly possible to find useful analytic approximation of the 4×4 transfer-matrix calculus introduced in chapters 1 and 2 if arbitrarily anisotropic structures and arbitrary propagation directions are considered. Thus, numerical computations of Fabry-Pérot modes in anisotropic planar microcavities are presented in this chapter. The principal characteristics of the complex mode energies and the polarization is deduced from a simplified model, and the discovered phenomena, especially related to mode degeneracies, are identified. A summary of the insights has been published in [Ric+17].
Finally, the effect of exciton-polaritons in anisotropic microcavities is shortly discussed in section 3.4.

3.1 Numerical methods

All computations shown in this thesis were carried out with MATLAB using double-precession floating-point format for real as well as imaginary parts of the complex numbers [Mata]. For the complex matrix exponential functions of the partial transfer matrices, the Padé approximation with scaling and squaring steps has been used [Mol+03]. In order to find the singularities in complex-energy space as minima of $|\det(\hat{J}_t^{-1})|$ for a given $\vec{k}_{||}$, two different numerical optimization methods have been used: Fast computations have been carried out with a Nelder-Mead simplex method which means, here, that a triangle in the two-dimensional complex-energy space is reflected, contracted and expanded in order to find the minimum [Lag+98]. Albeit rather fast, this algorithm lacks accuracy and, in some cases, does not converge. However, speed is an advantage especially if many complex-valued matrix exponentials have to be computed. More accurate computations have been performed with a Newton-like (gradient-based) method which computes the numerical derivative in the vicinity of a point in parameter (complex-energy) space in each iteration [Col+96]. Both methods rely on properly chosen initial values. This is especially important if different modes are close to each other in the complex-energy space (cf. e.g. Fig. 2.4, or consider the vicinity mode degeneracies). While the simplex method has a high risk of jumping between different modes then, the Newton-like method remains more reliable if initial values are sufficiently close to the singularities. In particular, initial values were extrapolated by piecewise cubic or spline functions from neighboring points in a $\vec{k}_{||}$ grid. Typical accuracies for obtained complex energies are in the order of less than 1µeV with around 1000 function evaluations, i.e. transfer-matrix computations.

As described above, mode polarizations are obtained from the kernel of the inverse transmission Jones matrix $\hat{J}_t^{-1}$, if the complex mode energy has already been obtained with high accuracy. To obtain the null eigenvectors, here, MATLAB makes use of the ZGEEV routine of the *Linear-Algebra PACKage* (LAPACK) Fortran-library[1] [Matb; And+99]. In practice, as the accuracy of the obtained complex energy is not perfect, the matrix will not be exactly singular but only very ill-conditioned. Hence, the eigenvector with vanishing eigenvalue is the one of the kernel. A numerical inaccuracy remains.

---

[1] In particular, the ZGEEV routine uses Schur factorization (i.e., transformation into an upper triangular matrix), in the case here [Int]. Also, a preliminary balancing step with scaling factor 2 is performed [Matb].

3.2 Model and findings for anisotropic, dielectric microcavities

When designing an optical microcavity, there is a large number of parameters to choose, reaching from the material properties coming to the individual layer thicknesses. In order to restrict the investigation to the most relevant aspects, an idealized $\lambda/2$ cavity is chosen as toy model. In particular, dielectric materials with constant (wavelength-independent) refractive indices are assumed. As cavity layer, an optically uniaxial, positively birefringent material is taken, i.e. $\varepsilon_{||} > \varepsilon_{\perp}$. Used material and structure parameters are summarized in Tab. 3.1. They are adopted and idealized from a real ZnO-based microcavity with DBRs consisting of Al_2O_3 and YSZ layers [Fra+12; Fra12]. For simplicity, a substrate is neglected, assuming the uniaxial cavity layer being symmetrically surrounded by DBRs consisting of isotropic media, and the whole structure being embedded in vacuum. For the example structure, λ_{DBR} is chosen as 496 nm ($E_{\mathrm{DBR}} = 2.5\,\mathrm{eV}$). Values for the cavity thickness are varied in a range such that the $\lambda/2$ cavity-photon mode ($m = 1$) is spectrally located in the Bragg stop-band. Hence $d_c \approx \lambda_{\mathrm{DBR}}/(2n_c) \approx 110\,\mathrm{nm} \pm \Delta d_c$. The effect of varying d_c is discussed below.

For demonstration of the principal mode dispersions, Figs. 3.1 and 3.2 show

Table 3.1: Parameters used for the anisotropic microcavity. The cavity layer has a positive birefringence of 2.7 %. The DBR parameters result in a Bragg-stop-band width of $w_{\mathrm{DBR}} \approx 0.3\,\mathrm{eV}$ according to Eq. 2.14. Values for N_{DBR} and d_c have been varied.

ambient/substrate refractive index	$n_a = n_s$	1
DBR layer 1 thickness	d_{DBR1}	56.4 nm
DBR layer 2 thickness	d_{DBR2}	68.9 nm
DBR layer 1 refractive index	n_{DBR1}	2.2
DBR layer 2 refractive index	n_{DBR2}	1.8
number of DBR layer pairs	N_{DBR}	8 (0-15)
cavity layer refractive indices	$n_{c\perp}$	2.20
	$n_{c\|\|}$	2.26
cavity layer thickness	d_{c}	130 nm (70-150) nm

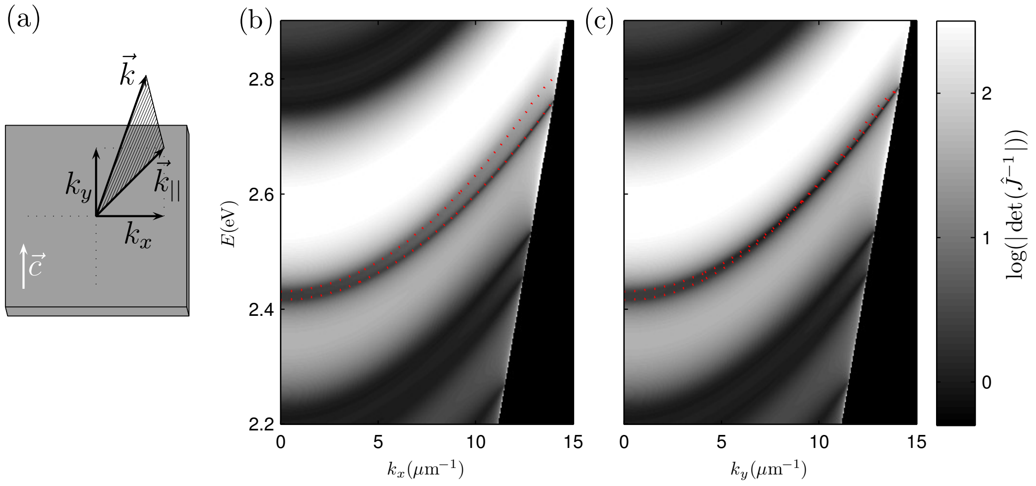

Figure 3.1: (a): Schematics of the chosen coordinate system for the momentum space with the cavity layer's optic axis aligned parallel to y. Note that $\vec{k}$ is the wave vector in the ambient; only its in-plane component $\vec{k}_{||}$ is conserved in the sample. (b,c) Determinant of the inverse transmission Jones matrix, representing the optical modes as minima, depending on the in-plane wave-vector $\vec{k}_{||}$ and a real-valued photon energy E. A microcavity with 130 nm-thick, uniaxial cavity layer and DBRs of $N_{\mathrm{DBR}} = 8$ layer pairs is assumed (parameters according to Tab. 3.1). Two different propagation directions are shown: (a): along k_x ($k_y = 0$). (b): along k_y ($k_x = 0$). The cavity mode energies are plotted as dotted lines for clarity. E_c can degenerate for propagation along the optic axis (b) but not for propagation perpendicular (a); see also Fig. 3.2. While one mode gets broader, the other one becomes narrower for increasing $k_{||}$. The black areas in the corner mark the regions of guided modes.

the $k_{||}$ dependent determinant of the inverse transmission Jones matrix for a microcavity with $d_c = 130\,\mathrm{nm}$ and the optic axis of the cavity medium aligned parallel to the cavity plane (like m- or a-plane oriented ZnO). Here and further, the optic axis is chosen to be aligned along the y direction. At $k_{||} = 0$, both mode energies are smaller than 2.5 eV because $n_c d_c > \lambda_{\mathrm{DBR}}/2$ has been chosen by selecting $d_c = 130\,\mathrm{nm}$. First of all, the computations show that the $\lambda/2$ mode is split (if not degenerate) into only two modes. This holds also arbitrary directions of $\vec{k}_{||}$ with respect to the optic axis of the cavity layer and contrasts proposals that the mode splits up into two TE-polarized, and two TM-polarized modes for arbitrary anisotropies [Stu+11]. The reason for this contradiction is that approaches to separate the mode computation into

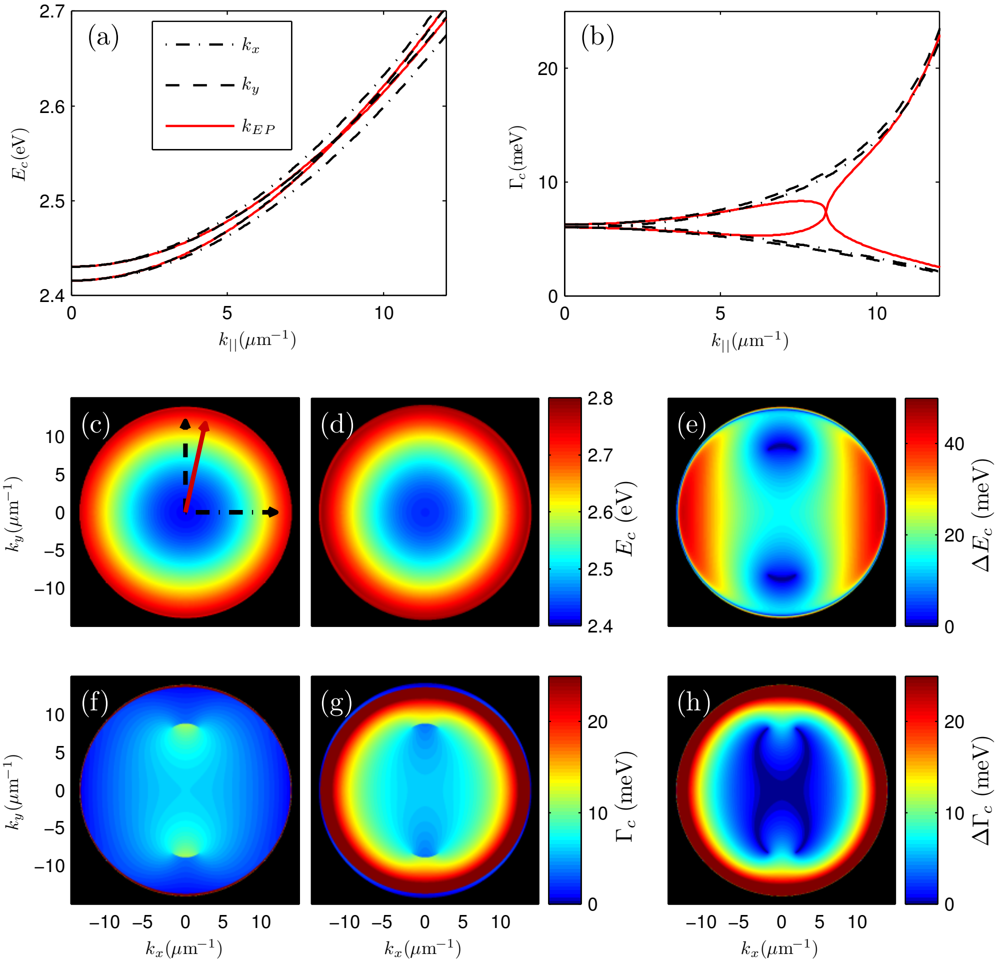

Figure 3.2: Dispersion of the complex mode energies $\tilde{E}_c$ for an anisotropic microcavity with the parameters given in Tab. 3.1 with $d_c = 130\,\mathrm{nm}$ and eight-period DBRs ($N_{\mathrm{DBR}} = 8$). The optic axis of the cavity medium is oriented along the y direction. (a,b): real and imaginary parts of $\tilde{E}_c$ for both modes considering the propagation directions indicated in (c). k_{EP} assigns a direction hitting an exceptional point. Simultaneous degeneracy of E_c and Γ_c occurs only for propagation directions crossing an exceptional point (red lines). (c,d,e): E_c for both modes along the entire $\vec{k}_{||}$ space and respective energetic mode splitting. (f,g,h): Γ_c depending on $\vec{k}_{||}$, and difference of the mode broadenings. Panels (c,f) represent the energetically lower mode 1, (d,g) the energetically higher mode 2.

independent problems for TE and TM polarization do not account for their coherent superpositions[2].

Figure 3.2 (c-h) shows the $\vec{k}_{||}$ dependence of the complex mode-energies $\tilde{E}_c$ and degeneracies of E_c and Γ_c for the entire hemisphere covered by the radiative modes. Here and later, at any $\vec{k}_{||}$, mode 1 is assigned the energetically lower, mode 2 the energetically higher one, $E_{c1} \leq E_{c2}$. Both mode energies increase with increasing $|k_{||}|$. While one mode is getting broader for large $|k_{||}|$, the other one becomes narrower (cf. also Fig. 3.1 again). There are mutually excluding trajectories in $\vec{k}_{||}$ space where either E_c or Γ_c degenerate, as clearly visible in Figs. 3.2 (e) and (h). The end points of those trajectories overlap and establish four exceptional points (see appendix A.2) where both, E_c and Γ_c degenerate simultaneously. They occur for propagation direction nearly but not exactly along the optic axis of the anisotropic cavity medium. The characteristics is very similar to the situation of singular optic axes and the related degeneracies of the Fresnel wave-surface as discussed in section 1.1.3 and illustrated in Fig. 1.6 (b) and (c). In figure 3.2, the modes are sorted by energy E_c. This yields a discontinuity in Γ_c along the trajectory of degenerate E_c (Figs. 3.2 (f) and (g)). This discontinuity can be resolved by exchanging mode 1 and mode 2 upon passing it. However, this would result in a discontinuity for E_c along the $\Gamma_{c1} = \Gamma_{c2}$ trajectory. This again is an indication for the complex-square-root topology of the complex-energy surfaces which will be discussed below. In fact, there are also E_c degeneracies near the horizon for large $|k_y|$ which shall not be discussed in detail here. Nonetheless, this hints on additional pairs of exceptional points hidden in the guided modes.

Figure 3.3 shows the modes themselves in terms of their polarization as projected Stokes vector $\vec{\tilde{S}}$. For $\vec{k}_{||} = \vec{0}$, one mode is polarized parallel, the other perpendicular to the optic axis of the cavity-layer medium. For $\vec{k}_{||} \neq \vec{0}$ and propagation neither parallel nor perpendicular to this optic axis, the modes become generally elliptically polarized, i.e. $\tilde{S}_3 \neq 0$. For comparison, respective mode polarization patterns for microcavities with cylindrical symmetry

---

[2] Indeed, reflection and transmission spectra for TE and TM polarization which ignore polarization conversation, i.e. considering only the diagonal entries of a Jones matrix, show two modes in each spectrum at slightly differing energetic positions. Those seemingly four different mode energies result from the spectral overlap of the modes which is generally different for TE and TM polarization.

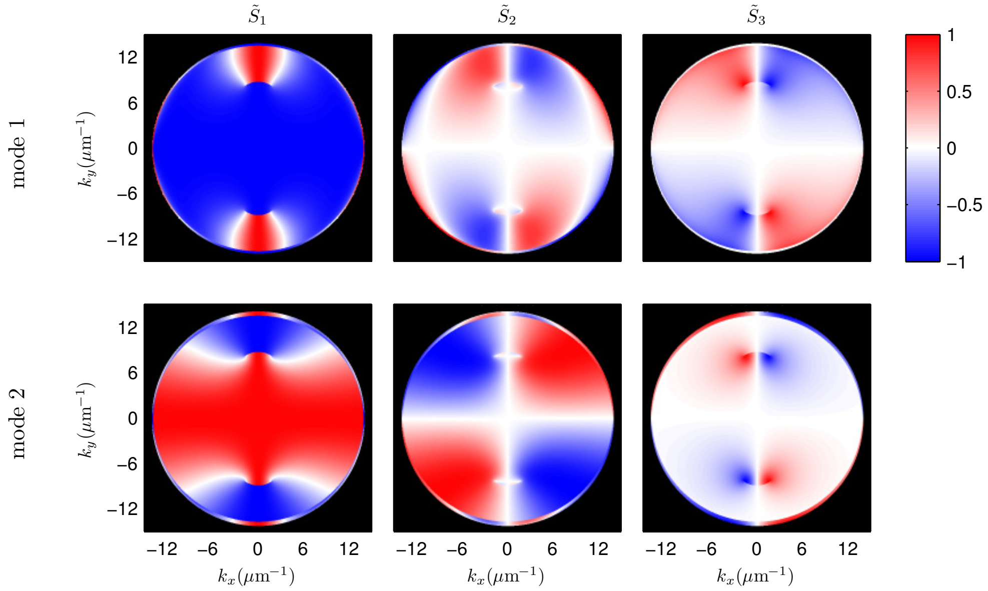

Figure 3.3: Mode polarization patterns for the microcavity presented in Figs. 3.1 and 3.2. The Stokes vector is projected according to Eq. 2.23.

are shown in appendix A.4. Only TE- and TM-polarized modes occur then. Thus, the modes are always orthogonal to each other in cylindrically symmetric microcavities. For the anisotropic microcavity, however, the circularity ($\tilde{S}_3$) of the two modes at any $\vec{k}_{||}$ has the same sign for both. This means, both obtain at the same time either right or left circular polarization contributions. Consequently, the modes are generally (especially if $\tilde{S}_3 \neq 0$) not orthogonal to each other anymore. The above mentioned exceptional points are characterized by fully coinciding polarization states which are either left or right circular. Thus, both, complex mode-energies and eigenmode polarization-vectors degenerate at the exceptional points. The exceptional points occur pair-wise, where one exhibits left- the other right circular polarization. This is again similar to singular optic axes. Finally, the orientation of the linear polarization is winding around the exceptional points in $\vec{k}_{||}$ space, as will be discussed in detail below (Fig. 3.8). As introduced, the assignment in Fig. 3.3 is such that mode 2 obtains the higher energy E_c. This yields again discontinuities in the momentum space along trajectories of degenerate E_c which can be resolved if the modes are exchanged upon passing such a trajectory. This discontinuity is especially remarkable in the $\tilde{S}_1$ component.

The effect of shifting the cavity mode energies with respect to E_{DBR} by

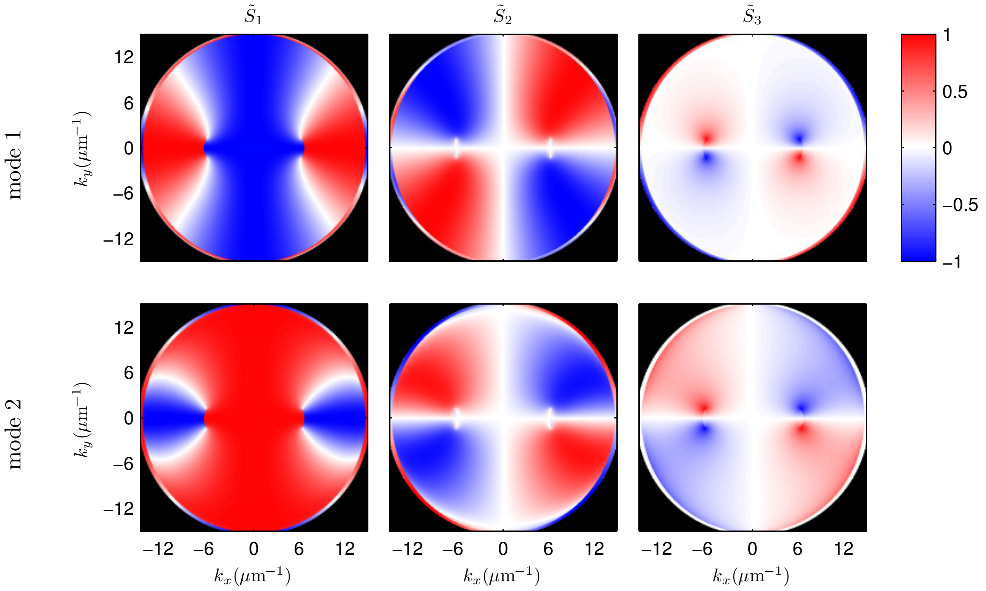

Figure 3.4: Mode polarization patterns in terms of the Stokes vector for a microcavity similar to Fig. 3.3 but with cavity layer thickness $d_c = 90\,\mathrm{nm}$. The exceptional points occur for directions close to $k_y = 0$. It can also be noted that the smaller cavity thickness yields higher mode energies E_c and hence larger values for the maximum accessible $k_{||}$, compared to d_c=130 nm. Further, the mode broadening is slightly reduced.

varying the cavity layer thickness d_c is shown exemplarily in Fig. 3.4. Here, d_c is decreased to 90 nm. While for $d_c > \lambda_{\mathrm{DBR}}/(2n_c) \approx 110\,\mathrm{nm}$, the exceptional points have occurred at directions nearly but not exactly parallel to the optic axis of the anisotropic cavity medium, the exceptional points have shifted now towards directions nearly perpendicular to it for $d_c < \lambda_{\mathrm{DBR}}/(2n_c)$. It should be noted that in general, the same effect is observed if d_c is kept at 130 nm but a positively birefringent cavity layer is replaced by a negatively birefringent one ($n_{c\perp} > n_{c||}$). Figure 3.5 depicts the systematic dependence of the mode degeneracies and exceptional points on d_c. If d_c is much larger than $\lambda_{\mathrm{DBR}}/(2n_c)$ the exceptional points occur for directions close to parallel to the optic axis. With decreasing d_c, they move towards larger k_y values. At the same time k_x increases such that for $d_c < \lambda_{\mathrm{DBR}}/(2n_c)$, the exceptional points occur at directions nearly perpendicular to the optic axis of the cavity layer. With further decrease of d_c they approach the origin again. If the mode broadenings are sufficiently small, here provided by a large number of DBR layer pairs N_{DBR},

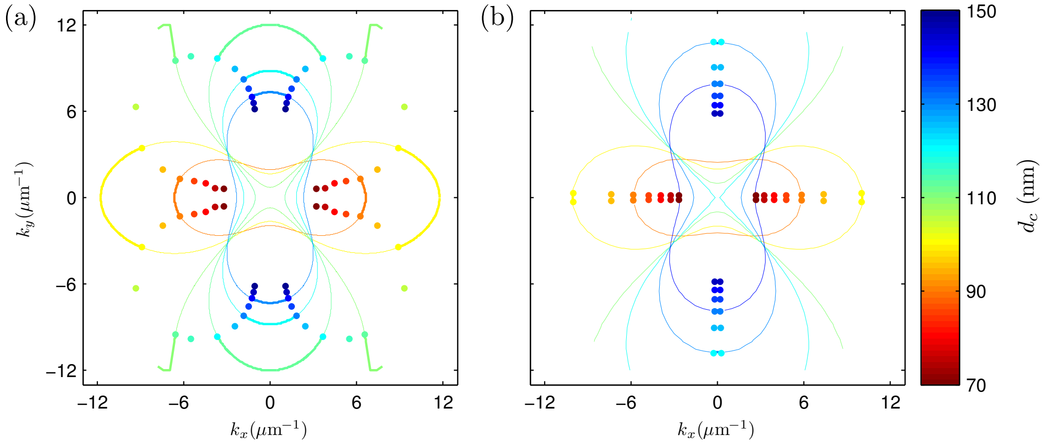

Figure 3.5: Exceptional points (dots) for selected values of the cavity thickness d_c (color). Structure parameters are given in Tab. 3.1. Lines mark the directions in $\vec{k}_{||}$ space of degenerate energy E_c (thick lines) and broadenings Γ_c (thin lines). (a): for a microcavity with DBRs of $N_{\mathrm{DBR}} = 8$ layer pairs; (b): $N_{\mathrm{DBR}} = 15$ layer pairs. Only the relevant trajectories are shown. Further $E_{c1} = E_{c2}$ trajectories can occur near the horizon; see Fig. 3.2. Note that the thick lines in (b) are mostly hidden behind the dots.

no exceptional points are observed if $d_c \approx \lambda_{\mathrm{DBR}}/(2n_c)$. Hence, they are pushed out of the light cone, as illustrated in Fig. 3.5 (b). There may be exceptional points in guided modes then, which, however, are beyond the scope of this thesis. For values of d_c smaller/larger than 70/150 nm, the cavity modes are spectrally close to the edge of the Bragg stop-band and disappear soon.
Instead of varying d_c or the birefringence of the anisotropic cavity layer, λ_{DBR} could be varied with a similar result. Interestingly, if the top and bottom DBR have opposite *detuning*, i.e., $\lambda_{\mathrm{DBR}}^{top} \gtrless 2n_c d_c \gtrless \lambda_{\mathrm{DBR}}^{bottom}$ they compensate each other. Hence, effectively, a perfectly tuned microcavity, $n_c d_c \approx \lambda_{\mathrm{DBR}}/2$, results. To summarize, a detuning between $\frac{m}{2}\lambda_{\mathrm{DBR}}$ and $n_c d_c$ is generally necessary to observe exceptional points within the vacuum light cone.

Changing d_c or λ_{DBR} in a range as shown above, or changing the anisotropy of the cavity layer, does not primarily affect the spectral broadening of the cavity-photon mode. The broadening can be varied directly by changing the number of DBR layer pairs. The effect is demonstrated in Fig. 3.6, where top and bottom DBRs are varied with respect to the number of layer pairs

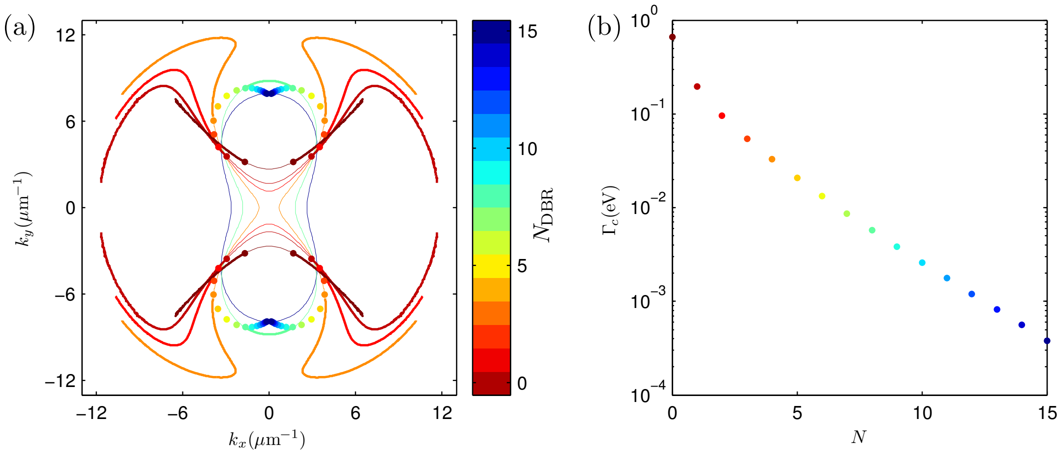

Figure 3.6: Exceptional points (dots) depending on the number of DBR layer pairs N_{DBR} (color) for $d_c = 130\,\mathrm{nm}$ and the structure parameters given in Tab. 3.1. (a): Directions in $\vec{k}_{||}$ space of degenerate energy E_c (thick lines) and broadenings Γ_c (thin lines). (b): Mode broadening in terms of Γ_c at the exceptional points.

N_{DBR}. As already indicated by Fig. 3.5, a fewer number of DBR layers increases the angular splitting between two exceptional points which are connected by the trajectory of degenerate real part of the mode energies E_c. If the modes become very broad, the exceptional points come closer together again. This general behavior is also known from singular optic axes, where the angular splitting of a classic optic axis into a pair of singular axes is wide if both, the anisotropy (difference of the refractive indices or real parts of $\hat{\varepsilon}$) and the absorption (imaginary part of $\hat{\varepsilon}$) are large, or if both are small. The angular splitting of two singular axes is usually small if the anisotropy is large and the absorption small or vice-versa [Gru+17b; Voi02; Stu+16]. In the case of microcavities, the mode broadening is described by the energy's imaginary part and hence, a loss rate or pseudo-absorption. Thus, the largest splitting of exceptional points in $\vec{k}_{||}$ space represents a similarly balanced condition with respect to the cavity anisotropy $n_{||}/n_{\perp}$ and the mode broadening Γ_c. The mode broadening at the exceptional points is almost exponentially dependent on the number of DBR-layer pairs, as depicted in Fig. 3.6 (b). Furthermore, the non-zero circular polarization components ($\tilde{S}_3$) will be wider spread in $\vec{k}_{||}$ space if the modes are broader, yielding blurred exceptional points [Gru+17a]. Even if the DBRs are completely removed ($N_{\mathrm{DBR}} = 0$), the layer thickness oscillations of a single cavity-layer can be described as cavity-photon modes

and exceptional points are found. However, mode distinction becomes difficult then, because of the broadening. See section 2.1.
Another remarkable aspect visible in Fig. 3.6 (a) is that, with increasing N_{DBR}, the $E_{c1} = E_{c2}$ trajectory at large k_y values merges. Another E_c degeneracy appears close to the horizon, i.e. edge of the vacuum light cone (not shown in Fig. 3.6 (a)). For $N_{\mathrm{DBR}} = 8$ this separate E_c degeneracy near the horizon is visible in Figs. 3.2 (e) and 3.3. It can be expected that these trajectories are terminated by other pairs of exceptional points embedded in the momentum-space range of guided modes.

Of interest is also the effect of inclining the optic axis of the uniaxial cavity medium. If the optic axis is still aligned parallel to y, no difference for the complex mode energies must occur for $+k_y$ and $-k_y$ if a mid-plane symmetric structure is considered. However, the mode polarization may differ. This is indeed observed in numerical computations, although not explicitly shown here. According to those computations, the general characteristics of a microcavity with e.g. r-plane oriented ZnO cavity layer and an a- or m-plane oriented one, is not different. The cylindrical symmetry of the structure is lifted in both cases. Only a slight asymmetry of the mode polarization of states propagating with $+k_y$ and $-k_y$ is observed for r-plane oriented structures, if the optic axis is aligned with the yz plane.

In summary, a mid-plane symmetric microcavity structure with optically uniaxial cavity layer which is oriented to break the structure's cylindrical symmetry is characterized by the following properties:

- It bears two cavity-photon modes for a given mode number m.
- They are generally elliptically polarized and non-orthogonal to each other.
- The modes can degenerate at distinct $\vec{k}_{||}$, yielding exceptional points where both, complex mode energies and polarization states, degenerate.
- Those exceptional points occur pair-wise. The trajectories of degenerate E_c and Γ_c are mutually excluding connection lines of the exceptional points in $\vec{k}_{||}$ space, and establish discontinuities which can be resolved if the modes are exchanged upon passing them.
- Exceptional points are circularly polarized with one point in a pair being right, the other left circular.

- The orientation of the linear polarization of the modes is wound around the exceptional points in $\vec{k}_{||}$ space.

The occurrence of such exceptional points and their location in $\vec{k}_{||}$ space can be efficiently controlled by i) the cavity layer thickness d_c, ii) the central DBR-wavelength λ_{DBR}, iii) the cavity's anisotropy $n_{c\perp}$ vs. $n_{c||}$, and iv) the photonic confinement (loss rate) determined by the number of DBR-layer pairs N_{DBR}. The influence of a substrate, and hence lifting of the mirror-symmetry of the microcavity structure, will be discussed in chapter 4.

3.3 Classification and discussion

As pointed out above, the characteristics of anisotropic planar microcavities are governed by the occurrence of exceptional points. The observed complex-energy surfaces with avoided degeneracies of (real-valued) mode energies and mode broadenings are typical phenomena related to exceptional points [Hei12; Wie11; Yoo+11]. First experimental observation of exceptional points in quasi-optical cavity systems have been reported for microwave cavities [Dem+01].

Conditions for the occurrence of exceptional points within the vacuum light cone can generally be deduced from [Stu+11] by considering propagation along the principal directions, perpendicular and parallel to the optic axis of the cavity medium. If exceptional points are present, the (real part of the) mode energies E_c degenerate either for a propagation direction perpendicular or parallel to the (projection) of the optic axis in the xy plane. Even exceptional points at larger $k_{||}$ than covered by the vacuum light cone, i.e. exceptional points in guided modes, affect the radiative modes near the horizon. In general, the position of exceptional points is determined by the complex interplay between the birefringence in the cavity layer and the phase upon reflection off a DBR at its boundaries. Accordingly, exceptional points can not only occur for cavity-photon modes but also for Bragg-stop-band edge modes. This latter aspect will be discussed in more detail chapter 4.

3.3.1 General characteristics of exceptional points in anisotropic microcavities

The microcavity investigated above is mid-plane symmetric, i.e. the cavity plane is a mirror plane of the structure. As a consequence, a transmission Jones matrix $\hat{J}_t$ and its inverse are complex, symmetric matrices [Pot04]. Then, $\hat{J}_t^{-1}$ takes the following form at an exceptional point:

$$\hat{J}_t^{-1} = \begin{pmatrix} a & \pm ia \\ \pm ia & -a \end{pmatrix} , \tag{3.1}$$

where $a \in \mathbb{C}$ is any non-zero number. This matrix is singular, due to the mode condition Eq. 2.11, and zero is its two-fold eigenvalue. The respective null-eigenvectors are also degenerate and directly given as $(1, \pm i)^{\mathrm{T}}$. In conclusion, the symmetric transmission Jones matrices yield necessarily circularly polarized exceptional points [Hei+01]. The eigenspace of the modes consists of either left- or right-circularly polarized Jones vectors. It should be noted that this is only possible with non-vanishing imaginary parts in the entries of the Jones matrix, i.e. $\hat{J}_t$ being non-Hermitian. Otherwise, the off-diagonal elements would have to vanish if zero is demanded to be a two-fold eigenvalue. This would result in a (Hermitian) zero-matrix, which again means that any vector is null-eigenvector, establishing a two-dimensional eigenspace. This would formally correspond to diabolical points (cf. chapter 1.1.3) and occurs for microcavities with cylindrical rotation symmetry at $\vec{k}_{||} = \vec{0}$ (cf. appendix A.4).

The strict conclusion that only a circular polarization is allowed for exceptional points can in principle be lifted if the matrix operator is not symmetric anymore. Details of the mathematical formalism of exceptional points are discussed in appendix A.2.

It has been noted above that the complex mode-energies reveal discontinuities in the momentum space if the modes are strictly sorted e.g. by the real part of their energy. An alternative representation of the complex energies is the 3D-surfaces shown in Fig. 3.7. As can be seen, there are actually no discontinuities anymore. This was already observed above by noting that *the discontinuities can be resolved when exchanging the modes.* However, this has an important consequence if a single exceptional point is encircled in $\vec{k}_{||}$

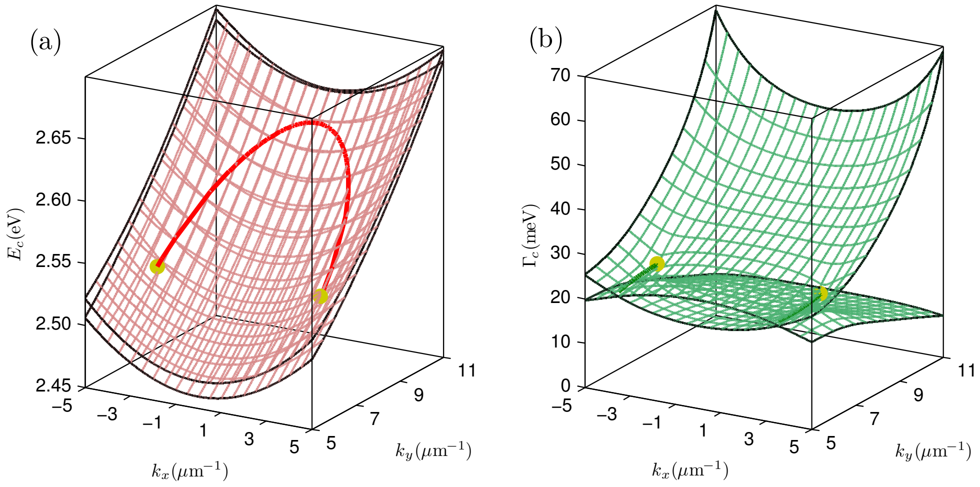

Figure 3.7: Complex mode energies $\tilde{E}_c$ near exceptional points (yellow dots) for a microcavity structure with DBRs consisting of 5 layer pairs, $d_c = 130\,\mathrm{nm}$ and the other structure parameters as listed in Tab. 3.1. (a): $E_c = \mathrm{Re}(\tilde{E}_c)$ with mode degeneracies (thick red lines). (b): $\Gamma_c = -\mathrm{Im}(\tilde{E}_c)$ with respective degeneracies (thick green lines). Cf. also Figs. A.1 and 1.6 (b), (c).

space: It needs to be encircled twice in order to arrive again at the starting point [Dem+01; Dem+04; Hei12; Cao+15]. The reason is that the trajectories of $E_{c1} = E_{c2}$ and $\Gamma_{c1} = \Gamma_{c2}$ are mutually excluding. Encircling a single exceptional point only once opens a way to continuously move from one mode to the other while ending up at the same point in momentum space. This property is characteristic for a complex-square-root topology and is inherent to exceptional points which are sometimes called *square-root singularities* [Cao+15]. The topology of the complex-energy surfaces reveals locally the same topology as a complex square-root. See also Fig. A.1 in appendix A.2.

3.3.2 Polarization vortices and singular optics

Considering the complex-square-root topologies, exceptional points act like a screw. This hints on their nature as vortex centers. When investigating vortices as optical singularities, it has to be distinguished between scalar and vector fields. The first ones are commonly observed as phase vortices at wavefront dislocations [Sos+01]. Similarly to a Burgers vector for disclinations, encircling such a dislocation yields a phase offset. Encircling it twice, yields twice the offset. This is rather similar to a complex logarithm instead of a complex

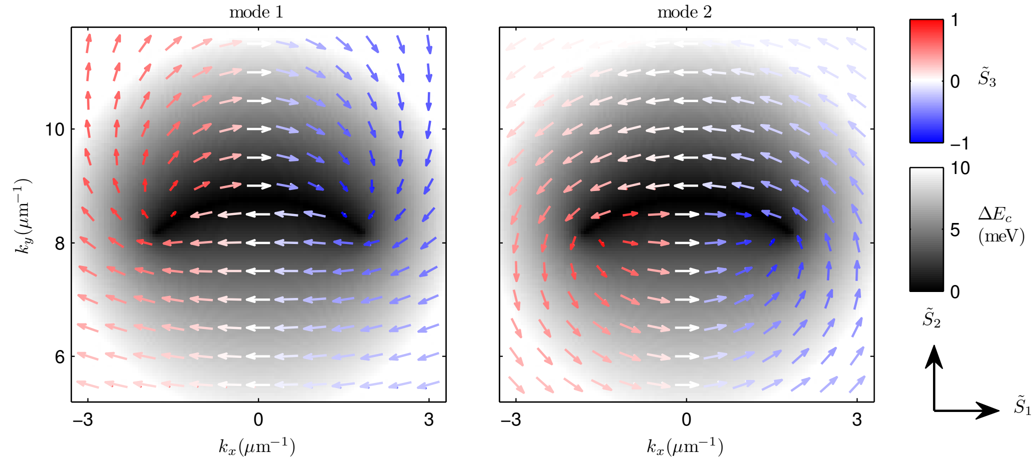

Figure 3.8: Detailed view of the mode polarization near a pair of exceptional points (same microcavity as in Figs. 3.1 and 3.3). Arrows represent the linear-polarization Stokes-vector $(\tilde{S}_1, \tilde{S}_2)^{\mathrm{T}}$ which becomes a zero vector for fully circular polarization. Circular components are represented by the arrows' colors ($\tilde{S}_3$). The energetic mode splitting is depicted by the gray scale. Each exceptional point is a vortex center with winding number 1/2.

square-root. Hence, there is an important qualitative difference between such phase vortices in real space and the exceptional points in momentum space here. Furthermore, scalar phase vortices often require vanishing intensity at the vortex center, as known from Laguerre-Gaußian modes or Sommerfeld's edge vortices [Den+09; Ang+02]. This is not the case here. To study singularities of vector optics, the orientation of the linear polarization is of interest. Again, the linear polarization can *disappear* if a propagation direction corresponding to an exceptional point is considered. Then the light is fully circularly polarized as discussed above. But still, the modes are present. No suppression of the electromagnetic fields has to occur.

Figure 3.8 depicts the linear polarization as Stokes vector of the modes in the vicinity of a pair of exceptional points. Far from the exceptional points, the modes are nearly orthogonal, resulting in $(\tilde{S}_1, \tilde{S}_2)^{\mathrm{T}}$ arrows pointing to opposite directions for the two modes. However, the arrows become shorter, i.e. the degree of linear polarization decreases, when the exceptional points are approached. Both modes obtain the same circularity then. Upon encircling the exceptional points, it is clear that a single exceptional point is a vortex center with winding number +1/2; a pair carries winding number +1. The other pair situated at opposite k_y values carries a vortex with winding number +1 as well, i.e. the sign is the same. Instead of $(\tilde{S}_1, \tilde{S}_2)^{\mathrm{T}}$, the orientation of the linear polarization, i.e. the orientation of the main axis of the polarization ellipse, could be plotted as double arrow. When encircling the pair, it would be rotated by 180°. This would correspond to winding number 1/2. It should be mentioned that planar microcavities with cylindrical symmetry reveal a trivial polarization vortex at the origin which results from the projection of the TE- and TM-polarized modes onto the xy laboratory coordinate system. It has winding number +2 for the pseudospin/Stokes vector and is depicted in appendix A.4[3].

In the context of singular polarization-optics investigating wavefront discontinuities, exceptional points would be called C points because of their circular polarization. They do also yield local complex-square-root topology [Den+09; Nye97; Den01]. Another important aspect are trajectories where the circular polarization components cancel completely, leaving purely linear polarization. Such lines are called L lines[4]. For anisotropic microcavities, these would be the principal axes with either $k_x = 0$ or $k_y = 0$, if the optic axis of the anisotropic cavity medium is aligned within the xz or yz plane.

3.3.3 Net topology of the system

Winding numbers of vortices are topological charges [Fre+02; Ang+02; Den01; Lee10]. Hence the occurrence of polarization vortices and the sum of their winding numbers is directly related to the system's topology. In order to properly investigate if an anisotropic planar microcavity reveals a non-trivial net-topology, one can calculate their Chern number C [Lu+14; Jan16]. It gives an expression of whether the wave function collects an additional absolute phase if the entire momentum space is encircled, similar to Burgers vectors for

---

[3] It cannot be concluded that the sum of winding numbers of all vortices is generally conserved. In particular, it can happen that more than two pairs of exceptional points appear if the energy dependence of a real material is such that it changes e.g. from positive to negative birefringence within the range of the mode energies. See section 3.4. The effect of the polarization vortices on the system's topology is discussed in section 3.3.3.

[4] Sometimes, L lines are referred to as S lines or -contours [Nye97; Ang+02].

dislocations [Sos+01; Nye97]. Hence, $C \neq 0$ for non-trivial topologies.

With the wave function of a cavity photon state $\Xi = (\mathcal{E}_x, \mathcal{E}_y)^{\mathrm{T}}$, the Berry connection $\vec{A}$ can be calculated as

$$\vec{A}(\vec{k}_{||}) = -i\Xi^* \vec{\nabla}_{\vec{k}_{||}} \Xi \,. \tag{3.2}$$

Integration of $\vec{A}$ along the edge of the light cone would yield Berry's phase. However, $\vec{A}$ can be taken as vector potential for the Berry curvature $\vec{F} = \vec{\nabla}_{\vec{k}} \times \vec{A} = F\vec{e}_{k_z}$ which formally behaves like a magnetic field, oriented normal to the xy plane [Lu+14]. For the two-dimensional system here, $\vec{F}$ is given as [Jan16]

$$\begin{aligned} F(\vec{k}_{||}) &= -i\left(\frac{\partial \Xi^*}{\partial k_x}\frac{\partial \Xi}{\partial k_y} - \frac{\partial \Xi^*}{\partial k_y}\frac{\partial \Xi}{\partial k_x}\right) & (3.3)\\ &= -i\left(\frac{\partial \mathcal{E}_x^*}{\partial k_x}\frac{\partial \mathcal{E}_x}{\partial k_y} + \frac{\partial \mathcal{E}_y^*}{\partial k_x}\frac{\partial \mathcal{E}_y}{\partial k_y} - \frac{\partial \mathcal{E}_x^*}{\partial k_y}\frac{\partial \mathcal{E}_x}{\partial k_x} - \frac{\partial \mathcal{E}_y^*}{\partial k_y}\frac{\partial \mathcal{E}_y}{\partial k_x}\right). & (3.4) \end{aligned}$$

The Berry curvature is real-numbered and defines the Chern number $C \in \mathbb{Z}$ by integration over the whole $\vec{k}_{||}$ plane:

$$\begin{aligned} C &= \frac{1}{2\pi}\int_{\vec{k}_{||}} d^2\vec{s}_{\vec{k}}\vec{F}(\vec{k}'_{||}) & (3.5)\\ &= \frac{1}{2\pi}\int_{\vec{k}_{||}} d^2k'_{||}F(\vec{k}'_{||}) & (3.6)\\ &= \frac{1}{2\pi}\int_0^{k_{||}^{\max}}\int_0^{2\pi} dk'_{||}d\varphi k'_{||}F(k'_{||},\varphi)\,, & (3.7) \end{aligned}$$

with normal vector $\vec{s}_{\vec{k}} = \vec{e}_{k_z}k_{||}$ and $\vec{k}_{||} = (k_x, k_y)^{\mathrm{T}} = k_{||}(\cos\varphi, \sin\varphi)^{\mathrm{T}}$.
It turns out that despite the occurrence of the polarization vortices, the Chern number of the modes is $C = 0$. In particular, each polarization half-vortex, established by a single exceptional point, is a positive or negative source of the Berry curvature. This is illustrated in Fig. 3.9. In fact, the Berry curvature reflects the circular polarization component as shown in Fig. 3.3. There is no net flux because all topological flux charges, i.e. half-vortices, occur pairwise as dipoles. *There are no magnetic monopoles*, if the Berry curvature is understood as kind of magnetic field. The finding that the topology of the system is trivial coincides with the observation that none of the two modes covers the whole Bloch or Poincaré sphere, when integrated over all available $\vec{k}_{||}$ values, which would otherwise correspond to a non-trivial topology [Jan16].

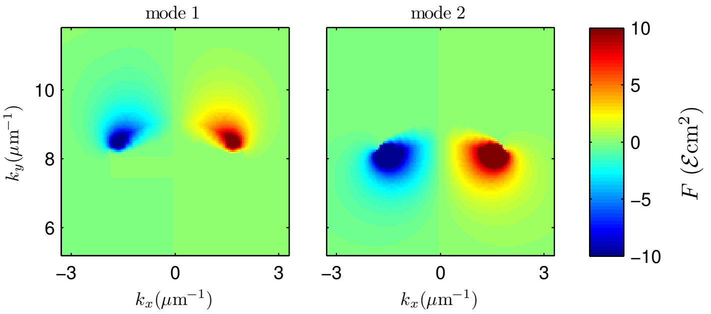

Figure 3.9: Berry curvature F computed for the microcavity shown in Figs. 3.2 and 3.3 revealing a pair of exceptional points as dipole (cf. also Fig. 3.8). Apart from the vicinity of the exceptional points, F remains zero.

Summarizing, the observed polarization vortices behave topologically neutral as long as the exceptional points remain paired. The net topology of the system remains trivial[5]. Finding anisotropic microcavity configurations to unpair exceptional points could affect the topology of radiative and guided cavity modes.

3.3.4 Effective-medium approaches

A microcavity structure consists of a number of layers of different media. There exist different approaches to describe the whole stack as one effective composite medium. The easiest concepts are based on homogenization theory according to Bruggeman [Bru35] or Garnett [Gar06]. Voigt waves have indeed been found in such composite effective media with biaxial symmetry which consisted e.g. of uniaxial media [Mac+00; Mac+03]. Similar approaches are used in descriptions of layered meta-materials as effective anisotropic tensor [Che13]. However, all those simple effective medium approaches lack generality. They are either only valid for certain polarizations or photon energies, or are restricted to the description of propagation along certain directions. Furthermore, they can only account for the volume fractions of the different materials involved, and to some extend to the geometry of material inclusions (e.g. needle-, plate-, or sphere-like). But the exact particular layer thicknesses

---

[5] Analogously to the Berry curvature and Chern number, the genus g is defined for a closed, orientable geometrical surface by integration of the Gaußian curvature. A sphere is characterized by $g = 0$. Hence, a trivial topology is sometimes referred to as *spherical*.

Table 3.2: Point groups in Schönflies notation for different microcavity structures with uniaxial cavity medium. Orientation labeling as for wurtzite crystals.

orientation	c-plane	m/a-plane	r-plane
mid-plane symmetric:	D_{4h}	D_{2h}/V_h	C_{2h}
with substrate:	C_{4v}	C_{2v}	C_s/C_{1h}
	uniaxial	biaxial	

do not matter in those approaches. As described above, especially the exact thickness of the cavity layer does crucially affect the modes of an anisotropic cavity. Hence, the mentioned descriptions as effective tensor of the dielectric function are not meaningful. Finally, the cavity-photon modes impose a strict mapping between direction and energy. A dielectric tensor does not describe this. It would also be questionable how an effective dielectric tensor should account for mode broadening.

However, there are remarkable similarities of the mode characteristics in anisotropic microcavities with optically biaxial, absorptive bulk media. Considering the symmetries of the structure allow comparison of both systems. Table 3.2 shows the point group symmetries associated with different microcavity designs. Independent of the existence of a substrate, a microcavity with cylindrical symmetry is uniaxial. The cavity modes of such a system degenerate at $\vec{k}_{||} = \vec{0}$, with a two-dimensional eigenspace. This is similar to an optically uniaxial bulk medium where classic optic axes are observed. This behavior is independent of absorption or dissipation, respectively. As soon as the cylindrical symmetry of a microcavity is lifted, the structure becomes biaxial. This is the case which leads to the occurrence of exceptional points. For an absorbing bulk medium, biaxiality is the requirement for the occurrence of singular optic axes [Stu+16]. A comparison with Tab. 1.1 confirms this reasoning. Both, singular optic axes and exceptional points in anisotropic microcavities, have similar characteristics:

- Both define directions in the momentum space along which only one (circular) polarization is allowed to propagate.
- Both establish vortex centers for the linear polarization [Voi02].

- Both reveal a complex-square-root topology, as visible in Fig. 3.7 and 1.6.
- The imaginary part of the wave vector plays a crucial role in both systems. It is mediated either by $\mathrm{Im}(\hat{\varepsilon})$ or $\mathrm{Im}(\tilde{E}_c)$.
- The directions of either two singular optic axes or two exceptional points are well separated if both, anisotropy and absorption are either large or small. They are close together if only one, either absorption or anisotropy is large [Gru+17b; Stu+16].

In summary, exceptional points in anisotropic microcavities correspond most highly to singular optic axes. They can be viewed as singular axes of the biaxial microcavity structure[6]. Though, it should be noted that, while the considerations for a dielectric tensor and singular axes as discussed in section 1.1.3 are only valid for a single photon-energy at a time, the cavity mode energy varies if different propagation directions are considered. Furthermore, in contrast to singular axes in absorptive biaxial media, anisotropic microcavities can be completely dielectric. The imaginary part of the complex energy is rather related to photonic loss by emission than to absorption.

3.3.5 Quasi-particle approaches

The cavity photon modes can still be described as quasi-particles (cavity photons) as introduced in section 2.3. However, in contrast to cavities with cylindrical symmetry, strong non-parabolic effects would occur for anisotropic microcavities lacking rotational invariance. In other words, the effective mass of a cavity photon is strongly $\vec{k}_{||}$-dependent now.

The more important question is if mode splittings and polarization can be described by suitable Hamiltonians. For cylindrically symmetric microcavities,

---

[6] A distinction between optic ray axes and optic normal axes seems not meaningful because the modes are described by the electromagnetic fields in isotropic ambient. Ray and wave vector coincide here. However, it should be noted that inside the cavity, modes are split into ordinary and extra-ordinary components. This is also true at exceptional points. In the planar system, ordinary and extra-ordinary components can still coherently interfere such that both contribute to a mode. This is not possible e.g. for whispering-gallery modes in hexagonal microwire-cavities [Nob+04; Mic+14], prohibiting the occurrence of exceptional points in such systems.

this is commonly achieved through a Zeeman-like splitting caused by a quasi-magnetic field $\vec{\mathcal{B}}_P$ in pseudospin space [Kav+04; She+05; She+10]. Each cavity mode is then symmetrically split according to the polarization pseudospin $\vec{P}$ ($|P| = 1/2$) as

$$E_{c1/2} = E_{c0} + \vec{\mathcal{B}}_P \vec{P}\,, \tag{3.8}$$

where $E_{c0} = \frac{1}{2}(E_{c1} + E_{c2})$ is the mean energy and $\mathcal{B}_P = \Delta E_c$. The quasi-field behaves only formally as a magnetic field[7] but has no real meaning. Its value depends on $\vec{k}_{||}$ as the mode splitting ΔE_c does. Its orientation depends also on $\vec{k}_{||}$ such that the eigenstates, which are defined as $\vec{P}$ being parallel or anti-parallel to $\vec{\mathcal{B}}_P$, are the TE- and TM-polarized states. An illustration can be found by Fig. A.3 in appendix A.4. Although this description is rather artificial it can be used to describe pseudospin-related scattering and relaxation processes [Kav+04; She+05; She+10].

The pseudospin Hamiltonian introduced in Eq. 3.8 relies on orthogonally polarized states. However, anisotropic microcavities yield not generally orthogonal modes. Although the mode splittings vanish if the pseudospins are collinear (i.e. at the exceptional points), it is hardly possible to describe the energetically degenerate modes of different polarization and broadening along a $E_{c1} = E_{c2}$ trajectory. This is also critical because Eq. 3.8 considers only the real part of the complex mode-energy.

In the literature, there are approaches to extend the quasi-magnetic field approach in order to describe anisotropic cavities near $\vec{k}_{||} = \vec{0}$ by introducing additional quasi-magnetic fields which do not depend on $\vec{k}_{||}$ [Amo+09]. Still, it remains unclear if and when effects of the classic TE/TM splitting and o/eo splitting can occur simultaneously. This questions the mentioned approach. In the end, a Zeeman-like Hamiltonian can by no means describe the effects in anisotropic cavities in general, including E_c and Γ_c degeneracies and exceptional points.

---

[7] Units can arbitrarily be defined by introducing pre-factors such as the Bohr magneton μ_B into Eq. 3.8.

3.3.6 Other familiar systems and phenomena

Remarkable similarities with exceptional points in anisotropic planar microcavities can be found for so called (optical) *bound states in the continuum* [Zhe+14]. These are emission directions for modes in two-dimensional photonic crystal slabs at which the mode broadening tends toward zero and hence the light is perfectly *bound* in the structure. The nature of such anomalies seems to be somehow similar to Wood anomalies, though, two-dimensional structuring is required here. If polarization is rigorously considered in the calculation of the photonic band structure, it turns out that those bound states are vortex centers for the linear polarization of the modes in momentum space. The winding numbers are 1 if the orientation of the linear polarization is considered, and 2 if the Stokes vector/pseudospin is investigated. Hence, bound states in the continuum create polarization vortices similar to the trivial $\vec{k}_{||} = \vec{0}$ vortex in planar microcavities with cylindrical symmetry. However, the field intensity has to vanish at the vortex center.

Another vortex of the linear polarization with the same winding number occurs if unpolarized light is Rayleigh-scattered e.g. at the molecules of the air. This can be observed at the sky. The respective vortex center is the direction of the light source, i.e. sun or moon[8], which remains brightest but unpolarized. Clearly, another similar vortex center arises at the opposite direction on the sky (*anti-sun*), establishing an axis. The origin of those phenomena is the polarization dependence of Rayleigh scattering. Unscattered light remains unpolarized at the vortex centers. Interestingly, if multiple scatter events occur, each vortex center splits into two, resulting in four unpolarized points at the sky, in total [Cha50; Gál+01; Ber+04]. Although at first glance similar to the transition from a classic to a pair of singular optic axes, no circular polarization components occur. Also the origin is different: The four points reflect depolarized light which results from incoherent superposition of differently linearly polarized light from different scatter events. In particular, these points evolve as a consequence of the ground and horizon which break the spherical symmetry of the sky for an observer standing on the earth.

Coming back to microcavity systems, most of the observed phenomena related to polarization vortices are due the *optical spin Hall effect* [Kav+06;

---

[8] Although no active light source, the moon acts as such for the night sky.

Ley+07; Mar+11; Amo+09]. Here, the intrinsic TE/TM-polarization mode-splitting yields a beating of TE- and TM-polarized emission at slightly different energies. In a simple model, this can be described as precession of the pseudospin due to a quasi-magnetic field as explained in section 3.3.5. For propagating condensates of exciton-polaritons, this leads to real-space polarization-patterns with vortices of the linear polarization and areas (rather not distinct points) of circular polarization [Kam+12; Cil+16]. Those patterns are not stable but evolve in time and space. Such behavior can be modified by external magnetic fields [Mor+13] or a quasi-magnetization due to a polarized population of excitons [Cil+15]. Another effect caused by the TE/TM splitting in isotropic planar microcavities consists in polarization-dependent phase vortices upon transmission of a polarized light beam through the microcavity under oblique angle [Man+11]. This is a typical example for disturbed wavefronts as widely studied in the field of singular optics [Den+09; Sos+01; Flo+05]. Finally, if a planar microcavity is radially vaulted, real-space polarization-vortices can be observed in the emission pattern [Duf+15]. Though, the intensity vanishes at the vortex centers, then. All those TE/TM-splitting-related effects are qualitatively different from exceptional points in anisotropic planar microcavities as they arise from the splitting into two orthogonally polarized modes (see section 3.3.5). Mostly, they have only the trivial vortex center at the origin ($\vec{k}_{||} = \vec{0}$ or $\vec{r} = \vec{0}$, see appendix A.4). Further, it is important to mention that most phenomena based on the optical spin Hall effect perform only if there is a sufficient spectral overlap of the TE- and TM-polarized modes. Otherwise, their superposition and seemingly circular polarization can only be observed if the light is not or only badly spectrally resolved.

Indeed, there seems to be one kind of polarization vortices in microcavities with a high degree of similarity to the anisotropic microcavities discussed in this thesis. It is referred to as *half-quantum vortices* in exciton-polariton condensates [Lag+09]. These are simultaneous real-space vortices of the phase and the polarization vector. Both have winding number $1/2$, as is the case for the exceptional points. In fact, the vortex cores have non-vanishing intensity and are circularly polarized. Though in real space, this is very close to the exceptional points here. The half-quantum vortices are local excitations which originate from local inhomogeneities. So, they are probably related to locally induced anisotropies. These condensate vortices in real space connect the various phenomena of real-space vortices in distorted wavefronts (mostly with zero intensity at the vortex cores) and the momentum-space vortices related to exceptional points in anisotropic planar microcavities (with circularly polarized centers). It should even be possible to describe these half-quantum vortices as exceptional points where differently polarized condensate modes degenerate.

A system very similar to anisotropic planar microcavities studied here is a film of nematic liquid crystals. The polarization of light of a single photon-energy, transmitted through such a film, reveals exactly the same polarization vortices, including C points and L lines in momentum space [Kis07]. The particular polarization pattern can be controlled by manipulating the liquid crystal. Again, establishing effectively biaxial symmetries, the effect seems familiar to singular optic axes in absorbing biaxial crystals.

Very recently, another example of exceptional points in planar microcavities has been demonstrated [Gao+17]. Here, condensed exciton-polaritons are manipulated by optical potentials, yielding real-space vortices in the flowing condensate. Exceptional points arise here due to degeneracy of different condensate modes and are not polarization-related, similar to earlier work on spatial manipulation of exciton-polariton condensates [Gao+15]. Chirality is manifested by a phase difference of $\pi/2$ in the superposition of the original states.

In summary, anisotropic microcavities and exceptional points in the momentum space differ qualitatively from most of the polarization patterns, vortices or degeneracies observed so far in planar microcavities. Similar observations have only been found in real space when studying half-quantum vortices in exciton-polariton condensates [Lag+09]. Various other systems with similar polarization vortices have not only different origins but also their vortex centers differ from those of exceptional points. Instead of circularly polarized light, either unpolarized or no light at all is found. Great coincidences of origin and phenomena are only found between the exceptional points in anisotropic microcavities and singular optic axes in biaxial crystals which have been discussed in section 1.1.3.

3.4 Anisotropic exciton-polaritons

Finally, exciton-polaritons shall be considered in the case of an optically uniaxial cavity medium. For this purpose, excitonic resonances are introduced in the dielectric function of the cavity layer for the microcavity structure discussed in section 3.2. As idealized model, Lorentz oscillators at two different energies, $E_\perp$ and $E_{||}$, shall represent excitons which are dipole-active for polarization perpendicular and parallel to the optic axis, respectively. The cavity medium is now dichroic, not only birefringent. Higher exciton states, exciton continua, exciton-phonon complexes and band-to-band transitions are neglected here. According to section 2.3, six modes occur now in general, as two cavity photon modes are involved and each of them can couple to two excitons. For each of the two cavity photon modes, the Hamiltonian as stated by Eq. 2.33 reads

$$\begin{pmatrix} \tilde{E}_\perp & 0 & V_\perp \\ 0 & \tilde{E}_{||} & V_{||} \\ V_\perp^* & V_{||}^* & \tilde{E}_c \end{pmatrix} . \tag{3.9}$$

However, the coupling strengths $V_{\perp/||}$ depend strongly on $\vec{k}_{||}$ and the cavity photon's polarization, now. As a result of the investigations presented in section 3.2, the cavity photon modes are generally not trivially TE- or TM-polarized and not even orthogonal to each other. This makes the estimation of the expected overlap of the electric field of the mode with that of the respective exciton dipoles generally very difficult. Furthermore, excitons may be inactive for certain combinations of propagation direction and polarization (no electric field overlap). Some particular cases: Considering the cavity's optic axis is aligned exactly with y, the exciton polarized parallel to the optic axis ($E_{||}$) is not active in TM polarization for propagation exactly along k_x ($k_y = 0$) or in TE polarization along k_y ($k_x = 0$). This reduces the Hamiltonian 3.9 for those polarizations to two dimensions. Similar considerations hold for the exciton polarized perpendicular to the optic axis ($E_\perp$) which is not visible in TE polarization for propagation exactly along k_x ($k_y = 0$). For the mentioned cases, the total number of cavity modes reduces from 6 to 5 (along k_y here) and 4 (along k_x). If those principal propagation directions are left, i.e. $k_y \neq 0$ and $k_x \neq 0$, the Hamiltonian remains three-dimensional for all polarizations, resulting in 6 cavity modes. If k_x is small and the polarization close to TE, the

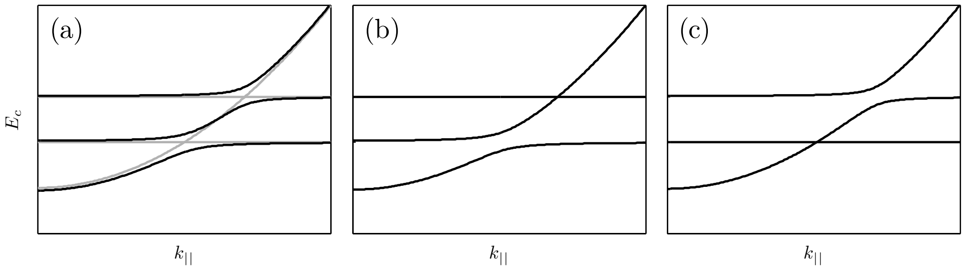

Figure 3.10: Schematics for anisotropic cavity polariton dispersions according to Eq. 3.9. (a): both excitons couple similarly to the cavity photon, $V_\perp = V_{||}$. Gray lines show the uncoupled cavity photon and exciton dispersions. (b,c): strongly suppressed coupling for one of the excitons. With $E_{||} > E_\perp$ it holds (b): $V_{||} = 0.001 V_\perp$, (c:) $V_\perp = 0.001 V_{||}$. Anti-crossing (strong coupling) occurs only for the exciton with large coupling strength. The other exciton is only weakly coupled and the modes cross each other. Note that the dispersions are still slightly affected by the weak coupling. It depends on the propagation direction $\vec{k}_{||}$ and the polarization of the cavity photon mode whether situation (a), (b) or (c) applies.

dispersions take the form depicted in Fig. 3.10 (b) if $E_{||} > E_\perp$. For polarization close to TM, it resembles Fig. 3.10 (c) in this case. The same would result for small k_y and polarization close to TE. Eventually, Fig. 3.10 (b) would also hold for small k_y and polarization close to TM. In all those cases, the coupling to one of the excitons is strongly suppressed because of a largely reduced overlap of the electric field polarizations of the cavity photon mode and the excitonic dipole. As a result, anti-crossing polariton branches are only observed involving one of the excitons but mode crossing occurs for the exciton with reduced coupling strength $V_{\perp/||}$. The latter is referred to as *weak coupling.* If $|\Gamma_X - \Gamma_c| > 4|V|$ for a coupling Hamiltonian $\begin{pmatrix} \tilde{E}_X & V \\ V^* & \tilde{E}_c \end{pmatrix}$ (cf. section 2.3), the two polariton solutions for $\tilde{E}_X = \tilde{E}_c$, i.e. $\tilde{E}_1$ and $\tilde{E}_2$, will only differ in their broadening, $\Gamma_1 \neq \Gamma_2$, but not energetically, $E_1 = E_2$ [Sav+99]. Still, the dispersions will be slightly affected but no anti-crossing is observed for weak coupling. For the numerical mode computations there is no difference between weak ($|\Gamma_X - \Gamma_c| > 4|V|$) and strong ($|\Gamma_X - \Gamma_c| < 4|V|$) coupling.

Table 3.3: Parameters additional to Tab. 3.1 as used for the Lorentz oscillators (Eq. 1.23) in the dielectric tensor $\hat{\varepsilon} = \mathrm{diag}(\varepsilon_\perp, \varepsilon_\perp, \varepsilon_{||})$ of the cavity medium. The same values of Γ_X and Δ_{LT} are chosen for both excitons. Values represent a hypothetical model-material.

A/B exciton energy	$E_\perp$	2.53 eV
C exciton energy	$E_{\|\|}$	2.55 eV
exciton broadening	Γ_X	0.5 meV
longitudinal-transverse splitting	Δ_{LT}	0.3 meV

In the following, numerical computations of $\lambda/2$ cavity-polariton modes ($m = 1$) will be discussed[9]. Parameters used for the exemplary model are given in Tabs. 3.1 and 3.3[10]. Qualitatively (not in terms of absolute energies), the dielectric function of the cavity layer mimics the characteristics of e.g. ZnO which reveals so called A-, B- and C-excitons. While the C-exciton is polarized parallel to the optic axis, A- and B-excitons occur for polarization perpendicular to it [Neu15]. Typically, at higher temperatures, the A- and B-excitons are not well separated and can approximately be described as merged into one effective exciton [Kli+10]. It holds $E_{||} > E_\perp$. The resulting dispersions of the cavity polariton branches are depicted in Fig. 3.11 for selected propagation directions. For $k_x = 0$ or $k_y = 0$, the number of existing modes reduces from 6 to 5 and 4, as shown in Fig. 3.11 (a,d) and (b,e), respectively. This corresponds to the situations discussed above. For arbitrary $\vec{k}_{||}$ ($k_x \neq 0$, $k_y \neq 0$), six modes occur as expected and exemplarily shown in Fig. 3.11 (c,f). It turns out that even for $k_x \neq 0$ and $k_y \neq 0$ two of the modes are always only weakly coupled

---

[9] As examined in section 2.2, there is always a range of modes with mode number $m \geq 1$. However, the $\lambda/2$ *LPB*s are clearly distinguishable from the $m > 1$ modes if sufficiently far from the exciton energy. Mostly, this is the case here. The range of $m > 1$ middle polariton branches is observed at energies close to $E_\perp$, but accurate numerical computations allow distinction between $m = 1$ and $m > 1$ modes also here. The *UPB*s with $m = 1$ are anyway clearly distinguishable because no modes at $m < 1$ occur simultaneously.

[10] It should be noted that while the coupling strengths in the quasi-particle Hamiltonian, $V_{\perp/||}$, are functions of $\vec{k}_{||}$, the amplitudes of the Lorentz oscillators given by Δ_{LT} are constant. The $\vec{k}_{||}$ dependence of $V_\perp$ and $V_{||}$ are a consequence of the electric field projections perpendicular and parallel to the cavity medium's optic axis, which depend on $\vec{k}_{||}$ and the respective mode polarization.

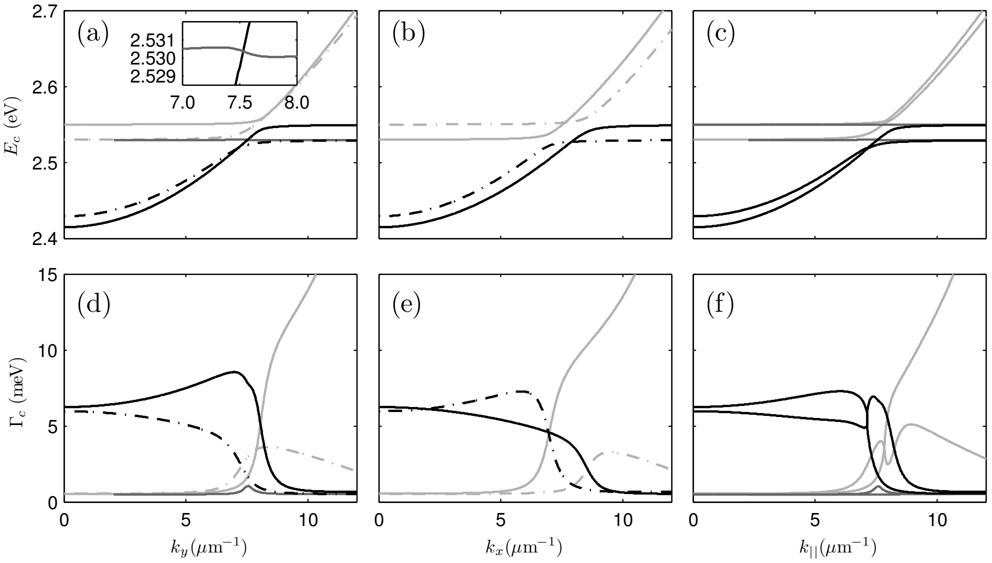

Figure 3.11: Dispersion of the complex energies $\tilde{E}_c$ of the cavity polariton modes of an anisotropic planar microcavity with the parameters given in Tabs. 3.1 and 3.3 with $d_c = 130\,\mathrm{nm}$ and DBRs of eight layer pairs. The optic axis of the cavity medium is oriented along the y direction. (a-c): real part of the energy E_c, (d-f): imaginary part (broadening) Γ_c. (a,d): propagation along k_y ($k_x = 0$), (b,e): along k_x ($k_y = 0$), (c,f): along a direction 18° tilted against k_y. The respective directions are indicated in Fig. 3.12 (a). In (a,b,d,e), solid lines mark TM, dash-dotted lines TE polarization. For (c,f) the polarization of the modes is neither TE nor TM nor constant along $k_{||}$. LPBs, EBs and UPBs are plotted in black, dark gray and light gray, respectively.

and remain at energies close to $E_\perp$ and $E_{||}$. In the following, they will be assigned as $EB1$ and $EB2$ because they are practically exciton-like branches. It holds $E_\perp \approx E_{EB1} < E_{EB2} \approx E_{||}$. The EB modes are those which vanish for the principal directions, k_x and k_y, reducing the total number of cavity modes as mentioned above: For $k_x = 0$ (parallel to the optic axis), $EB2$ disappears, for $k_y = 0$ (perpendicular to the optic axis), both EBs disappear. The other modes are in the following referred to as LPBs and UPBs as indicated in Fig. 3.11. It should be noted that even the weak coupling has a non-negligible influence on the mode dispersions in general. This is visible in the inset in Fig. 3.11 (a) and also in the mode broadenings e.g. in Fig. 3.11 (f).

As mentioned, the chosen model parameters are in principal not far from real material parameters but any absorption at energies higher than $E_{||}$ is completely ignored. Hence, it can be expected that the obtained UPBs and the

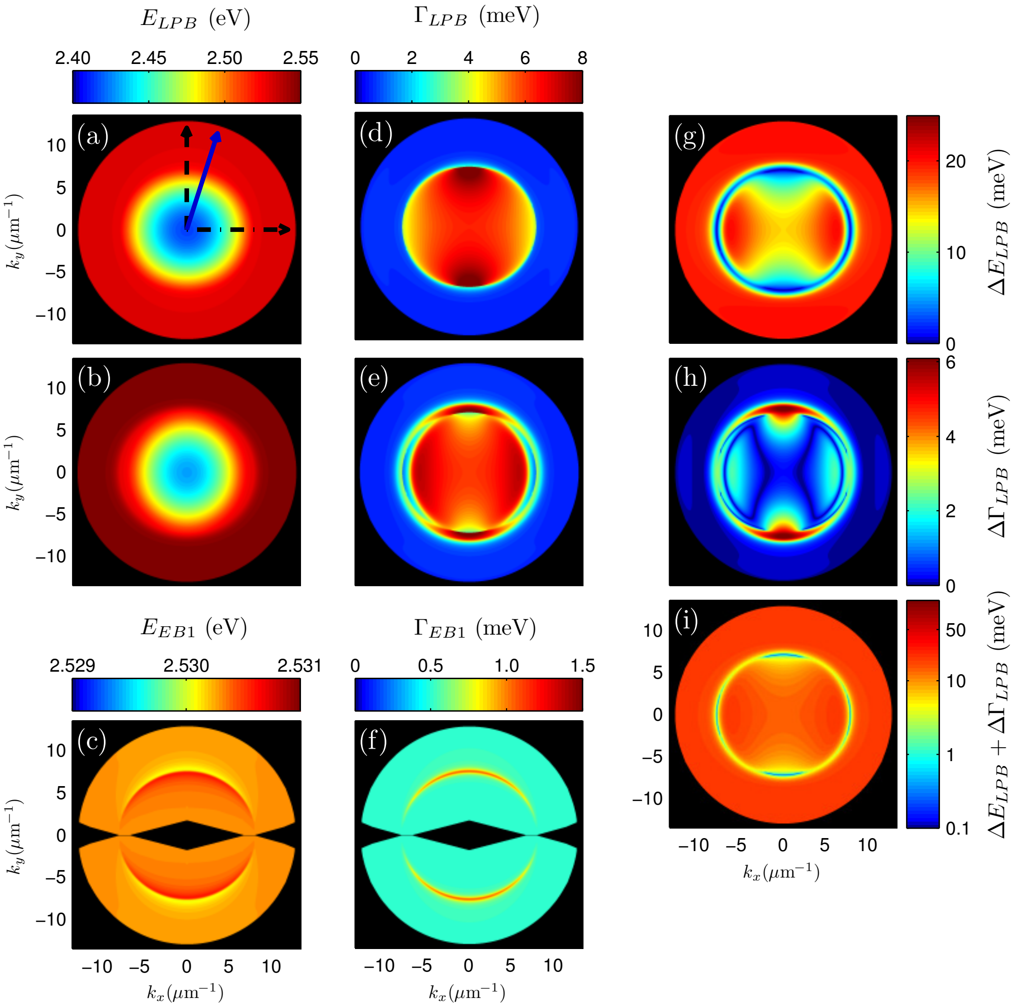

Figure 3.12: Dispersion of the complex mode energies $\tilde{E}_c$ depending on $\vec{k}_{||}$ for selected modes of the anisotropic microcavity as presented in Fig. 3.11. The optic axis of the cavity medium is oriented along the y direction. (a-c): real parts E_c, (d-f): imaginary parts Γ_c. (a,d): $LPB1$, (b,e): $LPB2$, (c,f): $EB1$ which does not exist for $k_y = 0$ and could not always be computed for small $|k_y|$ (black areas). Note again that the assignment is always such that $E_{LPB1} \leq E_{LPB2}$. (g): $\Delta E_c = E_{LPB2} - E_{LPB1}$, (h): $\Delta\Gamma_c = |\Gamma_{LPB2} - \Gamma_{LPB1}|$, (i) the sum of ΔE_c and $\Delta\Gamma_c$. Note that the color scale in (i) is logarithmic while it is linear for the other plots. Arrows in (a) indicate the directions shown in Fig. 3.11 (a) (dashed black), (b) (dash-dotted black) and (c) (solid blue).

$EB2$ of the idealized model differ strongly from real situations. However, the LPBs should represent the relevant characteristics rather well. Still, also the $EB1$ may experimentally be hard to access unless at cryogenic temperature. Figure 3.12 shows the entire $\vec{k}_{||}$ dependence of the LPBs and $EB1$. Again, the LPBs are sorted such that $E_{LPB1} \leq E_{LPB2}$. While $LPB1$ approaches $E_{\perp}$ for large $|k_{||}|$, $LPB2$ approaches $E_{||}$. In contrast to the dielectric microcavities discussed above in sections 3.2 and 3.3, the LPBs apparently cross each other along an entire circle, i.e. a closed trajectory in $\vec{k}_{||}$ space as shown in Fig. 3.12 (g). This is possible because with increasing energy, the cavity medium turns from being positively birefringent ($n_{||} > n_{\perp}$) well below the band gap to negatively birefringent ($n_{||} < n_{\perp}$) close to $E_{\perp}$ because $E_{\perp} < E_{||}$ (cf. also Fig. 4.2 below - ZnO becomes pseudo-isotropic near 3.2 eV). In particular, different $E_{LPB1} = E_{LPB2}$ trajectories coalesce and become hardly distinguishable. Though, the degeneracy does not originally occur along an entirely closed trajectory. This indicates that for the LPBs not only two but even four pairs of exceptional points can occur which are hard to separate. This becomes clear by investigating also the mode broadenings. When becoming exciton-like, the LPBs take the broadenings of the excitons. Prior to that, for $k_y \approx 7\,\mu\text{m}^{-1}$ and small k_x values, a similar Γ_{LPB} discontinuity, or rather exchange, along the $E_{LPB1} = E_{LPB2}$ trajectory occurs, similar to the dielectric microcavities discussed above (Fig. 3.12 (d,e)). The $\Delta\Gamma_{LPB}$ pattern, Fig. 3.12 (h), reveals more complex, distinct $\Gamma_{LPB1} = \Gamma_{LPB2}$ trajectories. Again, closed lines occur but also four terminated ones. For exceptional points, it should hold that $\tilde{E}_{LPB1} = \tilde{E}_{LPB2}$. Accordingly, the sum of ΔE_{LPB} and $\Delta\Gamma_{LPB}$, Fig. 3.12 (i), indicates that indeed 4 pairs of exceptional points occur at the ends of these terminated trajectories. A respective direction in $\vec{k}_{||}$ space is the one shown in Fig. 3.11 (c,f). It depicts the simultaneous degeneracy of E_{LPB} and Γ_{LPB} at an exceptional point of the LPBs. This direction is also close to an exceptional point of the UPBs which, within this idealized model, show similar general characteristics with respect to the occurrence of exceptional points. The properties of $EB1$ remain rather independent of the LPBs although not unaffected by the crossings with the LPB modes, as shown in Fig. 3.12 (c,f).

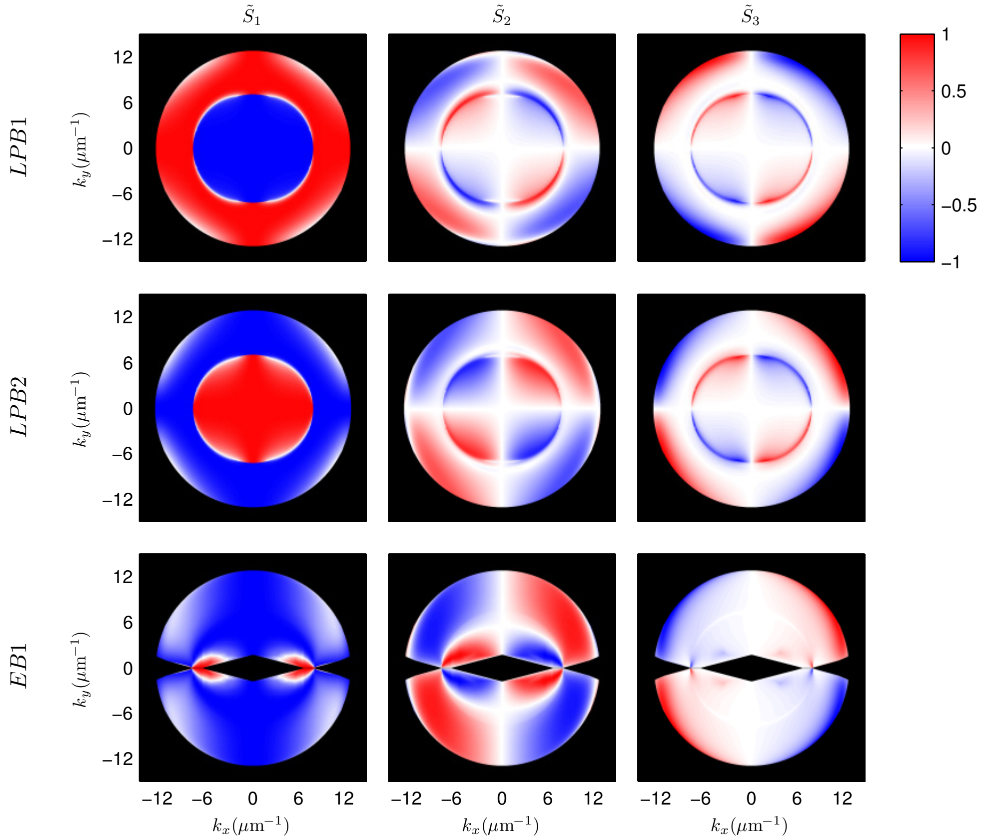

Figure 3.13: Mode polarization in terms of the Stokes vectors $\tilde{S}(\vec{k}_{||})$ for the cavity polariton modes shown in Fig. 3.12. It holds $E_{\mathrm{LPB1}} < E_{\mathrm{LPB2}}$.

The corresponding mode polarization of the LPBs and $EB1$ is shown in Fig. 3.13. Upon crossing of the LPB modes, their strongest polarization component, $\tilde{S}_1$, is exchanged as expected from the transition of the cavity medium from positive to negative birefringence with increasing energy. When the LPB modes are very exciton-like, they take mostly the polarization of the respective exciton dipole. This is observable at large $|k_{||}|$. Interestingly, the $EB1$ becomes mainly linearly polarized only for propagation perpendicular to the optic axis near its crossing with the LPB at small $|k_y|$. Otherwise, it is mostly linearly polarized parallel to the optic axis despite $E_{EB1} \approx E_{\perp}$. The $EB1$ shows also non-zero $\tilde{S}_2$ and $\tilde{S}_3$ values at distinct $\vec{k}_{||}$. Its origin is not intuitively clear. For the LPBs, circularly polarized exceptional points are found as expected. The circular polarization is spread along the circular trajectory of small ΔE_{LPB}+$\Delta\Gamma_c$ values in momentum space (Fig. 3.12 (i)), making proper separation of the individual exceptional points difficult. The $\tilde{S}_3$ values close to the horizon have opposite signs for $LPB1$ and $LPB2$, indicating that no exceptional points of these modes occur beyond the vacuum light cone. This is reasonable because they are energetically well separated, $E_{LPB1} \approx E_{\perp}$ and $E_{LPB2} \approx E_{||}$. Potentially, $LPB1$ interacts with $EB1$ here. Remarkably, the signs of $\tilde{S}_2$ differ for the two LPBs at $|\vec{k}_{||}|$ values smaller than those of the $E_{LPB1} = E_{LPB2}$ crossing. They are the same for larger $|\vec{k}_{||}|$ values approaching the horizon.

The example of anisotropic cavity polaritons discussed here represents one typical situation where the circularity of two exceptional points in one quadrant of the $\vec{k}_{||}$ space is the same for both exceptional points therein. Depending on the exact tuning with respect to the DBRs and the exact energy-dependent refractive indices, also different situations are possible, namely also with exceptional points carrying opposite circularity being located in one quadrant. Obviously, many other situations can be implemented. The occurrence of more than two pairs of exceptional points has no consequences on the topology. Neither do the particular signs of the circularity matter as long as exceptional points generally remain paired (see section 3.3.3).

In conclusion, the nature of anisotropic microcavities does not in principal differ for dielectric microcavities and those revealing exciton-polaritons. Nonetheless, phenomena may be richer for polaritons. An expectedly typical situation (with e.g. ZnO-like cavity medium) has been discussed here. Due to the spectral variation of the refractive indices with positive birefringence well below the excitonic resonances and negative birefringence close to them, the degree of anisotropy is swept through the considered spectral range, making the occurrence of more than two pairs of exceptional points of the LPBs likely. Mode patterns of cavity polaritons have been computed for further, modified models, all yielding in principle similar characteristics with the two weakly coupling EBs and with the occurrence of exceptional points in the LPBs (and UPBs). If the cavity polaritons are described as quasi-particles using coupling Hamiltonians, the introduced coupling strengths can by no means be considered independent of $\vec{k}_{||}$ and the cavity photon's polarization. This makes application of such quasi-particle Hamiltonions to anisotropic microcavities very difficult.

As additional aspect it should be noted that the polariton dispersions and related exceptional points could be altered by manipulating the excitonic properties, e.g. by external magnetic fields or alike [Sol+08; Mor+13; Jan+16]. Finally, for the case of polariton condensation, rich dynamics of exceptional points can be expected, because strong pumping alters the dielectric function of the cavity medium, making it dependent on the charge carrier density [Ver+12].

Chapter 4

Experiment: ZnO-based planar microcavities

In order to confront the predictions from the numerical computations with experimental data, planar microcavities based on ZnO as optically uniaxial medium are studied by polarization-resolved optical spectroscopy. Three different samples are presented here. The designs were chosen in order to study

i) the effect of varying the cavity layer thickness,

ii) the difference between configurations with the optic axis either in the cavity plane or inclined,

iii) the impact of varying the top DBR and hence the asymmetry between top and bottom of the microcavity.

All microcavities have been designed for λ cavity ($m = 2$) modes with energies near $3\,\mathrm{eV}$, i.e. perform in the transparent range of the used materials. While the first sample is a perfect λ microcavity and observation of exceptional points is not expected, the second and third microcavity aim to promote observation of exceptional points by detuning the cavity mode energies with respect to the central DBR energy E_{DBR}. Here, $n_c d_c > \lambda_{\mathrm{DBR}}$ was chosen.

With all microcavities, transmission experiments have been performed. The third sample allowed also to measure photoluminescence spectra. Additionally, theoretical computations have been done for comparison. These are based on transfer matrix models obtained by spectroscopic ellipsometry. In contrast to the idealized designs presented in chapter 3, all experimentally implemented

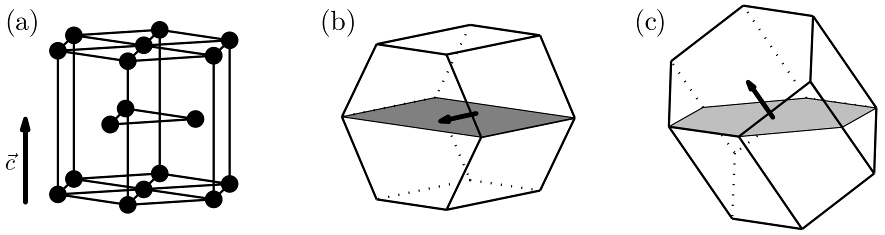

Figure 4.1: (a): Hexagonal unit cell of wurtzite ZnO, depicting the hexagonal close-packed structure. The basis (dots) consists of a pair of zinc and oxygen atom, aligned along the crystallographic c axis (arrow). (b): m-plane crystal orientation of the surface (gray plane), $\{10\bar{1}0\}$. (c): For r-plane orientation, $\{1\bar{1}02\}$, the c axis is inclined against the surface plane. Note that the hexagonal unit cell is not a primitive one.

microcavity structures contain substrates. Hence, they are not mid-plane symmetric. For the mode computations, this has been rigorously considered by determining transfer matrices which transfer TE- and TM-polarized modes in the ambient vacuum into the respective eigenmodes in the uniaxial substrates for a given $\vec{k}_{||}$ (cf. section 1.2.1).

4.1 Microcavity samples

The investigated samples have been grown by Jesús Zúñiga-Pérez and Christiane Deparis at *Centre de Recherche sur l'Hétéro-Epitaxie et ses Applications* (CRHEA), *Centre national de la recherche scientifique* (CNRS), Valbonne, France by means of molecular-beam epitaxy [Zúñ+16]. All investigated microcavities are based on wurtzite-type ZnO, epitaxially grown on either m-plane, or r-plane oriented substrates. As depicted in Fig. 4.1, the optic axis, which is the c axis of the hexagonal unit cell, is oriented with the surface plane for the m-plane case and inclined by approximately 47.2° for r-plane, see Fig. 4.1. All cavity layers are respectively oriented ZnO layers. The bottom DBRs consist of alternating ZnO and $\mathrm{Mg}_x\mathrm{Zn}_{1-x}\mathrm{O}$ layers with Mg content x between 0.23 and 0.29. With those stoichiometries, $\mathrm{Mg}_x\mathrm{Zn}_{1-x}\mathrm{O}$ is still wurtzite-type and all prepared layers of the bottom DBR are similarly m- or r-plane oriented. The electronic bandgap of $\mathrm{Mg}_x\mathrm{Zn}_{1-x}\mathrm{O}$ is blue-shifted against ZnO and accordingly, the refractive indices in the transparent spectral range are lower than for ZnO.

Table 4.1: Overview of the presented microcavities in reverse stacking order. The gray numbers indicate internal sample names.

`M1` ZMH1569	m-plane ZnO substrate, 16x($ZnO/Mg_{0.23}Zn_{0.77}O$), λ cavity ZnO, 15x($Mg_{0.23}Zn_{0.77}O/ZnO$)
`M2` ZRH1648	r-plane ZnO substrate, 16x($ZnO/Mg_{0.23}Zn_{0.77}O$), $^9/_8\,\lambda$ cavity ZnO, 15x($Mg_{0.23}Zn_{0.77}O/ZnO$)
`M3` ZMH1713-S1971	m-plane ZnO substrate, 16x($ZnO/Mg_{0.29}Zn_{0.71}O$), $^9/_8\,\lambda$ cavity, ZnO + YSZ-buffer, 6x(Al_2O_3/YSZ)

The top DBRs consist either of, again, epitaxial $ZnO/Mg_xZn_{1-x}O$ (`M1` and `M2`) or Al_2O_3/YSZ[1] layers (`M3`). The latter has been prepared by pulsed laser deposition with the help of Chris Sturm and Lukas Trefflich at Universität Leipzig (*Semiconductor Physics Group*). In order to prevent the growth of an absorbing gahnite (spinel-type $ZnAl_2O_4$) interface layer between the ZnO-cavity and the first Al_2O_3 layer, a YSZ-buffer layer was introduced between the ZnO cavity layer and the first Al_2O_3 layer. Unlike the ZnO and $Mg_xZn_{1-x}O$ layers, the Al_2O_3 and YSZ layers are non-epitaxial. They are amorphous or microcrystalline, respectively [Fra12]. Hence, both are optically isotropic. Table 4.1 gives an overview of the sample structures. The energy-dependent refractive indices of the used materials are shown in Fig. 4.2. The effect of exciton-polaritons can be observed in the dispersion of the refractive index of ZnO already near 3 eV. However, this has negligible influence on the microcavity modes and is not in the focus here.

---

[1] Yttria-stabilized zirconia, i.e. ZrO_2 which has been stabilized in its cubic crystal form by adding some percentage of Y_2O_3 to the raw material.

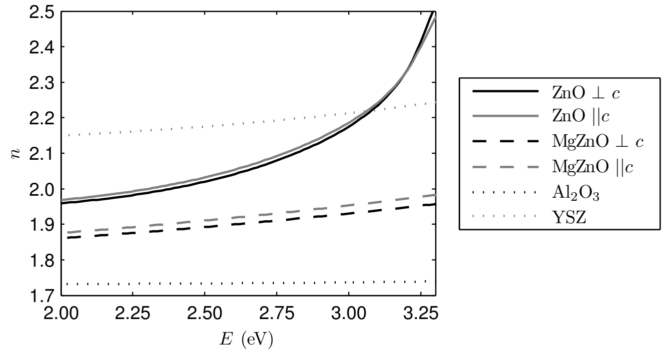

Figure 4.2: Experimentally obtained refractive indices depending on the photon energy E for the materials used for the microcavities. The Mg content of MgZnO is approximately 23% here. ZnO and MgZnO are positively birefringent in the visible spectral range. The ZnO layers here become optically isotropic around 3.2 eV, and negatively birefringent for even higher energies. All materials are non-absorbing in the shown spectral range.

4.2 Experimental methods

Basic optical characterization of the microcavity sample was done by variable-angle spectroscopic ellipsometry, using a commercial instrument. Layer thicknesses have been verified by scanning-electron microscopy on cross-sections of the samples. With those information, transfer-matrix models were developed by modeling the ellipsometry spectra. These are the basis for theoretical mode computations which are compared to the experimentally obtained modes.

The cavity mode structure has been investigated by polarization- and angular-resolved spectroscopy at different sample orientations using a self-built goniometer setup (Fig. 4.3). The simplest way to study the optical modes of microcavity structures is polarization-resolved transmission experiments: Depolarized white light containing any polarization state at any photon energy is provided as input light, and the polarization of the transmitted light is analyzed. Only light is transmitted which fits a mode in terms of photon energy and polarization for the respective propagation direction[2]. In practice, depo-

---

[2] In principle, a similar technique would be possible in reflection configuration, either with unpolarized incident light or in terms of generalized ellipsometry. However, because of the limited dynamic range of a detector, investigating peaks of transmitted or emitted light spectra is more sensitive compared to investigating dips in reflection spectra.

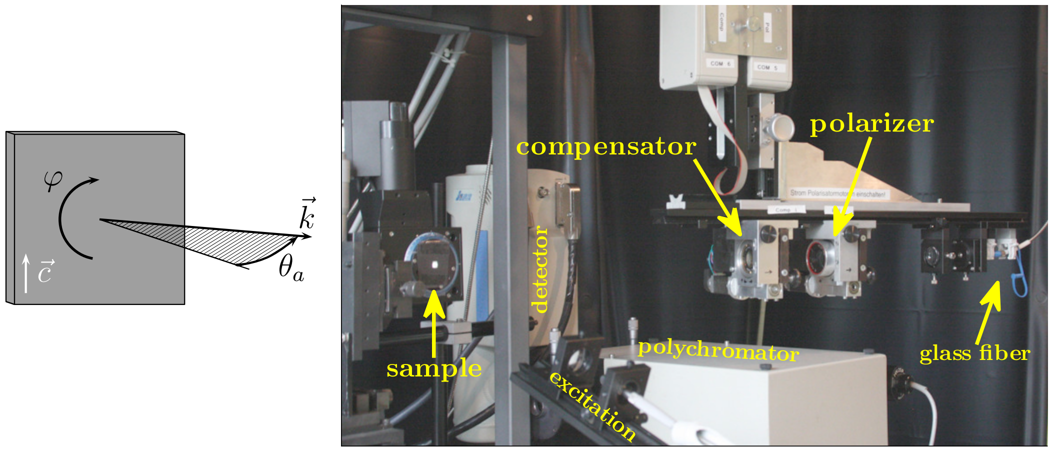

Figure 4.3: Sketch and photograph of the goniometer. The sample is mounted on a rotation stage and rotated by angle φ around its surface normal. The goniometer arm varies the detection angle angle θ_a in order to scan $\vec{k}_{||}$. With the above introduced definitions, it holds $\varphi = 0°$ if the c axis is aligned perpendicular to the detection plane spanned by the surface normal and $\vec{k}$ in the ambient. The white light input at the backside of the sample for the transmission measurements is not seen in the photograph.

larized white light from a Xe lamp was exposed from a glass fiber to the rough backside of the substrates where it scattered towards all directions and allows probing different θ_a at the front side of the sample. As a second method, non-resonantly excited photoluminescence was utilized. Here, a 355 nm cw laser was used at a rather low excitation density of estimated $4\,\mathrm{W/cm^2}$ (whereof 50% are lost by reflection). Spot sizes on the sample have been estimated to approximately 800 µm in diameter for transmission and 200 µm for the photoluminescence. All experiments were performed at room temperature. It should be noted that while reflection and transmission experiments probe the electronic and photonic density of states, photoluminescence gives access occupation. In particular, a microcavity mode is not necessarily populated and observed in a luminescence experiment although it exists.

In both experiments, transmission and photoluminescence, the polarization of the detected light was investigated with a rotatable compensator (achromatic quarter-wave plate of quartz and MgF) and a polarizer (Glan-prism of calcite), as shown in Fig. 4.3. In particular, the polarizer was kept at fixed angle (45°) while intensity spectra at typically 7 different azimuth angles of the compensator (e.g. 0°, 50°, 100°, ...) were measured. The light was guided by a glass fiber to a grating spectrometer (focal length 320 mm, 1200 groves/mm) with CCD detector (liquid-nitrogen cooled, pixel width 26 µm). The spectrometer entrance slit was set such that the spectral resolution in the experiments was around 2 meV. In order to obtain the $\vec{k}_{||}$ dependence of the modes, the emission or transmission angle θ_a was varied by the goniometer arm while the sample was rotated about its surface normal with a rotation angle φ (see Fig. 4.3). This allowed scanning the respective momentum space. The angular resolution given by the detected solid angle was approximately 1 msr.

Having measured the sets of intensity spectra with different compensator angles for each $\vec{k}_{||}$, the transmission spectra were normalized by the spectrum of the Xe lamp. The Stokes-vector spectra $\vec{S}(E)$ were then calculated for each energy E by direct linear regression using ordinary least-squares optimization in form of Moore-Penrose pseudo-inversion in a Müller matrix formalism (see e.g. [Her17] or [Ric12]). For this evaluation, the exact photon-energy-dependent phase shift of the compensator has been used. It had priorly been obtained by spectroscopic ellipsometry. Transformation of $\vec{S}(E)$ into $\vec{\tilde{S}}(E)$ is performed according to Eq. 2.24. Evaluation of the Stokes-vector spectra $\tilde{S}_0(E)$, $\tilde{S}_1(E)$, $\tilde{S}_2(E)$ and $\tilde{S}_3(E)$ was then performed through simultaneous modeling, assuming the two cavity modes as Lorentzian peaks (cf. Eq. 2.25) along with a polynomial background. In order to avoid numerical artifacts, a total degree of polarization of 100% has been demanded for the peaks.

The accuracy of the normalized Stokes spectra $\frac{1}{S_0}\vec{S}(E)$ or $\frac{1}{\tilde{S}_0}\vec{\tilde{S}}(E)$) is in the order of 0.02. However, the accuracy of the $\frac{1}{\tilde{S}_0}\vec{\tilde{S}}$ values assigned to the cavity peaks by the modeling depends strongly on the shape, absolute intensity and overlap of the cavity mode peaks. For small $\tilde{S}_0$ and $\Delta E_c = E_{c2} - E_{c1}$, it can even exceed 0.15, i.e. 15%.

When measuring a spectrum of light emitted from or transmitted through the sample under a certain angle θ_a, the in-plane wave-vector $\vec{k}_{||}$ is not constant along the measured spectrum but depends on the photon energy according to Eq. 2.21. This is considered after evaluation of the Stokes-vector spectra and yields a small distortion in the measured grids when wave-vector values are assigned to the observed cavity resonances. The so obtained maps $\tilde{E}_c(\vec{k}_{||})$ with $\vec{k}_{||} = (k_x, k_y)^{\mathrm{T}} = \frac{E}{\hbar c_0}\sin(\theta_a) \cdot (\cos(\varphi), \sin(\varphi))^{\mathrm{T}}$ (cf. Fig. 4.3) are directly compared to theoretical computations.

4.3 Experimental results vs. theoretical computations

λ m-plane cavity (`M1`)

This microcavity sample has been presented in [Zúñ+16] as an example for non-polar, epitaxial growth of ZnO/MgZnO heterostructures. It consists of ZnO and $\mathrm{Mg_{0.23}Zn_{0.77}O}$ layers with thicknesses of 44.5 nm and 55.5 nm, respectively. The cavity layer has exactly four times the thickness of a ZnO layer of the DBRs, hence a perfect tuning between optical cavity thickness and central DBR wavelength, $n_c d_c = \lambda_{\mathrm{DBR}}$, is achieved. Cavity-photon modes are observable in transmission up to angles $\theta_a \approx 50^\circ$, where for angles larger than 40°, only one mode can be tracked in the experimental spectra. Figure 4.4 shows exemplarily the obtained Stokes-vector spectra depending on the transmission angle θ_a for two different sample orientations ϑ. It can be seen that the energetically lower cavity mode is mostly linearly polarized parallel to the c axis, the energetically higher one mostly perpendicular. For $\theta_a \neq 0$, and hence $\vec{k}_{||} \neq \vec{0}$, a slight circular polarization contribution is visible. Hence, the modes are slightly elliptically polarized. Circular polarization is also observed strongly for modes energetically above the Bragg stop-band, and weakly in the background, i.e. within the range of the Bragg stop-band.

For each angular configuration (φ, θ_a), the obtained Stokes-vector spectra $\vec{S}(E)$ are projected into the xy laboratory frame, yielding $\vec{\tilde{S}}(E)$. In order to determine the cavity mode energies and polarization, each set of Stokes-vector spectra is simultaneously modeled, as exemplarily shown in Fig. 4.5.

The results for the complex mode energies $\tilde{E}_c = E_c - i\Gamma_c$, along with theoretically computed values, are shown in Fig. 4.6. The (real part of the) mode energies coincide well with the theory. As expected, no energetic mode degeneracies are observed. The experimentally obtained values for (half) the spectral broadening Γ_c scatter strongly and do not allow meaningful comparison with the theoretical expectations. Generally, the obtained broadenings are larger than expected. This could be a matter of local inhomogeneities. In particular,

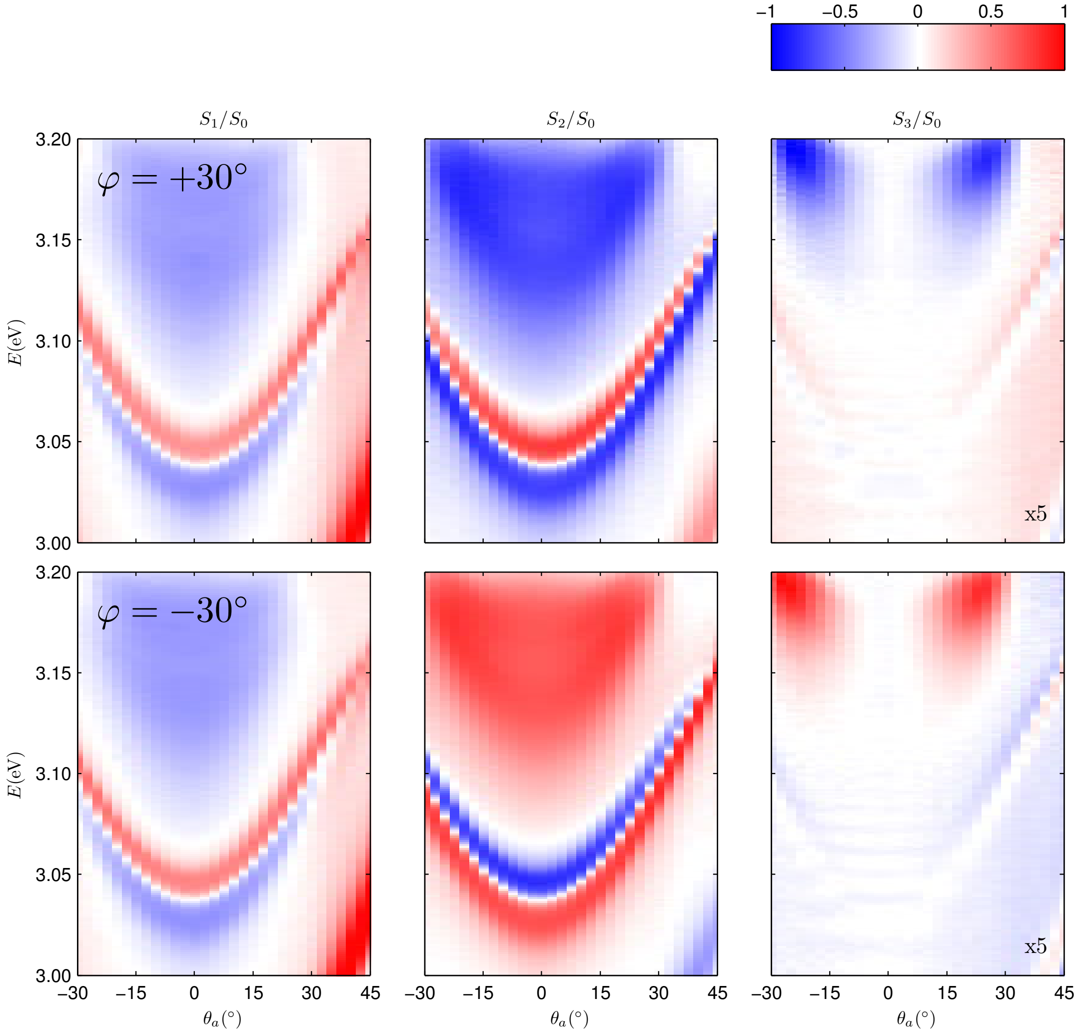

Figure 4.4: Normalized transmission Stokes-vector spectra $\frac{1}{S_0}\vec{S}(E)$ for the m-plane oriented λ cavity (`M1`) when scanning θ_a for two different rotation angles of the sample given by φ (top and bottom row). The definition of S_1 and S_2 is according to TE/TM polarization. The S_3 spectra are 5 times enhanced. Note the strong circular contributions in the edge modes energetically above the Bragg stop-band. $\varphi = 0°$ corresponds to the c axis perpendicular to the POI.

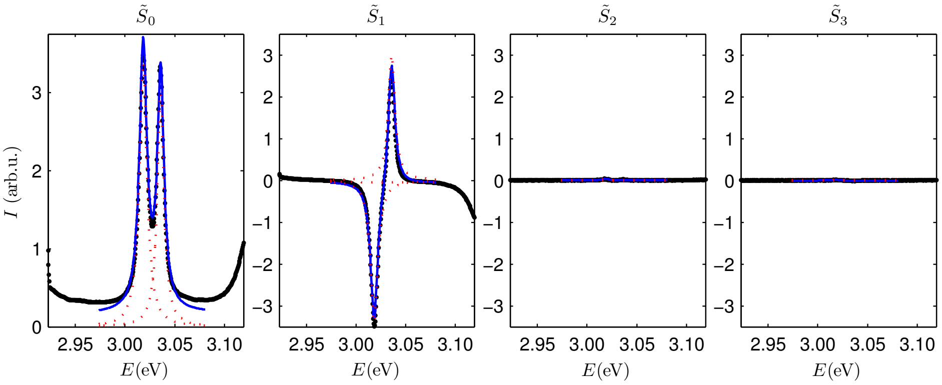

Figure 4.5: Unnormalized transmission Stokes-vector spectra $\vec{\tilde{S}}(E)$ as obtained (dots) for $\vec{k}_{||} = \vec{0}$ for the m-plane oriented λ cavity (`M1`). The two cavity-photon modes have been modeled as Lorentzian peaks (red dotted lines) along with a polynomial background in the narrow spectral range indicated by the modeled spectra (blue lines). The c axis is aligned with y.

this sample reveals cracks every some 10 µm, i.e. on a length scale well below the size of the light spot in the experiment.

The corresponding mode polarization is presented in Fig. 4.7. The observations match the expectations very well. Mostly, the energetically lower mode (mode 1) is polarized parallel to the c axis, the higher one (mode 2) perpendicular to it. Nevertheless, $\tilde{S}_2$ and $\tilde{S}_3$ take non-zero values for $\vec{k}_{||} \neq \vec{0}$. While the signs of the small $\tilde{S}_3$ values of mode 1 differ from the expectation, the signs of the rather strong $\tilde{S}_2$ values of both modes match the predictions and indicate that they are generally not orthogonal to each other. As discussed in chapter 3, this is a fundamental qualitative difference to microcavities with cylindrical symmetry. It should be noted that the signs of the small $\tilde{S}_3$ components for the cavity peaks are not unambiguous when modeling the $\vec{\tilde{S}}(E)$ spectra. This results in a large uncertainty for $\tilde{S}_3/\tilde{S}_0$ if $\tilde{S}_0$ is small either. This uncertainty could explain the unexpected experimental $\tilde{S}/\tilde{S}_0$ for mode 1 (Fig. 4.7).

In summary, this microcavity sample proves the theoretical prediction that i) the cavity-photon modes of an anisotropic planar microcavity are generally not orthogonal. And ii) no exceptional points occur for the cavity modes if the optical thickness of the cavity layer corresponds almost exactly to a multiple of half the central wavelength of the DBRs, $n_c d_c \approx \frac{m}{2}\lambda_{\mathrm{DBR}}$, and the mode confinement is sufficiently strong (Γ_c not too large). Furthermore, strong

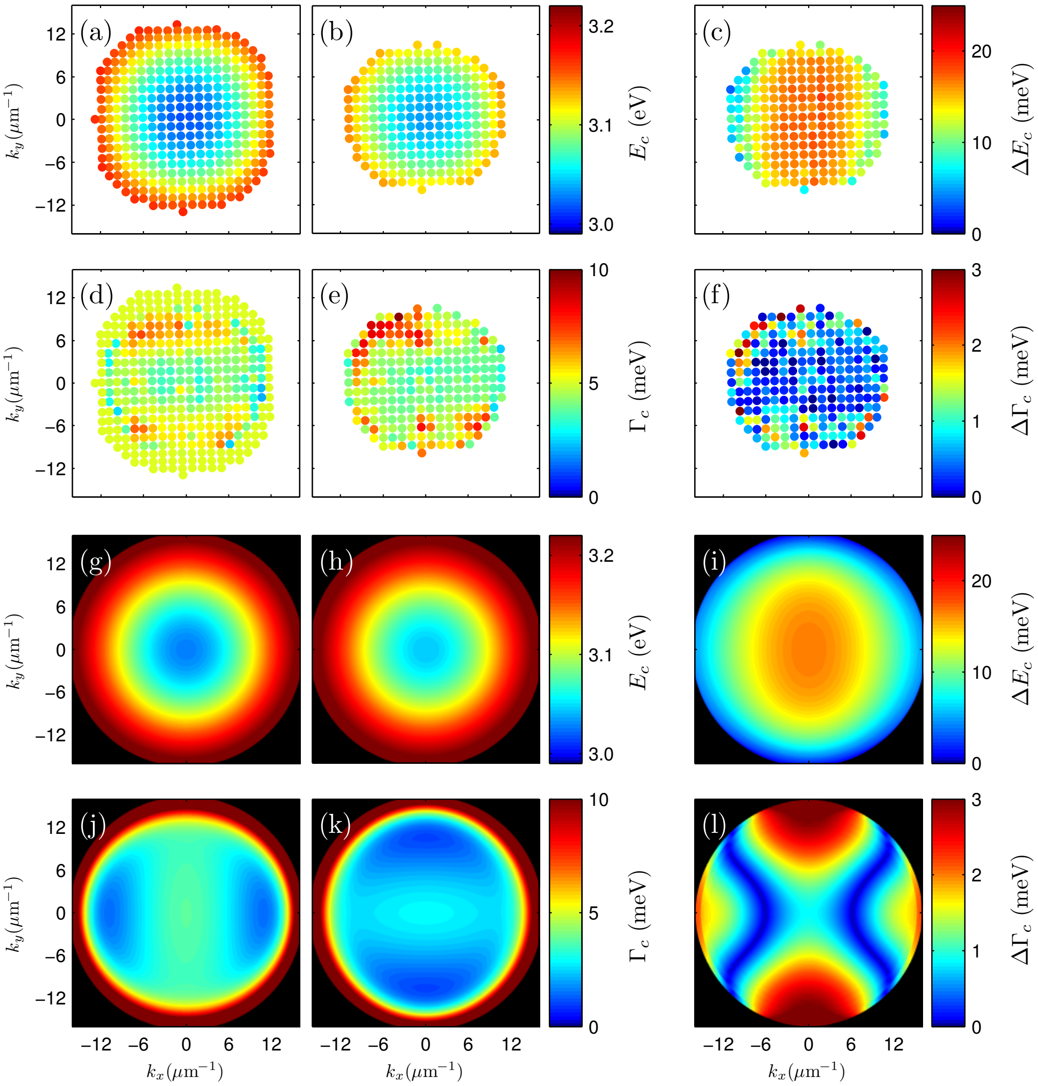

Figure 4.6: Complex mode energy, depending on $\vec{k}_{||}$ for the m-plane oriented λ cavity (`M1`), with c axis aligned with y. (a-f): Experimentally obtained values from transmission experiments, (g-l): theoretically computed. (a,b,g,h): Mode energies E_c, (c,i): mode splitting ΔE_c, (d,e,j,k): half the mode broadening Γ_c, (f,l): their difference. The first (second) column represents the energetically lower (higher) mode. Note that every data point in (a-f) represents the result of a simultaneous line-shape fit of the Stokes-vector spectra.

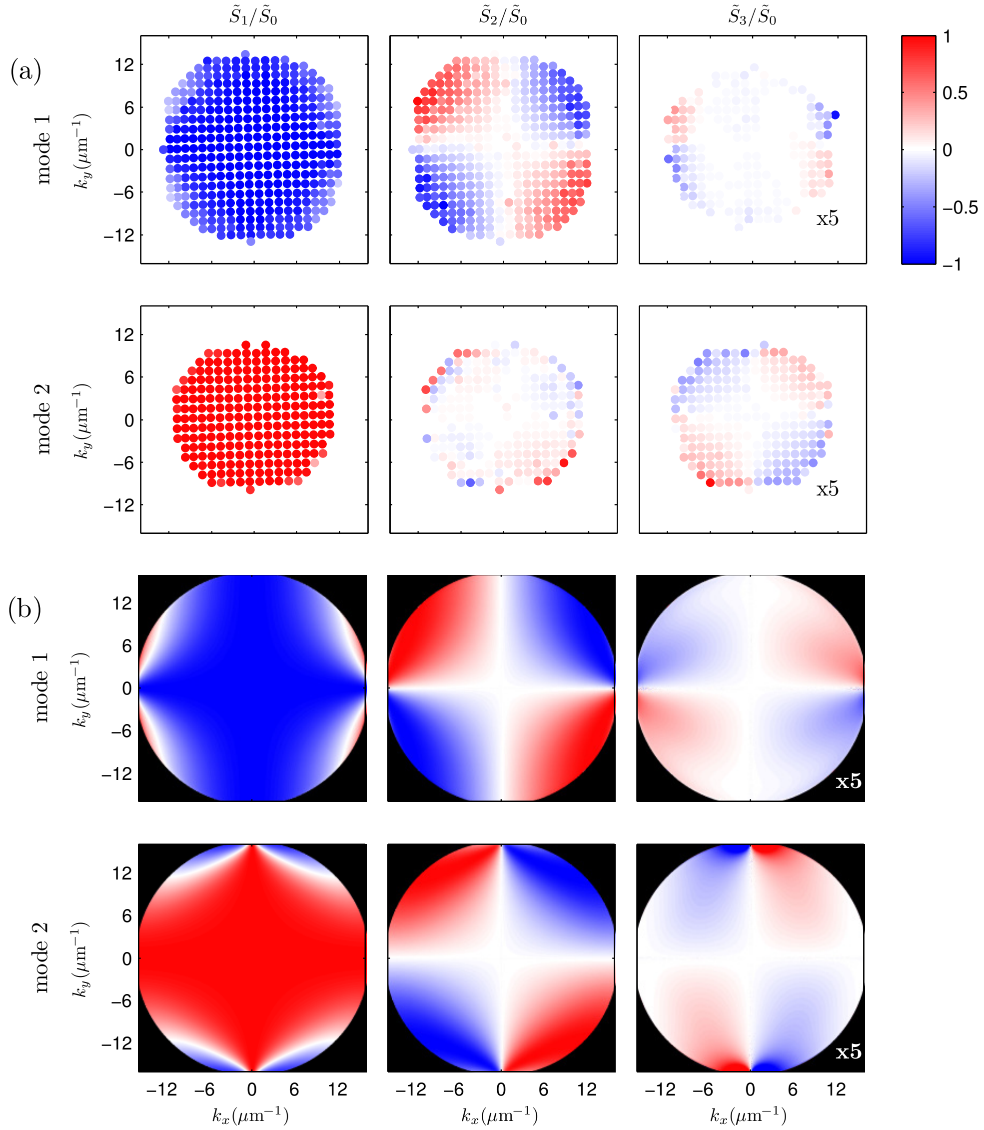

Figure 4.7: Polarization patterns in terms of $\frac{1}{\tilde{S}_0}\vec{\tilde{S}}$ for the m-plane oriented λ cavity (`M1`). The c axis is aligned with the y direction. (a): experimentally obtained values from transmission evaluation, (b): theoretically computed. Panels of the left, middle and right column show $\tilde{S}_1$, $\tilde{S}_2$ and $\tilde{S}_3$, respectively. The $\tilde{S}_3/\tilde{S}_0$ values are 5 times enhanced. Every data point in (a) represents the result of a simultaneous fit of the Stokes-vector spectra.

circular polarization is visible for Bragg band edge modes (see Fig. 4.4). Such modes can generally be treated similarly to cavity modes [Fau+09; Ric+05], and probably they reveal exceptional points. Nevertheless, attempts of mode separation and modeling of the experimental data was not successful here due to the large broadening of these modes.

$^9/_8\,\lambda$ r-plane cavity (`M2`)

The second microcavity sample follows the same design recipe as the first one but i) has been grown on an r-plane oriented substrate, and ii) its cavity layer thickness is increased by a factor of 9/8. Consequently, the cavity mode energies E_c are slightly decreased. In the transmission experiment, the cavity modes can be observed for angles up to $\theta_a \approx 45°$. The experimentally determined complex mode energies, obtained from modeling the spectra of the Stokes parameters, are depicted in Fig. 4.8. First of all, no general difference to the m-plane oriented microcavity is visible. Although the symmetry of the structure is lowered from orthorhombic to monoclinic (see Tab. 3.2), the difference between modes at $+k_y$ and $-k_y$ is hardly visible here, neither in the experimental nor in the computed data. The mode energies E_c match roughly the expectation while the mode broadenings scatter a lot and are larger than the theoretical values. The energetic mode splitting ΔE_c shows that degeneracies, expectedly exceptional points, are found within the observable $\vec{k}_{||}$ range for this microcavity. The mode polarization, Fig. 4.9, reveals that indeed those mode degeneracies are strongly connected to circular polarization. These circular polarization components express also the asymmetry between $+k_y$ and -k_y induced by the inclined c axis. In general, the asymmetry is mainly visible in the polarization. In particular, for an r-plane configuration, an asymmetry in $\tilde{E}(\vec{k}_{||})$ can only be observed due to the substrate which breaks the mid-plane symmetry. Polarization can uncover the inclination of the optic axis in any case. Though circular polarization components arise near the mode degeneracies, the modes do not become completely circularly polarized. Even finer $\vec{k}_{||}$ scans have been performed in the vicinity of the mode degeneracies but yielded the same result. Even if the inaccuracy in the modeling of the Stokes parameter spectra is considered, 100% circular polarization is definitely not found. The role of the spot size and local inhomogeneities could again matter.

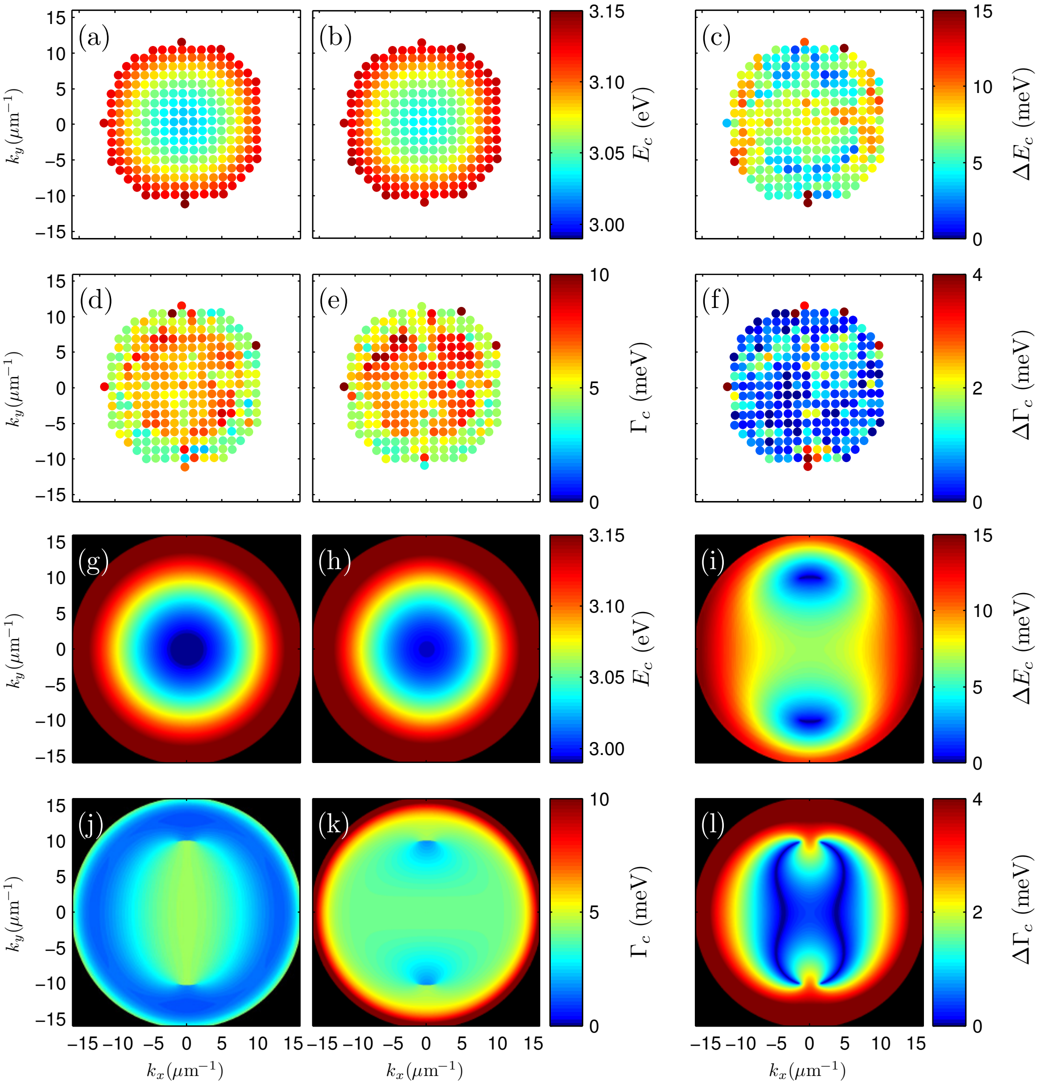

Figure 4.8: Complex mode energies E_c in momentum space $\vec{k}_{||}$ for the $^9/_8\,\lambda$ r-plane cavity (`M2`). The c axis is aligned in the yz plane pointing towards the surface for $k_y < 0$. (a-f): experimental results, (g-l): theoretical computations. (a,b,g,h): mode energies E_c, (c,i): mode splitting ΔE_c, (d,e,j,k): mode broadening Γ_c, (f,l): their difference. Every data point in (a-f) represents the result of simultaneous modeling of the transmission Stokes parameter spectra.

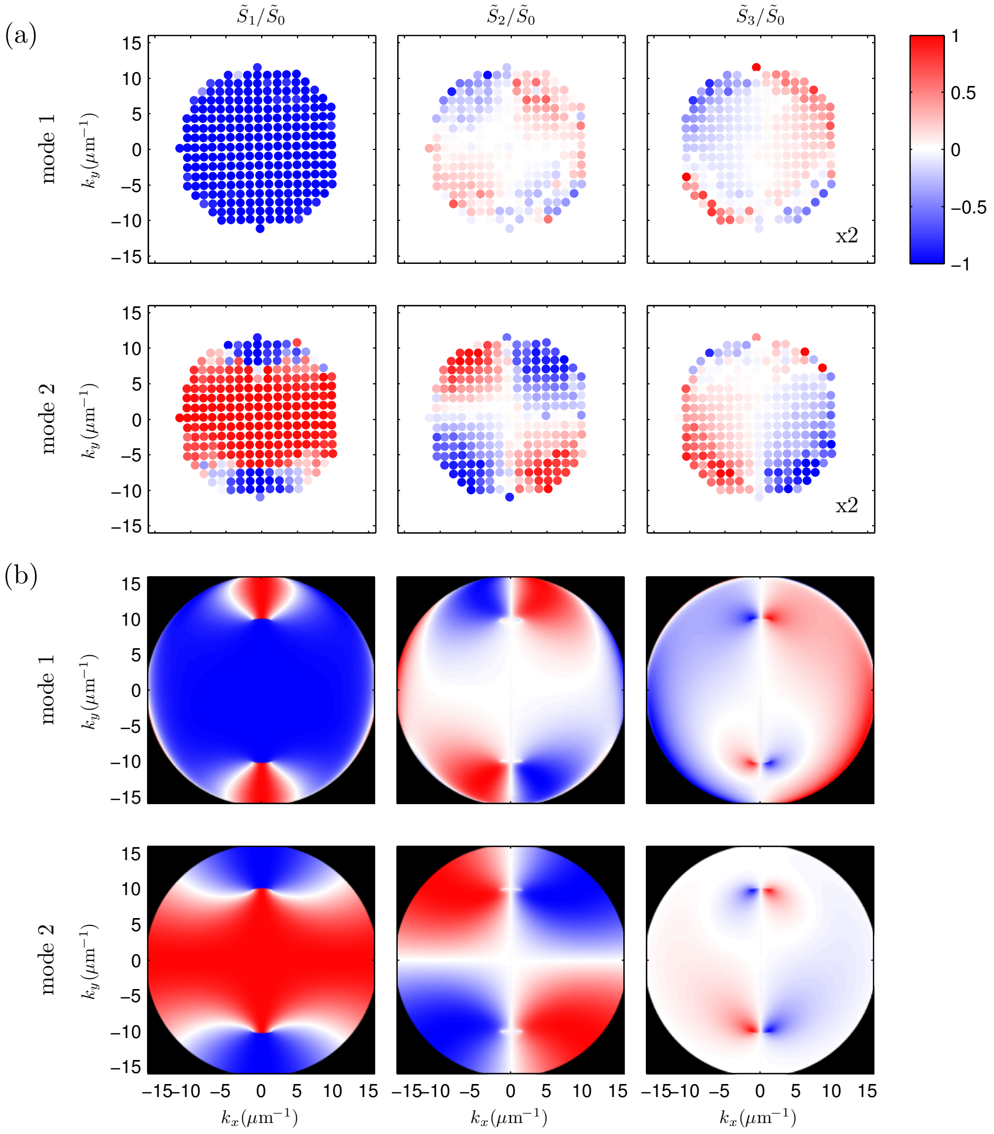

Figure 4.9: Polarization pattern for the $^9\!/_8\,\lambda$ r-plane cavity (`M2`), with c axis aligned in the yz plane and pointing towards the surface for $k_y < 0$. (a): Experimental results, (b) theory. The experimental $\tilde{S}_3/\tilde{S}_0$ values are 2 times enhanced in order to emphasize the broken symmetry with respect to $+k_y$ and $-k_y$. Panels of the left, middle and right column show $\tilde{S}_1$, $\tilde{S}_2$ and $\tilde{S}_3$, respectively. Mode 1 (2) is the energetically lower (higher) one. Every data point in (a) represents the result of a simultaneous spectral fit of the transmission Stokes vectors.

In particular, `M2` has a small lateral gradient of the layer thickness. A finite light spot does effectively average different over different sample thicknesses. This could lead to the blurred distribution of the circular polarization observed in the experiments (Fig. 4.9). Another source of inaccuracy may again be improper modeling of the Stokes-vector spectra, especially if both modes come energetically close together. Avoidance of such artifacts is done by demanding the degree of polarization being 100% for the modeled Lorentzian peaks. Still, the $\tilde{S}_1$ component of mode 1 for large $|k_y|$ hints on problematic modeling.
In theory, circularly polarized exceptional points are a consequence of the transmission Jones matrix being symmetric (see section 3.3 and appendix A.2). This again is not generally given if the structure lacks mid-plane symmetry due to the substrate. However, theoretical computations have been performed with higher resolution and revealed, within the numerical accuracy, circularly polarized exceptional points. This means, the transmission Jones matrix becomes symmetric at the exceptional points despite not being symmetric in general.

In conclusion, this microcavity sample proves that i) an inclined optic axis (r-plane) yields a slight asymmetry but no general difference to microcavities with the cavity's optic axis aligned in the cavity plane. More important, ii) it proves that detuning the cavity with respect to λ_{DBR} enables observation of exceptional points within the vacuum light cone. Still, the modes are, within the experimental accuracy, definitely not completely circularly polarized. This contrasts the theoretical calculations but could be caused by experimental imperfections such as spatial inhomogeneities of the microcavities and the limited spatial resolution of the setup.

$^9/_8\,\lambda$ *m*-plane cavity (`M3`)

The modes at energies above 3 eV are energetically not far from the bandgap and exciton resonances of ZnO. Hence, it is possible to generate light by photo- or electroluminescence and utilize scattering processes (e.g. p-band emission by exciton-exciton scattering [Hva74], m-band emission which is probably biexciton-related [Kli+81], or phonon-induced scattering of exciton-polaritons [Mic+14; Stu11; Kli+10]) to *pump* the cavity modes. Also luminescence by deep electronic defects is possible. Luminescence experiments require not only a light emitting medium as cavity layer but also the DBRs, especially the top one, being dielectric. A ZnO/MgZnO top DBR prohibits proper luminescence experiments because light originates not only from the cavity layer but also from the DBR layers above. With a dielectric top DBR consisting of Al_2O_3 and YSZ layers, sample `M3` allows luminescence experiments. Furthermore, Al_2O_3 and YSZ have a larger contrast in refractive indices than ZnO and MgZnO (cf. Fig. 4.2). An Al_2O_3/YSZ top DBR of 10 layers has approximately the same reflectivity as the 16-pair bottom-DBR of ZnO and MgZnO. Here, the top DBR has been designed with even fewer layer pairs and hence lower reflectivity in order to support the outcoupling of light towards the front side.

For `M3`, modes are observed for angles up to $\theta_a \approx 60°$ in transmission and from 30 to 65° in photoluminescence experiments. In the first case, the limitation is most likely inefficient scattering of light towards large $k_{||}$. In the latter case, the spectral emission profile of ZnO does not allow observation of modes at energies lower than those of the modes at $\theta_a \approx 30°$. Nevertheless, it has been found that photoluminescence is not very efficient at the present microcavity. Due to long integration times, only one quadrant of the momentum space was scanned completely and is shown in Figs. 4.10 and 4.11. Again, the complex mode energies shown in Fig. 4.10, do roughly coincide if obtained by transmission, by photoluminescence, or computed. However, note that the scaling for Γ_c is different here for experimentally obtained and computed values because the experimental values are much smaller. The origin of this discrepancy is not clear but most likely related to an imperfect transfer matrix model for the computations on the one hand, and imperfect Stokes spectra modeling by the Lorentz oscillators (cf. Fig. 4.12) on the other hand. Nonetheless, even the Γ_c degeneracies are visible in Fig. 4.10 (f). The degeneracies are again strong indications for an exceptional point structure. The respective mode polarization is presented in Fig. 4.11. Note that the $\tilde{S}_3/\tilde{S}_0$ values are not enhanced here. Except for some scattering points, the experimentally observed and computed mode patterns agree rather well. In the experiment, the circular contributions are more washed out and occur at lager $|k_{||}|$ values compared to the computations. Also here, better resolved $\vec{k}_{||}$ scans did not result in larger degrees of circular polarization, as discussed for `M2`. This may again be a hint that local sample inhomogeneities are averaged by the large light spot. Nevertheless, generally there is a good agreement between experimental observations

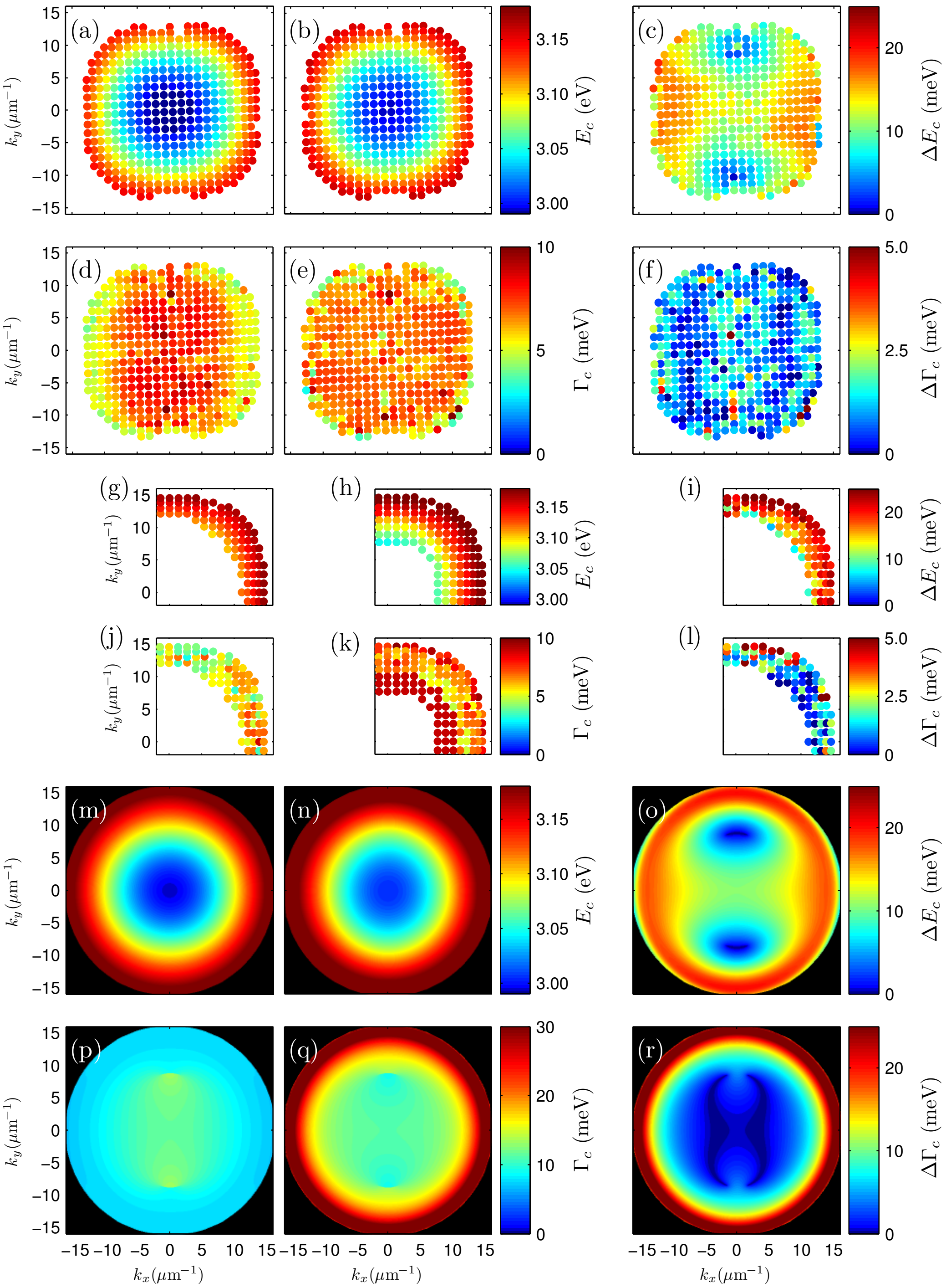

Figure 4.10: Complex mode energies depending on $\vec{k}_{||}$ for the $^{9}/_{8}\,\lambda$ m-plane microcavity (`M3`). The c axis is aligned with y. (a,b,g,h,m,n): Mode energies E_c, (c,i,o): mode splitting ΔE_c, (d,e,j,k,p,q): half the mode broadenings Γ_c, (f,l,r): their difference $\Delta\Gamma_c$. (a-f) represent data obtained from transmission experiments, (g-l) data from photoluminescence experiments, and (m-r) computed values. Panels in the left (middle) column show the energetically lower (higher) mode.

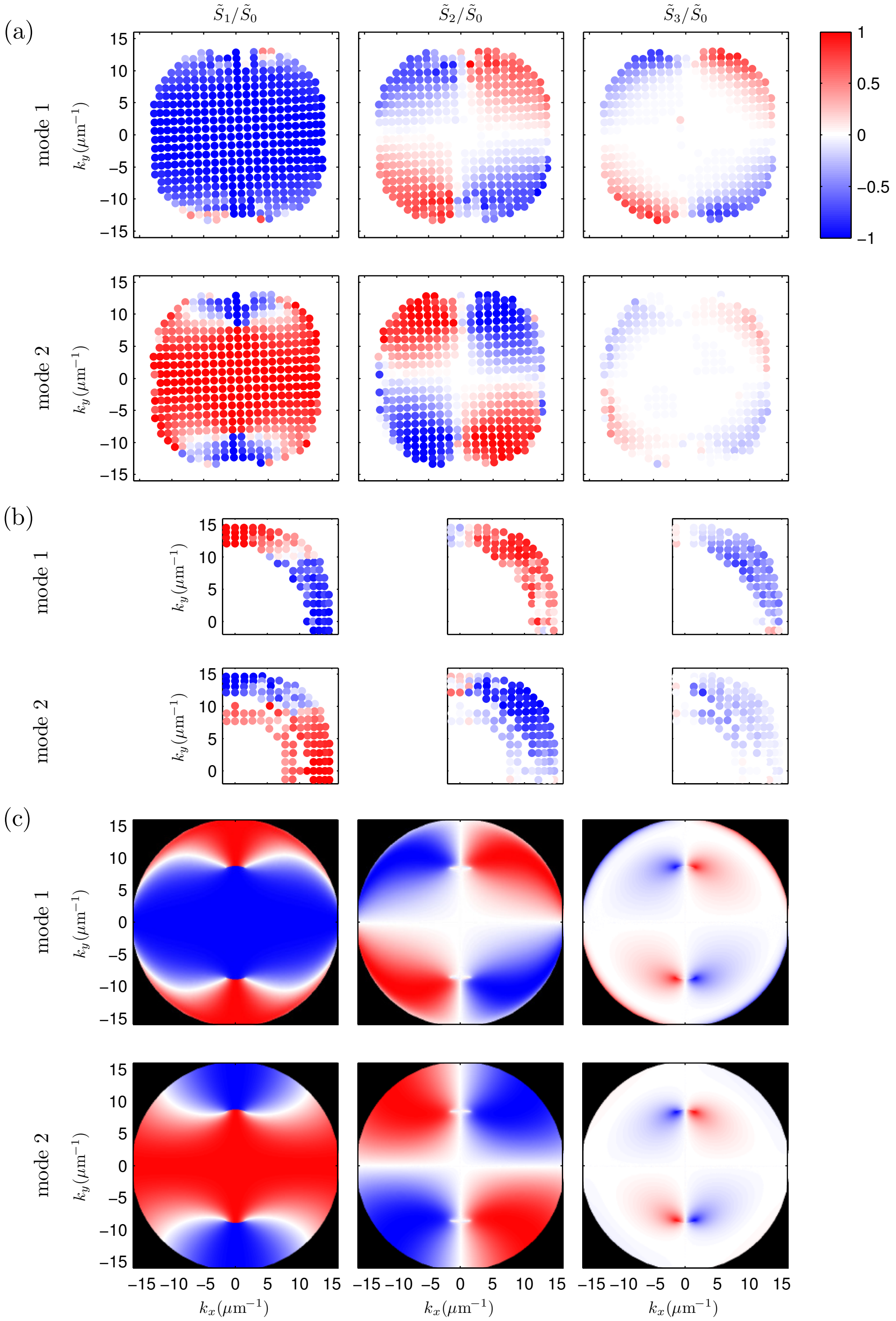

Figure 4.11: Polarization patterns in terms of the normalized Stokes vectors $\frac{1}{\tilde{S}_0}\vec{\tilde{S}}$ depending on $\vec{k}_{||}$ for the $9/8\,\lambda$ m-plane microcavity (`M3`). Panels (a) represent data from the transmission experiments, (b) data from the photoluminescence experiments, and (c) computed data. Mode 2 is always the energetically higher one. Panels of the left, middle and right column show $\tilde{S}_1$, $\tilde{S}_2$ and $\tilde{S}_3$, respectively.

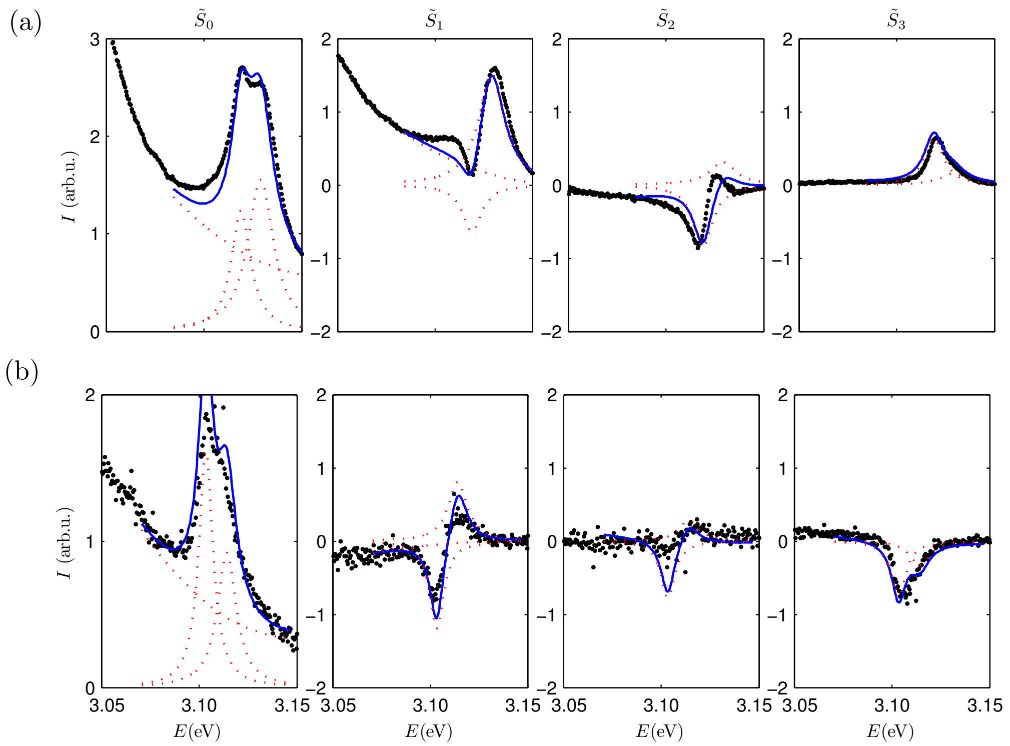

Figure 4.12: Unnormalized Stokes-vector spectra $\vec{\tilde{S}}(E)$ as experimentally obtained (dots) for `M3`, and model (blue line) consisting of the two cavity-photon peaks and a polynomial background (red dotted lines). (a): Transmission data with $\theta_a \approx 50°$, (b): photoluminescence data with $\theta_a \approx 45°$, hence slightly higher energies in (a). For both cases, sample rotation is $\varphi \approx 65°$, i.e. first quadrant in Fig. 4.11, and $k_y > k_x$. Modeling was done simultaneously for all components of $\vec{\tilde{S}}(E)$ in the narrow spectral range indicated by the modeled spectra, demanding the degree of polarization being 100% for the cavity peaks.

and theoretical predictions for the observed polarization. Remarkably, the sign of the circularity differs in transmission and photoluminescence experiments. This observation has been verified (also for other quadrants of the momentum space) and is not the result of a different sign definition. In fact, the schemes for sample orientation and light detection were identical in both experiments, transmission and photoluminescence. Figure 4.12 shows exemplary modeling of the Stokes-vector spectra near an exceptional point for both, transmission and photoluminescence. The examples shown correspond to spectra with the highest degree of circular polarization observed, i.e. approximately 60% and 40% in photoluminescence, and 30% and 15% in transmission, for mode 1 and

2 respectively. The higher degree of circular polarization in the photoluminescence experiments is probably related to the smaller spot size. The generally higher degree of circular polarization for mode 2 compared to mode 1 could be a matter of improper modeling of the Stokes-vector spectra. It is hard to exclude that the closely overlapping peaks can artificially yield one mode preferentially becoming circularly polarized in the model. As can be seen in Fig. 4.12, modeling is far from being perfect. Simple Lorentz oscillators are only a coarse approximation and do not exactly match the line shapes of the experimentally observed peaks. However, the line-shape model was chosen as simple as possible for the evaluations in order to keep the number of parameters small, here. Also proper modeling of the large, partially polarized background is difficult. In both, photoluminescence and transmission, the background originates from the approaching edge of the Bragg stop-band. The observed sign of $\tilde{S}_3$ for the cavity modes in the transmission experiments coincides with the theoretical predictions. This is reasonable because the theoretical computations are based on transmission Jones matrices. Photoluminescence does not directly probe the modes but its occupation. The sign of the circularity in the photoluminescence experiments must be intrinsically related to emission origin affecting the phase shift of different wave components. The exact mechanism is not clear yet.

In summary, this microcavity sample i) confirms again that exceptional points can be observed if the optical cavity layer thickness does not match a multiple of the central DBR wavelength, $n_c d_c \neq \frac{m}{2}\lambda_{\mathrm{DBR}}$. Within the experimental resolution, it can be assumed that ii), indeed, the exceptional points are circularly polarized. Surprisingly, the sign of the circularity is opposite in photoluminescence experiments compared to that in transmission experiments.

4.4 Summary and discussion

ZnO-based microcavity samples with m- and r-plane oriented cavity layer, fabricated by molecular beam epitaxy [Zúñ+16], have been investigated. To obtain the cavity-photon modes, polarization-resolved transmission and photoluminescence experiments were performed. While in transmission, the rough backsides of the samples were illuminated by unpolarized white light, photoluminescence was done only for the one sample with a dielectric top DBR.

The theoretically expected complex mode energies $\tilde{E}_c$ of the λ modes ($m=2$) were generally well reproduced in the experiments, despite the experimentally obtained values scatter largely. Degeneracies of E_c in the momentum space are, within experimental accuracy, observed as predicted. For `M3`, also the Γ_c degeneracies can be recognized. Exceptional points do only occur if there is a slight detuning between the central DBR wavelength and the optical cavity thickness, i.e. $n_c d_c \neq \frac{m}{2}\lambda_{\mathrm{DBR}}$. This allows also the appearance of exceptional points for optical modes which are not cavity-photon modes (e.g. Bragg edge modes). As predicted, there is no qualitative difference between m- and r-plane oriented cavity layers, i.e. microcavity structures with orthorhombic and monoclinic symmetry, respectively. Also, experimentally obtained mode polarizations agree well with the theoretical calculations. Exceptional points are related to circular polarization, albeit the experiments do not reveal 100% circular polarization. In the computations, however, the exceptional points are circularly polarized even for microcavities without mid-plane symmetry.

A potential non-ideality, on the model side, is that the polariton effect of the ZnO is not rigorously considered: When the modes are computed based on tabulated data for the energy-dependent dielectric functions (as obtained by spectroscopic ellipsometry), this does not allow accounting for the effect of the imaginary part of the complex energy on the complex refractive index. Hence, $\hat{\varepsilon}(\tilde{E}) \approx \hat{\varepsilon}(E)$ has to be assumed. Though, the cavity-photon modes are energetically rather far from the excitonic resonances and Γ_c rather small. Thus, it can be expected that this model-based non-ideality has a negligible effect (see Fig. 1.8). The finite angular and spectral resolution during the measurement can most likely also be excluded as origin of the discrepancy between experiment and theory. For the transmission experiments, it is not clear if the actually depolarized incident light is biased in terms of polarization when it scatters through the rough backside of the anisotropic substrate into all directions. This could happen especially for large angles θ_a. Nevertheless, it can be expected that the effect of such a non-ideality is rather small. Although modeling of the Stokes-vector spectra is not always perfect (compare Fig. 4.5 and 4.12) and can occasionally fail, it is generally robust and cannot explain the differences between experimental results and theoretical predictions. Nevertheless, imperfect modeling causes an additional uncertainty especially if the total peak intensity in a spectrum, $\tilde{S}_0$, is small. This is the case e.g. for large $|k_{||}|$ in the transmission experiment.

Eventually, the discrepancy can most likely be explained by the large spot size which averages over local inhomogeneities along the sample. Even a small local change of the cavity layer thickness can result in strong shifts of the position of exceptional points and hence averaging of different polarization patterns. In general, one should note that exceptional points are very sensitive to perturbations [Kat66]. Even from the mathematical point of view, it can be expected that it is harder to exactly match the direction of an exceptional points than e.g. the direction of a classic optic axis in a biaxial medium (diabolical point, conical refraction). Again, this hints at the experimental limitation due to the large spot size.

The most important remaining question is why the circularity reveals the opposite sign in photoluminescence compared to transmission experiments. This should be an intrinsic property and may be related to polarization scattering of exciton-polaritons from the energetic level of the excitons towards the cavity-photon mode which actually are LPBs.

Chapter 5

Conclusion

Anisotropic planar optical microcavities, consisting of a cavity layer which is surrounded by distributed Bragg reflectors (DBRs), have been investigated theoretically and experimentally: Within a plane-wave approach, the theory of mode computation has been advanced and applied in order to obtain cavity-photon modes without before-hand restricting their polarization. For this purpose, a complex 4×4 transfer matrix calculus has been used for the formulation of the mode condition. Finally, the problem reduces to investigations of inverse transmission Jones matrices of the microcavity structure.

Using this formalism, numerical computations of cavity-photon modes of planar microcavities with optically uniaxial cavity medium have been carried out. For any in-plane wave-vector $\vec{k}_{||}$, a $\frac{m}{2}\lambda$ cavity-photon mode (mode number m) is generally split into two modes which principally carry elliptic polarization and are non-orthogonal to each other. The modes can degenerate at certain $\vec{k}_{||}$ in real and imaginary part of the complex mode energy $\tilde{E}_c = E_c - i\Gamma_c$, yielding so called exceptional points. This means, exceptional points define directions along which modes degenerate in energy E_c and broadening $\Gamma_c \approx HWHM$. The complex mode-energies reveal a complex-square-root topology in the in-plane momentum space.

At an exceptional point, the modes become circularly polarized. The exceptional points occur always pair-wise where one of them is left, the other one right circularly polarized. Furthermore, such a pair is a vortex center for the linear polarization of the modes: The Stokes-vector component describing the linear polarization reveals a vortex with winding number one when a pair of

exceptional points is encircled in momentum space.
The occurrence of exceptional points within the range of radiative modes, i.e. within the vacuum light cone, requires a broken cylinder symmetry of the microcavity (resulting in a biaxial symmetry of the structure), and a slight detuning between the optical cavity layer thickness and the central DBR wavelength, $n_c d_c \neq \frac{m}{2}\lambda_{\mathrm{DBR}}$.

With the generally elliptically polarized, non-orthogonal modes and the occurrence of exceptional points, anisotropic planar microcavities behave like absorptive biaxial media, even if they consist only of dielectric materials. In absorptive biaxial media, exceptional points in momentum space are singular optic axes. Anisotropic microcavities with broken cylindrical symmetry are biaxial structures and the exceptional points of the cavity-photon modes mark effective singular axes. Absorption is replaced here by photonic loss due to emission. In both cases, the light dissipation is formally expressed by imaginary components of either mode energies or the dielectric function tensor, and hence eventually of the wave vectors. A non-vanishing imaginary part of the propagation operators is a mathematical requirement for the occurrence of exceptional points in such systems. Mathematically, they are described here by degenerate eigenvalues and eigenvectors of a complex, non-Hermitian 2×2 matrix. For a complex, symmetric matrix, this results directly in *chiral* eigenstates. Singular axes and the exceptional points in anisotropic microcavities are great examples of what chirality can mean: Circular polarization results from the $\frac{\pi}{2}$ phase-shifted superposition of TE and TM polarization. In other physical systems with exceptional points, the definition of chirality is often somewhat formal, e.g. a phase condition for incident light on front and backside of a structure [Fen+14], or just a superposition of two modes with a phase difference of $\frac{\pi}{2}$, independent of polarization [Jam+17].
From the topological point of view, the anisotropic microcavities studied here are trivial. The reason is that the exceptional points occur pairwise. Each exceptional point, which is center of a half-vortex for the linear polarization, represents a source of Berry curvature. The sign of the curvature corresponds to the sign of the circular polarization carried by the exceptional point. The paired appearance of exceptional points with opposite sign of the circular polarization prohibits monopoles, and the dipoles yield a trivial net-topology.

For planar optical microcavities, a number of polarization-related phenomena have been studied during the last years. However, they differ qualitatively from the anisotropic microcavities here in that they usually exploit only the intrinsic TE/TM mode splitting of a microcavity with cylindrical symmetry. Or, if anisotropies occur, only regions of the momentum space are considered which are far away from potential exceptional points. In general, the commonly used quasi-particle descriptions, which base on introduction of a pseudo-magnetic field in the polarization Hilbert-space, fail for the anisotropic microcavities because of the non-orthogonality of the modes. The probably closest observation in planar microcavity systems are simultaneous polarization and phase vortices in real space at a propagating condensate of exciton-polaritons, referred to as *half-quantum vortices* [Lag+09]. However, this effect is rather randomly caused by local defects.

First experimental demonstrations of anisotropic microcavities have been shown using ZnO-based m- and r-plane oriented microcavities. They proved the mode structure in terms of complex energies as predicted by the numerical computations, and indicate the occurrence of exceptional points. Also, the exceptional points, are clearly connected to circular polarization. Nevertheless, no 100% circularly polarized modes could be observed in the experiments. Most likely, this is due to local inhomogeneities which are concurrently probed by the macroscopic light spot. Eventually, exceptional points are expected to be generally very sensitive to perturbations [Kat66].

Outlook

With the theoretical analysis performed yet, it remains to be investigated if an asymmetric structure can yield elliptically instead of circularly polarized exceptional points. So far, computations revealed that, despite the transmission Jones matrices generally not being symmetric then, in the case of exceptional points, they become symmetric and yield circular polarization. However, the experimental results obtained from the r-plane oriented microcavity deviate apparently from circularly polarized modes near the exceptional points.

Another interesting theoretical question is whether it is possible to separate two exceptional points of a pair such that only one remains in the range of the radiative modes while the other one occurs at in-plane wave-vectors larger

than the vacuum light cone. This way, the topology of the radiative modes could be changed. Such a situation could be possible by utilizing mono- or triclinic cavity media. From monoclinic media it is known that the singular axes split up asymmetrically [Stu+16].
A research direction, easier to implement experimentally but harder to compute theoretically, is extending microcavities with uniaxial cavity medium by lateral structuring. Such an in-plane periodicity would allow coupling between $+\vec{k}_{||}$ and $-\vec{k}_{||}$ propagating modes, resulting in an additional *in-plane* photonic band structure. Especially combined with an inclined optic axis of the cavity medium like in an r-plane oriented microcavity, this could result in another kind of exceptional points with an additional degree of freedom [Wie16].

So far, the focus was on dielectric microcavities. Implementing microcavities which are tuned closer to excitonic resonances (e.g. of ZnO) would allow to study anisotropic cavity exciton-polaritons. Beyond the characteristics discovered in this thesis, this would allow investigations of non-linear effects induced by the coupling to the excitons: One of the most interesting questions would be how the anisotropic mode structure influences scattering towards the ground state and how the modes and exceptional points would evolve when approaching lasing or Bose-Einstein-like condensation. Rich dynamics can be expected because the optical constants change upon high excitation which is commonly observed as blueshift of exciton-polariton condensates. One can imagine that exceptional points are strongly shifted and may even dynamically appear or disappear. Another question is how the sensitivity of exceptional points to perturbations can be used e.g. to probe the dependence of excitons on temperature or external magnetic fields. Effects of magneto-optic coupling could be drastically enhanced.

When exploring exciton-polaritons and, generally, for further luminescence experiments, a dielectric bottom DBR would be desirable. This will be a future challenge for epitaxy or requires a flip-chip technique. For further experiments, polarization-resolved Fourier imaging with a microscope objective would also be preferable. Though, this will be a challenge in terms of polarization optics because the objective will introduce a number of non-idealities.

May be, in the future, anisotropic microcavities can help building intrinsically circularly polarized devices, striving after spintronics with light.

Appendix A

A.1 Determining optic axes

In the following, optically biaxial media are considered, independent on whether they are absorptive or not. The formalism applies also to uniaxial media, with some trivial degeneracies. In contrast to biaxial media, optic normal axes and optic ray axes coincide in the uniaxial case. A symmetric dielectric tensor $\hat{\varepsilon}$ is considered. It can be arbitrarily rotated by means of Euler matrices according to Eq. 1.20. Without loss of generality, propagation in the z direction is discussed: It is defined either by a wave vector $\vec{k} \parallel \vec{e}_z$ or a Poynting vector $\vec{\mathcal{S}} \parallel \vec{e}_z$. First, the principal refractive indices $\tilde{n}_{a/b}$, and eigenstate polarizations $\vec{\mathcal{D}}_{a/b}$ and $\vec{\mathcal{E}}_{a/b}$ are obtained for either case. They correspond to the principal axes of the cross-section ellipses in the ellipsoid representations, Fig. 1.4, and determine the distance from the origin for the wave surfaces, Fig. 1.5, respectively. Then the conditions for optic axes are investigated.

With the principal refractive indices $\tilde{n}_{a/b}$ and $\vec{k}^2 = \frac{\omega^2}{c_0^2}\tilde{n}_{a/b}^2$, the wave equation 1.8 reads

$$\begin{aligned} &\vec{\nabla} \times (\vec{\nabla}\vec{\mathcal{E}}) + \frac{1}{c_0^2}\mu\hat{\varepsilon}\frac{\partial^2}{\partial t^2}\vec{\mathcal{E}} = \vec{\nabla}(\vec{\nabla}\vec{\mathcal{E}}) - \vec{\nabla}^2\vec{\mathcal{E}} + \frac{1}{c_0^2}\mu\hat{\varepsilon}\frac{\partial^2}{\partial t^2}\vec{\mathcal{E}} \\ &= -\vec{k}(\vec{k}\vec{\mathcal{E}}) + \vec{k}^2\vec{\mathcal{E}} - \frac{\omega^2}{c_0^2}\mu\hat{\varepsilon}\vec{\mathcal{E}} = \vec{0}\,. \end{aligned} \tag{A.1}$$

One can also rewrite this for the magnetic field $\vec{\mathcal{H}}$ as

$$\vec{\nabla} \times \hat{\varepsilon}^{-1}(\vec{\nabla} \times \vec{\mathcal{H}}) + \frac{1}{c_0^2}\mu\frac{\partial^2}{\partial t^2}\vec{\mathcal{H}} = \vec{0}\,. \tag{A.2}$$

Wavefronts and optic normal axes

For $\vec{k} = (0, 0, k)^{\mathrm{T}}$, it holds according to Eq. A.1

$$-\vec{k}(\vec{k}\vec{\mathcal{E}}) + \vec{k}^2\vec{\mathcal{E}} - \frac{\omega^2}{c_0^2}\mu\hat{\varepsilon}\vec{\mathcal{E}} = -k^2\begin{pmatrix}0\\0\\\mathcal{E}_z\end{pmatrix} + k^2\begin{pmatrix}\mathcal{E}_x\\\mathcal{E}_y\\\mathcal{E}_z\end{pmatrix} - \frac{\omega^2}{c_0^2}\mu\hat{\varepsilon}\begin{pmatrix}\mathcal{E}_x\\\mathcal{E}_y\\\mathcal{E}_z\end{pmatrix}\,, \tag{A.3}$$

and hence the following determinant has to vanish ($\hat{\mu} = \hat{\mathbb{1}}$) [Yeh88; Ems+83; Cle66]:

$$\left|\begin{pmatrix}\tilde{n}^2 & 0 & 0\\ 0 & \tilde{n}^2 & 0\\ 0 & 0 & 0\end{pmatrix} - \begin{pmatrix}\varepsilon_{xx} & \varepsilon_{xy} & \varepsilon_{xz}\\ \varepsilon_{xy} & \varepsilon_{yy} & \varepsilon_{yz}\\ \varepsilon_{xz} & \varepsilon_{yz} & \varepsilon_{zz}\end{pmatrix}\right| = 0\,. \tag{A.4}$$

This, with $\hat{\varepsilon}^{-1} =: \hat{\mathfrak{z}}$ is equivalent to

$$\left| \begin{pmatrix} \mathfrak{z}_{xx} & \mathfrak{z}_{xy} & 0 \\ \mathfrak{z}_{xy} & \mathfrak{z}_{yy} & 0 \\ \mathfrak{z}_{xz} & \mathfrak{z}_{yz} & 0 \end{pmatrix} - \begin{pmatrix} \frac{1}{\tilde{n}^2} & 0 & 0 \\ 0 & \frac{1}{\tilde{n}^2} & 0 \\ 0 & 0 & \frac{1}{\tilde{n}^2} \end{pmatrix} \right| = 0\,, \tag{A.5}$$

which is the respective expression in $\vec{\mathcal{D}}$ and can be reduced to

$$\begin{vmatrix} \mathfrak{z}_{xx} - \frac{1}{\tilde{n}^2} & \mathfrak{z}_{xy} \\ \mathfrak{z}_{xy} & \mathfrak{z}_{yy} - \frac{1}{\tilde{n}^2} \end{vmatrix} = 0\,. \tag{A.6}$$

Thus, the squared principal refractive indices $\tilde{n}^2_{a/b} = 1/\mathfrak{z}_{a/b}$ for a wave front propagating along z are given by the inverse of the eigenvalues of $\begin{pmatrix} \mathfrak{z}_{xx} & \mathfrak{z}_{xy} \\ \mathfrak{z}_{xy} & \mathfrak{z}_{yy} \end{pmatrix}$. Consequently, an optic normal axis is found, if those eigenvalues degenerate.

Under the conditions of a complex symmetric 2 × 2 matrix, there are two qualitatively different cases which can occur if the eigenvalues degenerate (cf. section A.2): Either the matrix becomes diagonal, with two linearly independent eigenvectors; or, if off-diagonal elements remain, its eigenspace reduces to vectors describing either left or right circular polarization (see below). No other cases as those two can occur for the symmetric matrices. The respective conditions are discussed in the following.

For transparent biaxial media, an optic normal axis aligned with z is directly found if

$$\begin{pmatrix} \mathfrak{z}_{xx} & \mathfrak{z}_{xy} \\ \mathfrak{z}_{xy} & \mathfrak{z}_{yy} \end{pmatrix} \equiv \mathfrak{z}_a \hat{\mathbb{1}}\,. \tag{A.7}$$

If a wave front propagates along z, the propagation constant $\tilde{n}_a$ is independent of the polarization. Nevertheless, there are two linearly independent eigenvectors $\vec{\mathcal{D}}_{a/b}$ which describe linear polarization states. An arbitrarily polarized or unpolarized wave corresponds to a superposition of them. Any related Poynting vector is generally tilted against $\vec{k}$ and its orientation depends on the light polarization. A given wave front consists of at least two different light ray components, hence Poynting vectors. In the extreme case (all polarization components exist), there can be infinitely many, as observed as *internal* conical refraction [Lan+67].

For absorptive biaxial media, $\mathrm{Im}(\tilde{n}_a) \neq 0$, and a singular normal axis [Voi02;

Stu+16] is aligned with z if

$$\begin{pmatrix} \text{ɜ}_{xx} & \text{ɜ}_{xy} \\ \text{ɜ}_{xy} & \text{ɜ}_{yy} \end{pmatrix} \equiv \text{ɜ}_a \hat{\mathbb{1}} + \text{ɜ}_\eta \begin{pmatrix} 1 & \pm i \\ \pm i & -1 \end{pmatrix} \equiv \begin{pmatrix} \text{ɜ}_{xx} & \pm i \frac{\text{ɜ}_{xx} - \text{ɜ}_{yy}}{2} \\ \pm i \frac{\text{ɜ}_{xx} - \text{ɜ}_{yy}}{2} & \text{ɜ}_{yy} \end{pmatrix} . \tag{A.8}$$

Now, $\begin{pmatrix} \text{ɜ}_{xx} & \text{ɜ}_{xy} \\ \text{ɜ}_{xy} & \text{ɜ}_{yy} \end{pmatrix}$ has a degenerate eigenvalue ɜ_a (algebraic multiplicity two). Furthermore, the eigenspace consists in only one eigenvector $\vec{\mathcal{D}}_a \propto \begin{pmatrix} 1 \\ \pm i \end{pmatrix}$ (geometric multiplicity one; cf. section A.2). However, it should be noted that despite usage of the term *singular* axis, $\begin{pmatrix} \text{ɜ}_{xx} & \text{ɜ}_{xy} \\ \text{ɜ}_{xy} & \text{ɜ}_{yy} \end{pmatrix}$ is not singular but still a regular, invertible matrix. The value of ɜ_η is in principle arbitrary (as long as $\text{ɜ}_\eta \neq 0$) because $\begin{pmatrix} 1 & \pm i \\ \pm i & -1 \end{pmatrix} \vec{\mathcal{D}}_a = \vec{0}$. It depends on the given crystal[1].

Within the plane-wave approach and the assumption $\mathrm{Im}(\vec{\tilde{k}}) \parallel \mathrm{Re}(\vec{\tilde{k}})$ here, only circularly polarized light waves are allowed to propagate along a singular normal axis [Kha62; Voi08]. Also, such a wave is decomposed into differently oriented rays. Furthermore, it is damped.

Light rays and optic ray axes

To examine light rays, one can introduce a ray vector $\vec{s}$ such that $\vec{k} \times \vec{\mathcal{H}} = -\omega \vec{\mathcal{D}}$ turns into $\vec{s} \times \vec{\mathcal{H}} = -\omega \vec{\mathcal{E}} = \frac{1}{\varepsilon_0} \hat{\varepsilon}^{-1} (\vec{k} \times \vec{\mathcal{H}})$. Hence, $\vec{s} \parallel \vec{\mathcal{S}}$. Accordingly, it holds $\hat{\varepsilon}^{-1}(\vec{\nabla}\times) = i\hat{\varepsilon}^{-1}(\vec{k}\times) = i\varepsilon_0(\vec{s}\times)$. Substituting this into Eq. A.2 yields

$$\begin{aligned} &\vec{\nabla} \times \hat{\varepsilon}^{-1}(\vec{\nabla} \times \vec{\mathcal{H}}) + \frac{1}{c_0^2} \mu \frac{\partial^2}{\partial t^2} \vec{\mathcal{H}} = \vec{0} \\ &= -\varepsilon_0^2 \hat{\varepsilon} (\vec{s} \times (\vec{s} \times \vec{\mathcal{H}})) - \frac{\omega^2}{c_0^2} \mu \vec{\mathcal{H}} = \varepsilon_0^2 \hat{\varepsilon} \left(-\vec{s}(\vec{s}\vec{\mathcal{H}}) + \vec{s}^2 \vec{\mathcal{H}} \right) - \frac{\omega^2}{c_0^2} \mu \vec{\mathcal{H}} . \end{aligned} \tag{A.9}$$

Now, the divergence $\vec{s}\vec{\mathcal{H}}$ vanishes. Furthermore, one knows $\vec{s}^2 = \frac{1}{\varepsilon_0^2 \tilde{n}^4} \vec{k}^2 = \frac{\omega^2}{\varepsilon_0^2 c_0^2 \tilde{n}^2}$. Then, for $\vec{s} \parallel \vec{e}_z$, $\mathcal{H}_z = 0$, the following determinant has to vanish for

---

[1] For the exceptional points in optical modes, the inverse transmission Jones matrix $\hat{J}_t^{-1}$ corresponds to a singular matrix of the same shape with $\text{ɜ}_a = 0$.

a light ray propagating in z direction:

$$\left| \begin{pmatrix} \varepsilon_{xx} & \varepsilon_{xy} & 0 \\ \varepsilon_{xy} & \varepsilon_{yy} & 0 \\ \varepsilon_{xz} & \varepsilon_{yz} & 0 \end{pmatrix} - \begin{pmatrix} \tilde{n}^2 & 0 & 0 \\ 0 & \tilde{n}^2 & 0 \\ 0 & 0 & \tilde{n}^2 \end{pmatrix} \right| = 0\,. \tag{A.10}$$

This again, reduces to

$$\begin{vmatrix} \varepsilon_{xx} - \tilde{n}^2 & \varepsilon_{xy} \\ \varepsilon_{xy} & \varepsilon_{yy} - \tilde{n}^2 \end{vmatrix} = 0\,. \tag{A.11}$$

Hence, the principle refractive indices $\tilde{n}_{a/b} = \sqrt{\varepsilon_{a/b}}$ for a light ray propagating along z are the square roots of the eigenvalues of $\begin{pmatrix} \varepsilon_{xx} & \varepsilon_{xy} \\ \varepsilon_{xy} & \varepsilon_{yy} \end{pmatrix}$. This result could actually already be expected from Eq. A.4 when inserting $\vec{\mathcal{E}} = (\mathcal{E}_x, \mathcal{E}_y, 0)^{\mathrm{T}}$, which is fulfilled for any involved wave vector. Optic ray axes are found by the degeneracy of the eigenvalues $\varepsilon_{a/b}$.

For transparent biaxial media, an optic ray axis aligned with z is directly found if

$$\begin{pmatrix} \varepsilon_{xx} & \varepsilon_{xy} \\ \varepsilon_{xy} & \varepsilon_{yy} \end{pmatrix} \equiv \varepsilon_a \hat{\mathbb{1}}\,. \tag{A.12}$$

If a light ray propagates along z, the propagation constant $\tilde{n}_a$ is independent of the polarization. An arbitrarily polarized or unpolarized wave consists in a superposition of the two linearly polarized eigenvectors $\vec{\mathcal{E}}_{a/b}$. In general, different wave fronts belong to such a light ray. The Poynting vector is tilted against any related wave vector $\vec{k}$ and the orientation of the wave fronts depend on the polarization components. *External* conical refraction describes that infinitely many wave fronts are associated with a light ray propagating along an optic ray axis [Lan+67].

For absorptive biaxial media ($\mathrm{Im}(\tilde{n}_a) \neq 0$), a singular ray axis is aligned with z if

$$\begin{pmatrix} \varepsilon_{xx} & \varepsilon_{xy} \\ \varepsilon_{xy} & \varepsilon_{yy} \end{pmatrix} \equiv \varepsilon_a \hat{\mathbb{1}} + \varepsilon_\eta \begin{pmatrix} 1 & \pm i \\ \pm i & -1 \end{pmatrix} \equiv \begin{pmatrix} \varepsilon_{xx} & \pm i \frac{\varepsilon_{xx} - \varepsilon_{yy}}{2} \\ \pm i \frac{\varepsilon_{xx} - \varepsilon_{yy}}{2} & \varepsilon_{yy} \end{pmatrix}\,. \tag{A.13}$$

Now, $\begin{pmatrix} \varepsilon_{xx} & \varepsilon_{xy} \\ \varepsilon_{xy} & \varepsilon_{yy} \end{pmatrix}$ has a degenerate eigenvalue ε_a along with only one circularly polarized eigenvector $\vec{\mathcal{E}}_a \propto \begin{pmatrix} 1 \\ \pm i \end{pmatrix}$. The value of ε_η is in principle arbitrary again and depends on the given crystal.

A.2 Exceptional points

Under certain conditions, the eigenvalues of any complex 2x2 matrix - may it be a Jones matrix, dielectric function matrix, Hamiltonian or whatsoever - can degenerate. This one eigenvalue is said to possess algebraic multiplicity two. In certain cases it can occur that even the eigenvectors degenerate, leaving the eigenvalue's algebraic multiplicity and hence the dimension of the eigenspace at one, even without the matrix being singular. This is commonly referred to as exceptional points and is inherent to the group of non-Hermitian matrices/operators [Ber04; Hei04b; Hei04a].

As the eigenspace of a matrix is invariant when adding multiples of the identity matrix $\hat{\mathbb{1}}$, the following complex matrix $\hat{m}$ with $a, b, c \in \mathbb{C}$ can be considered without losing generality:

$$\hat{m} = \begin{pmatrix} a & b \\ c & -a \end{pmatrix} , \tag{A.14}$$

with the eigenvalues $\mu_{1,2} = \pm\sqrt{a^2 + bc}$. In case of degeneracy, $\mu_1 = \mu_2 = 0$ and $a = \pm i\sqrt{bc}$. Then the eigenvectors $\vec{m}$ are given as

$$\vec{m} \propto \begin{pmatrix} \sqrt{b} \\ \pm i\sqrt{c} \end{pmatrix} . \tag{A.15}$$

Now, there are two general cases: Either the geometric multiplicity is two, which means there exist two linearly independent eigenvectors, or it is one and the eigenspace becomes one-dimensional. The first case corresponds to $\hat{m}$ being a zero-matrix, which is equivalent to any identity matrix and represents cases like classic optic axes. Then, any arbitrary vector is eigenvector of $\hat{m}$. This is also the case for diabolical points, see section 1.1.3 and [Ber+08].

The second case with non-zero matrix entries refers to exceptional points. There are two general requirements for the occurrence of exceptional points:

1. From above it is clear that if $b = c^*$, then $\mathrm{Re}(a) = 0$. Hence, either $a = 0$ leads again to a zero-matrix (i.e. no exceptional point) or a is purely imaginary. Consequently, exceptional points cannot occur with Hermitian matrices.

2. The second requirement is closely connected: a non-vanishing imaginary part of the matrix. If $a, b, c \in \mathbb{R}$, then $a^2 = -bc$ could only be fulfilled

if they all are zero again. Otherwise, not even the eigenvalues could degenerate.

Reviewing the eigenvalue equation above, it is clear that exceptional points are a degeneracy of a complex square root in (a, b, c)-parameter space. This is the reason why exceptional points are occasionally called square-root singularities[2] [Cao+15]. An example of the complex-square-root topology is shown in Fig. A.1. In this example, μ is effectively expressed by two real-valued parameters (A, B), replacing (a, b, c). A typical characteristic of this topology, is mutual mode exchange when encircling an exceptional point in parameter space. Unless carrying out jumps between the two solutions $\mu_{1/2}$, the same solution is only reached if an exceptional point is encircled twice in the parameter space [Dem+04].

Exceptional points have been described in various physical systems and parameter spaces, e.g. [Hei12; Wie11; Lin+11; Yoo+11; Zhe+15; Gru+17b]. Even the transition from weak to strong coupling in the cavity-polariton theory is provided via an exceptional point in the parameter space spanned by the coupling strength V and the difference in the broadening of cavity photon and exciton, $\Delta_\Gamma = |\Gamma_X - \Gamma_c|$: According to Eq. 2.29, if the (real part of the) uncoupled energies of exciton and cavity-photon equal each other (*crossing point*), $E_X = E_c$, it holds $\tilde{E}_{LPB/UPB} = E_X - i\frac{\Gamma_X+\Gamma_\Lambda}{2} \pm \sqrt{4|V|^2 - \Delta_\Gamma^2}$. The case $\Delta_\Gamma < 4|V|$ is referred to as *strong coupling* and yields $E_{LPB} \neq E_{UPB}$ (cf. Eq. 2.31) while $\Gamma_{LPB} = \Gamma_{UPB}$. *Weak coupling* refers to the opposite case with different broadenings but degenerate real energy. At the transition between weak and strong coupling, $\Delta_\Gamma = 4|V|$, and LPB and UPB degenerate indistinguishably [Sav+99; Hei00; Rod16].

Regarding the eigenvector related to an exceptional point, the case of complex symmetric matrices is important: If $b = c$ above, $\hat{m}$ yields a circular or chiral eigenvector for an exceptional point [Hei+01]:

$$\vec{m} \propto \begin{pmatrix} 1 \\ \pm i \end{pmatrix} . \tag{A.16}$$

This is important e.g. for singular optic axes because the dielectric tensor (and its inverse) are symmetric. Also, if a transmission Jones matrix at an

---

[2] It should be noted that diabolical points are also square-root singularities in that sense.

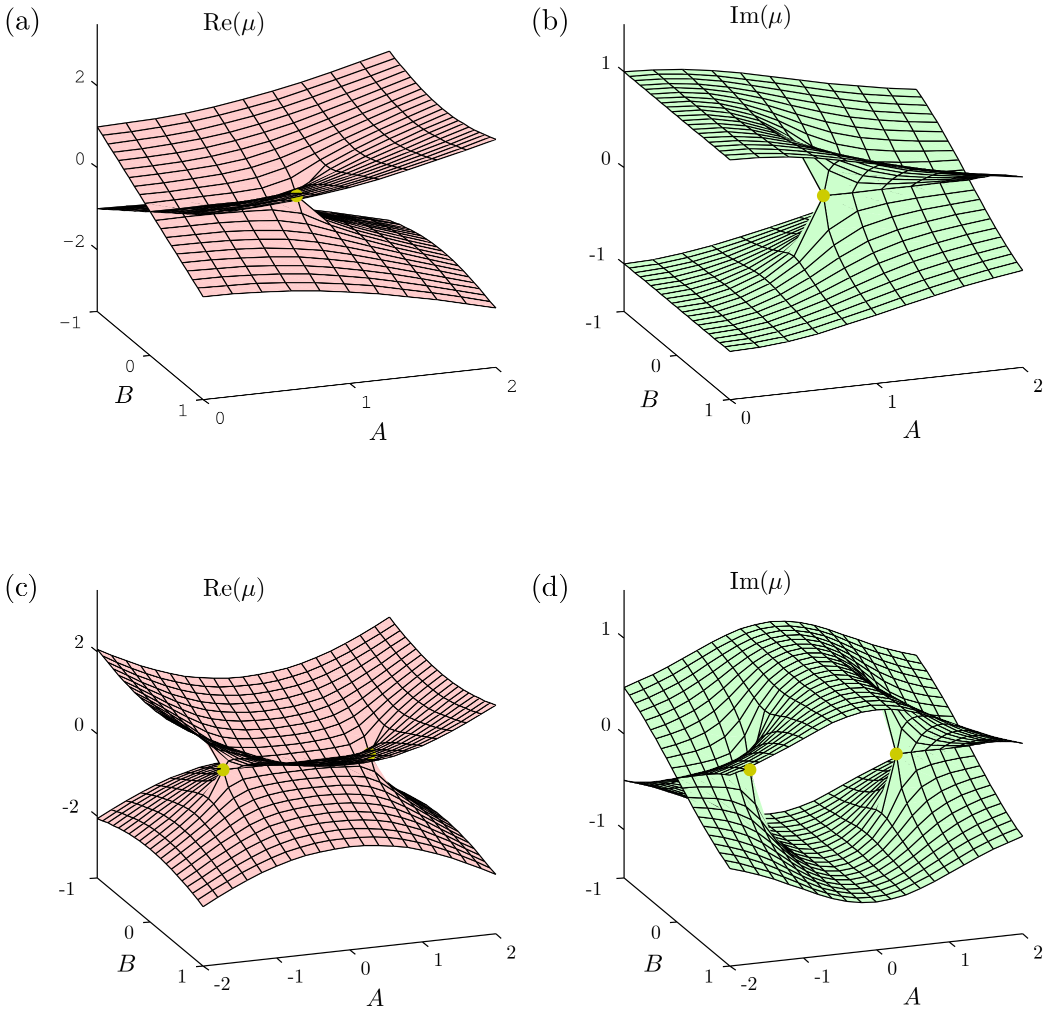

Figure A.1: Complex-square-root topology of the two-parameter eigenvalue surface $\mu = \pm\sqrt{A^2 + (B+i)^2}$, $A, B \in \mathbb{R}$, near exceptional points: (a,b): single exceptional point (yellow dot) within the (A, B)-parameter range. (c,d): Parameter range comprising two exceptional points (yellow dots). (a) and (c) represent the real part of the eigenvalue, (b) and (d) its imaginary part. At the exceptional points, both the real- and the imaginary-component surfaces degenerate. The surfaces are locally equivalent to the surfaces shown in Fig. 1.6 (b), (c) and 3.7.

exceptional point of an anisotropic microcavity is symmetric, this results in circularly polarized mode-degeneracies (see section 3.3).
In fact, in the same manner, if either $b = 0$ or $c = 0$, this results in $\vec{m} \propto (1,0)^{\mathrm{T}}$ or $\vec{m} \propto (0,1)^{\mathrm{T}}$. In the notation of a Jones vector, this would correspond to TE- or TM-polarized light [Gru+17a]. Similarly, $b = -c$ would result in eigenvectors $\vec{m} \propto (1, \pm 1)^{\mathrm{T}}$, representing $\pm 45°$-oriented linearly polarized light in the standard Jones vector notation.

Finally, it should be mentioned that exceptional points can, of course, also occur in higher-dimensional parameter spaces [Hei04a; Lin+16; Din+16].

A.3 Expressions in Gaußian CGS units

Often in literature, the Gaußian CGS unit system is used. Definitions of the electric and magnetic fields and fluxes differ then compared to the SI unit convention. A good overview and comparison of the different systems can be found in [Jac83] and [Yu+03]. Maxwell's equations 1.1-1.4 read in Gaußian CGS units

$$
\begin{aligned}
\vec{\nabla}\vec{\mathcal{D}} &= 4\pi\rho\,, && \text{(A.17)}\\
\vec{\nabla}\vec{\mathcal{B}} &= 0\,, && \text{(A.18)}\\
\vec{\nabla}\times\vec{\mathcal{E}} &= -\frac{1}{c_0}\frac{\partial}{\partial t}\vec{\mathcal{B}}\,, && \text{(A.19)}\\
\vec{\nabla}\times\vec{\mathcal{H}} &= \frac{1}{c_0}\frac{\partial}{\partial t}\vec{\mathcal{D}}+\frac{4\pi}{c_0}\vec{j}\,, && \text{(A.20)}
\end{aligned}
$$

and the constitutive relations Eqs.1.5 and 1.6 become

$$
\begin{aligned}
\vec{\mathcal{D}} &= \vec{\mathcal{E}}+4\pi\vec{\mathcal{P}} = \hat{\varepsilon}\vec{\mathcal{E}}\,, && \text{(A.21)}\\
\vec{\mathcal{B}} &= \vec{\mathcal{H}}+4\pi\vec{\mathcal{M}} = \hat{\mu}\vec{\mathcal{H}}\,. && \text{(A.22)}
\end{aligned}
$$

The optical conductivity (cf. Eqs. 1.13 and 1.14) in Gaußian CGS units is given as

$$
\hat{\sigma} = -i\frac{E}{2h}\hat{\varepsilon}\,. \qquad \text{(A.23)}
$$

4×4 transfer matrix formalism

Commonly, the transfer matrix formalism is expressed also in Gaußian CGS units, e.g. [Sch05; Sch96]. The differential transfer matrix $\hat{\Delta}_j$ in medium j (Eq. 1.33) becomes

$$
\hat{\Delta}_j = \begin{pmatrix}
-\sigma_x\frac{\varepsilon^j_{31}}{\varepsilon^j_{33}} & -\sigma_x\frac{\varepsilon^j_{32}}{\varepsilon^j_{33}} & 0 & 1-\frac{\sigma_x^2}{\varepsilon^j_{33}}\\
0 & 0 & -1 & 0\\
\frac{\varepsilon^j_{23}\varepsilon^j_{31}}{\varepsilon^j_{33}}-\varepsilon^j_{21} & \sigma_x^2-\varepsilon^j_{22}+\frac{\varepsilon^j_{23}\varepsilon^j_{32}}{\varepsilon^j_{33}} & 0 & \sigma_x\frac{\varepsilon^j_{23}}{\varepsilon^j_{33}}\\
\varepsilon^j_{11}-\frac{\varepsilon^j_{13}\varepsilon^j_{31}}{\varepsilon^j_{33}} & \varepsilon^j_{12}-\frac{\varepsilon^j_{13}\varepsilon^j_{32}}{\varepsilon^j_{33}} & 0 & -\sigma_x\frac{\varepsilon^j_{13}}{\varepsilon^j_{33}}
\end{pmatrix}. \qquad \text{(A.24)}
$$

The connection between magnetic and electric fields in isotropic media is given as $\vec{\mathcal{B}} = \tilde{n}(-\mathcal{E}_y, \mathcal{E}_x)^{\mathrm{T}}$ in CGS units. Accordingly, Eqs.1.34 and 1.35 differ from the expressions in SI convention:

$$\hat{T}_{I/O}^{a/s} = \begin{pmatrix} 0 & 0 & \frac{\sqrt{n_{a/s}^2-\sigma_x^2}}{n_{a/s}} & -\frac{\sqrt{n_{a/s}^2-\sigma_x^2}}{n_{a/s}} \\ 1 & 1 & 0 & 0 \\ -\sqrt{n_{a/s}^2 - \sigma_x^2} & \sqrt{n_{a/s}^2 - \sigma_x^2} & 0 & 0 \\ 0 & 0 & n_{a/s} & n_{a/s} \end{pmatrix}, \qquad (A.25)$$

and

$$(\hat{T}_{I/O}^{a/s})^{-1} = \frac{1}{2} \begin{pmatrix} 0 & 1 & \frac{-1}{\sqrt{n_{a/s}^2-\sigma_x^2}} & 0 \\ 0 & 1 & \frac{1}{\sqrt{n_{a/s}^2-\sigma_x^2}} & 0 \\ \frac{n_{a/s}}{\sqrt{n_{a/s}^2-\sigma_x^2}} & 0 & 0 & \frac{1}{n_{a/s}} \\ \frac{-n_{a/s}}{\sqrt{n_{a/s}^2-\sigma_x^2}} & 0 & 0 & \frac{1}{n_{a/s}} \end{pmatrix}. \qquad (A.26)$$

Normalization of the eigenmodes as discussed in section 1.2.1 would be given in Gaußian CGS units as $\mathcal{E}_y\mathcal{E}_y^* + \frac{\mathcal{H}_y}{\tilde{n}_j}\left(\frac{\mathcal{H}_y}{\tilde{n}_j}\right)^* = 1$.

A.4 Polarization patterns of *isotropic* microcavities

For comparison with the mode polarization patterns presented in chapter 3, the same is shown here for microcavities with cylindrical symmetry, i.e. with a cavity layer of isotropic material or of uniaxial material with its optic axis aligned parallel to the surface normal as e.g. *c*-plane oriented ZnO. By definition, the modes are degenerate at $\vec{k}_{||} = \vec{0}$. However, this case is not equivalent to exceptional points because the polarization eigenspace is two-dimensional and the cavity modes are independent of the polarization. Hence, the situation is more comparable to classic optic axes.
For $\vec{k}_{||} \neq \vec{0}$, the cavity splits into a TE- and TM-polarized mode. Depending on the tuning between λ_{DBR} and $n_c d_c$, either one or the other reveals the higher energy. Even energetic mode degeneracies can occur. Still, the modes have different broadenings in that case. The TE-polarized mode becomes narrower for large in-plane wave-vectors, while the TM-polarized one becomes broader [Stu+11]. This is due to the nature of the Fresnel equations.

Figures A.2 and A.3 show the mode polarization in terms of the projected Stokes vector $\vec{\tilde{S}}$ in two different ways. As TE and TM polarization are independent of each other, no superposition and hence circular polarization ($\tilde{S}_3$) occurs. Around $\vec{k}_{||} = \vec{0}$, an intrinsic vortex with winding number 2 can be seen. This is a trivial vortex originating from the projection of the TE and TM fields onto the xy laboratory coordinate system and is directly related to the so called *optical spin Hall effect* [Kav+06; Ley+07; Mar+11]. The winding number would reduce to 1 if not $(\tilde{S}_1, \tilde{S}_2)^{\mathrm{T}}$ but the orientation of the linear polarization would be considered (e.g. as double-arrows).

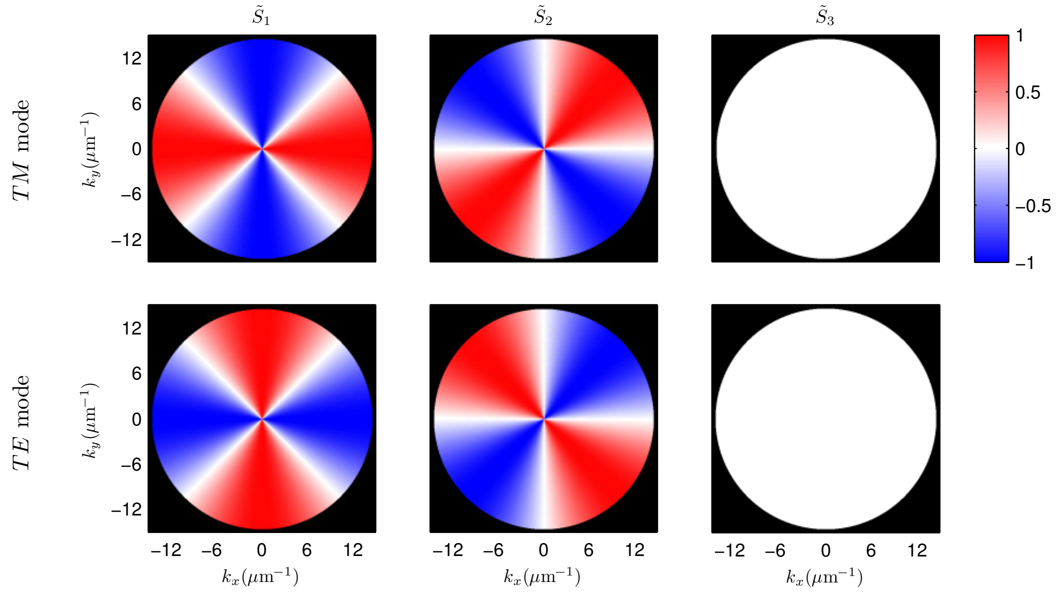

Figure A.2: Mode polarization in terms of the Stokes vector $\vec{\tilde{S}}$ according to Eq. 2.24 for a microcavity with cylindrical symmetry.

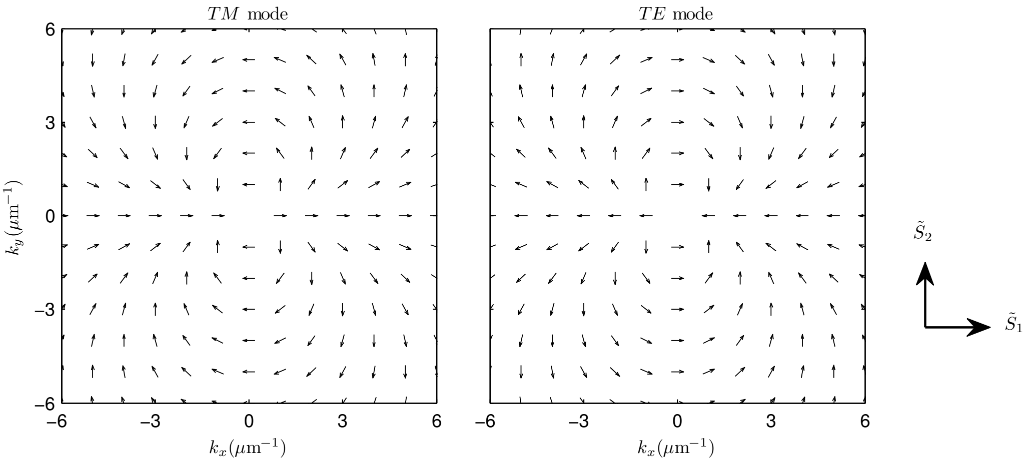

Figure A.3: Linear polarization components $(\tilde{S}_1, \tilde{S}_2)^{\mathrm{T}}$ for a microcavity with cylindrical symmetry.

Bibliography

[Agr72] V. M. Agranovich: *Optical properties of crystals in the excitonic region of the spectrum (excitons, photons, polaritons)*, in: *Optical Properties of Solids*, ed. by F. Abelès, North-Holland Publishing, 1972, chap. 6, ISBN: 0-7204-0204-2.

[Amo+09] A. Amo *et al.*: *Anisotropic optical spin Hall effect in semiconductor microcavities*, Phys. Rev. B **80** (16), 165325 (2009), DOI: `10.1103/PhysRevB.80.165325`.

[Amo+10] A. Amo *et al.*: *Exciton-polariton spin switches*, Nat. Photon. **4**, 361 (2010), DOI: `10.1038/nphoton.2010.79`.

[And+99] E. Anderson *et al.*: *LAPACK Users' Guide*, 3rd ed., SIAM, 1999, ISBN: 0-89871-447-8, URL: `www.netlib.org/lapack`.

[And95] L. C. Andreani: *Optical Transitions, Excitons, and Polaritons in Bulk and Low-Dimensional Semiconductor Structures*, in: *Confined Electrons and Photons*, ed. by E. Burstein and C. Weisbuch, vol. 340, NATO ASI Series, Springer, 1995, p. 57, ISBN: 978-1-4615-1963-8, DOI: `10.1007/978-1-4615-1963-8`.

[Ang+02] O. Angelsky *et al.*: *The relationship between topological characteristics of component vortices and polarization singularities*, Opt. Commun. **207**, 57 (2002), DOI: `10.1016/S0030-4018(02)01479-7`.

[Art10] O. Arteaga Barriel: *Mueller matrix polarimetry of anisotropic chiral media*, PhD thesis, Universitat de Barcelona, 2010.

[Art14] O. Arteaga: *Useful Mueller matrix symmetries for ellipsometry*, Thin Solid Films **571**, 584 (2014), DOI: `10.1016/j.tsf.2013.10.101`.

[Azz+77] R. M. Azzam and N. M. Bashara: *Ellipsometry and polarized light*, North-Holland Publishing, 1977, ISBN: 0-7204-0694-3.

[Ber+03] M. V. Berry and M. R. Dennis: *The optical singularities of birefringent dichroic chiral crystals*, Proc. R. Soc. Lond. A **459** (2033), 1261 (2003), DOI: `10.1098/rspa.2003.1155`.

[Ber+04] M. V. Berry, M. R. Dennis and R. L. Lee Jr.: *Polarization singularities in the clear sky*, New J. Phys. **6**, 162 (2004), DOI: `10.1088/1367-2630/6/1/162`.

[Ber+08] M. V. Berry and M. R. Jeffrey: *Conical diffraction: Hamilton's diabolical point at the heart of crystal optics*, in: *Progress in Optics*, ed. by E. Wolf, vol. 50, 2008, chap. 2, p. 13, DOI: `10.1016/S0079-6638(07)50002-8`.

[Ber04] M. V. Berry: *Physics of nonhermitian degeneracies*, Czech. J. Phys. **54** (10), 1039 (2004), DOI: `10.1023/B:CJOP.0000044002.05657.04`.

[Ber72] D. W. Berreman: *Optics in Stratified and Anisotropic Media:* 4 × 4-*Matrix Formulation*, J. Opt. Soc. Am. **62** (4), 502 (1972), DOI: `10.1364/JOSA.62.000502`.

[Bha+16] A. Bhattacharya *et al.*: *Output polarization characteristics of a GaN microcavity diode polariton laser*, Phys. Rev. B **94** (3), 035203 (2016), DOI: `10.1103/PhysRevB.94.035203`.

[Bli+08] K. Y. Bliokh *et al.*: *Singular polarimetry: Evolution of polarization singularities in electromagnetic waves propagating in a weakly anisotropic medium*, Opt. Express **16** (2), 695 (2008), DOI: `10.1364/OE.16.000695`.

[Blo+97] J. Bloch *et al.*: *Strong-coupling regime in pillar semiconductor microcavities*, Superlattice Microst. **22** (3), 371 (1997), DOI: `10.1006/spmi.1996.0317`.

[Bor+80] M. Born and E. Wolf: *Principles of optics*, 6th ed., Pergamon Press, 1980, ISBN: 0-08-026481-6.

[Bru35] D. A. G. Bruggeman: *Berechnung verschiedener physikalischer Konstanten von heterogenen Substanzen. I. Dielektrizitätskonstanten und Leitfähigkeiten der Mischkörper aus isotropen Substanzen*, Ann. Phys. **416** (7), 636 (1935), DOI: `10.1002/andp.19354160705`.

[Byk+13] D. A. Bykov and L. L. Doskolovich: *Numerical methods for calculating poles of the scattering matrix with applications in grating theory*, J. Lightwave Technol. **31** (5), 793 (2013), DOI: `10.1109/JLT.2012.2234723`.

[Byr16] S. J. Byrnes: *Multilayer optical calculations*, arXiv:1603.02720v2, 2016.

[Cao+15] H. Cao and J. Wiersig: *Dielectric microcavities: Model systems for wave chaos and non-Hermitian physics*, Rev. Mod. Phys. **87** (1), 61 (2015), DOI: `10.1103/RevModPhys.87.61`.

[Car+13] F. Cardano *et al.*: *Generation and dynamics of optical beams with polarization singularities*, Opt. Express **21** (7), 8815 (2013), DOI: `10.1364/OE.21.008815`.

[Cha+05] P. C. Y. Chang, J. G. Walker and K. I. Hopcraft: *Ray tracing in absorbing media*, J. Quant. Spectrosc. Radiat. Transf. **96** (3), 327 (2005), DOI: `10.1016/j.jqsrt.2005.01.001`.

[Cha50] S. Chandrasekhar: *Radiative transfer*, Oxford University Press, 1950.

[Che+11] J. Chen and H. Lu: *Generalized laws of reflection and refraction from real valued boundary conditions*, Opt. Commun. **284**, 3802 (2011), DOI: `10.1016/j.optcom.2011.04.022`.

[Che+95] Y. Chen, A. Tredicucci and F. Bassani: *Bulk exciton polaritons in GaAs microcavities*, Phys. Rev. B **52** (3), 1800 (1995), DOI: `10.1103/PhysRevB.52.1800`.

[Che13] R.-L. Chern: *Spatial dispersion and nonlocal effective permittivity for periodic layered metamaterials*, Opt. Express **21** (14), 16514 (2013), DOI: `10.1364/OE.21.016514`.

[Cil+15] P. Cilibrizzi *et al.*: *Polariton spin whirls*, Phys. Rev. B **92** (15), 155308 (2015), DOI: `10.1103/PhysRevB.92.155308`.

[Cil+16] P. Cilibrizzi *et al.*: *Half-skyrmion spin textures in polariton microcavities*, Phys. Rev. B **94** (4), 045315 (2016), DOI: `10.1103/PhysRevB.94.045315`.

[Cle66] P. C. Clemmow: *The Plane Wave Spectrum Representation of Electromagnetic Fields*, ed. by A. Cullen, V. Fock and J. Wait, vol. 12, International Series of Monographs in Electromagnetic Waves, Pergamon Press, 1966.

[Col+96] T. F. Coleman and Y. Li: *An Interior Trust Region Approach for Nonlinear Minimization Subject to Bounds*, SIAM J. Optim. **6** (2), 418 (1996), DOI: `10.1137/0806023`.

[Dem+01] C. Dembowski *et al.*: *Experimental Observation of the Topological Structure of Exceptional Points*, Phys. Rev. Lett. **86** (5), 787 (2001), DOI: `10.1103/PhysRevLett.86.787`.

[Dem+04] C. Dembowski *et al.*: *Encircling an exceptional point*, Phys. Rev. E **69** (5), 056216 (2004), DOI: `10.1103/PhysRevE.69.056216`.

[Den+09] M. R. Dennis, K. O'Holleran and M. J. Padgett: *Singular Optics: Optical Vortices and Polarization Singularities*, Prog. Optics **53**, 293 (2009), DOI: `10.1016/S0079-6638(08)00205-9`.

[Den+10] H. Deng, H. Haug and Y. Yamamoto: *Exciton-polariton Bose-Einstein condensation*, Rev. Mod. Phys. **82** (2), 1489 (2010), DOI: `10.1103/RevModPhys.82.1489`.

[Den01] M. R. Dennis: *Topological Singularities in Wave Fields*, PhD thesis, University of Bristol, 2001.

[Dev07] B. Deveaud, ed.: *The Physics of Semiconductor Microcavities*, Wiley-VCH, 2007, ISBN: 978-3-527-40561-9.

[Dev15] B. Deveaud: *Exciton-Polariton Bose-Einstein Condensates*, Annu. Rev. Condens. Matter Phys. **6**, 155 (2015), DOI: `10.1146/annurev-conmatphys-031214-014542`.

[Din+16] K. Ding *et al.*: *Emergence, Coalescence, and Topological Properties of Multiple Exceptional Points and Their Experimental Realization*, Phys. Rev. X **6** (2), 021007 (2016), DOI: `10.1103/PhysRevX.6.021007`.

[Duf+15] S. Dufferwiel *et al.*: *Spin Textures of Exciton-Polaritons in a Tunable Microcavity with Large TE-TM Splitting*, Phys. Rev. Lett. **115** (24), 246401 (2015), DOI: `10.1103/PhysRevLett.115.246401`.

[Dup+94] M. A. Dupertuis, B. Acklin and M. Proctor: *Generalization of complex Snell-Descartes and Fresnel laws*, J. Opt. Soc. Am. A **11** (3), 1159 (1994), DOI: `10.1364/JOSAA.11.001159`.

[Ems+83] A. G. Emslie and J. R. Aronson: *Determination of the complex dielectric tensor of triclinic crystals: theory*, J. Opt. Soc. Am. **73** (7), 916 (1983), DOI: `10.1364/JOSA.73.000916`.

[Fau+08] S. Faure *et al.*: *Comparison of strong coupling regimes in bulk GaAs, GaN, and ZnO semiconductor microcavities*, Phys. Rev. B **78** (23), 235323 (2008), DOI: `10.1103/PhysRevB.78.235323`.

[Fau+09] S. Faure *et al.*: *Relaxation and emission of Bragg-mode and cavity-mode polaritons in a ZnO microcavity at room temperature*, Appl. Phys. Lett. **95**, 121102 (2009), DOI: `10.1063/1.3232228`.

[Fel01] D. Felbacq: *Numerical computation of resonance poles in scattering theory*, Phys. Rev. E **64** (4), 047702 (2001), DOI: `10.1103/PhysRevE.64.047702`.

[Fen+14] L. Feng *et al.*: *Demonstration of a large-scale optical exceptional point structure*, Opt. Express **22** (2), 1760 (2014), DOI: `10.1364/OE.22.001760`.

[Flo+05] F. Flossmann *et al.*: *Polarization Singularities from Unfolding an Optical Vortex through a Birefringent Crystal*, Phys. Rev. Lett. **95** (25), 253901 (2005), DOI: `10.1103/PhysRevLett.95.253901`.

[Fra+12] H. Franke *et al.*: *Ballistic propagation of exciton-polariton condensates in a ZnO-based microcavity*, New J. Phys. **14** (1), 013037 (2012), DOI: `10.1088/1367-2630/14/1/013037`.

[Fra12] H. Franke: *PLD-grown ZnO-based Microcavities for Bose-Einstein Condensation of Exciton-Polaritons*, PhD thesis, Universität Leipzig, 2012.

[Fre+02] I. Freund *et al.*: *Stokes singularity relations*, Opt. Lett. **27** (7), 545 (2002), DOI: `10.1364/OL.27.000545`.

[Fuj07] H. Fujiwara: *Spectroscopic Ellipsometry, Principles and Applications*, Wiley, 2007, ISBN: 0-470-01608-6.

[Gál+01] J. Gál *et al.*: *Polarization patterns of the summer sky and its neutral points measured by full-sky imaging polarimetry in Finnish Lapland north of the Arctic Circle*, Proc. R. Soc. A **457**, 1385 (2001), DOI: `10.1098/rspa.2000.0726`.

[Gao+15] T. Gao *et al.*: *Observation of non-Hermitian degeneracies in a chaotic exciton-polariton billiard*, Nature **526**, 554 (2015), DOI: `10.1038/nature15522`.

[Gao+17] T. Gao *et al.*: *Chiral modes at exceptional points in exciton-polariton quantum fluids*, arXiv:1705.09752v1, 2017.

[Gar06] J. C. M. Garnett: *Colours in Metal Glasses, in Metallic Films, and in Metallic Solutions. II*, Phil. Trans. R. Soc. A **205** (387), 237 (1906), DOI: `10.1098/rsta.1906.0007`.

[Ger+07] D. Gerace and L. C. Andreani: *Quantum theory of exciton-photon coupling in photonic crystal slabs with embedded quantum wells*, Phys. Rev. B **75** (23), 235325 (2007), DOI: `10.1103/PhysRevB.75.235325`.

[Gir+12] R. Giri *et al.*: *Giant photoinduced Faraday rotation due to the spin-polarized electron gas in an n-GaAs microcavity*, Phys. Rev. B **85** (19), 195313 (2012), DOI: `10.1103/PhysRevB.85.195313`.

[Gol59] H. Goldstein: *Classical mechanics*, Addison-Wesley, 1959.

[Gon+15] S.-H. Gong *et al.*: *Giant Rabi Splitting of Whispering Gallery Polaritons in GaN/InGaN Core-Shell Wire*, Nano Lett. **15** (7), 4517 (2015), DOI: `10.1021/acs.nanolett.5b01023`.

[Gru+17a] M. Grundmann *et al.*: *Exceptional points in anisotropic photonic structures: from non-Hermitian physics to possible device applications*, Proc. SPIE, 101050K (2017), DOI: `10.1117/12.2260816`.

[Gru+17b] M. Grundmann *et al.*: *Optically Anisotropic Media: New Approaches to the Dielectric Function, Singular Axes, Raman Scattering Intensities and Microcavity Modes*, Phys. Status Solidi RRL **11** (1), 1600295 (2017), DOI: `10.1002/pssr.201600295`.

[Gru06] M. Grundmann: *The Physics of Semiconductors, An Intoduction Including Devices and Nanophysics*, Springer, 2006, ISBN: 3-540-25370-X.

[Gui+11] T. Guillet *et al.*: *Polariton lasing in a hybrid bulk ZnO microcavity*, Appl. Phys. Lett. **99** (16), 161104 (2011), DOI: `10.1063/1.3650268`.

[Has+14] T. Hasegawa *et al.*: *High-sensitivity polarization modulation reflectance spectroscopy of cavity polaritons in a ZnO microcavity*, Appl. Phys. Express **7** (3), 032003 (2014), DOI: `10.7567/APEX.7.032003`.

[Hei+01] W. D. Heiss and H. L. Harney: *The chirality of exceptional points*, Eur. Phys. J. D **17** (2), 149 (2001), DOI: `10.1007/s100530170017`.

[Hei00] W. D. Heiss: *Repulsion of resonance states and exceptional points*, Phys. Rev. E **61** (1), 929 (2000), DOI: `10.1103/PhysRevE.61.929`.

[Hei04a] W. D. Heiss: *Exceptional points of non-Hermitian operators*, J. Phys. A: Math. Gen. **37** (6), 2455 (2004), DOI: `10.1088/0305-4470/37/6/034`.

[Hei04b] W. D. Heiss: *Exceptional Points - Their Universal Occurrence and Their Physical Significance*, Czech. J. Phys. **54** (10), 1091 (2004), DOI: `10.1023/B:CJOP.0000044009.17264.dc`.

[Hei12] W. D. Heiss: *The physics of exceptional points*, J. Phys. A: Math. Theor. **45** (44), 444016 (2012), DOI: `10.1088/1751-8113/45/44/444016`.

[Hen98] K. Henneberger: *Additional Boundary Conditions: An Historical Mistake*, Phys. Rev. Lett. **80** (13), 2889 (1998), DOI: `10.1103/PhysRevLett.80.2889`.

[Her17] O. Herrfurth: *Development of a femtosecond time-resolved spectroscopic ellipsometry setup*, Master thesis, Universität Leipzig, 2017.

[Hop58] J. J. Hopfield: *Theory of the Contribution of Excitons to the Complex Dielectric Constant of Crystals*, Phys. Rev. **112** (5), 1555 (1958), DOI: `10.1103/PhysRev.112.1555`.

[Hou+94] R. Houdré *et al.*: *Measurement of Cavity-Polariton Dispersion Curve from Angle-Resolved Photoluminescence Experiments*, Phys. Rev. Lett. **73** (15), 2043 (1994), DOI: `10.1103/PhysRevLett.73.2043`.

[Hun08] C. Hunte: *The Jones-Mueller transformation*, Fizika A **17**, 51 (2008).

[Hva74] J. M. Hvam: *Exciton Interaction in Photoluminescence from ZnO*, Phys. Status Solidi B **63** (2), 511 (1974), DOI: `10.1002/pssb.2220630210`.

[Int] Intel Corp.: *Developer Reference for Intel Math Kernel Library 2017 - Fortran*, URL: `software.intel.com/en-us/mkl-developer-reference-fortran`.

[Jac83] J. D. Jackson: *Klassische Elektrodynamik*, ed. by G. Heber, trans. by K. Müller, 2nd ed., de Gruyter, 1983, ISBN: 3-11-009579-3.

[Jam+17] O. Jamadi *et al.*: *Edge-emitting polariton laser and amplifier based on a ZnO waveguide*, arXiv:1708.00501v1, 2017.

[Jan+16] A. Janot, B. Rosenow and G. Refael: *Topological polaritons in a quantum spin Hall cavity*, Phys. Rev. B **93** (16), 161111 (2016), DOI: `10.1103/PhysRevB.93.161111`.

[Jan16] A. Janot: *Quantum Condensates and Topological Bosons in Coupled Light-Matter Excitations*, PhD thesis, Universität Leipzig, 2016.

[Jel98] G. E. Jellison Jr.: *Spectroscopic ellipsometry data analysis: measured versus calculated quantities*, Thin Solid Films **33**, 313 (1998), DOI: `10.1016/S0040-6090(97)00765-7`.

[Kam+12] E. Kammann *et al.*: *Nonlinear Optical Spin Hall Effect and Long-Range Spin Transport in Polariton Lasers*, Phys. Rev. Lett. **109** (3), 036404 (2012), DOI: `10.1103/PhysRevLett.109.036404`.

[Kas+06] J. Kasprzak *et al.*: *Bose-Einstein condensation of exciton polaritons*, Nature **443**, 409 (2006), DOI: `10.1038/nature05131`.

[Kat66] T. Kato: *Perturbation theory for linear operators*, Die Grundlehren der mathematischen Wissenschaft 132, Springer, 1966.

[Kav+03] A. Kavokin, G. Malpuech and B. Gil: *Semiconductor microcavities: towards polariton lasers*, MRS Internet J. Nitride Semicond. Res. **8** (3) (2003), DOI: `10.1557/S1092578300000466`.

[Kav+04] K. V. Kavokin *et al.*: *Quantum Theory of Spin Dynamics of Exciton-Polaritons in Microcavities*, Phys. Rev. Lett. **92**, 017401 (2004), DOI: `10.1103/PhysRevLett.92.017401`.

[Kav+06] A. Kavokin, G. Malpuech and G. Mikhail: *Optical Spin Hall Effect*, Phys. Rev. Lett. **95**, 136601 (2006), DOI: `10.1103/PhysRevLett.95.136601`.

[Kav+07] A. V. Kavokin *et al.*: *Microcavities*, ed. by R. Nicholas and H. Kamimura, Series on Semiconductor Science and Technology 16, Oxford University Press, 2007, ISBN: 978-0-19-922894-2.

[Kav06] A. Kavokin: *PHYS6012: Coherent Light, Coherent Matter*, University lectures, 2006.

[Kha62] A. P. Khapalyuk: *On the theory of circular optical axes*, Opt. Spectrosc. (USSR) **12**, 52 (1962).

[Kis07] A. D. Kiselev: *Singularities in polarization resolved angular patterns: transmittance of nematic liquid crystal cells*, J. Physics: Cond. Matter **19** (24), 246102 (2007), DOI: `10.1088/0953-8984/19/24/246102`.

[Kli+10] C. Klingshirn *et al.*: *65 years of ZnO research - old and very recent results*, Phys. Status Solidi B **247** (6), 1424 (2010), DOI: `10.1002/pssb.200983195`.

[Kli+81] C. Klingshirn and H. Haug: *Optical properties of highly excited direct gap semiconductors*, Phys. Rep. **70** (5), 315 (1981), DOI: `10.1016/0370-1573(81)90190-3`.

[Kli07] C. F. Klingshirn: *Semiconductor Optics*, 3rd ed., Springer, 2007, ISBN: 3-540-21328-7.

[Kło+06] Ł. Kłopotowski *et al.*: *Optical anisotropy and pinning of the linear polarization of light in semiconductor microcavities*, Solid State Commun. **139** (10), 511 (2006), DOI: `10.1016/j.ssc.2006.07.016`.

[Knö86] H. Knörrer: *Die Fresnelsche Wellenfläche*, in: *Arithmetik und Geometrie*, vol. 3, Mathematische Miniaturen, Birkhäuser, 1986.

[Kos+08] H. Kosaka *et al.*: *Coherent Transfer of Light Polarization to Electron Spins in a Semiconductor*, Phys. Rev. Lett. **100** (9), 096602 (2008), DOI: `10.1103/PhysRevLett.100.096602`.

[Kri+06] D. N. Krizhanovskii *et al.*: *Rotation of the plane of polarization of light in a semiconductor microcavity*, Phys. Rev. B **73** (7), 073303 (2006), DOI: `10.1103/PhysRevB.73.073303`.

[Lag+09] K. G. Lagoudakis *et al.*: *Observation of Half-Quantum Vortices in an Exciton-Polariton Condensate*, **326** (5955), 974 (2009), DOI: `10.1126/science.1177980`.

[Lag+98] J. C. Lagarias et al.: *Convergence Properties of the Nelder-Mead Simplex Method in Low Dimensions*, SIAM J. Optim. **9** (1), 112 (1998).

[Lag77] J. Lagois: *Dielectric theory of interacting excitonic resonances*, Phys. Rev. B **16** (4), 1699 (1977), DOI: `10.1103/PhysRevB.16.1699`.

[Lan+67] L. D. Landau and E. M. Lifschitz: *Elektrodynamik der Kontinua*, ed. by G. Heber, vol. VIII, Lehrbuch der theoretischen Physik, Berlin: Akademie-Verlag, 1967.

[Lee10] S.-Y. Lee: *Geometrical phase imprinted on eigenfunctions near an exceptional point*, Phys. Rev. A **82** (6), 064101 (2010), DOI: `10.1103/PhysRevA.82.064101`.

[Ley+07] C. Leyder *et al.*: *Observation of the optical spin Hall effect*, Nat. Phys. **3**, 628 (2007), DOI: `10.1038/nphys676`.

[Li+13] F. Li *et al.*: *From Excitonic to Photonic Polariton Condensate in a ZnO-Based Microcavity*, Phys. Rev. Lett. **110** (19), 196406 (2013), DOI: `10.1103/PhysRevLett.110.196406`; F. Li *et al.*: *Fabrication and characterization of a room-temperature ZnO polariton laser*, Appl. Phys. Lett. **102** (19), 191118 (2013), DOI: `10.1063/1.4804986`.

[Lic] G. C. Lichtenberg, *Ueber die Kopfzeuge. Eine Apologie für die Frauenzimmer-Moden und ihre Abbildungen im Kalender*, in: *Taschenbuch zum Nutzen und Vergnügen fürs Jahr 1780 (Göttinger Taschen Calender vom Jahr 1780)*, publ. by J. C. Dieterich, 1779, p. 115 (original spelling "allesammt"), URL: `http://resolver.sub.uni-goettingen.de/purl?PPN680326618`.

[Lin+11] Z. Lin *et al.*: *Unidirectional Invisibility Induced by $\mathcal{PT}$-Symmetric Periodic Structures*, Phys. Rev. Lett. **106** (21), 213901 (2011), DOI: `10.1103/PhysRevLett.106.213901`.

[Lin+16] Z. Lin *et al.*: *Enhanced Spontaneous Emission at Third-Order Dirac Exceptional Points in Inverse-Designed Photonic Crystals*, Phys. Rev. Lett. **117** (10), 107402 (2016), DOI: `10.1103/PhysRevLett.117.107402`.

[Lin+84] P. J. Lin-Chung and S. Teitler: 4 × 4 *Matrix formalisms for optics in stratified anisotropic media*, J. Opt. Soc. Am. A **1** (7), 703 (1984), DOI: `10.1364/JOSAA.1.000703`.

[Lu+14] L. Lu, J. D. Joannopoulos and M. M. Soljačić: *Topological photonics*, Nat. Photon. **8**, 821 (2014), DOI: `10.1038/nphoton.2014.248`, URL: `https://arxiv.org/abs/1408.6730`.

[Mac+00] T. G. Mackay and W. S. Weiglhofer: *Homogenization of biaxial composite materials: dissipative anisotropic properties*, J. Opt. A: Pure Appl. Opt. **2** (5), 426 (2000), DOI: `10.1088/1464-4258/2/5/313`.

[Mac+03] T. G. Mackay and A. Lakhtakia: *Voigt wave propagation in biaxial composite materials*, J. Opt. A: Pure Appl. Opt. **5** (2), 91 (2003), DOI: `10.1088/1464-4258/5/2/303`.

[Mac61] W. Macke: *Wellen, Ein Lehrbuch der theoretischen Physik*, 2. Aufl., Leipzig: Akademische Verlagsgesellschaft Geest & Portig, 1961.

[Mak94] T. Makino: *Threshold condition of DFB semiconductor lasers by the local-normal-mode transfer-matrix method: correspondence to the coupled-wave method*, J. Lightwave Technol. **12** (12), 2092 (1994), DOI: `10.1109/50.350622`.

[Man+11] F. Manni *et al.*: *Spin-to-orbital angular momentum conversion in semiconductor microcavities*, Phys. Rev. B **83** (24), 241307 (2011), DOI: `10.1103/PhysRevB.83.241307`.

[Mar+02] M. D. Martín *et al.*: *Polarization Control of the Nonlinear Emission of Semiconductor Microcavities*, Phys. Rev. Lett. **89** (7), 077402 (2002), DOI: `10.1103/PhysRevLett.89.077402`.

[Mar+11] M. Maragkou *et al.*: *Optical analogue of the spin Hall effect in a photonic cavity*, Opt. Lett. **36**, 1095 (2011), DOI: `10.1364/OL.36.001095`.

[Mar+73] A. A. Maradudin and D. L. Mills: *Effect of Spatial Dispersion on the Properties of a Semi-Infinite Dielectric*, Phys. Rev. B **7** (6), 2787 (1973), DOI: `10.1103/PhysRevB.7.2787`.

[Mata] MATLAB, version 7.7.0.471 (R2008b), The MathWorks Inc., Natick, Massachusetts, USA.

[Matb] MATLAB webserver, Pushkov Institute of Terrestrial Magnetism, Ionosphere and Radiowave Propagation (Russian Academy of Sciences), URL: `matlab.izmiran.ru`.

[Mic+14] T. Michalsky *et al.*: *Phonon-assisted lasing in ZnO microwires at room temperature*, Appl. Phys. Lett. **105** (21), 211106 (2014), DOI: `10.1063/1.4902898`.

[Mic17] T. Michalsky: *Propagating exciton-polariton states in one- and two-dimensional ZnO-based cavity systems*, submitted PhD thesis, Universität Leipzig, 2017.

[Mol+03] C. Moler and C. V. Loan: *Nineteen Dubious Ways to Compute the Exponential of a Matrix, Twenty-Five Years Later*, SIAM Review **45** (1), 3 (2003).

[Mor+13] S. Morina, T. C. H. Liew and I. A. Shelykh: *Magnetic field control of the optical spin Hall effect*, Phys. Rev. B **88** (3), 035311 (2013), DOI: `10.1103/PhysRevB.88.035311`.

[Nak+08] M. Nakayama *et al.*: *Observation of Exciton Polaritons in a ZnO Microcavity with HfO_2/SiO_2 Distributed Bragg Reflectors*, J. Phys. Soc. Jpn. **77** (9), 093705 (2008), DOI: `10.1143/JPSJ.77.093705`.

[Neu15] M. Neumann: *Einfluss der Elektron-Loch-Wechselwirkung auf die dielektrische Funktion von ZnO, MgO und hexagonalem MgZnO*, PhD thesis, Technische Universität Berlin, 2015.

[Nob+04] T. Nobis *et al.*: *Whispering Gallery Modes in Nanosized Dielectric Resonators with Hexagonal Cross Section*, Phys. Rev. Lett. **93** (10), 103903 (2004), DOI: `10.1103/PhysRevLett.93.103903`.

[Nye97] J. F. Nye: *Line Singularities in Wave Fields*, Phil. Trans. **355** (1731), 2065 (1997).

[Old89] C. Oldano: *Electromagnetic-wave propagation in anisotropic stratified media*, Phys. Rev. A **40** (10), 6014 (1989), DOI: `10.1103/PhysRevA.40.6014`.

[Oro+11] L. Orosz *et al.*: *Fabrication and optical properties of a fully-hybrid epitaxial ZnO-based microcavity in the strong-coupling regime*, Appl. Phys. Express **4** (7), 072001 (2011), DOI: `10.1143/APEX.4.072001`.

[Oue+15] C. Ouellet-Plamondon *et al.*: *Multiple polariton modes originating from the coupling of quantum wells in planar microcavity*, Phys. Rev. B **92** (7), 075313 (2015), DOI: `10.1103/PhysRevB.92.075313`.

[Pan+99a] G. Panzarini and L. C. Andreani: *Quantum theory of exciton polaritons in cylindrical semiconductor microcavities*, Phys. Rev. B **60** (24), 16799 (1999), DOI: `10.1103/PhysRevB.60.16799`.

[Pan+99b] G. Panzarini *et al.*: *Exciton-light coupling in single and coupled semiconductor microcavities: Polariton dispersion and polarization splitting*, Phys. Rev. B **59** (7), 5082 (1999), DOI: `10.1103/PhysRevB.59.5082`.

[Pau+95] S. Pau *et al.*: *Microcavity exciton-polariton splitting in the linear regime*, Phys. Rev. B **51** (20), 14437 (1995), DOI: `10.1103/PhysRevB.51.14437`.

[Pek58] S. I. Pekar: *The theory of electromagnetic waves in a crystal in which excitons are produced*, Sov. Phys. JETP **6** (4), 785 (1958).

[Pet+13] Y. Petit *et al.*: *Recent advances in monoclinic crystal optics*, Laser Photonics Rev. **7** (6), 920 (2013), DOI: `10.1002/lpor.201200078`.

[Pot04] R. J. Potton: *Reciprocity in optics*, Rep. Prog. Phys. **67** (5), 717 (2004), DOI: `10.1088/0034-4885/67/5/R03`.

[Rév+10] F. Réveret *et al.*: *Modelling of strong coupling regime in bulk GaN microcavities using transfer matrix and quasiparticle formalisms*, Solid State Commun. **150**, 122 (2010), DOI: `10.1016/j.ssc.2009.09.036`.

[Rév+12] F. Réveret *et al.*: *Influence of optical confinement and excitonic absorption on strong coupling in a bulk GaN microcavity grown on silicon*, Superlattice Microst. **52**, 541 (2012), DOI: `10.1016/j.spmi.2012.06.002`.

[Ric+05] M. Richard *et al.*: *Consequences of strong coupling between excitons and microcavity leaky modes*, Appl. Phys. Lett. **86**, 071916 (2005), DOI: `10.1063/1.1861979`.

[Ric+15] S. Richter *et al.*: *Maxwell consideration of polaritonic quasi-particle Hamiltonians in multi-level systems*, Appl. Phys. Lett. **107** (23), 231104 (2015), DOI: `10.1063/1.4937462`.

[Ric+17] S. Richter *et al.*: *Exceptional points in anisotropic planar microcavities*, Phys. Rev. A **95** (2), 023836 (2017), DOI: `10.1103/PhysRevA.95.023836`.

[Ric12] S. Richter: *Exciton-Polaritons in ZnO-based Microresonators: Pseudospin and Magnetic Fields*, Master thesis, Universität Leipzig, 2012.

[Rod16] S. R.-K. Rodriguez: *Classical and quantum distinctions between weak and strong coupling*, Eur. J. Phys., EJP **37** (2), 025802 (2016), DOI: `10.1088/0143-0807/37/2/025802`.

[Sal+15] V. G. Sala *et al.*: *Spin-Orbit Coupling for Photons and Polaritons in Microstructures*, Phys. Rev. X **5** (1), 011034 (2015), DOI: `10.1103/PhysRevX.5.011034`.

[Sav] V. Savona: *Linear Optical Properties of Semiconductor Microcavities with Embedded Quantum Wells*, University lecture notes.

[Sav+94] V. Savona *et al.*: *Quantum theory of quantum-well polaritons in semiconductor microcavities*, Phys. Rev. B **49** (13), 8774 (1994), DOI: `10.1103/PhysRevB.49.8774`.

[Sav+95] V. Savona *et al.*: *Quantum well excitons in semiconductor microcavities: Unified treatment of weak and strong coupling regimes*, Solid State Commun. **93** (9), 733 (1995), DOI: `10.1016/0038-1098(94)00865-5`.

[Sav+99] V. Savona *et al.*: *Optical properties of microcavity polaritons*, Phase Transit. **68**, 169 (1999), DOI: `10.1080/01411599908224518`.

[Sch+10] R. Schmidt-Grund *et al.*: *Two-dimensional confined photonic wire resonators - strong light-matter coupling*, Phys. Status Solidi B **247** (6), 1351 (2010), DOI: `10.1002/pssb.200945530`.

[Sch05] M. Schubert: *Theory and Application of Generalized Ellipsometry*, in: *Handbook of Ellipsometry*, ed. by H. Tompkins and E. Irene, William Andrew Publishing/Springer, 2005, chap. 9, ISBN: 0-8155-1499-9.

[Sch07] R. Schmidt-Grund: *Dielectric Function of ZnO and MgZnO and Application to Bragg Reflectors and Micro-Resonators*, PhD thesis, Universität Leipzig, 2007.

[Sch96] M. Schubert: *Polarization-dependent optical parameters of arbitrarily anisotropic homogeneous layered systems*, Phys. Rev. B **53** (8), 4265 (1996), DOI: `10.1103/PhysRevB.53.4265`.

[She+04] I. Shelykh *et al.*: *Semiconductor microcavity as a spin-dependent optoelectronic device*, Phys. Rev. B **70** (3), 035320 (2004), DOI: `10.1103/PhysRevB.70.035320`.

[She+05] I. A. Shelykh, A. V. Kavokin and G. Malpuech: *Spin dynamics of exciton polaritons in microcavities*, Phys. Status Solidi B **242** (11), 2271 (2005), DOI: `10.1002/pssb.200560965`.

[She+10] I. A. Shelykh *et al.*: *Polariton polarization-sensitive phenomena in planar semiconductor microcavities*, Semicond. Sci. Technol. **25**, 013001 (2010), DOI: `10.1088/0268-1242/25/1/013001`.

[Sol+08] D. D. Solnyshkov *et al.*: *Magnetic field effect on polarization and dispersion of exciton-polaritons in planar microcavities*, Phys. Rev. B **78** (16), 165323 (2008), DOI: `10.1103/PhysRevB.78.165323`.

[Sos+01] M. S. Soskin and M. V. Vasnetsov: *Singular optics*, Prog. Optics **42**, 219 (2001), DOI: `10.1016/S0079-6638(01)80018-4`.

[Str41] J. A. Stratton: *Electromagnetic Theory*, ed. by D. Dudley, IEEE Press Series on Electromagnetic Wave Theory, Reissued, IEEE Press and Wiley-Interscience, 2007, orig. 1941, ISBN: 0-470-13153-5.

[Stu+11] C. Sturm *et al.*: *Cavity-photon dispersion in one-dimensional confined microresonators with an optically anisotropic cavity material*, Phys. Rev. B **83** (20), 205301 (2011), DOI: `10.1103/PhysRevB.83.205301`.

[Stu+16] C. Sturm and M. Grundmann: *Singular optical axes in biaxial crystals and analysis of their spectral dispersion effects in* $\beta-\mathrm{Ga_2O_3}$, Phys. Rev. A **93** (5), 053839 (2016), DOI: `10.1103/PhysRevA.93.053839`.

[Stu11] C. Sturm: *Exciton-Polaritons in ZnO-based Microresonators: Dispersion and Occupation*, PhD thesis, Universität Leipzig, 2011.

[Sun+08] L. Sun *et al.*: *Direct Observation of Whispering Gallery Mode Polaritons and their Dispersion in a ZnO Tapered Microcavity*, Phys. Rev. Lett. **100** (15), 156403 (2008), DOI: `10.1103/PhysRevLett.100.156403`.

[Ver+12] M. A. M. Versteegh, D. Vanmaekelbergh and J. I. Dijkhuis: *Room-Temperature Laser Emission of ZnO Nanowires Explained by Many-Body Theory*, Phys. Rev. Lett. **108** (15), 157402 (2012), DOI: `10.1103/PhysRevLett.108.157402`.

[Vla+96] M. R. Vladimirova, A. V. Kavokin and M. A. Kaliteevski: *Dispersion of bulk exciton polaritons in a semiconductor microcavity*, Phys. Rev. B **54** (20), 14566 (1996), DOI: `10.1103/PhysRevB.54.14566`.

[Voi02] W. Voigt: *VII. On the behaviour of pleochroitic crystals along directions in the neighbourhood of an optic axis*, Philos. Mag. 6th ser. **4** (19), 90 (1902), DOI: `10.1080/14786440209462820`; W. Voigt: *Beiträge zur Aufklärung der Eigenschaften pleochroitischer Krystalle*, Götting. Nachr. **1**, 48 (1902), URL: `www.digizeitschriften.de/dms/resolveppn/?PID=GDZPPN002499207`; W. Voigt: *Beiträge zur Aufklärung der Eigenschaften pleochroitischer Krystalle*, Ann. Phys. **314** (10), 367 (1902), DOI: `10.1002/andp.19023141006`; W. Voigt: *Weiteres zur Aufklärung der Eigenschaften plechroitischer Krystalle*, Götting. Nachr. **5**, 269 (1902), URL: `www.digizeitschriften.de/dms/resolveppn/?PID=GDZPPN00249941X`.

[Voi08] W. Voigt: *Ein optisches Paradoxon*, Ann. Phys. **332** (15), 1023 (1908), DOI: `10.1002/andp.19083321505`.

[Wei11] T. Weiss: *Advanced numerical and semi-analytical scattering matrix calculations for modern nano-optics*, PhD thesis, Universität Stuttgart, 2011.

[Wie11] J. Wiersig: *Structure of whispering-gallery modes in optical microdisks perturbed by nanoparticles*, Phys. Rev. A **84** (6), 063828 (2011), DOI: `10.1103/PhysRevA.84.063828`.

[Wie16] J. Wiersig: *Sensors operating at exceptional points: General theory*, Phys. Rev. A **93** (3), 033809 (2016), DOI: `10.1103/PhysRevA.93.033809`.

[Wöh+88] H. Wöhler *et al.*: *Faster* 4×4 *matrix method for uniaxial inhomogeneous media*, J. Opt. Soc. Am. A **5** (9), 1554 (1988), DOI: `10.1364/JOSAA.5.001554`.

[Woo10] J. A. Woollam Co. Inc.: *Guide to Using WVASE32*, Lincoln, Nebraska, USA, 2010.

[Yar+84] A. Yariv and P. Yeh: *Optical Waves in Crystals*, Wiley series in pure and applied optics, John Wiley & Sons, 1984, ISBN: 0-471-09142-1.

[Yeh80] P. Yeh: *Optics of anisotropic layered media: A new* 4×4 *matrix algebra*, Surf. Sci. **96**, 41 (1980), DOI: `10.1016/0039-6028(80)90293-9`.

[Yeh88] P. Yeh: *Optical Waves in Layered Media*, Wiley series in pure and applied optics, John Wiley & Sons, 1988, ISBN: 0-471-82866-1.

[Yoo+11] G. Yoo, H.-S. Sim and H. Schomerus: *Quantum noise and mode nonorthogonality in non-Hermitian $\mathcal{PT}$-symmetric optical resonators*, Phys. Rev. A **84** (6), 063833 (2011), DOI: `10.1103/PhysRevA.84.063833`.

[Yu+03] P. Y. Yu and M. Cardona: *Fundamentals of Semiconductors, Physics and Materials Properties*, Springer, 2003, ISBN: 3-540-41323-5.

[Zam+02] M. Zamfirescu *et al.*: *ZnO as a material mostly adapted for the realization of room-temperature polariton lasers*, Phys. Rev. B **65** (16), 161205 (2002), DOI: `10.1103/PhysRevB.65.161205`.

[Zhe+14] B. Zhen *et al.*: *Topological Nature of Optical Bound States in the Continuum*, Phys. Rev. Lett. **113** (25), 257401 (2014), DOI: `10.1103/PhysRevLett.113.257401`.

[Zhe+15] B. Zhen *et al.*: *Spawning rings of exceptional points out of Dirac cones*, Nature **525**, 354 (2015), DOI: `10.1038/nature14889`.

[Zúñ+16] J. Zúñiga-Pérez *et al.*: *Homoepitaxial nonpolar (10-10) ZnO/ZnMgO monolithic microcavities: Towards reduced photonic disorder*, Appl. Phys. Lett. **108** (25), 251904 (2016), DOI: `10.1063/1.4954796`.

Symbols and Abbreviations

General notation:

X	scalar value
$\vec{X}$	vector
$\vec{e}_X$ ($\vec{X} = X\vec{e}_X$)	(Cartesian) unit vector with respect to $\vec{X}$
$\hat{X}$	matrix (tensor)
$\tilde{X}$	mostly complex-valued, also for modified definitions
X^*	complex conjugate
$(...)^{\mathrm{T}}$	transpose

Electromagnetic-wave description:

$\mathcal{E}$, $\vec{\mathcal{E}}$	electric field
$\mathcal{D}$, $\vec{\mathcal{D}}$	dielectric displacement
$\mathcal{P}$, $\vec{\mathcal{P}}$	electric polarization
$\mathcal{M}$, $\vec{\mathcal{M}}$	magnetization
$\mathcal{H}$, $\vec{\mathcal{H}}$	magnetic field
$\mathcal{B}$, $\vec{\mathcal{B}}$	magnetic flux density
$\vec{j}$	electric current density
ρ	free charge carrier density
$\vec{k} = k\vec{e}_k$ ($\vec{k_0} = k_0\vec{e}_k$)	wave vector (vacuum)
$\vec{\tilde{k}} = \vec{k} + i\vec{\eta}$	complex wave-vector (inhomogeneous wave)
$\vec{r} = (x, y, z)^{\mathrm{T}}$	spatial coordinate vector
t	time
$\mathcal{S}$, $\vec{\mathcal{S}}$	Poynting vector

Material properties:

$\varepsilon = \varepsilon_1 + i\varepsilon_2$, $\hat{\varepsilon}$	dielectric function (permittivity)
$\chi_\mathcal{E}$, $\chi_\mathcal{H}$ ($\hat{\chi}_\mathcal{E}$, $\hat{\chi}_\mathcal{H}$)	electric/magnetic susceptibility
$\tilde{n} = n + i\kappa = \sqrt{\varepsilon}$, $\hat{\tilde{n}}$	complex refractive index
n, $\hat{n}$	refractive index
κ, $\hat{\kappa}$	extinction coefficient
σ, $\hat{\sigma}$	(optical) conductivity tensor
μ, $\hat{\mu}$	magnetic permeability

Complex frequencies[3]**:**

$\tilde{E} = E - i\Gamma$	complex (photon) energy
$E = \mathrm{Re}(\tilde{E})$	(photon) energy
$\Gamma = -\mathrm{Im}(\tilde{E})$	approx. corresponding to spectral broadening as $HWHM$
$\tilde{\omega} = \omega - i\gamma$	complex angular frequency
$f = \omega/(2\pi)$	frequency
λ (λ_0)	wavelength (in vacuum)

Electromagnetic-wave calculus:

$\vec{k}_{\|\|} = (k_x, k_y)^\mathrm{T} = k_{\|\|}\vec{e}_{\|\|} = k_{\|\|}\,(\cos(\varphi), \sin(\varphi))^\mathrm{T}$	in-plane wave-vector
$k_\perp = k_z$	out-of-plane wave-vector
I	intensity
R	reflectance
T	transmittance
A	absorbance
$\tilde{r}$	complex reflection coefficient
$\tilde{t}$	complex transmission coefficient

---

[3] Throughout this thesis, the term *energy* is used as synonym to frequency, i.e. $E = \hbar\omega = hf$, not referring to intensity. In those rare cases the term *field energy* is explicitly used.

Ψ, Δ: $X = \tan\Psi e^{i\Delta}$	complex number parametrization in Jones-calculus context
$\hat{J}$	Jones matrix
$\hat{S}$	scattering matrix
$\vec{J}$	Jones vector
P	pseudo spin, Bloch vector with basis states TE, TM
$\tilde{P}$	pseudo spin, Bloch vector with basis states $\vec{\mathcal{E}}\vert\vert\vec{x}$, $\vec{\mathcal{E}}\vert\vert\vec{y}$ (projection)
$\vec{S} = (S_0, S_1, S_2, S_3)^{\mathrm{T}}$	Stokes vector
$\hat{M}$	Müller matrix
$\hat{T}$	transfer matrix
$\hat{\Delta}$, $\hat{\Delta}^j$	differential transfer matrix (medium j)
θ, θ_j	angle of incidence (in medium j), i.e. angle of the normal to the front of constant phase of a wave (with respect to the surface normal)
d, d_j	layer thickness (layer j)
$\hat{\mathcal{R}}$	Euler rotation matrix
(ϕ, ϑ, ξ)	Euler angles
$\sigma_x = n_i \sin(\theta_i)$	tangential wave-vector projection ($k_x = \frac{E}{\hbar c_0}\sigma_x$)

Discrete energies and related:

E_Λ	free photon energy
Λ	photon-like Hopfield coefficient
$\tilde{E}_c = E_c - i\Gamma_c$	complex energy of the cavity-photon mode
m_c	cavity photon mass
m	mode number
E_{DBR}, λ_{DBR}	central energy/wavelength of a DBR (at normal incidence)

$E_{X0} = E_\mathrm{T}$	transverse exciton energy
$E_{XL} = E_\mathrm{L}$	longitudinal exciton energy
Δ_LT	longitudinal-transverse splitting
$\mathcal{F}$	oscillator strength
$\hat{H}$	Hamiltonian
V	coupling strength
Ξ	wave function

Others:

$\hat{\mathbb{1}}$	identity matrix
$\nabla = (\frac{\partial}{\partial x}, \frac{\partial}{\partial y}, \frac{\partial}{\partial z})^\mathrm{T}$	nabla operator
φ	phase of a complex number
$\mathbb{Z}$	integer-number range
$\mathbb{R}$	real-number range
$\mathbb{C}$	complex-number range
$\vec{A}$	Berry connection
$\vec{F}$	Berry curvature
C	Chern number

Constants (in SI units):

ε_0	vacuum permittivity	$8.854 \cdot 10^{-12}\,\frac{\mathrm{As}}{\mathrm{Vm}}$
μ_0	vacuum permeability	$1.257 \cdot 10^{-6}\,\frac{\mathrm{Vs}}{\mathrm{Am}}$
c_0	vacuum speed of light	$2.998 \cdot 10^{8}\,\frac{\mathrm{m}}{\mathrm{s}}$
h	Planck constant	$4.136 \cdot 10^{-15}\,\mathrm{eVs}$
$\hbar = \frac{h}{2\pi}$	reduced Planck constant	$6.582 \cdot 10^{-16}\,\mathrm{eVs}$

SI units of the electromagnetic field quantities:

$\mathcal{E}$	$\frac{\mathrm{V}}{\mathrm{m}}$
$\mathcal{H}$	$\frac{\mathrm{A}}{\mathrm{m}}$
$\mathcal{D}$	$\frac{\mathrm{As}}{\mathrm{m}^2}$
$\mathcal{B}$	$\frac{\mathrm{Vs}}{\mathrm{m}^2} = \mathrm{T}$
$\vec{k}$, k	$\frac{1}{\mathrm{m}}$
$\mathcal{S}$	$\frac{\mathrm{VA}}{\mathrm{m}^2} = \frac{\mathrm{W}}{\mathrm{m}^2}$

Abbreviations:

AOI	angle of incidence
POI	plane of incidence
TE, s	transverse electric polarization ($\vec{\mathcal{E}}$ *senkrecht* to POI)
TM, p	transverse magnetic polarization ($\vec{\mathcal{E}}$ *parallel* to POI)
eo / o	extra-ordinary / ordinary
R/L	right/left circular polarization
arb.u.	arbitrary units
SI	Système international d'unités (international system of units)
CGS	centimeter-gram-second system of units
DBR	distributed Bragg reflector
$HWHM$	half width at half maximum
L/T	longitudinal/transverse (energies)
LPB	lower polarion branch
UPB	upper polariton branch
r.h.s.	right hand side
l.h.s.	left hand side
cw	continous wave
YSZ	Yttrium-stabilized Zirconium oxide
PLD	pulsed laser deposition
MBE	molecular-beam epitaxy
$SO(3)$	3-dimensional rotation group (special orthogonal group)
$SU(2)$	2-dimensional special unitary group

Authored and co-authored publications directly related to this thesis

- [Ric+17]: Steffen Richter, Tom Michalsky, Chris Sturm, Bernd Rosenow, Marius Grundmann and Rüdiger Schmidt-Grund: *Exceptional points in anisotropic planar microcavities*, Phys. Rev. A **95** (2), 023836 (2017)
- [Gru+17b]: Marius Grundmann, Chris Sturm, Christian Kranert, Steffen Richter, Rüdiger Schmidt-Grund, Christiane Deparis and Jesús Zúñiga-Pérez: *Optically Anisotropic Media: New Approaches to the Dielectric Function, Singular Axes, Raman Scattering Intensities and Microcavity Modes*, Phys. Stat. Sol. RRL **11** (1), 1600295 (2017)
- [Gru+17a]: Marius Grundmann, Steffen Richter, Tom Michalsky, Chris Sturm, Jesús Zúñiga-Pérez and Rüdiger Schmidt-Grund: *Exceptional points in anisotropic photonic structures: from non-Hermitian physics to possible device applications*, Proc. SPIE 101050K (2017)
- [Ric+15]: Steffen Richter, Tom Michalsky, Lennart Fricke, Chris Sturm, Helena Franke, Marius Grundmann and Rüdiger Schmidt-Grund: *Maxwell consideration of polaritonic quasi-particle Hamiltonians in multi-level systems*, Appl. Phys. Lett. **107** (23), 231104 (2015)

Acknowledgments

Starting with a remaining puzzle from my master thesis, after a while, rigorous computation of anisotropic planar microcavity structures turned out to be a very rich direction of research. I would like to thank Rüdiger Schmidt-Grund and Prof. Marius Grundmann for giving me the time and freedom to gain experience and figure out all important aspects as well as misunderstandings and mistakes. Getting into new concepts is always hard work. For the most stimulating discussions and ideas I am deeply indebted to Tom Michalsky and Lennart Fricke. Chris Sturm, Prof. Bernd Rosenow and Heinrich-Gregor Zirnstein helped me a lot with substantial and intensive discussions. Thank you for taking all the time! I'm very grateful to Jesús Zúñiga-Pérez and Christiane Deparis (both CRHEA) for providing excellent MBE-grown samples *on demand*, and Prof. Marius Grundmann for initiating the cooperation. Experimental realization would not have been possible without this support! For help with the PLD-growth of top DBRs, I owe thanks to Lukas Trefflich and Chris Sturm. I would also like to thank Fabian Klüpfel, Christian Kranert, Alexander Janot, Prof. Bernd Rheinländer, Oliver Herrfurth, Max Kneiß, Robert Karsthof, Christian Heinrichs, Axel Schüler, Holger Täubig, André Heber and Rüdiger Kürsten for smaller and larger discussions, remarks and hints. For all kinds of technical support in different labs or offices, I thank Jörg Lenzner, Roswitha Riedel, Gabi Benndorf, Daniel Splith and Carsten Bundesmann (*Leibniz-Institut für Oberflächenmodifizierung* (IOM)). Here, I would like to mention Chris Sturm again as the original builder of the goniometer. Hard work was also sometimes necessary on the administrative site. Therefore, I thank Anja Heck and Birgit Wendisch most sincerely for taking care of all the paper work and complicated issues related to a number of working contracts I could sign during the years!

What is a good topic for a dissertation? The way toward the anisotropic cavities was not exactly a straight one. In between, I spent a lot of time trying to advance the technique of *time-resolved spectroscopic ellipsometry*. For a long time, the attempts had not been successful, though. After the *7th International Conference on Spectroscopic Ellipsometry* in June 2016 in Berlin, however, a new and great cooperation opened new possibilities to really implement time-resolved spectroscopic ellipsometry. Eventually, after four years working at the university, I ended up with two topics worth writing a PhD thesis about: I would like to very cordially thank the RP4 team at *ELI beamlines*, Dolní Břežany, Czech Republic, for all the great time we had in and outside the lab. Many thanks especially to Shirly Josefina Espinoza Herrera, Mateusz Rębarz, Oliver Herrfurth, Miroslav Kloz and Jakob Andreasson! I hope we will continue working together soon.

The last years at the *Semiconductor Physics Group* (HLP) were a great time also aside physics. I remember a number of barbecues, bicycle tours, conferences, coffee breaks, breakfast sessions, volleyball matches, BuildMoNa modules, ... (and also late and weekend sessions in the lab) we experienced together. Of those not already mentioned above, I would like to name in particular also Helena Franke, Martin Thunert, Anna Reinhardt, Peter Schlupp, Abdurashid Mavlonov, Holger von Wenckstern, Tammo Böntgen, Marcel Wille and Vitaly Zviagin. At this point also special thanks again to Rüdiger Schmidt-Grund as head of the ellipsometry group within the HLP!

Finally, I would like to express my gratitude to friends not mentioned yet, as well as to my family, for all the support during the last years, especially when I struggled with the scientific system!

During the time as PhD student I benefited from various funding opportunities, mainly from Universität Leipzig (research area *complex matter*), Freistaat Sachsen (project *COSIMA*), Deutsche Forschungsgemeinschaft DFG (Sonderforschungsbereich SFB 762 *Funktionalität oxidischer Grenzflächen*, and project *Bose-Einstein-Kondensation und Supraflüssigkeit von Exziton-Polaritonen bei Raumtemperatur*), and European Social Fund ESF (Nachwuchsforschergruppe *Effiziente Energienutzung: Neue Konzepte und Materialien*). Further support came from the Leipzig graduate School BuildMoNa, Research Academy Leipzig, Wilhelm und Else Heraeus-Stiftung, DFG (Forschergruppe FOR 1616 *Dynamik und Interaktion von Halbleiternanodrähten für die Optoelektronik*), Mediterranean Institute of Fundamental Physics, and ELI beamlines.

Aug 2017, Steffen Richter

Curriculum Vitae

Personal Information

Name	Steffen Richter
Date of Birth	October 1, 1987
Place of Birth	Leipzig
Nationality	German

Education and Employment

Sep 1998 - Jul 2006	Secondary school (Gymnasium): Thomasschule zu Leipzig, Graduation: Abitur
Sep 2006 - Aug 2007	Civil service
Oct 2007 - Sep 2010	Physics Studies: Universität Leipzig Graduation: Bachelor of Science (B.Sc.) Aug 2009 - Jan 2010: Linköpings universitet, Sweden, Erasmus exchange studies
Oct 2010 - Dec 2012	Physics Studies: Universität Leipzig Graduation: Master of Science (M.Sc.) Jul - Sep 2011: Deutsches Elektronen-Synchrotron, DESY, Summer Student Programme
Jan 2013 - Dec 2017	Scientific Employee (Doktorand) at Universität Leipzig, Semiconductor Physics Group

Research experience

2012 Master thesis: *Exciton-Polaritons in ZnO-based Microresonators: Pseudospin and Magnetic Fields*

Universität Leipzig, Fakultät für Physik und Geowissenschaften, Institut für Experimentelle Physik II, Halbleiterphysik (Dr. Rüdiger Schmidt-Grund, Dr. Chris Sturm, Prof. Dr. Marius Grundmann)

2011 DESY summer student programme: *A MATLAB Program for Beam Spot Evaluation at the PG2 Beamline Diagnostics Port at FLASH*

DESY - Deutsches Elektronen-Synchrotron, HASYLAB (Dr. Natalia Gerasimova)

2010 Bachelor thesis: *Quantitative Na Detection in* $Cu(In,Ga)Se_2$ *Thin Film Solar Cells Using Ion Beam Analysis*

Universität Leipzig, Fakultät für Physik und Geowissenschaften, Institut für Experimentelle Physik II, Nukleare Festkörperphysik (Dr. Daniel Spemann, Prof. Dr. Tilman Butz)

2009 Advanced project in applied physics: *Deposition and characterization of ZrSiN Films*

Linköpings universitet, Institutionen för fysik, kemi och biologi (IFM), Nanostructured materials group (Dr. Naureen Ghafoor; joint project with Elena Tajuelo Rodríguez and Christian Bur)

2006 Internship: *Untersuchung von* ZnO-MgO-ZrO_2 *- Bragg-Reflektor- und Resonatorstrukturen*

Universität Leipzig, Fakultät für Physik und Geowissenschaften, Institut für Experimentelle Physik II, Halbleiterphysik (Dr. Rüdiger Schmidt-Grund, Prof. Dr. Bernd Rheinländer, Prof. Dr. Marius Grundmann)

Changes to the document

The following changes have been applied with respect to the originally submitted version of this thesis:

- Second paragraph on page 8: corrected mistake about the orthogonal tripods.
- Corrected caption of Fig. A.1 (Parameters A and B had been exchanged).
- If known, typographical errors and misprints have been corrected.
- The CV was updated.

Mar 2018, Steffen Richter